Advanced Techniques to Process Differential Phase Measurements for Polarimetric X-band Weather Radars

Reinoso Rondinel, Ricardo

DOI
10.4233/uuid:75e75d2f-68fe-4fa0-9f33-43bf2b7cfc89

Publication date
2018

Document Version
Final published version

Citation (APA)
Reinoso Rondinel, R. (2018). *Advanced Techniques to Process Differential Phase Measurements for Polarimetric X-band Weather Radars*. [Dissertation (TU Delft), Delft University of Technology]. https://doi.org/10.4233/uuid:75e75d2f-68fe-4fa0-9f33-43bf2b7cfc89

Advanced Techniques to Process Differential Phase Measurements for Polarimetric X-band Weather Radars

ADVANCED TECHNIQUES TO PROCESS DIFFERENTIAL PHASE MEASUREMENTS FOR POLARIMETRIC X-BAND WEATHER RADARS

Proefschrift

ter verkrijging van de graad van doctor
aan de Technische Universiteit Delft,
op gezag van de Rector Magnificus prof. dr. ir. T.H.J.J. van der Hagen,
voorzitter van het College voor Promoties,
in het openbaar te verdedigen op vrijdag 21 september 2018 om 12:30 uur

door

Ricardo REINOSO-RONDINEL

Master of Science in Electrical and Computer Engineering,
University of Oklahoma, Norman, The United States of America,
geboren te Lima, Peru.

Dit proefschrift is goedgekeurd door de promotor

Samenstelling promotiecommissie:

Rector Magnificus,	voorzitter
Prof. Dr. H.J.W. Russchenberg,	Technische Universiteit Delft, promotor
Onafhankelijke leden:	
Prof. dr. A. Yarovoy	Technische Universiteit Delft
Prof. dr. C. Simmer	University Bonn, Germany
Prof. dr. V. Chandrasekar	Colorado State University, USA
Dr. A. Berne	Ecole Polytechnique Federale de Lausanne, Switzerland
Dr. D. Moisseev	University of Helsinki, Finland
Dr. H. Leijnse	Koninklijk Nederlands Meteorologisch Instituut
Prof. ir. P. Hoogeboom	Technische Universiteit Delft, reservelid

This research was supported by the European Union's INTERREG IVB NWE programme through the RainGain project.

Department of Geosciences and Remote Sensing, Delft University of Technology

Keywords: weather radar, signal processing, rain observations, convective storms, radar polarimetry

Citation: Reinoso-Rondinel, R. (2018), Advanced techniques to process differential phase measurements for polarimetric X-band weather radars. PhD thesis, Delft University of Technology.

ISBN 978-94-6366-063-1

Cover courtesy of the GVR group: A. Savazzi and E. Martens.

An electronic version of this dissertation is available at
http://repository.tudelft.nl/.

Typeset by the author with the LaTeX Documentation System.

CONTENTS

ACKNOWLEDGMENTS

This thesis could not be realized without the support of my family, supervisors, colleagues, and friends. Many thanks for believing in me!

The journey has been long, maybe too long, but it has allowed me meeting extraordinary people and living unforgettable adventures in few places of the world. My first experiences started at home and during my early years in high-school, where I received discipline from my family members, especially my parents, and teachers. My grades never stood out until I took the courses of Arithmetic and Algebra, given by two teachers who truly inspired me. It is there where the passion for mathematics together with a curiosity of what is beyond high-school begun and went from bachelor studies in Peru to master studies in the USA, and a doctorate program in the Netherlands. Thank you again, Florinda Rondinel-Lagos, Justino Reinoso-Moran, and Rosalinda Reinoso-Rondinel because your support through all aspects of my life has been, without question, a primary resource for motivation and success.

I'm grateful to my instructors along my career because they have challenged me to give the best of me. Thank you to my advisors from the radar master program at the University of Oklahoma (OU-ARRC), Bob, Tian, Sebastian, and Phillip who introduced me to the weather radar world and taught me how research is done and what it means. Thanks to my ARRC colleagues, Danny, Brad, Yadong, and Hernan. More good memories come from my former roommates Jose, Carlos, Jose Manuel, Alex, and Hamish and all my Peruvian and Venezuelan friends and family. Let's not forget the good moments at PANAM and the Library bar! Thank you, OU international office: Karen, Sheena, and Kye, for your support in immigration regulations and for organizing multi-cultural events.

The long distance between Peru and the USA was not an excuse to continue having a good friendship with my buddies from the Pontifical Catholic University of Peru (PUCP), Landazuri prom '97, and my neighborhood. Thank you, Jose, Walter, William, Joselo, Alex, and family for your unconditional friendship and amusing anecdotes during our undergraduate studies, football tournaments, El Elos, summer beach time, and welcome/farewell parties.

Of course, I wouldn't have been here in the Netherlands if Herman Russchenberg and his atmospheric research group would not have selected me as a Ph.D. candidate for the RainGain project at Delft University of Technology (TU Delft - GRS). Thank you, Herman, Christine, Tobias, Yann, RainGain partners, KNMI, and Secretaries Rebeca, Lidwien, Debbie, and Suzanne, for this professional opportunity, your support, and collaboration which have allowed me to achieve my Ph.D. degree. Special thanks to my Ph.D. committee members for their efforts put in reviewing my work and for offering their comments, suggestions, and corrections. Also to my paranymphs David Jimenez-Lluva and Lukas Klespe who decided to assist me during my thesis defense.

This thesis would not have been a success without the social and fun aspects offered in TU Delft. Following my Latin instincts, I found, the SoSalsa student association. I

want to thanks my board members Aline, Lisanne, Can, and Paul for showing me and explaining me more about the Dutch culture and the way Dutch people work, think and behave. Extended gratitude goes to Vicki, Vivian, and of course Zaid and Joaquin! I will remember your advice and those moments during the crazy Antilles Festivals in Belgium. In the same way, I want to thank my football buddies from the Sports Center for the opportunity to play the Monday's tournament as well as those who play on Tuesdays. Such a stress relieve founded in the fields.

In a similar manner, I want to thank my colleagues from the GRS group, Delft friends, and family for their advice, the energetic coffee breaks, and also the long nights in Delft. Thank you Olga, Raluca, Alexandru, Dimitra, Reenu, Karolina, Yunlong, Davide, Igor, Yann, Francesco, Simone, Jiapeng, Tobias, Natalia, Julien, Marcel, Thomas, Gert, Floris, Giovanni, Veronica, Taco, Siavash, Karen, Stephanie, Lorenzo, Ramses, Sarah, Monica, Francesca, Edouard, Vincent, Prabu, Han, Antoon, Steven, Jonathan, Seyed, Lukas, Raymond, Yanqing, Kaixuan, Joana, Miguel, Silvia, Kevin, Manuel, Mariska, Beatrice, Laura, Christos, Michelle, and more. Can't forget those memories in the city center of Delft such as Beestenmarkt, Tango, Doerak, Bepop, and the magical Oude Jan.

Another aspect that has impacted my life in Delft comes from my former and current roommates/flatmates of the legendary Phoenixstraat 68 house. Thanks, Erio, David, Lukas, Francesco, Miriam, Marilisa, Alex, Grazia, Esther, and Giulia. I have never felt alone in the house because of your warm company and your great sense of humor. I have really enjoyed sharing the house with you all, in which, I have learned a lot from each of you. Thanks my Delft Latinos friends for making me feel home while speaking and joking with you, mainly joking.

The sacrifice of being far away from my family and culture has rewarded me to meet one of the most important persons in my life, mi amor Agnes Broer. This work would not have been a success without your unconditional patience, understanding, support, discipline, and love, lots of love, which have changed and made me a more valuable person in life. My gratitude also goes to Agnes' mother Marjolein Weima and father Dick Jan Broer as well as the Broer family members. They have represented my family in the Netherlands.

No podria acabar estos párrofos de agradecimiento sin mencionar a los miembros que componen la gran familia Reinoso, por parte de mi padre, y Rondinel, por lado de mi madre. Muchos de ellos me han visto nacer, crecer, errar, pero también lograr poco a poco cada una de mis metas. Gracias a mis tías Susana, Felícitas, Olga, y Beatriz. Mis tíos Vicente, Pablo, Lucho, Adrian, y Mario. Y los que desafortunadamente no nos acompañan más en tierra, mis queridísimas abuelas Antonia y Rosalina, tías Lourdes y Yolanda y mi tío Juan, Q.E.P.D.. También quiero extender mis agradecimientos a mis primos Julio, Juan, Luis, Carito, Luchin, Mariluz, Ana, Rosa, Jorge, Rosita, y Raúl, así como también a mi único cuñado Claudio y sobrina Rosalyn. Al lado de Uds he pasado momentos muy alegres e inolvidables en Lima, Ica, Ayacucho, Madrid, y California. Aunque habramos pasado dificultades en nuestro camino en la vida, hemos logrado salir adelante con la ayuda de cada uno de nosotros, quienes conformamos una familia muy unida y muy alegre.

Gracias, Thank you, Dankjewel

SUMMARY

Observations of weather phenomena have attracted many researchers because of their microphysical complexity, space-time variability, and more important, their impact on human life. In the efforts of studying weather, researchers have used a diverse number of instruments to obtain both in-situ (towers, tethered balloons, and weather station networks) and remote (radar, lidar, satellite) measurements. In this study, weather measurements are obtained using ground-based weather radars, which are able to scan over a large space domain. Radar measurements require complex processes to extract reliable information that can be used by weather institutions, companies, and citizens. In this thesis, innovative methods are presented to process weather radar measurements, acquired at X-band frequencies, with the aim of capturing the natural variability of storm events.

Weather radars acquire data from scanned hydrometeor targets, such as groups of rain and ice particles. In **Chapter 2**, general concepts regarding weather radars and scattering theory are discussed, with an emphasis on X-band frequencies. At these frequencies, the signal that is transmitted and received by the radar can be significantly attenuated by hydrometeors. One way to mitigate such limitation is by using polarimetric technology in which two signals are transmitted, one in the horizontal and one in the vertical plane. In this context, polarimetric variables such as reflectivity Z, differential reflectivity Z_{DR}, specific differential phase K_{DP}, specific attenuation A, and backscattering differential phase δ_{hv} are defined and their relations in rain are studied using scattering simulation.

The benefits and limitations of using a polarimetric X-band radar for the observation of convective weather are examined in **Chapter 3**. For such purpose, a squall line event over North-Western Europe is used and multiple data sources, which are available in the Netherlands (NL), are introduced. Radar observations are obtained from two operational C-band radars and one research polarimetric X-band radar, hereafter IDRA, to compare Z observations at different spatial and temporal resolutions. It is demonstrated that the observations from IDRA, at 30 m and 1 min resolution, provide a more detailed structure of a specific region of the squall line compared to those from C-band radars at 1 km and 5 min resolution. However, observations behind regions of heavy rain were not possible using IDRA due to total attenuation.

In **Chapter 4**, a method is proposed to estimate accurate K_{DP} in rain at X-band frequencies. In the formulation of the K_{DP} estimator, measurements of Z and Z_{DR}, after attenuation correction, are included to obtain K_{DP} estimates at range resolution scales. This method is demonstrated using four storm events, associated with light and heavy rain, observed in the NL by the X-band IDRA radar. It is shown that the proposed method is able to accurately estimate K_{DP} in both light and heavy rain with standard deviation values in the order of $0.1\,^{\circ}\,\mathrm{km}^{-1}$ while maintaining the structure of the storms.

Based on the method given in Chapter 4, **Chapter 5** suggests advanced methods to

improve estimates of A and δ_{hv} in convective storm cells that are observed at X-band frequencies. Three established methods to estimate A are implemented while two methods to estimate K_{DP} are considered. The five methods are examined using three storm events, observed within a maximum range of 15 km. Because the three methods to estimate A require K_{DP} estimates, the analyses show that improved estimates of A are possible when the K_{DP} technique given in Chapter 4 is employed. In contrast, incorrect estimates of A are seen when K_{DP} is calculated by the conventional range-filtering method. Moreover, δ_{hv}-K_{DP} scatterplots exhibited significant agreement to empirical relations and quantitative analyses showed that the accuracy of δ_{hv} is on the order of 1.5°.

SAMENVATTING

Het waarnemen van weersverschijnselen is iets dat een grote aantrekkingskracht uitoefent op vele onderzoekers; vanwege de complexe microfysica achter het weer, de ermee gepaarde variabiliteit in tijd en ruimtelijke zin, en nog belangrijker: de invloed van het weer op het dagelijks leven. Met het oog op het bestuderen van weersomstandigheden is door onderzoekers een divers instrumentarium ontwikkeld om metingen te kunnen doen, zowel ter plekke (meetmasten, verankerde weerballonen en netwerken van weerstations) als gebruikmakende van remote sensing technieken (radar, lidar of satelliet). In deze studie staan radarmetingen vanaf het aardoppervlak, met een groot ruimtelijk meetbereik, aan de basis voor weerwaarnemingen. De omzetting van radarmetingen tot betrouwbare informatie voor zowel meteorologische instituten, bedrijven als het grote publiek, vraagt om complexe verwerkingsmethoden. In dit proefschrift staan innovatieve methoden centraal om weerradardata (verkregen in de X-band frequenties) te verwerken om zo de natuurlijke variabiliteit van stormen aan het licht te brengen.

Weerradars doen metingen aan verschillende typen neerslag, zoals regen of ijsdeeltjes. **Hoofdstuk 2** behandelt de algemene begrippen ten aanzien van weerradar en verstrooiingstheorie, met speciale aandacht voor X-band frequenties. In dit frequentiebereik kunnen de signalen die worden verzonden en ontvangen door de radar aanzienlijk gedempt worden door neerslag. Een van de manieren om met deze beperking om te gaan is het gebruik van polarimetrische technieken, waarbij twee signalen worden verzonden, één in het horizontale vlak en één in het verticale. Deze context behoeft verschillende polarimetrische variabelen, te weten: de reflectiviteit Z, de differentiële reflectiviteit Z_{DR}, de specifieke differentiële fase K_{DP}, de specifieke demping A, en de terugverstrooiende differentiële fase δ_{hv}. Met een verstrooiingssimulatie voorzie ik in nader begrip over de onderlinge afhankelijkheden van deze variabelen.

Hoofdstuk 3 gaat in op de voordelen en beperkingen van het gebruik van polarimetrische X-band-radar voor observatie van convectieve weertypen. Voor dit doeleinde gebruik ik een buienlijn boven Noordwest-Europa en introduceer ik meerdere typen data die beschikbaar zijn in Nederland. Om observaties van Z te vergelijken op verschillende ruimtelijke en tijdsresoluties, gebruik ik radarmetingen van twee operationele C-band-radars en één experimentele polarimetrische X-band-radar (hierna IDRA genoemd). Hieruit volgt dat de observaties gedaan met IDRA, bij een 30 m ruimtelijke resolutie en een 1 min tijdsresolutie, een gedetailleerdere blik op de structuur van een specifiek deelgebied van de buienlijn bieden dan van de C-band-radars bij een resolutie van 1 km en 5 min. Daarentegen bleken metingen met IDRA niet mogelijk achter gebieden met zware regen, als gevolg van een totale uitdemping van het signaal.

Hoofdstuk 4 bevat een voorstel voor een nauwkeurige schatting van K_{DP} in regen in de X-band frequenties. De formulering van de K_{DP}-schatter bevat metingen van Z en Z_{DR} (na een correctie voor demping) om K_{DP} te kunnen schatten met een hoge ruimtelijke resolutie. Ik pas de methode toe op observaties van de X-band IDRA-radar bij vier

voorvallen van een storm in Nederland die gepaard gingen met zowel lichte als zware regen. Hieruit volgt dat de voorgestelde methode een nauwkeurige schatting geeft voor K_{DP} in gevallen van zowel lichte als zware regen, met standaardafwijkingen met een ordegrootte van $0.1\,^{\circ}\,\mathrm{km}^{-1}$, waarbij de ruimtelijke structuur van de stormen goed in beeld blijft.

Voortbouwend op Hoofdstuk 4, biedt **Hoofdstuk 5** geavanceerde methoden om schattingen van A en δ_{hv} te verbeteren voor convectieve stormcellen geobserveerd met X-band frequenties. Ik beschouw drie bestaande methoden om A, en twee methoden om K_{DP} te schatten. De analyse past de vijf methoden toe op drie voorvallen van storm, alle geobserveerd op een afstand van minder dan 15 km. Doordat de drie methoden om A te schatten afhankelijk zijn van K_{DP}-schattingen, blijkt uit mijn analyse dat een verbeterde schatting van A mogelijk is wanneer gebruik wordt gemaakt van de K_{DP}-techniek uit Hoofdstuk 4. Daarentegen blijken de schattingen voor A onjuist wanneer de conventionele filter m.b.t bereik wordt toegepast voor K_{DP}. Bovendien laten spreidingsdiagrammen van δ_{hv}-K_{DP} een significante overeenkomst zien met empirische relaties; een kwantitatieve analyse laat zien dat de nauwkeurigheid van δ_{hv} van een ordegrootte van 1.5° is.

Thanks to Dr. Taco Broerse for translating the summary to Dutch

1

INTRODUCTION

1.1. MOTIVATION AND RESEARCH BACKGROUND

Since the work achieved by Ryde (1946), who studied the propagation properties of electromagnetic waves in clouds and precipitation at 10 cm wavelength, ground-based weather radars have contributed significantly to weather and hydrology studies (Johnston et al., 1998; Schuurmans et al., 2007). Achievements include the surveillance of severe weather, the discrimination of hydrometeors such as rain, snow, and hail, and the understanding of the dynamical and microphysical processes that determine the evolution of weather phenomena. Conventionally, a weather radar system obtains volumetric measurements by rotating a dish-antenna 360° in azimuth at a pre-determined number of elevations, with temporal and spatial resolutions of 5 min and 1 km, respectively (Steadham et al., 2002). A different manner to perform weather measurements is by steering the beam electronically using a phased-array of small antennas, which can perform multiple functions such as surveillance and storm tracking with faster update times, (Reinoso-Rondinel et al., 2010). The frequency bands at which most weather radars operate are S-band (~10 cm) and C-band (~5 cm) and, less often, X-band (~3 cm). One of the criteria to select a frequency band is related to the trade-off between attenuation, cost, and maximum range coverage. For example, S-band radars, most common in the USA, are expensive systems but they do not suffer from attenuation issues while C-band radars, more standard in Europe, are less expensive systems but they can suffer from attenuation. The maximum range coverage for both S- and C-band radars is typically given in the range of 200 to 250 km in order to avoid a significant gap between the earth surface and the radar beam height. Radar systems at X-band frequencies are small and less expensive radars whose maximum range is in the order of 60 km while their temporal and spatial resolutions are 1 to 2 min and few hundreds of meters, respectively. Although X-band radar systems might be able to provide observations at resolutions higher than conventional radars, a major problem of X-band radars is signal attenuation (Park et al., 2005a) .

By sending electromagnetic waves, weather radars collect data of distributed targets within a predetermined resolution volume, which shape is similar to a truncated cone.

1

Radar measurements depend on the scattering properties of a group of hydrometeors (i.e., wave-particle interactions) and the size distribution of hydrometeors in a given resolution volume (Doviak and Zrnić, 1993). The scattering properties can be described in terms of the frequency of the incident wave, the physical characteristics of particles (e.g., size, shape, and temperature), and wave scattering processes (i.e., how much power is returned back to the radar and absorbed by particles) (Oguchi, 1983). The size distribution of hydrometeor particles indicates the volume density of hydrometeors per unit diameter. For rain particles, the size distribution is referred to as DSD (drop size distribution) and provides information about rain microphysics (e.g., the formation of raindrops). Through the integration of returned signals from the group of hydrometeors and the application of digital signal processing techniques such as Fourier transform, autocorrelation, and noise filtering of weather signals, three main radar variables are obtained: the mean power, the mean Doppler velocity, and the spectrum width, which indicates the dispersion of moving particles around the mean Doppler velocity. If this integration process is applied to remaining resolution volumes along the radar beam, full radial profiles of similar integrated estimates are acquired. Moreover, a full display of these profiles, which is called a plan position indicator (PPI), is obtained once the antenna is rotated over 360°.

In the weather radar community, measurements of the mean power are used to express a more meaningful variable, which is related to the reflecting properties of hydrometeors and referred to as the reflectivity factor. Values of the reflectivity factor are in the order of large magnitudes and therefore they are conveniently expressed in logarithm scale and denoted as Z [dBZ]. For simplicity, Z will be referred to as reflectivity only. Z depends on the number, size, physical state, and shape of hydrometeors (Doviak and Zrnić, 1993). In case of raindrops, Z can be used to estimate rainfall rate R [mm h^{-1}] based on empirical power-law equations because both quantities are related to DSD moments. In order to obtain an empirical R-Z relation, several values for R and Z can be generated using a set of DSDs and simulating scattering properties of rain. DSDs are either simulated through DSD models or measured by disdrometers. The best fit to the R-Z data is given by a power-law relation, for example, the Marshall-Palmer (M-P) relation given by $Z_l = 200R^{1.6}$, where Z_l is given in units of mm^6 m^{-3} (Marshall and Palmer, 1948). Although this approach is simple, relations are found to be very unstable due to DSD variability since Z is proportional to the 6^{th} DSD moment while R is related to the 3^{rd} DSD moment. In addition, power, and thereby Z measurements, can suffer from attenuation levels, especially at short wavelengths, which can lead to biased estimates of R. Moreover, Z is sensitive to both radar miscalibration issues and presence of hail or other precipitation particles different than raindrops. One method to mitigate these issues is by working with polarimetric technology.

The idea of radar polarimetric is based on the transmission of two electromagnetic waves, one in the horizontal (H) and one in the vertical (V) plane, as shown in Fig. 1.1, panel a). Because hydrometeor particles are not spherical, unless they are very small, data collected from this dual configuration will better describe the dominant size and shape of particles from a given resolution volume (Zrnić, 1996). For example, for oblate-shaped raindrops, the returned power in the horizontal should be larger than in the vertical plane. By combining the returned signals in the H and V planes, the following polari-

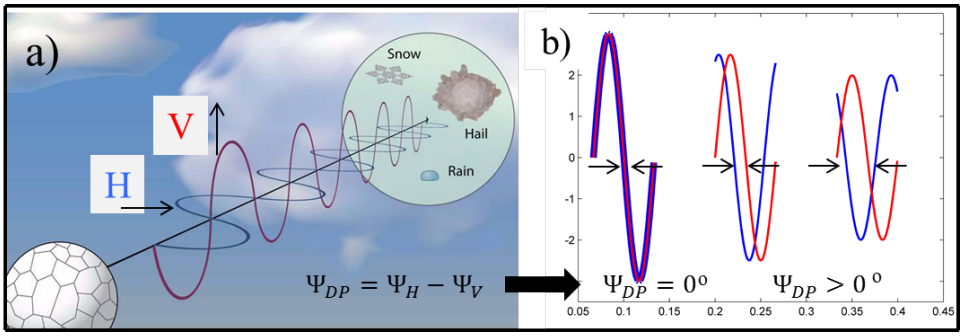

Figure 1.1: A schematic representation of a) the horizontally and vertically polarized transmitted waves and of b) the delay in phase of the horizontally polarized wave with respect to the vertically polarized wave gradually increasing as a function of time due to hydrometeros. *Panel a) adapted from Warning Decision Training Division, version 1109, under the "fair use" clause for research purposes.*

metric variables are defined (Zrnić and Ryzhkov, 1999; Bringi and Chandrasekar, 2001). The horizontal and vertical reflectivity (Z_H and Z_V in dBZ units), which are two special cases of the previously defined Z. The differential reflectivity Z_{DR} in dB units is defined as the difference between Z_H and Z_V and it measures the median raindrop diameter. It depends on the size, shape, orientation, density, and water content of hydrometeors. As the polarized waves propagate in the H and V planes through a group of hydrometeors, one of the transmitted waves will experience a deceleration with respect to the other one, mainly due to the dominant shape of hydrometeors. If the phase of the horizontal and vertical waves are indicated by Ψ_H and Ψ_V, the differential phase (Ψ_{DP} [°]) is defined as the accumulated phase difference between Ψ_H and Ψ_V along a propagation path or radar beam. Fig. 1.1 panel b) illustrates the increment of Ψ_{DP} in time; in which $\Psi_{DP} = 0°$ for spherical hydrometeors and $\Psi_{DP} > 0°$ for oblate-shaped hydrometeors. Note that, although the amplitudes of the signals decrease as a result of wave propagation, their phase shifts increase. Ψ_{DP} depends on the number, size, and shape of hydrometeors while it is independent of attenuation and miscalibration. One more polarimetric variable is the copolar-correlation coefficient ρ_{hv} which measures de-correlation between the backscattering signals at horizontal and vertical polarization. ρ_{hv} is near 1 for rain particles and decreases when hydrometeors have irregular shapes.

Researchers have found several applications of polarimetric variables in order to increase the reliability of weather radar measurements. Such applications include the identification of hydrometeors (i.e., spotting areas of specific hydrometeor type) (Ryzhkov et al., 2005b), the suppression of non-hydrometeor targets (Unal, 2009), the attenuation correction of Z_H and Z_{DR} (Testud et al., 2000), absolute radar calibration checks (Giangrande and Ryzhkov, 2005), more robust empirical relations to estimate rainfall rate (Gorgucci et al., 2001), as well as radar data quality control (Lakshmanan et al., 2013). In addition, the use of polarimetric variables has improved the understanding of microphysical processes in storms such as ice melting, aggregation of snow particles, coalescence and break up of raindrops, evaporation of small drops, and size sorting of particles (Kumjian, 2013). Meanwhile, dynamic forces associated with convective storms have

been studied using polarimetric observations and Doppler analyses, leading to a better identification and modelling of severe weather such as supercell storms, squall lines, tornado signatures, updraft-downdraft circulation, wind shear, and inflow jets (Bluestein et al., 1997; Kumjian and Ryzhkov, 2008). Most of the polarimetric capabilities have been demonstrated at S-band and C-band frequencies, while only limited research has been conducted at X-band frequencies.

In recent years, an increased interest on using small X-band radars for weather observation has been noticed because of the polarimetric capability of correcting attenuation issues. X-band weather radars are capable of providing observations at resolutions higher than those of S-band and C-band frequencies because they are designed to operate at short ranges (Brotzge et al., 2005). Given that X-band radars are cheaper than conventional radars, a network of X-band radars can be designed and placed to fill in the gaps resulting from observations at long ranges by conventional radars. For example, the Center for Collaborative Adaptive Sensing of the Atmosphere (CASA) developed a network of polarimetric X-band radars that can adaptively scan the regions of interest (McLaughlin et al., 2009). In Japan, the National Research Institute of Earth Science and Disaster Prevention (NIED) established a similar radar network in the Tokyo metropolitan area to cope with urban flooding (Maki et al., 2010). Furthermore, in Western Europe, polarimetric X-band radars were used to test the impact of rainfall rate inputs on urban hydrodynamic modelling outputs (Bruni et al., 2015; Ochoa-Rodriguez et al., 2015). Because of their small size, mobile polarimetric X-band radar platforms were also operated to obtain close observations of severe storms such as supercells (Bluestein et al., 2007). In addition to the Doppler capabilities of these radars, phased-array technology (i.e., electronic beam steering) was added to obtain rapid volumetric observations of fast-evolving convective weather such as tornadic storm events (Bluestein et al., 2010).

In spite of the benefits that polarimetric X-band radars can provide, several challenges related to the accuracy of estimated polarimetric variables appear, which should be addressed to fully unleash the benefits of using X-band radar systems. In this thesis, one of the variables of interest is Ψ_{DP} because it is independent of attenuation and miscalibration and is less sensitive to echoes resulting from hail particles, which is useful for accurate rainfall rate estimation. However, Ψ_{DP} measurements are very noisy and because it measures accumulated phase shifts along the propagation path, it is difficult to distinguish which areas contribute to the increase of a Ψ_{DP} profile and by how much. Therefore, a given Ψ_{DP} profile is derived with respect to range resulting in specific differential phase increments. More formally, the range derivative of the one-way Ψ_{DP} is defined as the specific differential phase K_{DP} [$^\circ\,\mathrm{km}^{-1}$] (Doviak and Zrnić, 1993). For illustration purposes, Fig. 1.2 shows values for a Ψ_{DP} profile and their corresponding K_{DP} values associated to areas with and without rain particles. In this graph, Ψ_{DP} increases gradually by 20°, 50°, and 10° due to the three rain areas. Note that the values of Ψ_{DP} remain the same in clear air. Each increment on Ψ_{DP} is given within a 5 km range path, and therefore, the corresponding values for K_{DP} are $2\,^\circ\,\mathrm{km}^{-1}$, $5\,^\circ\,\mathrm{km}^{-1}$, and $1\,^\circ\,\mathrm{km}^{-1}$ respectively, while the value for K_{DP} in clear air is $0\,^\circ\,\mathrm{km}^{-1}$. However, a direct range derivative of Ψ_{DP} at range resolution scales can lead to unreliable values of K_{DP} because Ψ_{DP} measurements are noisy, especially in areas of low signal-to-noise ratio (SNR). Therefore, profiles of Ψ_{DP} need to be carefully smoothed to increase the accu-

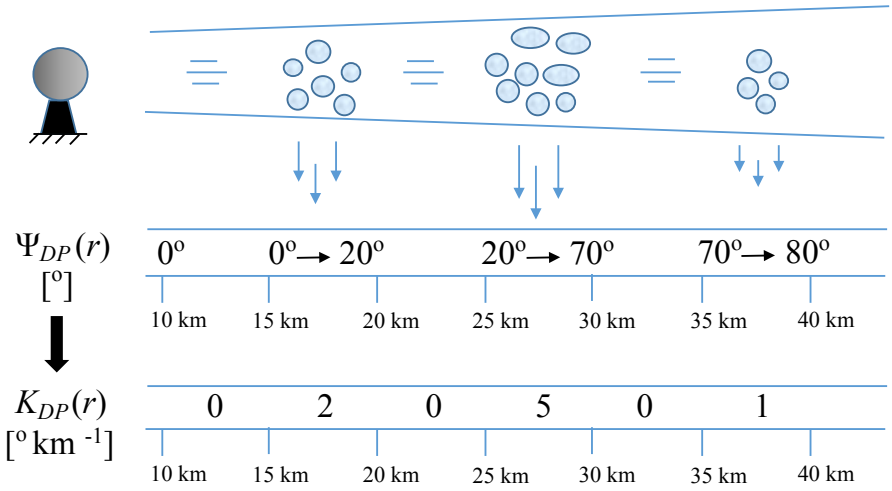

Figure 1.2: A schematic illustration of the accumulation behavior of the differential phase Ψ_{DP} through rain and clear air areas as a function of range. The corresponding values for the specific differential phase K_{DP} are also indicated.

racy of K_{DP} profiles while keeping the spatial variability of Ψ_{DP} (i.e., maintaining local and fast phase shift increments). Another challenge to estimate K_{DP} is that a given Ψ_{DP} profile may include unwanted differential phase shifts due to resonance effects which occur when the electric size of raindrops is similar to the incident wavelength (Oguchi, 1983). This phase shift contribution is referred to as the backscatter differential phase δ_{hv} [°] and could be significant at X-band and C-band frequencies (Ryzhkov and Zrnić, 2005). Despite the fact that unfiltered δ_{hv} can negatively impact the accuracy of K_{DP}, it has been reported that the estimation of δ_{hv} profiles can provide, in a similar manner to Z_{DR}, information concerning the dominant size of raindrops. However, the estimation of both K_{DP} and δ_{hv} profiles is not straightforward given their coupled nature and the noisy behavior of Ψ_{DP} profiles.

Another variable that is obtained from Ψ_{DP} is the specific attenuation $A_{H,V}$ [dB km^{-1}]. In contrast to K_{DP}, $A_{H,V}$ can be estimated at range resolution scales without the need of smoothing processes by using $Z_{H,V}$ measurements and the difference of Ψ_{DP} over range paths longer than the range resolution (Testud et al., 2000; Bringi et al., 2001). Similar to Ψ_{DP} and K_{DP}, $A_{H,V}$ is independent of error measurements associated with signal attenuation, radar miscalibration, and is a suitable candidate for rainfall rate estimation (Wang et al., 2013; Ryzhkov et al., 2014). However, established methods to estimate A are sensitive to DSD and temperature variabilities (Matrosov et al., 2014). In addition, the use of large range paths can increase the sensitivity to local DSD variability. Even though accurate estimation of K_{DP} and $A_{H,V}$ can be challenging, K_{DP} and $A_{H,V}$ values at X-band frequencies are larger than at C-band and S-band frequencies, which increases the interest of employing X-band radars for weather monitoring. For simplicity, Z_H and A_H will be referred to as Z and A, respectively.

1

1.2. PURPOSE OF RESEARCH AND OUTLINE

The objectives of this study are 1) examine the performance of X-band radars for the observation of convective storms and 2) provide robust algorithms for the estimation of K_{DP}, A, and δ_{hv} from measurements in rain at X-band frequencies, while maintaining the spatial variability of observed storms. The proposed objectives lead to the following research questions:

1. What are the advantages and disadvantages of using an X-band radar system for the observations of convective storms at resolutions higher than those of conventional radars?

2. Given that Z and Z_{DR} are measured at range resolution scales and can suffer from multiple sources of uncertainty, is it possible to include Z and Z_{DR} measurements for accurate estimates of K_{DP} at range resolution scales while reducing issues such as resonance effects, noise, attenuation, and also radar miscalibration?

3. How can we reduce the sensitivity of A to DSD variability in convective storms observed over short range paths? Additionally, how can we estimate δ_{hv} in order to depict the spatial variability of raindrop size in convective storms?

The thesis addresses these questions and is divided into 5 chapters, which will introduce, develop, and support novel ideas in order to accomplish the proposed objectives.

Chapter 2 introduces main concepts related to weather radar measurements with emphasis on the interaction between rain particles and electromagnetic waves at X-band frequencies. This chapter is divided into three sections. The first section presents the radar equation for distributed particles to explain which radar parameters affect power measurements and how power is converted into reflectivity. In the second section, the scattering properties of a single raindrop particle are reviewed in order to quantify how much power is returned back to the radar and how much is lost, taking into account the size and shape of raindrops. The third section formulates polarimetric variables resulting from a group of hydrometeors in terms of the scattering amplitude and size distribution. In addition, the consistency between polarimetric variables in rain is described using measured DSDs and scattering simulation. Moreover, the relations between polarimetric variables and rainfall rate are shown using the M-P exponential DSD model (Doviak and Zrnić, 1993). Discussions and results presented in Chapter 2 will be used for the development of the next chapters.

In order to answer research question 1, **Chapter 3** makes a comparison between the observations obtained from two radars systems; one at C-band and one at X-band frequencies, using one case study. Both radars are located in the Netherlands (NL); the C-band radar is part of the operational radars managed by the Dutch meteorological institute (KNMI) (Holleman et al., 2010) while the X-band radar is a research polarimetric radar operated by the Delft University of Technology (TU Delft) (Figueras i Ventura, 2009). The selected case study is a convective squall line that evolved across the North Sea and the NL on 03 January 2012. This chapter also shows a framework for the analyses of storm events using different data sources available in the NL, such as those installed in the Cabauw experimental site for atmospheric research (CESAR) (Leijnse et al., 2010).

In the following chapters, the radar system dedicated to answer questions 2 and 3 is the polarimetric X-band radar.

Chapter 4 presents a novel algorithm to estimate K_{DP} at range resolution scales while controlling its standard deviation in an adaptive manner (research question 2). The key of this approach is to use the self-consistency (SC) principle (Scarchilli et al., 1996) that exists in rain between K_{DP}, Z, and Z_{DR} in order to derive a parameter that downscales range derivatives of Ψ_{DP} over paths of length L [km] to range resolution scales. The accuracy of the K_{DP} estimator is controlled by formulating a theoretical relation between the standard deviation of K_{DP} and L. Resonance effects (i.e., δ_{hv} contamination) are reduced by controlling the derivatives of Ψ_{DP}. This method is demonstrated using four storm events and its performance is compared against those from Hubbert and Bringi (1995) and Otto and Russchenberg (2011).

Convective storm cells are special events that result from complex microphysical and dynamical processes and often present more challenging tasks to accurately correct Z measurements for attenuation, especially at X-band frequencies. Therefore, **Chapter 5** studies the impact of estimated Φ_{DP} profiles on the performance of the attenuation correction method given by Bringi et al. (2001) and proposes a new technique to calculate δ_{hv} in rain at X-band frequencies. For such purpose, two K_{DP} methods are used to obtain Φ_{DP} profiles, Hubbert and Bringi (1995) and the method introduced in Chapter 4. In addition, three attenuation methods from Bringi et al. (1990), Testud et al. (2000), and Bringi et al. (2001) are implemented to estimate A and correct Z. The δ_{hv} algorithm integrates the results obtained from Hubbert and Bringi (1995), Bringi et al. (2001), and the K_{DP} method of Chapter 4 together with an interpolation method. The methods to obtain improved estimates of A and δ_{hv} are demonstrated and assessed using three storm events and the consistency between K_{DP} and A and between K_{DP} and δ_{hv}.

Finally, **Chapter 6** provides the conclusions and outlook of the thesis.

2

RADAR METEOROLOGY

2.1. GENERAL CONCEPTS

The term RADAR stands for RAdio Detection And Ranging and originated from the U.S. Navy in 1940. A Doppler radar is an electromagnetic system that is able to detect the range, strength, and speed of the targets such as aircrafts, ships, vehicles, and weather activities. Basically, a radar operates by transmitting electromagnetic energy into space and receiving the echo reflected or backscattered from one or more objects. A brief explanation of how Doppler radars operate (adapted from Doviak and Zrnić (1993) and Reinoso-Rondinel (2011)) is presented next.

For transmission, the pulse generator modulates a continuous sinusoidal signal to produce a sequence of pulses $U(t)$ of width τ. The time between two consecutive pulses is termed the pulse repetition time (T_s), which is much larger than τ. The complex received signal $V(t)$ with Doppler information after demodulation is sampled to produce the in-phase $I(t)$ and the quadrature $Q(t)$ signals. These components of $V(t)$ are sometimes referred to as the Level I data and are represented mathematically as follows

$$V(t) = I(t) + iQ(t), \text{where} \tag{2.1}$$

$$I(t) = \frac{|A|}{\sqrt{2}} \cos\left(\frac{4\pi r}{\lambda} + \frac{4\pi v_r t}{\lambda} - \psi_t - \psi_s\right) U\left(t - \frac{2r}{c}\right), \tag{2.2}$$

$$Q(t) = -\frac{|A|}{\sqrt{2}} \sin\left(\frac{4\pi r}{\lambda} + \frac{4\pi v_r t}{\lambda} - \psi_t - \psi_s\right) U\left(t - \frac{2r}{c}\right), \tag{2.3}$$

where A is the amplitude of the received signal, λ is the radar wavelength, and c is the speed of the light. ψ_t, ψ_s, r, and v_r are the transmitted constant phase, the scattering phase shift, the range, and the radial velocity of the object, respectively. The range of a target from the radar can be expressed as $r = cT_r/2$, where T_r is the time it takes the transmitted signal to travel to the target and return to the radar. The radial velocity is the target's velocity projected in the beam direction and can be extracted from the phase of $V(t)$. For a target that is moving away from the radar, the radial velocity is defined as positive, otherwise it is negative. Range and velocity ambiguities are known as the Doppler

dilemma. The unambiguous range is given by $r_a = cT_s/2$ while the unambiguous velocity is determined by $v_a = \pm\lambda/(4T_s)$.

In contrast to the signal that comes from a point target, a weather signal results from echoes backscattered to the antenna by a large number of hydrometeors (e.g., water drops, snow, hailstones), but also by biological scatterers, aircrafts, or other objects in space (known as clutter). Because the returned echoes from hydrometeors that are located along a radar beam cannot be distinguished, the weather signal needs to be sampled at discrete ranges. The minimum separation in range by which two groups of hydrometeors at the same radial can be distinguished is called the range resolution. The volume where the hydrometeors contribute the most to the sample signal is called the radar resolution volume.

The radar resolution volume extends in range, azimuth, and elevation. A representation of the resolution volume is shown in Fig. 2.1. The resolution volume is illustrated

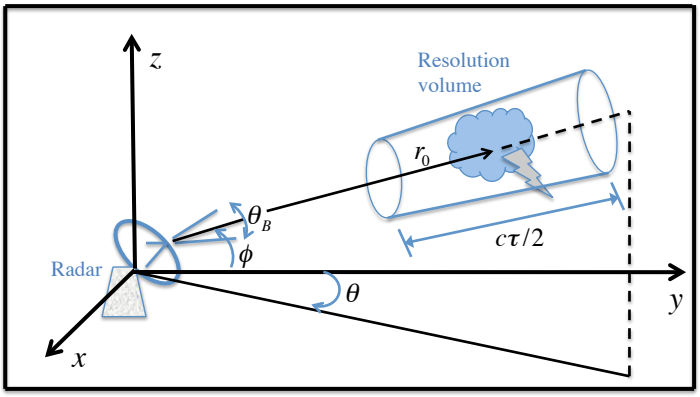

Figure 2.1: A schematic representation of the resolution volume. The radar is centered at the origin of the Cartesian coordinate. The angles θ and ϕ denote the azimuthal and elevation angles of beam direction, respectively. The resolution volume is centered at r_0, and the range and azimuthal extensions are given by $c\tau/2$ and θ_B, respectively. *Reprinted from Reinoso-Rondinel (2011).*

by a truncated cone containing the group of hydrometeors centered at range r_0 from the radar. The dimension of the resolution volume in range is defined by the convolution of the transmitted pulse shape with the receiver impulse response. The extent in range can be approximated by $c\tau/2$ if the envelope of the transmitted pulse is rectangular and the receiver frequency response has a Gaussian shape (Doviak and Zrnić, 1993). The dimension of the resolution volume in azimuth and elevation, assuming a circular beam, is determined by the radar beamwidth (θ_B), which is a function of antenna size and radar wavelength (Rinehart, 2004). Note that the dimension of the resolution volume depends on range.

The acquired data for each dwell time and resolution volume is processed into meteorologically meaningful information (meteorological variables) that is used to observe, investigate, and forecast weather activity. If the data from a given resolution volume is processed in the frequency domain (i.e., by means of Fourier transform), then a Doppler velocity distribution of power is obtained, which is referred to as the power spectral den-

sity. Three basic variables can be obtained from the power spectral density, known as the spectral moments (or the Level II data),

- The mean power (P [W]), or also called the zeroth moment because it is the sum of all the power components in the spectrum. It indicates the total strength of the returned echo signals. The power is related to the liquid water content of the hydrometeors within the resolution volume.
- The mean radial velocity (V_r [m s^{-1}]), or the first moment, provides the mean radial motion of the hydrometeors within the resolution volume.
- The spectrum width (σ_v [m s^{-1}]), or the second central moment, indicates the turbulence and shear associated with the velocity dispersion within the resolution volume. Sometimes it is practical to normalize σ_v as $\sigma_{vn} = 2\sigma_v T_s/\lambda$.

The mean power of weather signal samples is described by the weather radar equation as

$$P(r_0) = \frac{P_t g^2 c\tau\pi\theta_B^2\lambda^2\eta}{(4\pi)^3 16\ln 2 (r_0)^2 l(r_0)^2}, \tag{2.4}$$

where P_t is the transmitted power, g is the antenna gain, l is the one-way propagation loss due to hydrometeors, r_0 is the distance from the radar, and η is the reflectivity. If the size of hydrometeors are much smaller than λ, η is approximated as $\pi^5\lambda^{-4}|K_w|^2 Z^l$ where K_w is the dielectric factor of a hydrometeor and Z^l is the reflectivity factor. Z^l is related to signal power and depends on the number of hydrometeors per unit volume, the size of the hydrometeors, the physical state of the hydrometeors, and the shapes of the hydrometeors (Doviak and Zrnić, 1993). Conventional units of Z^l are given by mm^6 m^{-3}, but for convenience, it is normalized by 1 mm^6 m^{-3} and then measured on a logarithmic scale indicated by Z in units of dBZ, hereafter referred to as reflectivity. Thus, solving Eq. (2.4) for Z^l, Z [dBZ] is expressed as

$$Z = 10\log(P(r_0)) + 20\log(l(r_0)) + 20\log(r_0) - 10\log(C), \tag{2.5}$$

where C represents the radar calibration constant.

2.2. SCATTERING THEORY OF RAINDROPS

In order to quantify how much power is returned back to the radar and how much energy is lost when an electromagnetic wave hits a rain particle, the physical and electromagnetic properties associated with the shape, size, temperature, electric material, and wave scattering of single particles are studied next. For a more detailed and comprehensive study, the reader is referred to previous work such as (Oguchi, 1983) and (Doviak and Zrnić, 1993).

The relation between the size and the shape of a raindrop is defined by the axis ratio (a_{yx}), which is given by $a_{yx} = a_y {a_x}^{-1}$, where a_x [mm] and a_y [mm] are the semi larger and semi smaller axis, respectively. Multiple relations have been proposed to model a_{yx} in terms of the equivolume diameter D_e [mm], which is indicated as $D_e = ({a_x}^2 a_y)^{1/3}$. Typically, a_{yx} is approximately equal to 1 for $D_e < 0.7$ mm while for larger drops polynomial relations are assumed (Pruppacher and Beard, 1970; Beard and Chuang, 1987; Beard

and Kubesh, 1991; Andsager et al., 1999; Keenan et al., 2001; Brandes et al., 2002; Thurai et al., 2007; Steinert and Chandra, 2008). In order to obtain a representative regional a_{yx}, hybrid models have been recommended. For example, in Paris, Gourley et al. (2009) suggested that for $D_e < 1.3$ mm, the model given by Andsager et al. (1999) should be used while for larger drops the polynomial model described by Illingworth et al. (2000), based on Goddard et al. (1982), is preferred. In The Netherlands, Otto and Russchenberg (2011) suggested to use a hybrid models for a_{yx} which consists of Keenan et al. (2001), Andsager et al. (1999), and Beard and Chuang (1987) according to D_e values as

$$a_{yx} = \begin{cases} 0.9939 + 0.00736 D_e - 0.018485 D_e^2 + 0.001456 D_e^3 & \text{if } D_e < 1.35 \\ 1.012 - 0.0144 D_e - 0.0103 D_e^2 & \text{if } D_e \in [1.35; 4.4] \\ 1.0048 + 0.00057 D_e - 0.02628 D_e^2 + 0.003682 D_e^3 - 0.0001677 D_e^4 & \text{if } D_e > 4.4 \end{cases} \tag{2.6}$$

Keenan et al. (2001) provided a good representation of a drop that grows without external components (i.e., naturally). Andsager et al. (1999) proposed a model that is representative in light to moderate rainfall, where raindrop oscillations produced by raindrop collisions are a small fraction of the oscillations produced intrinsically by vortex shedding. The model of Beard and Chuang (1987) is reasonable when electric forces are absence and it showed a more flat base-shaped than previous axis ratio relations in large drops. For comparison purposes, seven axis ratio models are shown in Fig. 2.2.

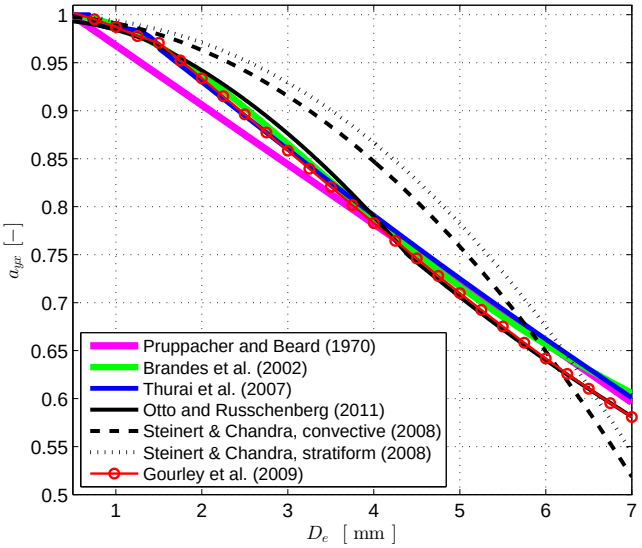

Figure 2.2: Seven axis ratio models for raindrops with D_e up to 8 mm.

For hail stones, oblate shapes are generally assumed, but irregular shapes can occur as well. Experiments conducted by Aydin et al. (1998) have shown that the axis ratio of hail is between 0.7 and 0.9 mm for diameters between 5 and 50 mm while for diameters smaller than 5 mm it is assumed spherical.

The interaction between electromagnetic fields and dielectric particles is studied in terms of the relative complex permittivity (Ray, 1972). Assuming that the permittivity of air is 1, the complex permittivity (ϵ_r) indicates the strength of the relation between an electromagnetic field and polarization of the particle. When a raindrop is excited by an external electromagnetic field, positive and negative charges shift from its equilibrium state forming dipoles and becoming dielectric polarized. When the external field is removed, charges come back to their initial state. The time to go back to their initial equilibrium state, is called the dielectric relaxation time. The real part of ϵ_r, hereafter $\Re(\epsilon_r)$, is called the dielectric constant and the imaginary part of ϵ_r, hereafter $\Im(\epsilon_r)$, is called the loss factor, and therefore, the study of dielectric properties is concerned with the storage and dissipation of electric energy in particles. Both, $\Re(\epsilon_r)$ and $\Im(\epsilon_r)$ depend of the radar wavelength, water state, and temperature.

The complex permittivity for raindrops can be estimated using the Debye model (Liebe et al., 1991). The Debye model calculates the dielectric relaxation response of an ideal noninteracting population of dipoles to an external electromagnetic field at a given raindrop temperature (T [°C]) and field frequency (f [GHz]). According to the Debye model, the complex permittivity ϵ_r, for $T < 60$°C and $f < 100$ GHz, is represented as

$$\epsilon_r(T,f) = \frac{\epsilon_0 - \epsilon_\infty}{1 - i(f f_D{}^{-1})} + \epsilon_\infty, \tag{2.7}$$

where ϵ_0 is the static dielectric constant given by $\epsilon_0 = 77.66 - 103.3T_D$ and $T_D = 1 - 300(273.15 + T)^{-1}$ whereas ϵ_∞ is the high-frequency dielectric constant. From polynomial fitting, ϵ_∞ is determined by $0.066\epsilon_0$ while the relaxation frequency f_D by $20.77 + 146.5T_D + 314T_D^2$. The dielectric factor K_w, previously used to describe η in Eq. (2.4), is defined as

$$K_w = \frac{\epsilon_r - 1}{\epsilon_r + 2}. \tag{2.8}$$

Resulted ϵ_r and $|K_w|^2$ for rain at X-band frequency of 9.475 GHz are shown in Fig. 2.3 as a function of T. The increasing behavior of $\Re(\epsilon_r)$ with temperature indicates that raindrops are much stronger polarized at high temperatures while the decreasing behavior of $\Im(\epsilon_r)$ means that raindrops lose less energy at high temperatures. It is seen that the factor $|K_w|^2$ is nearly independent of temperature and approximately equal to 0.93.

In the case of hail, Hufford (1991) developed a dielectric model to calculate ϵ_r. At the same frequency of 9.475 GHz and for $T = 0$°C, $\Re(\epsilon_r)$ resulted in 3.1 with a negligible $\Im(\epsilon_r)$ and $|K_w|^2$ equal to 0.18.

When a particle is illuminated by an incident electromagnetic wave, different types of scattering waves will occur from such particle. The following definitions are useful to classify different ways of wave scattering (Doviak and Zrnić, 1993).

- Scattering cross section (σ_s [mm^2]): It is the area by which waves are scattered from the particle.
- Absorption cross section (σ_a [mm^2]): It is the area by which energy is dissipated or absorbed by the particle.
- Radar cross section (σ_b [mm^2]): It is the area that contributes waves scatter back to the radar.

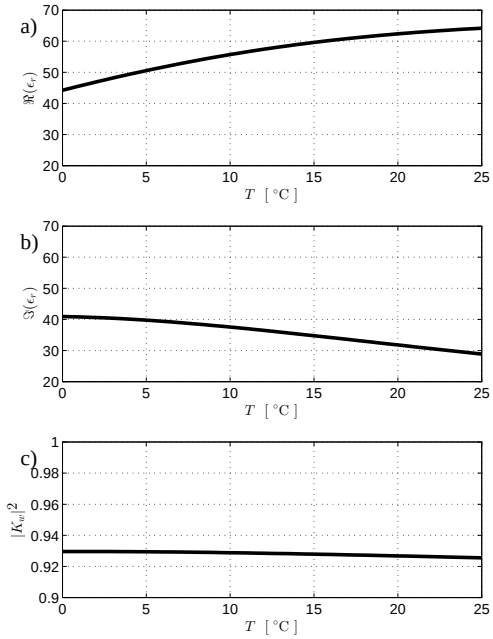

Figure 2.3: Complex permittivity ϵ_r for rain at X-band as a function of T. $\Re(\epsilon_r)$, $\Im(\epsilon_r)$, and $|K_w|^2$ are shown in panels a), b), and c), respectively.

In addition, the area by which the total energy is scattered and absorbed by the particle is referred to as the total or extinction cross section ($\sigma_t = \sigma_s + \sigma_a$ [mm^2]).

For spherical-shaped particles, two methods derived from Maxwell's equations are typically used to estimate cross sections: Rayleigh and Mie-scattering methods (Bringi and Chandrasekar, 2001). The main difference between both methods is that, the Rayleigh method describes a scattering pattern similar to a radiating dipole, while the Mie-scattering approximation expresses a scattering pattern that is more pronounced in the direction of the incident electromagnetic wave than in the backward direction. For a raindrop particle, the following equations are given by the Rayleigh method

$$\sigma_s = \frac{8\pi k^4 a_x^6}{3}|K_w|^2, \tag{2.9}$$

$$\sigma_a = \frac{4}{3}\pi a_x^3 k \times \Im(\epsilon_r) \times \left|\frac{3}{\epsilon_r + 2}\right|^2, \tag{2.10}$$

$$\sigma_b = 4\pi k^4 a_x^6 |K_w|^2, \tag{2.11}$$

where k is the wave number given by $2\pi\lambda^{-1}$ and λ is in mm unit. These equations are valid only for spherical particles whose diameters are smaller than λ. The Mie-scattering

method gives a general solution for the various cross sections as

$$\sigma_s = \frac{2\pi}{k^2}\sum_{n=1}^{\infty}(2n+1)(|a_n^s|^2+|b_n^s|^2), \tag{2.12}$$

$$\sigma_a = \frac{2\pi}{k^2}\sum_{n=1}^{\infty}(2n+1)\Re(a_n^s+b_n^s), \tag{2.13}$$

$$\sigma_b = \frac{\pi}{k^2}\left|\sum_{n=1}^{\infty}(-1)^n(2n+1)(a_n^s-b_n^s)\right|^2, \tag{2.14}$$

where n is the number of multiple expansion scattered lights, a_n^s and b_n^s are unknown scattered expansion coefficients.

The cross sections were calculated using both methods at X-band and $T = 15°C$ and they are shown in Fig. 2.4 as a function of D_e. ϵ_r was estimated using the Debye model re-

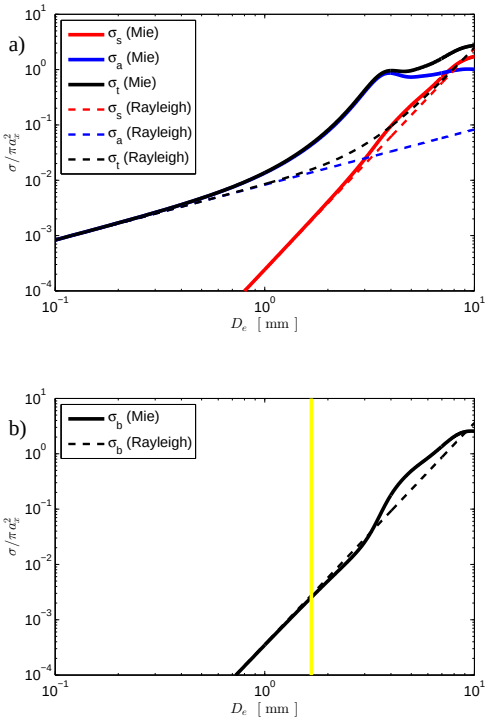

Figure 2.4: Normalized cross sections for spherical raindrop at X-band and 15°C as a function of D_e. Normalized σ_s, σ_a, and σ_t are shown in panel a) while normalized σ_b in panel b). Results obtained from Mie-scattering and Rayleigh methods are indicated by the solid and dashed lines, respectively. The vertical yellow line at 1.7 mm denotes the maximum size in which the normalized σ_b(Rayleigh) is acceptable.

sulting in $59 + i35$ and the cross sections were normalized by the spherical raindrop area for comparison purposes. Note that the normalized σ_s(Rayleigh) and σ_s(Mie-scattering) are similar for $D_e < 3$ mm because the scattering pattern of both methods are similar; however, the normalized σ_a(Rayleigh) deviates from σ_a(Mie-scattering) even for D_e in

the order of 0.7 mm due to the limited solution of the Rayleigh method. Note that the normalized σ_t(Mie-scattering) is dominated by σ_a rather than σ_s for $D_e < 4$ mm. In other words, the absorption of waves in a raindrop could be more significant than the scattering of waves at 30 mm wavelengths given that $\sigma_a > \sigma_s$ for $D_e < 7$ mm.

It can be seen that the normalized σ_b(Rayleigh) deviates from σ_b(Mie-scattering) for $D_e > 2$ mm because the Rayleigh method is not able to represent the scattering pattern for a relatively large particle. In order to safely use σ_b(Rayleigh), the following condition is suggested: if the absolute value of the difference between σ_b obtained from both methods is smaller than 10% the value of σ_b(Mie-scattering), then σ_b(Rayleigh) is still a valid approximation. At the given frequency and temperature, this condition is satisfied for $D_e \leq 1.7$ mm. In the case of spherical hail, not shown here, it was found that σ_b(Rayleigh), at X-band and 0°C, was valid only for $D_e < 5.6$ mm (i.e., small hail size) while σ_t was dominated mainly by σ_s for $D_e \in [2;50]$ mm.

As it was discussed before, raindrop particles tend to be oblate-shaped as the size of the particle increases. Therefore, the wave scattering in the horizontal (major axis) and vertical (minor axis) are expected to be different from one to another. In addition, the scattering is expected to follow a Mie-scattering pattern. In consequence, waves that scatter out of the particle in the same direction of the incident wave is referred to as the forward scattering while the scattering in the opposite direction is referred to as the backward scattering. In this context, the scattering properties of particles will be expressed as scattering amplitudes ($f_{H,V}$ [mm]) instead of cross sections where H and V denote the horizontal and vertical polarization, respectively. In the backward direction, they are related as $\sigma_b^{H,V} = 4\pi|f_{H,V}|^2$ while in the forward direction they are associated as $\sigma_t^{H,V} = 4\pi k^{-1}\Im(f_{H,V})$. Thus, the amplitudes in the backward and forward directions express the received power and attenuation, respectively. The general representation of both cross sections are valid for Rayleigh and Mie-scattering regimes because the magnitude of $f_{H,V}$ is proportional to the particle size in the forward and backward directions.

For comparison purposes, scattering amplitudes of an oblate particle are estimated using the numerical Fredholm Integral Method (FIM) (Holt and Shepherd, 1979) and the extended Rayleigh approach (Russchenberg, 1992). The inputs for the FIM simulation are the axis ratio, complex permittivity, temperature, the equivolume diameter, the wavelength, and angle of the incident wave. The outputs are the $f_{H,V}$ in the backward and forward directions for a given equivolume diameter. In contrast to the FIM method, the extended Rayleigh approach assumes that $f_{H,V}$ in the backward and forward directions are the same and they are calculated as follows

$$f_{H,V} = \frac{k^2}{3}\left(\frac{D_e}{2}\right)^3 \frac{\epsilon_r - 1}{1 + L_{x,y}(\epsilon_r - 1)}, \tag{2.15}$$

where L_x and L_y are the depolarization factors in the x and y axes, respectively, and both are a function of a_{yx}.

The results of $f_{H,V}$ in the backward direction using the FIM method at X-band and 15°C are shown in Fig. 2.5, assuming an incident angle of $\phi = 0°$and the axis ratio model suggested by Brandes et al. (2002). Note that that polarimetric signatures are more clear for D_e larger than 3 mm due to the oblateness of raindrops and that $|f_{H,V}|$ increase proportionally to D_e because of their relation to the backscattered power (i.e., σ_b). Results

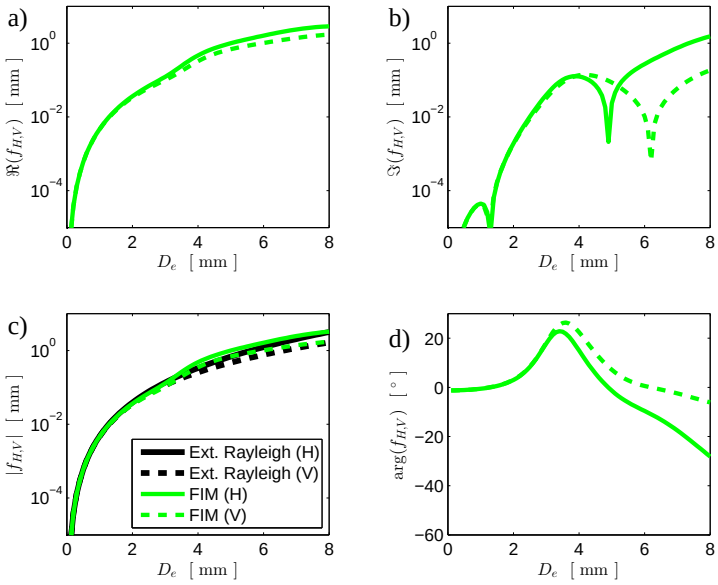

Figure 2.5: Backward scattering amplitudes for oblate raindrops using FIM scattering method at X-band and 15°C. The $\Re(f_{H,V})$, $\Im(f_{H,V})$, $|f_{H,V}|$, and arg($f_{H,V}$) are plotted in panels a), b), c), and d), respectively. Also resulted $|f_{H,V}|$ using the extended Rayleigh approach are plotted in panel c). Scattering amplitudes at the horizontal and vertical polarization are indicated by the solid and dashed lines, respectively.

of $|f_{H,V}|$ from the extended Rayleigh approach are also plotted in Fig. 2.5. It can be seen that, at the given frequency and temperature, both methods agree for D_e smaller than 3 mm approximately.

The results of $f_{H,V}$ in the forward direction are shown in Fig. 2.6. Similar as before, polarimetric signatures can be seen for D_e larger than 3 mm. Even though, the results of $|f_{H,V}|$ from both methods are comparable, their corresponding $\Re(f_{H,V})$ and $\Im(f_{H,V})$ are quite different. This difference is due to the limited solution provided by the extended Rayleigh approach. Recall that $\Im(f_H)$ provide an indication of the power loss of the incident wave due to scattering and absorption in raindrops. Similar results of wave scattering amplitudes but at S-band frequencies were shown by Zhang et al. (2001).

2.3. POLARIMETRIC VARIABLES

Polarimetric radar variables are signatures of electromagnetic waves scattering from a group of hydrometeors captured within the resolution volume and depend on the scattering amplitude and the hydrometeor size distribution. Thus, before defining polarimetric radar variables, a small introduction to hydrometeor size distribution $N(D_e)$ is given next. $N(D_e)$ [$m^{-3}\,mm^{-1}$] indicates the number of particles in a unit volume per unit bin size. Conventionally, three models have been used to represent $N(D_e)$ in rain. As a first attempt, (Marshall and Palmer, 1948) introduced the Marshall-Palmer (M-P)

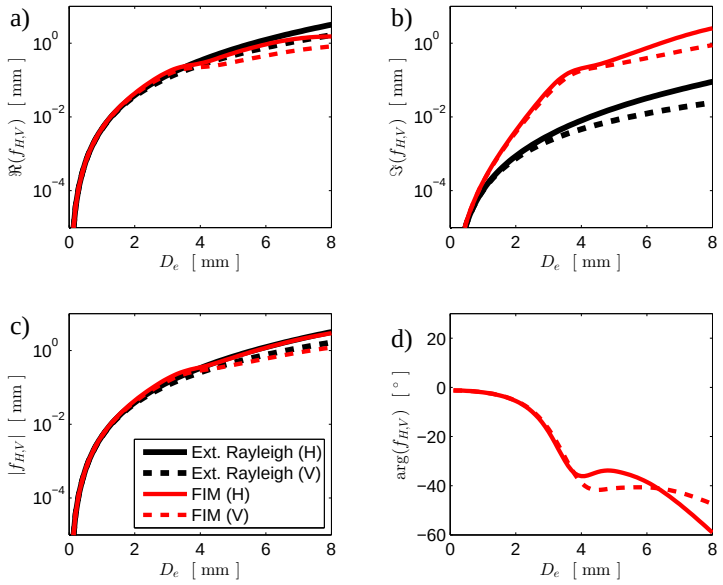

Figure 2.6: As in Fig. 2.5 but in the forward direction.

model, which is described as

$$N(D_e) = N_0 \exp(-\Lambda D_e), \tag{2.16}$$

where N_0 and Λ are equal to $8000\,\mathrm{m^{-3}\,mm^{-1}}$and $4.1R^{-0.21}$ $\mathrm{mm^{-1}}$, respectively, while R is the rainfall rate in $\mathrm{mm\,h^{-1}}$. To further improve and capture the nature variability of $N(D_e)$ in rain, two more model were proposed: the gamma model (Ulbrich, 1983) and the normalized gamma model (Willis, 1984; Illingworth and Blackman, 2002). The gamma $N(D_e)$ model is expressed as

$$N(D_e) = N_0 D_e^{\mu} \exp(-\Lambda D_e), \tag{2.17}$$

where N_0, μ, and Λ are referred to as the intercept, shape, and slope parameters, respectively. Note that if $\mu = 0$ and $N_0 = 8000\,\mathrm{m^{-3}\,mm^{-1}}$then the M-P is a specific distribution of the gamma $N(D_e)$. Haddad et al. (1996) demonstrated that the three parameters of the gamma distribution are not independent from one another. Thus, a convenient manner to model $N(D_e)$ is by normalizing the gamma $N(D_e)$ model with respect to the liquid water content, resulting in the normalized gamma model as a function of three independent parameters as

$$N(D) = N_w g(\mu) \left(\frac{D_e}{D_0}\right)^{\mu} \exp\left[-(3.67+\mu)\frac{D_e}{D_0}\right], \tag{2.18}$$

$$g(\mu) = 6 \times 3.67^{-4} \frac{(3.67+\mu)^{\mu+4}}{\Gamma(\mu+4)}, \tag{2.19}$$

where N_w [$m^{-3}\,mm^{-1}$] is the normalized concentration and Γ indicates the gamma function. D_0 is a rain radar variable which characterizes the raindrop size by which half of the liquid water content is contained in larger drops, equivalent to

$$\frac{\pi}{6}10^{-3}\int_0^{D_0} {D_e}^3 N(D_e)dD_e = \frac{1}{2}W, \tag{2.20}$$

where W [$g\,m^{-3}$] is the liquid water content given by

$$W = \frac{\pi}{6}10^{-3}\int {D_e}^3 N(D_e)dD_e. \tag{2.21}$$

Note that W is proportional to the third moment of $N(D_e)$. Rainfall rate is also related to the third moment as

$$R = 6\pi 10^{-4}\int D_e^3 v(D_e)N(D_e)dD_e, \tag{2.22}$$

where $v(D_e)$ [$m\,s^{-1}$] is the terminal raindrop falling velocity, expressed in terms of D_e. For example, the power-law form has been widely used which is determined as $v(D_e) = 3.78D_e^{0.67}$ (Doviak and Zrnić, 1993). Given this introduction about $N(D_e)$, the following polarimetric radar variables are explained according to Doviak and Zrnić (1993); Zrnić and Ryzhkov (1999).

Two reflectivities are defined based on the linear polarization of the transmitted wave. These are the horizontal reflectivity Z_H^l and and vertical reflectivity Z_V^l, both in units of $mm^6\,m^{-3}$, described as

$$Z_{H,V}^l = \frac{4\lambda^4}{\pi^4|K_w|^2}\int \left|f_{H,V}(\pi, D_e)\right|^2 N(D_e)dD_e, \tag{2.23}$$

where $f_{H,V}(\pi, D_e)$ denote the scattering amplitudes in the backward direction. $N(D_e)$ [$m^{-3}\,mm^{-1}$] and dD_e [mm] specify the hydrometeor size distribution and integration step, respectively. The corresponding reflectivities in dBZ units are given by $Z_{H,V} = 10\log(Z_{H,V}^l)$.

The ratio between Z_H^l and Z_V^l is referred to as the differential reflectivity and it is expressed as $Z_{DR} = 10\log(Z_H^l/Z_V^l)$ [dB]. It depends on hydrometeor size, shape, orientation, density, and water content. For example, if hydrometeors are spherical or randomly oriented then Z_{DR} is near 0 dB and it increases with increasing particle oblateness, density, or water content. Moreover, Z_{DR} does not depend on hydrometeors concentration, reflectivity calibration (assuming that the calibration constant in the horizontal and vertical polarization are the same), and it is a good measure of median volume diameter, hereafter D_0 [mm].

As the wave propagates through a medium, the incident electromagnetic wave is attenuated because of energy losses associated with the absorption (σ_a) and scattering (σ_s) of energy by each hydrometeor. The one-way specific attenuation in the vertical and horizontal polarizations expressed in $dB\,km^{-1}$ are given by

$$A_{H,V} = 8.686\times 10^{-3}\lambda\int \Im\left[f_{H,V}(0, D_e)\right]N(D_e)dD_e, \tag{2.24}$$

where $f_{H,V}(0, D_e)$ denote the scattering amplitudes in the forward direction. $A_{H,V}$ are more significant at short wavelengths because $\sigma_t^{H,V}$ increase as λ decreases (Doviak and Zrnić, 1993). The difference between A_H and A_V is defined as the specific differential attenuation, that is, $A_{DP} = A_H - A_V$ [dB km^{-1}]. $A_{H,V}$ and A_{DP} are independent of radar miscalibration and partial beam blockage and at short wavelengths A_H and A_{DP} are commonly used to correct $Z_{H,V}$ and Z_{DR} for attenuation and differential attenuation, respectively.

In addition to the losses associated with wave propagation through a medium, for instance rain, the horizontal polarized wave gradually decelerates relative to the vertical polarized wave as it encounters more liquid water in oblate raindrops. The difference between the horizontal and vertical polarization phase is defined as the differential phase shift Ψ_{DP} [°], which is independent of power attenuation, radar miscalibration, and relative immune to hail contamination. Ψ_{DP} characterizes the scattering process in the forward direction but it can also include scattering in the backward direction due to internal particle resonance in the Mie-region. Therefore, a Ψ_{DP} profile is represented as $\Psi_{DP} = \Phi_{DP} + \delta_{hv}$ where Φ_{DP} [°] and δ_{hv} [°] indicate the differential phase shift in the forward and backward directions, respectively. In the forward direction, a Φ_{DP} profile accumulates the phase shifts along its course including areas with rain and without rain. In order to distinguish such areas, the half derivative of Φ_{DP} is useful and is referred to as the one-way specific differential phase K_{DP} [° km^{-1}], which is described as

$$K_{DP} = \frac{180 \times 10^{-3} \lambda}{\pi} \int \Re[f_H(0, D_e) - f_V(0, D_e)] N(D_e) dD_e. \tag{2.25}$$

K_{DP} is linearly proportional to hydrometeor concentration and it increases with increasing oblateness, density, and water content of hydrometeors. K_{DP} can be low and noisy in light rain and snow, but it can be high in moderate to heavy rain and in oriented crystals. In the backward direction, δ_{hv} is defined as

$$\delta_{hv} = \frac{180}{\pi} \arg\left[\int \Re(F_{HV}) N(D_e) dD_e + i \int \Im(F_{HV}) N(D_e) dD_e \right], \tag{2.26}$$

$$F_{HV} = f_H^*(\pi, D_e) f_V(\pi, D_e), \tag{2.27}$$

where * is the conjugate operator. δ_{hv} is of significance at short wavelengths and it could be used to estimate D_0 because of its close relation to Z_{DR} (Otto and Russchenberg, 2010).

Two more variables, typically used to distinguish rain from other hydrometeors and non-meteorology targets, are the copolar-correlaton coefficient ρ_{hv} [-], where [-] indicates no units, and the linear depolarization ratio $L_{DR_{hv}}$ [dB]. Both variables are related to the scattering amplitudes in the backward direction similar to $Z_{H,V}^l$. To formulate ρ_{hv} and $L_{DR_{hv}}$, the notation of the scattering amplitudes are modified to include polarization diversity as follows: $f_H(\pi, D_e)$ is now denoted as $f_{HH}(\pi, D_e)$ which indicates the scattering amplitude in the horizontal polarization resulting from an incident electromagnetic field in the horizontal polarization (i.e., copolar polarization diversity). In a similar manner, $f_{VV}(\pi, D_e)$ is also defined but using the corresponding vertical polarizations. It is also possible to specify a cross polarization diversity, for example, $f_{HV}(\pi, D_e)$ which means that the scattering field is horizontally polarized while the incident field

is vertically polarized. Given that the scattering amplitudes associated to ρ_{hv} and $L_{DR_{hv}}$ are in the backward direction and taking into account the polarization diversity, the integration term in Eq. 2.23 will be given by $< |S_{bi}|^2 >= \int |f_{bi}(\pi, D_e)|^2 N(D_e) dD_e$, where the symbol <> indicates an integration operation while the subscript bi denotes four polarization diversity: HH, HV, VH, and VV. Using these defined symbols, ρ_{hv} is described as

$$\rho_{hv} = \frac{< S_{VV} S^*_{HH} >}{< |S_{HH}|^2 >^{0.5} < |S_{VV}|^2 >^{0.5}}. \tag{2.28}$$

Thus, ρ_{hv} indicates the relation between the vertical to horizontal size of a group of hydrometeors and it decreases with increasing oblateness, randomness orientation, and water content. For most hydrometeors, ρ_{hv} is very close to 1 and for non-meteorological echoes it is significantly lower than 1. In addition, ρ_{hv} decreases for a rapid deformation of particle shape due to oscillation or breakup.

On the other hand, $L_{DR_{hv}}$ indicates the ratio between cross polarization power and copolar polarization power as

$$L_{DR_{hv}} = 10 \log \left(\frac{< |S_{HV}|^2 >}{< |S_{VV}|^2 >} \right). \tag{2.29}$$

$L_{DR_{hv}}$ increases with irregular shaped hydrometeors or oblate wet particles (i.e., melting hydrometeors due to its high dielectric factor). Values of L_{DR} for hydrometeors are in the range of -40 to -10 dB while for rain L_{DR} is typically less than -25 dB. However, at short wavelengths, propagation effects can lead to increased L_{DR} values. For simplicity, $L_{DR_{hv}}$ will be denoted as L_{DR} in the following chapters.

Polarimetric variables are commonly related to one another. In order to observe the relations between polarimetric variables in rain medium, measurements of $N(D_e)$ and computation of $f_{H,V}(0, D_e)$ and $f_{H,V}(\pi, D_e)$ are necessary. During the years 2009 and 2010, several measurements of $N(D_e)$ in rain were conducted in the Cabauw observatory of the Netherlands (Leijnse et al., 2010). For the computations of scattering amplitudes, the FIM method is used where three axis ratio models were randomly selected from Brandes et al. (2002), Thurai et al. (2007), and Otto and Russchenberg (2011), while measurements of temperature were obtained by a weather station at 1.5 m also in Cabauw. The resulted relations between polarimetric variables and rainfall rate R [mm h^{-1}] at X-band are illustrated in Fig. 2.7 In each scatterplot, the best curve fitting is shown by black curves, demonstrating the strong relation between radar variables in rain.

Conventionally, measurements of Z and Z_{DR} are used to estimate R based on empirical relations. However, it has been shown that K_{DP} and A_H can improve estimates of R given that K_{DP} and A_H are accurately estimated. For the purpose of studying the relations between polarimetric variables and rainfall rate, the Marshall-Palmer model is used to simulate $N(D_e)$ as described in Eq. 2.16. In this way polarimetric variables at X-band and 15°C are calculated using the outputs of the FIM simulation and the M-P $N(D_e)$. Resulting variables, as a function of R, are shown in Figure 2.8. The results show more distinguished polarimetric signatures as R increases from 0.1 to 100 mm h^{-1}. For example, Z_H are slightly higher than those of Z_V, which is consistent for oblate-shaped raindrops, leading to values of Z_{DR} as high as 3 dB for heavy rainfall rate. K_{DP} and $A_{H,V}$

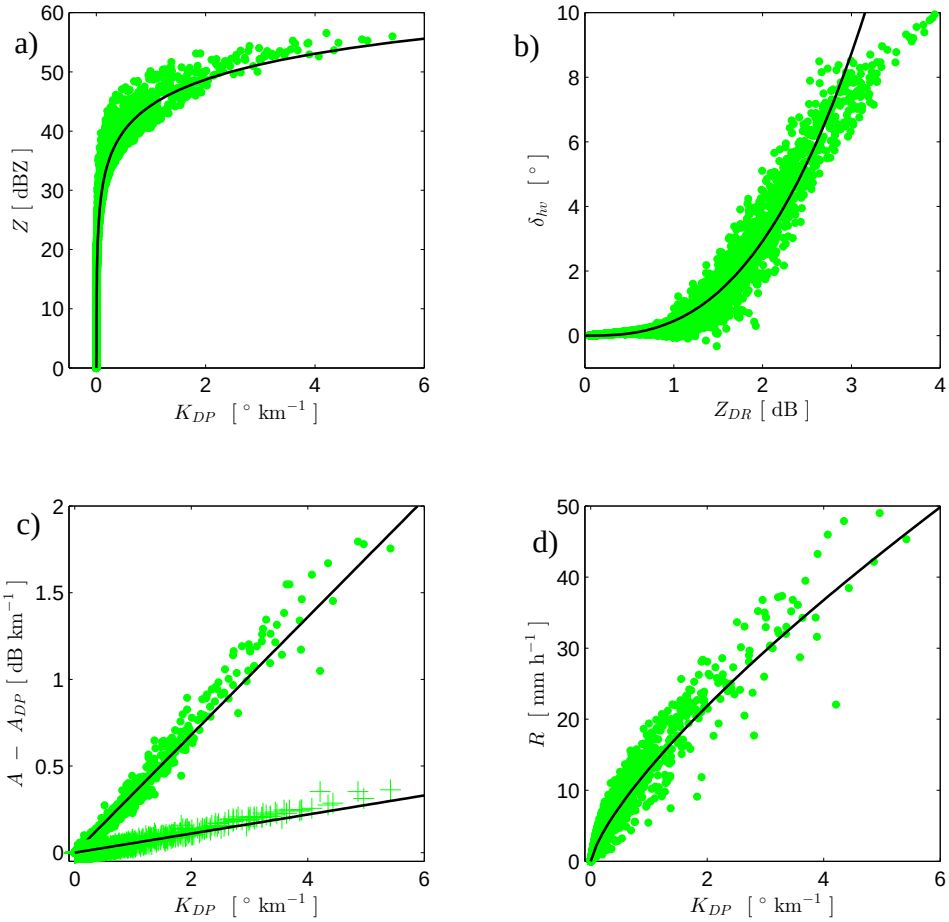

Figure 2.7: Relations between polarimetric variables at 9.475 GHz using measured $N(D_e)$ and scattering computation. The scatterplots Z-K_{DP}, δ_{hv}-Z_{DR}, and $A(A_{DP})$-K_{DP} are indicated by panels a), b), and c), respectively. The scatterplot A-K_{DP} is denoted by dot symbols while the A_{DP}-K_{DP} by plus-sign symbols. The scatterplot R-K_{DP} is illustrated in panel d). The best fits to the scatterplots are indicated by black curves.

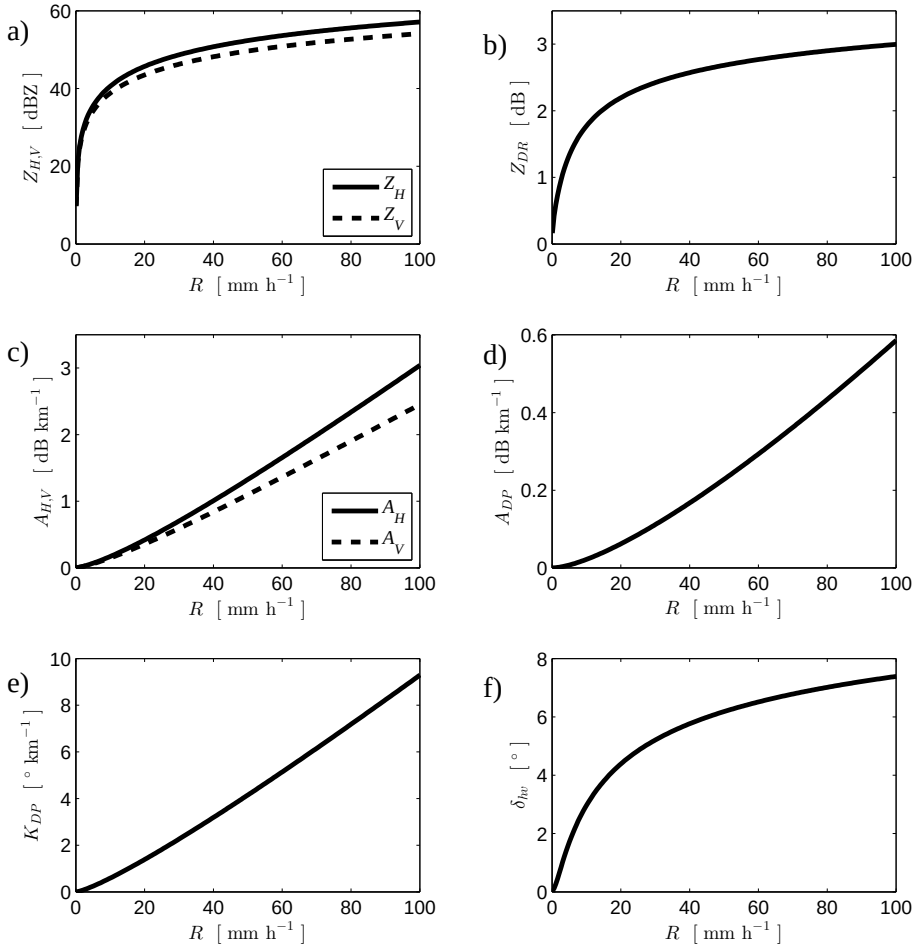

Figure 2.8: Polarimetric radar variables as a function of R at 9.475 GHz and 15°C. The FIM method is used to obtain scattering amplitudes and $N(D_e)$ is modeled using the M-P distribution with D_e up to 8 mm. The results on panels a)-f) represent $Z_{H,V}$,Z_{DR}, $A_{H,V}$, A_{DP}, K_{DP}, and δ_{hv}, respectively.

increase almost linearly with R, which is not the case for $Z_{H,V}$ and Z_{DR}. If the M-P $N(D_e)$ is assumed to be a very good model, it is possible to establish strong relationships between polarimetric variables and rainfall rate. However, $N(D_e)$ varies according to the regional location and storm type, making difficult to find a reliable model.

3

WEATHER RADAR OBSERVATIONS IN THE NETHERLANDS: A SQUALL LINE CASE STUDY

Abstract: Weather observations are conventionally performed by radars at S- and C-band frequencies with a temporal and spatial resolution of 5 min and 1 km, respectively. However, resolutions of such order may not be sufficient to detect small but hazardous storm features of fast-evolving weather events. One way to overcome this limitation is by using polarimetric technology on X-band weather radars. In this study, the benefits and limitations of using polarimetric X-band radars for the observation of convective weather at close range are examined. Additionally, this work aims to scheme a framework for the analyses of storm events using multiple data sources with specific emphasis on radar systems that are available in the Netherlands (NL). For such purpose, a squall line storm over North-Western Europe, monitored by two C-band radars and one polarimetric X-band radar in the NL, is used to compare observations at distinct spatial and temporal resolutions. It is demonstrated that reflectivity fields resulting from the C-band radars, given at resolutions of 5 min and 1 km, depicted large-scale features, such as the S-broken signature, and avoided fully attenuated signals. In the contrary, close-range observations at 1 min and 0.03 km resolution, obtained from the polarimetric X-band radar, exhibited detailed reflectivity signatures, such as the hook echo and the weak echo region. However, radar observables at X-band frequencies experienced significant attenuation levels including fully attenuated signals at range distances of few kilometers.

3.1. INTRODUCTION

Continuous upgrades on conventional weather radars have benefited research and operational weather communities. In Europe, the Operational Program for the Exchange of Weather Radar Information (OPERA) is currently the network of weather radars (Huuskonen et al., 2012). OPERA consists mainly of 194 single-polarization S- and C-bands radars with temporal and spatial resolutions of approximately 5 min and 1 km, respectively. The Netherlands (NL) has contributed to OPERA with two C-bands radars operated by the Royal Netherlands Meteorological Institute (KNMI in Dutch initials, Holleman et al. (2010)). Both C-band radars, hereafter KNMI radars, have improved the observation and understanding of multiple hazardous weather events. For example, Groenemeijer (2005) identified and described storm types associated with lightning activities, severe wind gusts, and large hail damages. In addition, Hazenberg et al. (2014) provided accurate radar rainfall rate of flash flooding storms while van de Beek et al. (2016) analyzed possible source of errors associated with rainfall rate estimation. Although the achievements from using conventional radars, their temporal and spatial resolutions might not be sufficient to detect small but threatening features of fast-evolving weather (e.g., Lane and Moore (2006) and Clark (2011)) and to accurately estimate localized rainfall amounts (Schellart et al., 2012).

One approach to acquire fast weather observations and improve the estimation of rainfall rate at close range is by using polarimetric X-band radars because i) their small size antennas allow for mobility and for reduced maintenance and ii) high spatial resolution can be obtained by setting reasonably short range coverage. For example, the Center for Collaborative Adaptive Sensing of the Atmosphere (CASA) consists of a network of polarimetric X-band radars that can adaptively scan storm regions of interest with temporal and spatial resolutions of 1 min and 100 m, respectively, (Brotzge et al., 2005; McLaughlin et al., 2009). In Japan, the National Research Institute of Earth Science and Disaster Prevention (NIED) established a X-band radar network in the city of Tokyo to develop operational warning systems to cope with severe rainfall damage (Maki et al., 2010). In Western Europe, the RainGain project focused on the implementation and usage of X-band radars to study the impact of the spatial and temporal variability of rainfall events on urban runoff processes (Ochoa-Rodriguez et al., 2015). Furthermore, Bluestein et al. (2007); Schwarz and Burgess (2011); Snyder et al. (2013) identified tornadic signatures in supercell storms to better interpret radar observables while Reinoso-Rondinel et al. (2013, 2014a,b) found similar signatures in a squall line storm. However, the main disadvantage of X-band radars is that the transmitted and received signals can be highly or fully attenuated by regions of heavy precipitation, decreasing the capability of measuring along an entire radial beam.

The purpose of this work is to test the performance of two radars located in the Dutch province of Utrecht: the KNMI C-band radar installed in DeBilt and the polarimetric X-band research radar, hereafter IDRA, located in Cabauw (Leijnse et al., 2010). In addition, this study aims to scheme a framework for the observation and data processing of convective storm events using radar systems that are available in the NL. For such purpose, a squall line storm over North-Western Europe on 03 January 2012 is used to compare observations at distinct spatial and temporal resolutions. The rest of this chapter is organized as follows. The data sources and the case study are introduced in section 2.2.

In section 2.3, reflectivity signatures obtained from the KNMI radars and from a KNMI numerical weather model (HARMONIE) are shown and discussed. Section 2.4 explains the steps to filter noisy areas and to mitigate attenuation issues from IDRA radar data. In section 2.5, observations resulting from the KNMI radar in De Bilt and the IDRA radar are compared to evaluate the advantages and disadvantages of both radar systems. Section 2.6 shows the conclusions of this chapter.

3.2. DATASET DESCRIPTION

3.2.1. DATA SOURCES

The KNMI operates two Doppler weather radars located in De Bilt (52.10°N, 5.18°E) and Den Helder (52.96°N, 4.79°E) towns of the Netherlands, see Fig. 3.1. The KNMI

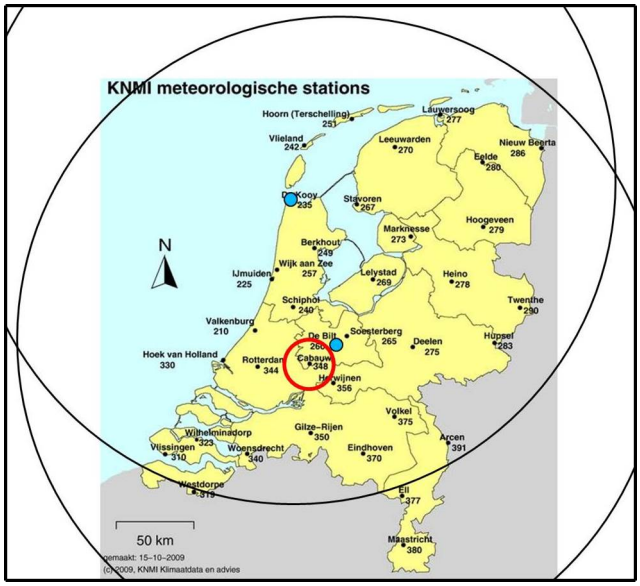

Figure 3.1: The map of the Netherlands showing the locations of the operational KNMI radars located in Den Helder (north cyan dot) and De Bilt (south cyan dot) along with their corresponding 200 km range coverage. The red circle indicates the coverage of the IDRA radar centered in Cabauw. The 35 weather stations are also plotted. *Adapted from Copyright © 2009, KNMI Klimaatdata en advies.*

radars are pulsed radars operating at C-band frequency of 5.6 GHz with a maximum range of 320 km and with a range resolution of 1 km (Beekhuis and Holleman, 2008). Each radar coverages a volumetric region every 5 min by rotating the antenna 360° in azimuth and tilting the antenna in elevation from 0.3° to 25°. The 3dB beamwidth is of 0.94° and the transmitted peak power of 250 kW. Radar calibration is performed using an extended version of the sun-signal method (Rinehart, 2004; Holleman et al., 2010). Volumetric measurements include unfiltered reflectivity, mean radial velocity, and spectrum width (available at http://data.knmi.nl). Clutter signals are filtered from reflectivity measurements using statistical filtering and a time-domain Doppler filter for the lowest elevation (non-Doppler) and higher elevations, respectively.

In order to obtain rainfall rate estimation, a composite reflectivity field at a constant height of 1.5 km is obtained by interpolating reflectivity pixels from both radars at elevations angles of 0.3, 1.1, 2.0, and 3.0° (Beekhuis and Holleman, 2008). The composite reflectivity fields are given at temporal and spatial resolutions of 5 min and 2.4 km, respectively. The conversion from reflectivity to rainfall rate data is determined by the relation $Z = 200R^{1.6}$, hereafter the R-Z relation (Marshall et al., 1955). Because the accuracy of rainfall rate decreases with range, among other factors, the maximum range from each KNMI radar is set to 200 km at the lowest elevation angle, indicated by the two black rings in Fig.3.1. In addition, the KNMI operates a network of 35 automatic weather stations (see Fig.3.1) to measure weather parameters such as temperature, pressure, wind, and precipitation depth every 10 min (Wauben, 2006). With the goal of improving radar measurements, the KNMI upgraded their radars from single-polarization to dual-polarization during the period 2016-2017. Therefore, the use of the KNMI polarimetric radar data during this study is not possible.

Besides the KNMI radars and weather station, KNMI also operates a numerical weather prediction model (NWP) to solve and forecast convective events and it is referred to as HIRLAM (high resolution limited area model) aladin regional mesoscale operational NWP In Europe (HARMONIE) (Unden, 2002; Krikken, 2012). As the year of 2012, this model is centered at De Bilt and its horizontal domain extends up to 750 km with a 2.5 km grid resolution and 60 vertical layers. The lowest level is at 10 m above ground level while the next 30 levels reach an altitude of 3.5 km. Outputs are normally generated every hour but it is also possible to generate data every 10 min. Using a single-moment bulk microphysical scheme and assuming an exponential hydrometeor size distribution, HARMONIE provides the tendency of hydrometeor mass mixing ratios and concentrations as prognostic variables, as well as horizontal wind, temperature, water vapor content, specific humidity, turbulence kinetic energy, among others. Physic properties considered in HARMONIE are mainly adapted from the AROME model (Seity et al., 2011) while dynamics processes are taken from ALADIN non-hydrostatic (NH) (Benard et al., 2010). Instantaneous rain is given as a flux in units of $\mathrm{kg\,m^{-2}\,s^{-1}}$, so that, comparable units to rainfall rate are obtained multiplying instantaneous rain by 3600.

Another data source is the polarimetric Doppler weather radar (IDRA) which operates at X-band frequency of 9.475 GHz (i Ventura and Russchenberg, 2009) and was designed by the Delft University of Technology. This research radar is a frequency modulated continuous wave system whose operational range is 15.3 km with a range resolution of 0.03 km, covering a limited area as shown by Fig. 3.1. IDRA is located at the Cabauw experimental site for atmospheric research (CESAR) observatory of the Netherlands at a height of 213 m above ground level and 23 km southwest from DeBilt (Leijnse et al., 2010). It scans at a fixed elevation angle of 0.5° and rotates the antenna over 360° every 1 min with a beamwidth of 1.8° and transmitted power of 20 W. It is important to mention that IDRA currently is not able to scan in elevation due to mechanical/electrical limitations. The variables measured by IDRA consist of reflectivity, differential reflectivity, differential phase, linear depolarization ratio, mean radial velocity, and spectrum width. Clutter echoes are removed by a filter based on spectral polarimetric processing (Unal, 2009).

3.2.2. CASE STUDY

Cold fronts lift warm moist air, triggering cloud vertical development which can produce severe squall lines and individual storm cells (Lamb and Verlinde, 2011). A squall line is a long-lived convective line of storms that forms along a cold front with a predominately trailing stratiform precipitation, associated with moderate wind shear between 10 and 20 m s^{-1} and with strong updraft air motion (Weisman and Rotunno, 2004; Storm et al., 2007).

The event presented in this chapter is a wintertime squall line storm that crossed the North Sea and the Netherlands on 03 January 2012 between 12:00 and 18:00 UTC. Observations by the infrared (IR) satellite SAT24-EISQ51 and the pressure surface analysis map at 12:00 UTC indicate that this storm was associated with a low pressure system and with a strong synoptic force as shown in Fig. 3.2. In-situ measurements from the CESAR observatory registered, at 14:30 UTC and 10 m from ground level, a temperature of 10° C, a wind speed of 65 km h^{-1}, and a pressure of 995 hPa. In addition, at 14:40 UTC, the rain gauge measured a maximum value of 15 mm h^{-1}, which corresponds to the pass of the convective region of the storm.

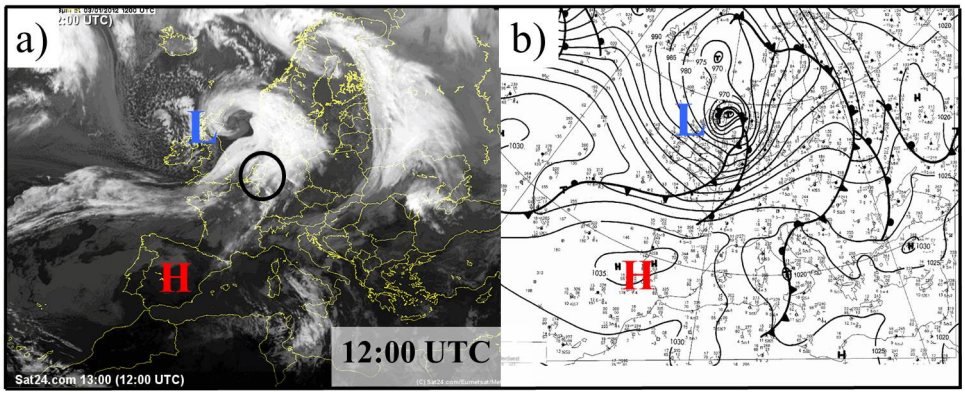

Figure 3.2: a) IR satellite imagery from SAT24-EISQ51 over Europe on 03 January 2012 12:00 UTC which shows a cyclonic system associated with a deep low pressure centered over the North Sea. The black circle indicates the location of the Netherlands. b) The corresponding synoptic chart at ground level where L and H represents areas of low and high pressure, respectively. *Adapted from http://Sat24.com Copyright © 2006 - 2017 The Meteo Company B.V. and the German weather service.*

Multiple photographs related to interesting weather events in Belgium and the NL are uploaded to the website https://weerwoord.be/photofeed/. In order to show an impression of the presented storm event, two photographs taken over the north part of the NL are given by Figs. 3.3 (at 14:00 UTC) and 3.4 (at 18:00 UTC). Fig. 3.3 was taken in the town of Lemmer (province of Friesland), showing splashing water in the in-land bay IJsselmeer due to a strong wind gust of 80 km h^{-1}, obtained by the weather station # 267 in Stavoren. This station measured a maximum wind gust of 97.8 km h^{-1} at 16:00 UTC. Fig. 3.4 was taken in the Terschelling island showing the rear side of the squall line storm. The weather station # 251 of Hoorn-Terschelling registered a wind gust of 50 km h^{-1} at 18:00 UTC while a maximum wind gust of 102.6 km h^{-1} was measured at 13:00 UTC.

Figure 3.3: A photograph of the in-land bay IJsselmeer of Lemmer, the Netherlands, 03 January 2012 at 14:00 UTC. *Photos courtesy of Roelf-Jan Drent, Stormachtig IJsselmeer.*

Figure 3.4: A photograph of the rear side of the squall line on 03 January 2012 at 18:00 UTC viewed from the Terschelling island, the Netherlands. *Photo courtesy of Sytse(Terschelling).*

3.3. OBSERVATIONS BY THE KNMI C-BAND RADARS AND THE HARMONIE MODEL

In contrast to the synoptic scale observations given by SAT24-EISQ51, the same weather event was observed by the operational KNMI radars and also modeled by HARMONIE. The evolution of the squall line storm between 12:00 and 17:00 UTC moving across the North Sea and the NL is represented by the composite reflectivity fields shown in Fig. 3.5. It can be inferred that areas of moderate to heavy precipitation are located along the convective line with reflectivity values larger than 30 dBZ. Note that, as the storm propagates through the NL, the convective line is embedded in a stratiform region and is broken into segments associated with a line echo wave pattern (LEWP), which may be due to a rear inflow jet (RIJ) force and wind shear effects (Nolen, 1959; Hagen, 1992). For a schematic representation of a squall line structure, the reader is referred to Fig. 3.6a).

For comparison purposes, rainfall rate fields modeled by HARMONIE at the high of 1.48 km and every 10 min, from 12:00 to 18:00 UTC, were converted to reflectivity using the R-Z relation. The measured and modeled reflectivity fields at 12:00 UTC are shown in Fig. 3.7, top panels. Note that the modeled reflectivity field shows a leading precipitation (i.e., the region in front of convective segments) with reflectivity values higher than those measured by the KNMI radars. This might be due to the microphysical scheme used by HARMONIE that leads to excessive amount of liquid water content. By comparing the evolution of the storm resulting from observation and simulation, not shown here, the reflectivity field from HARMONIE presented a temporal delay related to the propagation of the storm. As an example, the measured and modeled reflectivity fields at 14:35 and 15:50 UTC, respectively, are shown in Fig. 3.7, bottom panels. The deceleration of the storm motion may be due to a limited solution of dynamic processes affecting the predicted wind speed and direction of the storm. Nonetheless, HARMONIE was able to reproduce a similar segmentation pattern of the observed convective line.

As mentioned previously, the evolution of the squall line was characterized by broken segments. Those broken segments are also referred to as the "S-broken" reflectivity signature which has been associated with tornadic and non-tornadic storms, mainly shallow squall lines (McAvoy et al., 2000; Grumm and Glazewski, 2004; Clark, 2011). A schematic of the S-broken signature is indicated in Fig. 3.6 panel a), while an example of it is given in Fig. 3.7 panel c). Possible horizontal wind shear is expressed by black arrows, shifting segments ahead others and forming a S-shaped broken feature as indicated by the black curve. It has been reported that the detection of tornado and non-tornado vortex associated with the S-broken signature using conventional radars remain a challenging task (Lane and Moore, 2006; Davis and Parker, 2014). Therefore, storm observations at higher temporal and spatial resolutions such as those obtained by small X-band weather radars are desirable.

3.4. OBSERVATIONS BY THE IDRA X-BAND RESEARCH RADAR

Signal attenuation can be significant at short wavelengths and therefore Z and Z_{DR} measurements resulting from IDRA are represented by z and z_{dr}, respectively. The squall line storm was also observed by the IDRA radar, providing polarimetric observations at

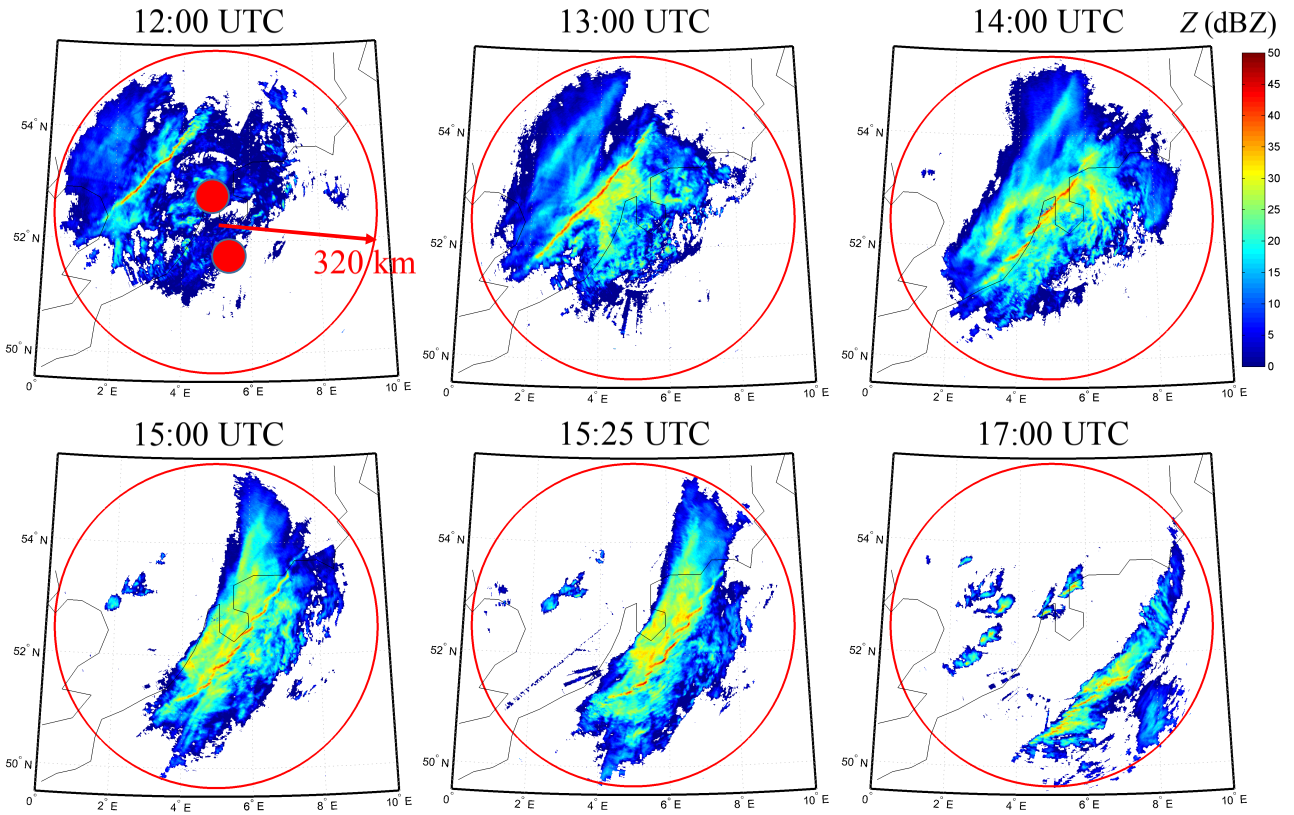

Figure 3.5: Evolution of the squall line storm on 03 January 2012 represented by the composite reflectivity at 1.5 km height obtained from the two KNMI radars, whose locations are marked by the two filled circles. The range coverage is indicated by the red circle, which is centered between both radars, while the coastlines of the United Kingdom and the NL are represented by the black contours.

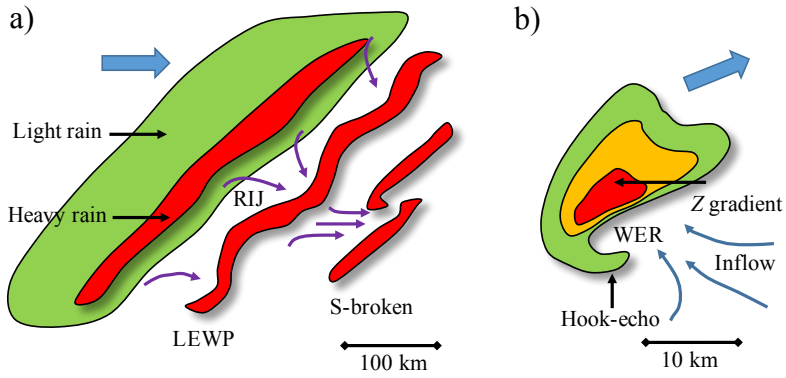

Figure 3.6: Schematic radar signatures at low-level related to two types of storms. a) A squall line storm is illustrated by a convective leading line (red) followed by a stratiform rain area (green). The purple arrows indicate the mid-level rear inflow jets (RIJs) that can produce a line echo wave pattern (LEWP). In case of an enhancing of the RIJs, the convective line is broken in two or more segments (S-broken). Adapted from Przybylinski (1995) and McAvoy et al. (2000). b) A supercell storm is represented by a strong Z gradient (green-red), a hook-echo, and a weak echo region (WER), the last two are associated with a rotating updraft. Adapted from Lemon and Doswell (1979). In both panels, the blue arrow indicates the storm motion.

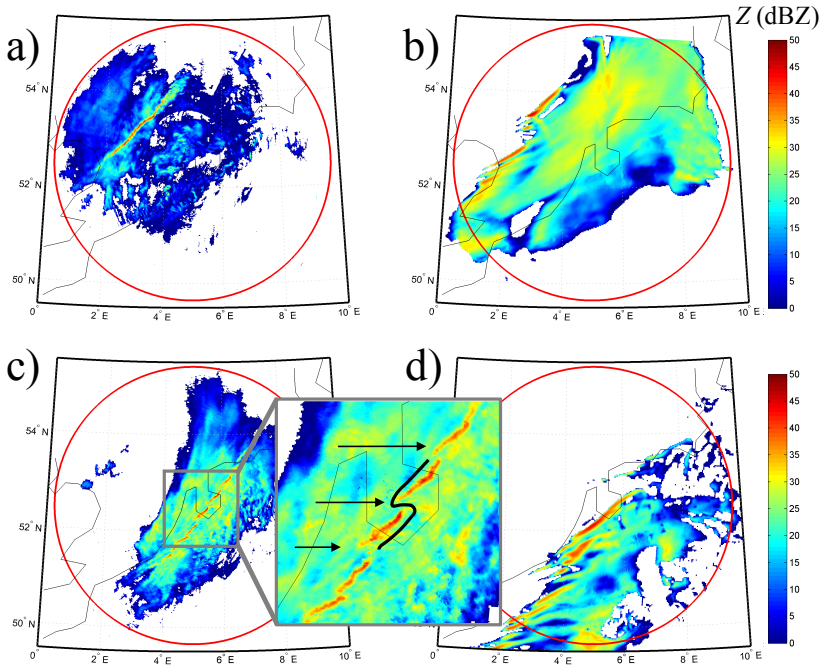

Figure 3.7: Reflectivity fields at 12:00 UTC obtained from a) the KNMI radars and b) the HARMONIE numerical model. Panel c) shows the KNMI reflectivity field at 14:35 UTC associated with a line echo wave pattern (LEWP) while panel d) represents the corresponding field derived from HARMONIE but at 15:50 UTC. In addition, a zoom-in of panel c) illustrates the S-broken signature and related wind shear.

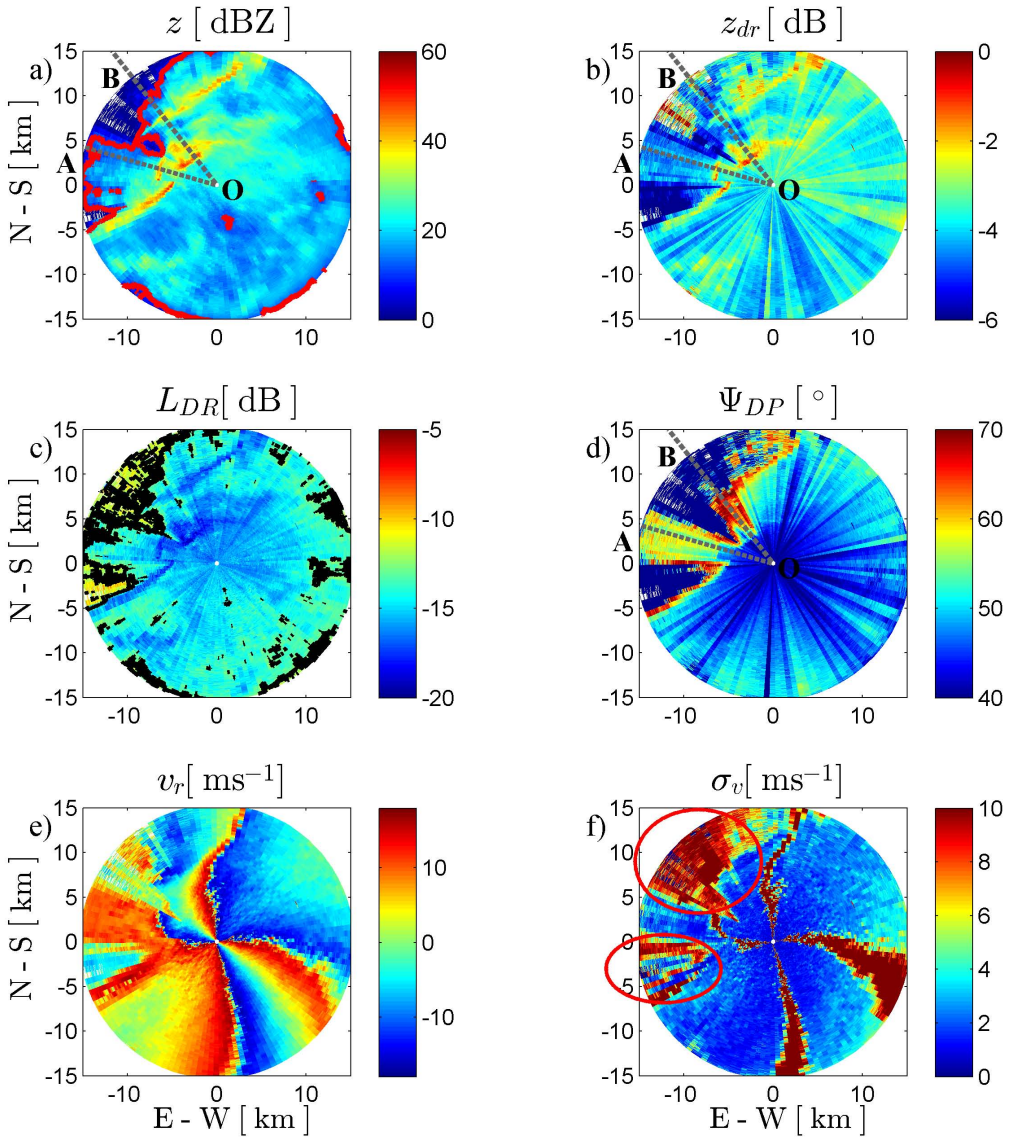

Figure 3.8: Observations by the IDRA radar in the NL on 03 January 2012 at 14:40 UTC. Fields of a) attenuated reflectivity, b) attenuated differential reflectivity, c) linear depolarization ration, d) differential phase, e) radial mean velocity, and f) spectrum width. The segments AO and BO represent the azimuthal radials of 286° and 322°, respectively. In panel a), the red contour lines indicate the 10 dBZ reflectivity level while in panel c), the black contour lines denote the −12 dB linear depolarization ratio level. In panel f), areas affected by high noise levels are indicated by two red ellipses.

high-resolution but limited to a range coverage of 15 km and to a fixed elevation angle of 0.50° as shown in Fig. 3.8. In some cases, areas behind strong echoes resulted in low val-

ues of signal to noise ratio (SNR), leading to erroneous measurements. For IDRA, areas with low SNR were associated with a substantial increase of σ_v as indicated in panel f) by the red ellipses. Note that, high values of σ_v are not exclusively related to high noise levels due to velocity aliasing issues (i.e., when v_a is smaller than the actual radial velocity) as it can be observed in panels e) and f). Ψ_{DP} range profiles were also characterized by a considerable rapid decrease in range (panel d), which is unusual when observing hydrometeors. Thus, for the purpose of filtering low SNR regions, an ad-hoc supervised approach based on IDRA observations is proposed, such that areas with $z < 10$ dBZ, $L_{DR} > -12$ dB, and a range decreasing behavior of Ψ_{DP} larger than 30° are suppressed for further processing. These thresholds used in the filtering method should be adjusted according to IDRA system performance (i.e., radar calibration, transmitting power, and received noise levels).

In order to correct z and z_{dr} measurements for attenuation and differential attenuation, respectively, the attenuation correction method introduced by Bringi et al. (1990) is adapted. In this method, the path integrated attenuation in reflectivity (PIA) and in differential reflectivity (PIA_{DP}) are given by $0.34\Delta\Phi_{DP}$ and $0.05\Delta\Phi_{DP}$, where both coefficients are obtained from scattering simulations according to Otto and Russchenberg (2011) while $\Delta\Phi_{DP}$ represents the difference of Φ_{DP} (i.e., the total span of an estimated Φ_{DP} profile). Conventionally, a Φ_{DP} profile is estimated by smoothing the measured Ψ_{DP} profile. Given that Ψ_{DP} profiles are estimated at Δr equal to 0.03 km, a linear regression fit over a 1 km window is applied to Ψ_{DP} profiles. In this way, Φ_{DP} profiles are obtained. To illustrate the results of the filtering approach and the attenuation correction method, the range profiles of z, z_{dr}, and Ψ_{DP} along the segments AO and BO are given in Figs. 3.9 and 3.10, respectively.

The segment AO is characterized by a noticeable increase profile of Ψ_{DP} due to rain and also noisy measurements beyond 12 km as a result of low SNR. The smoothed Φ_{DP} profile led to values of PIA and PIA_{DP} approximately equal to 6 and 1.5 dB, respectively, which are used to obtain attenuation corrected Z and Z_{DR}. The accuracy of this simple method to correct z from attenuation is in the order of ±1.5 dB, (Gorgucci and Chandrasekar, 2005). The local increase of Ψ_{DP} and Φ_{DP} around 7 km is an example of the δ_{hv} component, which is hard to filter using regression fits without significant smoothing. Similar to segment AO, results associated with segment BO show a fast increase of Ψ_{DP} until 10 km, in which Ψ_{DP} values decrease rapidly due to low SNR. Resulting Z and Z_{DR} profiles indicate attenuation values of 10 and 2 dB, respectively, at the range of 10 km as denoted PIA and PIA_{DP} profiles. Note that the profiles of z_{dr} and Z_{DR} are smaller than 0 dB in both radial segments. This means that measurements of Z_{DR} provided by IDRA are negative-biased due to radar calibration, which may indicate that measurements of Z are biased too. Otto and Russchenberg (2011) also suggested that measurements of Z by IDRA might not be well calibrated. For calibration purposes, the reader is referred to techniques that use hydrometeors as external targets and measurements of K_{DP} and A, which are independent of radar calibration (e.g., Giangrande and Ryzhkov (2005) and Trabal et al. (2014)).

The same procedure of filtering noisy regions and correcting for attenuation and differential attenuation is applied to the all azimuthal radials of Fig.3.8 and the resulted PPI's of Z and Z_{DR} are shown in Fig.3.11. Attenuation corrected values of Z and Z_{DR} are

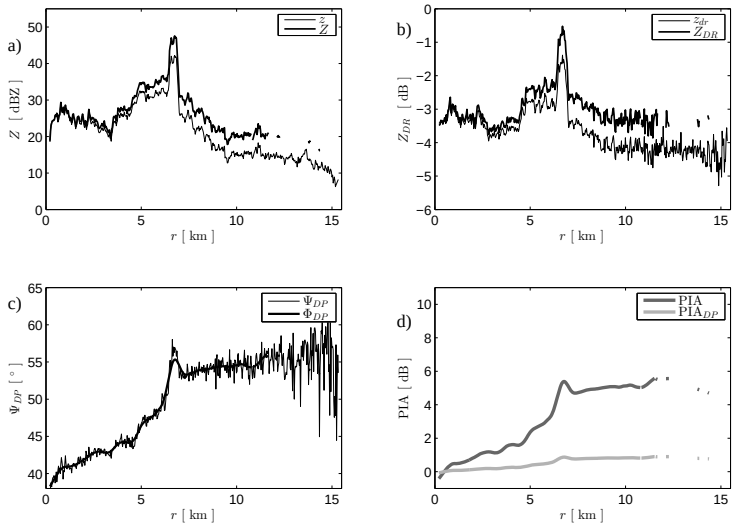

Figure 3.9: Range profiles at azimuthal radial of 286° (segment AO). a) The z profile is indicated by the thin line while the Z profile by the thick line. b) As in a) but for Z_{DR}. c) The measured Ψ_{DP} and the estimated Φ_{DP} profiles are denoted by the thin and thick lines, respectively. d) The resulted PIA and PIA_{DP} profiles are represented by the dark and light gray lines, respectively.

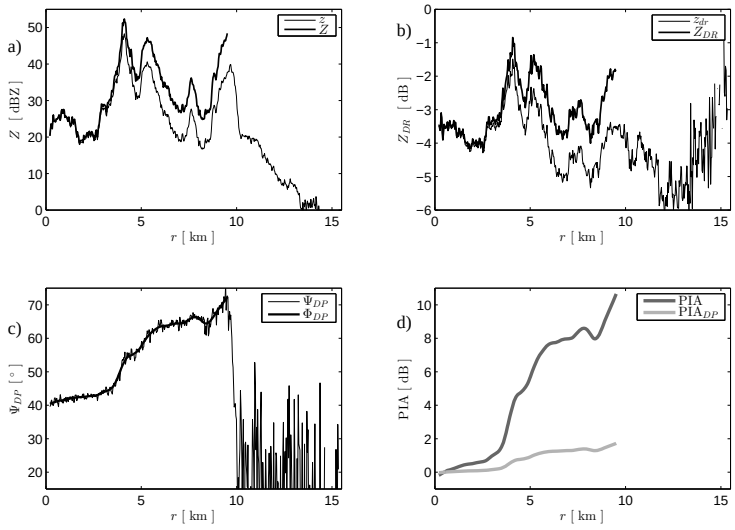

Figure 3.10: Similar to Fig. 3.9 but for the azimuthal radial of 322° (segment BO).

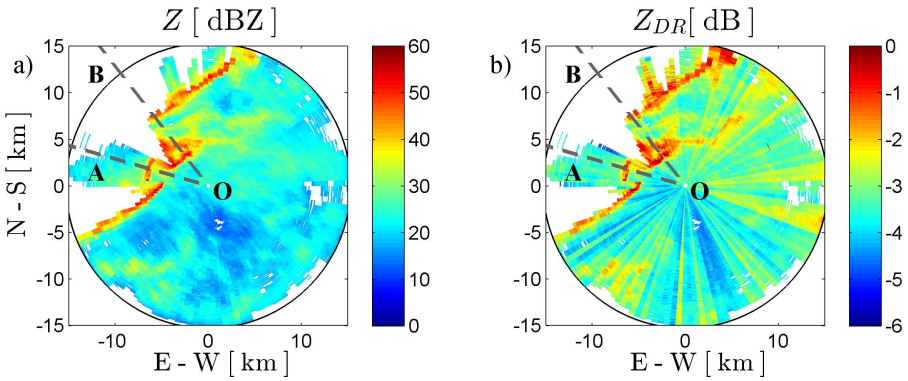

Figure 3.11: The attenuation corrected Z and differential attenuation corrected Z_{DR} fields, 03 January 2012 at 14:40 UTC, are indicated by panels a) and b), respectively. Segments AO and BO are the same as in Fig. 3.8.

more evident along the convective lines while areas behind these lines are suppressed and thus the attenuation correction is not possible. The performance of the attenuation correction method is sensitive to unfiltered δ_{hv} components and constant coefficients. More discussion and analyses with respect to the estimation of Φ_{DP} and correction of z and z_{dr} will be shown in Chapters 4 and 5, respectively.

Note a radial pattern in the Z_{DR} field of Fig. 3.11b. This radial pattern could be due to sources that are internal or external to the radar. For example, internal anomalies on the performance of the hardware components related to the horizontal and vertical channels may lead to noisy Z_{DR} measurements (Bringi and Chandrasekar, 2001). External sources such as wireless communications and nearby radar systems might also lead to noisy measurements. Moreover, anthropogenic structures such as towers and buildings in close proximity of the radar can produce a similar radial pattern in Z_{DR} measurements due to partial beam blockage. According to Giangrande and Ryzhkov (2005), the bias of Z_{DR} in precipitation that is caused by beam blockage is usually manifested by an apparent azimuthal modulation of Z_{DR}, leading to negative and positive biases. Such hypothesis was confirmed by the fact that an obvious azimuthal modulation was not longer noticeable when the Cimarron radar was tilted at higher elevation angles. In a similar manner, Gourley et al. (2006) and Gourley et al. (2009) realized that a security metallic fence, which surrounds a radar installed in the top of a tower in France, and an adjacent electronic box introduced bias on Z_{DR} that varies along azimuth. Vulpiani et al. (2012) also observed that Z_{DR} measurements obtained in Italy were characterized by an azimuthal-bias behavior due to nearby obstacles such as lightning rods and fencing. A metallic fence also surrounds the IDRA radar platform and it may be one of the sources that introduces an azimuthal-dependence bias in the Z_{DR} field, similarly to partial beam blockage effects. Nonetheless, this is a hypothesis and it is still unknown which sources, internal or external to IDRA, cause the observed radial pattern in Z_{DR}.

3.5. QUALITATIVE COMPARISON BETWEEN DE BILT C-BAND AND IDRA X-BAND RADARS

In this section, observations of reflectivity obtained by the De Bilt and IDRA radars resulting from the squall line storm are compared in order to study the benefits and limitations of radar systems similar to IDRA. For this reason, observations of the composite reflectivity at 1.5 km height are not considered. Despite the fact that Z values resulting from De Bilt radar may be attenuated whereas those from IDRA radar could be biased due to calibration, the comparison will be based on the structure and shape of the storm. In the following discussion, another radar signature is introduced, the so-called reflectivity hook echo. For a schematic illustration of a hook echo, the reader is referred to Fig. 3.6b) which shows the structure of a supercell storm at low levels. Although a supercell storm is not the case study, its reflectivity structures are useful to compare against the signatures observed by the De Bilt and IDRA radars.

Fields of Z sampled every 5 min at elevation angle of 0.4° by De Bilt radar are shown in Fig. 3.12. This elevation angle was selected because it reduces ground-clutter contamination and corresponds approximately to the observations obtained by IDRA, which is located 23 km southwest of the De Bilt radar. Note that Z values larger than 52 dBZ were filtered to further reduce ground-clutter contamination. Panels a) and b) illustrate the northern and southern segments associated with the S-broken signature, see also Fig. 3.6a). Panel c) depicts a hook appendage in the south-end of the northern segment, which may indicate the presence of vorticity or rotating updraft motion as suggested by Lane and Moore (2006). Five minutes after, in panel d), the hook echo is not longer evident while areas with attenuated echoes can be seen in the north and south part of the southern segment, which is located south of IDRA.

In order to compare the observations from De Bilt radar, reflectivity fields resulted from IDRA but sampled every 5 min are shown in Fig. 3.13. Panels a) and b) show similar characteristics of the S-broken signature as seen by the De Bilt radar, but with an increased spatial resolution. However, it is seen that multiple areas behind strong reflectivity segments were filtered due to significant noise. Notice that Z echoes at ranges larger than 10 km are characterized by bigger pixels. This is because the radar resolution volume increases with range. The reflectivity field in panel c) also shows the hook appendage but with a better spatial structure and shape to be associated with vorticity, see also Fig. 3.6b) for comparison purposes. The area of light rain that surrounds the hook echo is known as the weak echo region (WER) because this area is bounded horizontally and vertically by moderate to strong echoes. Although Doppler velocity data was available, the small value of v_a and the complexity of the wind field and storm motion made a difficult task to observe gate-to-gate wind shear associated with vorticity. Finally, panel d) provides a more detail structure of the south segment than the one showed in Fig. 3.12.

For a better visualization and comparison of the hook echo feature resulting from both radars, Fig. 3.14 displays zoom-in PPI's from Fig. 3.12 and Fig. 3.13 at 14:45 UTC. Despite the observations from both radars do not exactly overlap, it is seen that within the area of comparison, the Z field that results from De Bilt radar distorts the storm structure while the Z field from the IDRA radar provides a more detailed structure of the

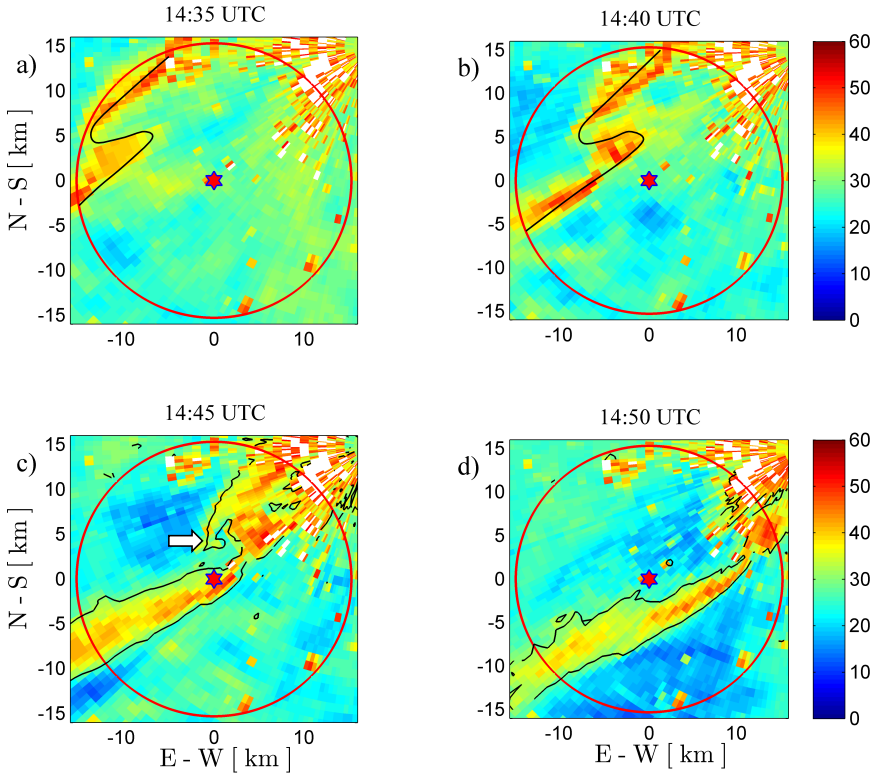

Figure 3.12: Z fields observed by De Bilt C-band radar at the elevation angle of 0.4° sampled every 5 min from 14:35 to 14:50 UTC on 03 January 2012. The S-broken signature is shown in panels a) and b) by the black curves while the hook-appendage is shown in panel c) by the white arrow. The black contours in panel c) and d) represent the 30 dBZ level. The x and y axes are centered at IDRA, which location is indicated by the red star symbol and range coverage by the red circle.

storm such as the hook echo and WER signature, compare Figs. 3.14 and 3.6b).

In contrast to the Z fields shown in Fig. 3.13, the Z fields obtained by IDRA every 1 min from 14:41 to 14:44 UTC are represented in Fig. 3.15. The higher temporal resolution, in addition to the spatial resolution, can allow an early identification of the hook appendage signature as well as to verify the consistency of the observations. The Z field at 14:46 UTC, not shown here, indicated that the hook signature is not longer strong, which is an advantage because it provides an early knowledge of the decay process of threatening signatures.

Although the presented analysis related to the squall line event is limited to horizontally scanned reflectivity observations, Reinoso-Rondinel et al. (2013, 2014a) provided rainfall analysis of the same event at different spatial resolutions resulting from the KNMI radars, the HARMONIE model, and the IDRA radar. Furthermore, Reinoso-Rondinel et al. (2014b) studied dynamic processes of the same squall line at high resolution using IDRA radar and a S-band radar which consists of three beams pointing at 60,

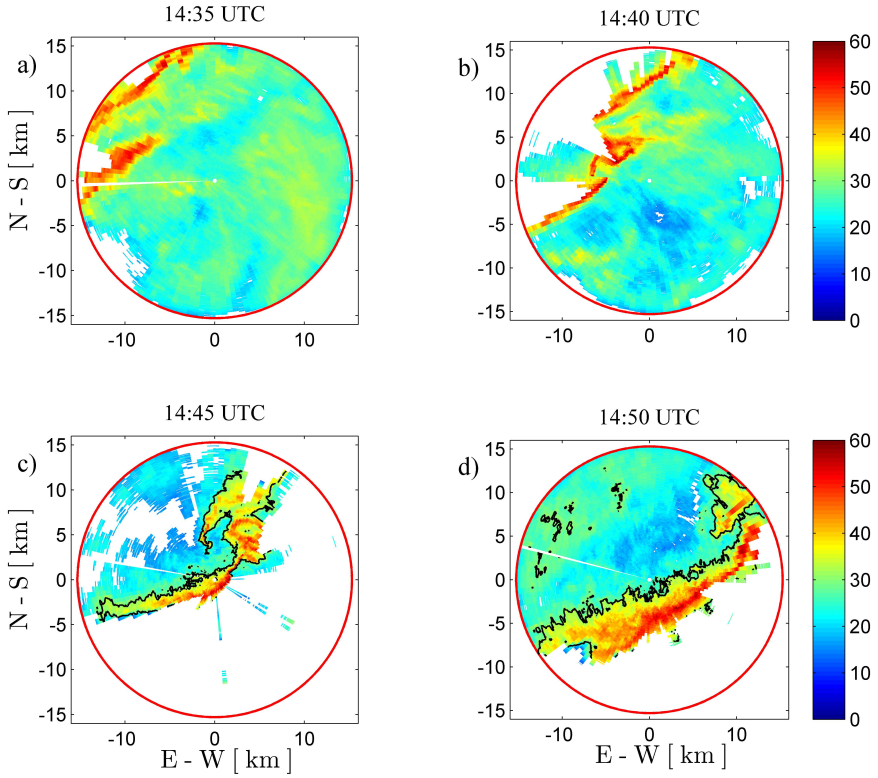

Figure 3.13: Attenuation corrected Z fields observed by IDRA X-band radar sampled every 5 min from 14:35 to 14:50 UTC on 03 January 2012. The black contour represents the 30 dBZ level whereas the red circle indicates the coverage of IDRA.

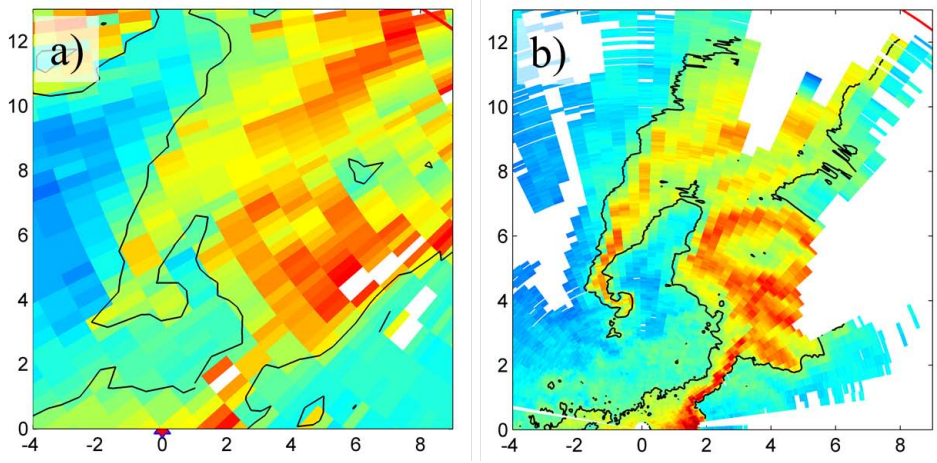

Figure 3.14: Zoom-in of the Z field at 14:45 UTC obtained from a) De Bilt C-band radar and b) IDRA X-band radar.

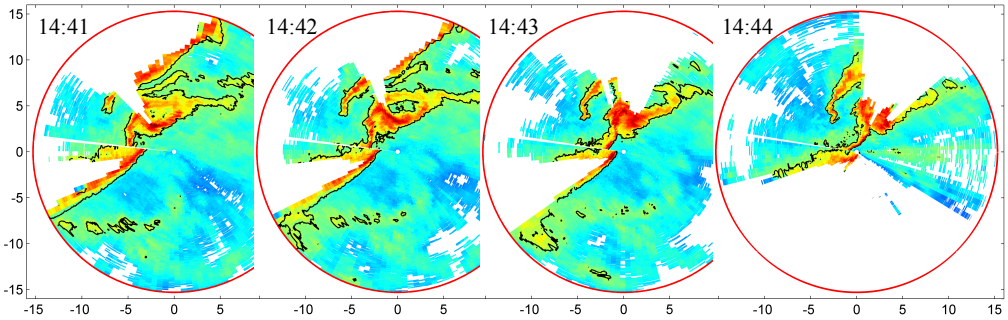

Figure 3.15: As in Fig. 3.13 but sampled every 1 min from 14:41 to 14:44 UTC.

75, and 90°, called TARA (Heijnen et al., 2000).

3.6. CONCLUSIONS

Weather observations have been conventionally performed by S- and C-band radars, but their spatial and temporal resolution can be limited for appropriate monitoring and studying of convective storms. X-band radars with polarimetry capability, in the contrary, may be suitable to obtain storm measurements at higher resolutions. In this work, the benefits and limitations of C- and X-band weather radars in the NL have been examined. Moreover, a framework to analyze convective events using available weather sensors has been provided.

A squall line storm was used to test the measuring capabilities of the operational KNMI C-band radars and the research IDRA X-band radar as well as the forecasting performance of the numerical weather model HARMONIE. The composite reflectivity resulting from the KNMI radars showed that the squall line progressively broke into multiple bowed-shaped segments associated with rear inflow notches and the S-broken reflectivity feature. HARMONIE was able to simulate the convective line structure of the storm; however, its spatial propagation appeared to be delayed compared to observations from the KNMI radars. Therefore, microphysical parameters linked with the storm motion may need further improvement. Signatures similar to those identified from the KNMI radars were also shown by the attenuation corrected reflectivity resulting from IDRA but at much higher spatial resolution. In addition, detailed observations every 1 min exhibited a temporal consistency of the hook echo and WER signature, which are mostly related to supercell or mini-supercell storms rather than squall lines. Attenuated reflectivity and differential reflectivity profiles, associated with IDRA, were corrected using a filter version of differential phase profiles. However, a similar correction procedure is not possible in areas where measurements are fully attenuated, leading to a limited observation of IDRA in range.

Although more data cases need to be analyzed, the understanding of the environmental conditions that are associated with a convective storm event, such as a squall line or a supercell storm, and the observations from ground based weather radars at different spatial and temporal scales are necessary to cope with the challenging task of

storm warning by weather forecasters. Also, to further enrich or complement the observation and documentation of storm events, it is beneficial to include data from ground weather stations and social media as illustrated in this work.

4

Adaptive and High-Resolution Estimation of Specific Differential Phase for Polarimetric X-Band Weather Radars

Abstract: One of the most beneficial polarimetric variables may be the specific differential phase (K_{DP}) due to its independence to power attenuation and radar miscalibration. However, conventional K_{DP} estimation requires a substantial amount of range smoothing due to the noisy characteristic of the measured differential phase (Ψ_{DP}). In addition, the backscatter differential phase (δ_{hv}) component of Ψ_{DP}, significant at C- and X-band frequencies, may lead to inaccurate K_{DP} estimates. In this work, an adaptive approach is proposed to obtain accurate K_{DP} estimates in rain from noisy Ψ_{DP}, in the case that δ_{hv} is of significance, at range resolution scales. This approach uses existing relations between polarimetric variables in rain to filter δ_{hv} from Ψ_{DP} while maintaining its spatial variability. In addition, the standard deviation of the proposed K_{DP} estimator is mathematically formulated for quality control. The adaptive approach is assessed using four storm events, associated with light and heavy rain, observed by a polarimetric X-band weather radar in the Netherlands. It is shown that this approach is able to retain the spatial variability of the storms at scales of range resolution. Moreover, the performance of the proposed approach is compared with two alternative methods. Results of this comparison show that the proposed approach outperforms the other two methods in terms of the correlation between K_{DP} and reflectivity, and K_{DP} standard deviation reduction.

4.1. INTRODUCTION

In the last 30 years, weather observations were conventionally performed by single-polarization S or C-band weather radars whereas in the last 5 years the polarization of these radars have been upgraded to dual-polarization. Although these radars have substantially improved weather monitoring, there are several limitations. For example, the spatial and temporal resolutions obtained from these conventional radars are undesirable for the early detection of small but threatening weather features as well as the detection of localized and heavy rainfall storms (Heinselman and Torres, 2011; Schellart et al., 2012; Berne and Krajewski, 2013). In contrast, single-polarization X-band weather radars are suited to obtain localized weather observations at resolutions higher than those of conventional radars. For example, a network of X-band weather radars in Hamburg, Germany, is used to observe precipitation at high-resolutions (Lengfeld et al., 2016). Nonetheless, power attenuation and radar miscalibration may reduce the accuracy of single-polarization radar observables (Gourley et al., 2009).

One technique to potentially mitigate these issues is polarimetric radar technology (Doviak et al., 2000; Bringi and Chandrasekar, 2001). For instance, in Western Europe, polarimetric X-band weather radars are used to obtain high-resolution rainfall rates in order to cope with urban flooding (Ochoa-Rodriguez et al., 2015). In this work, the polarimetric radar variable of interest is the specific differential phase (K_{DP}) because it can improve rainfall rate estimation compared to power-based measurements (Wang and Chandrasekar, 2010). However, the accuracy of K_{DP} is not yet sufficient because the measured differential phase (Ψ_{DP}) could be significantly noisy in light and moderate rain. In addition, Ψ_{DP} can include a non-negligible scattering component resulting from the Mie-scattering region which is known as the backscatter differential phase (δ_{hv}) (Matrosov et al., 2002; Trömel et al., 2013). Thus, accurate estimation of K_{DP} is necessary in order to unleash the potential of polarimetric weather radars.

Literature review reveals a large and continuous study to estimate K_{DP} and for simplicity it is divided into two groups. For the first group and in situations where δ_{hv} can be neglected (e.g., at S-band frequencies or light rain), straightforward approaches based on autoregressive average models are applied to smooth Ψ_{DP} (Bringi and Chandrasekar, 2001; Matrosov et al., 2006; Vulpiani et al., 2012). For the same group but in cases where δ_{hv} is of significance, Hubbert and Bringi (1995) introduced an iterative filtering approach to smooth Ψ_{DP} and filter δ_{hv}. A common problem in this group is that K_{DP} is estimated with inadequate spatial resolutions which could result in an underestimation of K_{DP} peaks and therefore lead to an inaccurate phase-based rainfall estimation (Ryzhkov and Zrnić, 1996). This limitation was reduced by Wang and Chandrasekar (2009), who developed an algorithm to filter δ_{hv} and to control the smoothing degree on Ψ_{DP} while maintaining its spatial resolution. For the second group, K_{DP} approaches included polarimetric relations in rain such as the self-consistency (SC) relation which formulates a dependency between K_{DP}, reflectivity (Z), and differential reflectivity (Z_{DR}) (Scarchilli et al., 1996; Goddard et al., 1994; Gorgucci et al., 1992) and the relation between δ_{hv} and Z_{DR}, hereafter δ_{hv}-Z_{DR}, (Scarchilli et al., 1993; Testud et al., 2000). Otto and Russchenberg (2011) were able to estimate K_{DP} at range resolution scales using both relations while Schneebeli and Berne (2012) included the δ_{hv}-Z_{DR} relation in their Kalman filter approach. Recently, Giangrande et al. (2013) introduced a linear programming method

which includes Z measurements whereas Huang et al. (2015) used the self-consistency relation to estimate K_{DP} at S, C, and X-band frequencies. A disadvantage of using polarimetric relations is that uncertainties on Z and Z_{DR} measurements might reduce the performance of these approaches. Lastly, approaches in both groups could be associated with significant errors when K_{DP} is estimated at range resolution scales (Grazioli et al., 2014; Zhiqun et al., 2015).

In this work, an adaptive approach that includes polarimetric relations is presented to estimate accurate K_{DP} from Ψ_{DP} in rain, whose δ_{hv} is of significance, at high spatial resolution. This paper is a follow-up of Otto and Russchenberg (2011) and is organized as follows. Two K_{DP} methods given by Hubbert and Bringi (1995), first group, and Otto and Russchenberg (2011), second group, are shortly described in section 4.2. They will be used for comparison with the proposed technique because i) the method of Hubbert and Bringi (1995) is widely accepted for K_{DP} estimation at C- and X-band frequencies and ii) the focus of this work is to improve the technique introduced by Otto and Russchenberg (2011). In section 4.3, the adaptive high-resolution approach is introduced to estimate K_{DP} and model its standard deviation. To demonstrate the capability of this approach in terms of δ_{hv} contamination and spatial resolution, one storm event is analyzed in section 4.4. In section 4.5, the performance of the adaptive approach is compared with those from section 4.2, using four storm events. In section 4.6, conclusions are drawn. Finally, the standard deviation of the proposed K_{DP} estimator is derived in Appendix A while the filter required by Hubbert and Bringi (1995) is designed in Appendix B. Moreover, a supplement material is given in Appendix C, which allows the formulation of more detailed discussions on the methodology, analysis, and assessment of the proposed approach.

4.2. SPECIFIC DIFFERENTIAL PHASE: BACKGROUND AND ESTIMATION

In polarimetric weather radars, the difference between the horizontal and vertical polarization phase is defined as the differential phase shift Ψ_{DP} [°]. A conceptual model for a Ψ_{DP} profile is expressed as

$$\Psi_{DP}(r) = \Phi_{DP}(r) + \delta_{hv}(r) + \epsilon, \tag{4.1}$$

where $\Phi_{DP}(r)$ [°] represents the cumulative propagation phase shift along its course while $\delta_{hv}(r)$ [°] indicates local backscattering phase shifts manifested as "blips" or "bumps". Random noise is represented by ϵ [°] and the range by r [km]. Depending on the weather environment, the standard deviation of Ψ_{DP}, hereafter σ_P [°], varies between 2 to 5° (Bringi and Chandrasekar, 2001).

The one-way specific differential phase K_{DP} [° km^{-1}] is half the derivative of Φ_{DP}:

$$K_{DP}(r) = \frac{1}{2}\frac{d\Phi_{DP}(r)}{dr}; \tag{4.2}$$

however, the estimation of accurate K_{DP} is not straightforward. For rainfall rate applications, K_{DP} should be estimated such that the normalized standard error (NSE) of rainfall rate is less than 20% (Gorgucci et al., 1999; Bringi and Chandrasekar, 2001). For instance,

assuming a standard deviation of Φ_{DP} equal to 3° and estimating K_{DP} as in Eq. (4.2) over a path length of 2 km, the standard deviation of K_{DP}, hereafter σ_K, would be $1\,^\circ\,\mathrm{km}^{-1}$. If rainfall rate and K_{DP} are given by a power-law relation with a power coefficient of 0.8 (Ryzhkov et al., 2005a; Wang and Chandrasekar, 2010), the value of σ_K is theoretically sufficient for K_{DP} larger than $4\,^\circ\,\mathrm{km}^{-1}$. However, for K_{DP} values smaller than $4\,^\circ\,\mathrm{km}^{-1}$, σ_K values are required to decrease accordingly, which can be achieved by increasing the path length with the sacrifice of spatial resolution.

4.2.1. CONVENTIONAL METHOD

Hubbert and Bringi (1995) introduced an iterative range filtering technique based on two steps. In the first step a low-pass filter is designed such that fluctuations due to δ_{hv} and ϵ at scales of the radar resolution (Δr [km]) are eliminated from a Ψ_{DP} profile. The magnitude response (H) of this filter is given in the range domain by defining its Nyquist frequency as $1/(2\Delta r)$. In this domain, H is specified by the filter order and $\Delta r / r_c$, where r_c [km] is the required cut-off scale such that $r_c > \Delta r$. This means that the filter will maintain (or "pass") spatial variations of $\Psi_{DP}(r)$ at scales larger than r_c. However, spatial variations smaller than r_c will not be effectively suppressed because H is characterized by a transition bandwidth from the "pass" band to the "stop" band. This transition can be faster if the order of the filter is heavily increased. However, a high order filter will strongly smooth the spatial variability of Ψ_{DP} leading to a coarse spatial resolution of K_{DP}. Thus, the order of the filter is selected such that H will suppress spatial variations at scales slightly larger than Δr without compromising the spatial resolution of K_{DP}. This filter is referred to as a "light" filter which will lead to reduced σ_P and thereby σ_K.

In the second step the light filter is applied several times to eliminate extended δ_{hv} fluctuations, up to r_c scales, as it would result from a "heavy" filter but without excessive smoothing. This process begins by filtering Ψ_{DP}, resulting in a first estimation of Φ_{DP} ($\tilde{\Phi}_{DP}$). The absolute difference between Ψ_{DP} and $\tilde{\Phi}_{DP}$ profiles at each range gate are employed to generate a modified Ψ_{DP} profile ($\tilde{\Psi}_{DP}$): if the absolute difference is larger than a threshold (τ), then $\tilde{\Psi}_{DP}(r) = \tilde{\Phi}_{DP}(r)$ holds; otherwise, $\tilde{\Psi}_{DP}(r) = \Psi_{DP}(r)$ holds. This threshold is predefined from the interval $[1.25;2]\sigma_P$. The process is iterated until $\tilde{\Psi}_{DP}$ from two consecutive iterations show insignificant changes. Next, $\tilde{\Psi}_{DP}$ from the last iteration is filtered one more time to obtain Φ_{DP} and thereby K_{DP} according to Eq. (4.2).

Even though this is an elegant approach to estimate K_{DP} in real-time, the following issues limit its purpose. First, spatial fluctuations larger than r_c will not be completely eliminated by the iterative step. Second, its performance is sensitive to the value of τ. For example, $\tau = 2\sigma_P$ will lead to a $\tilde{\Psi}_{DP}$ more correlated to Ψ_{DP} than to $\tilde{\Phi}_{DP}$ which might not be sufficient to eliminate unwanted fluctuations. Third, if r_c is increased or Δr is decreased, the order of the filter should be increased (Wang and Chandrasekar, 2009) which may exacerbate these issues. In summary, in the design of the filter and selection of the threshold, there is a trade-off between the smoothing extent and spatial resolution required to estimate K_{DP} with small standard deviation and reduced bias.

4.2.2. HIGH-RESOLUTION METHOD

In contrast to the conventional approach, Otto and Russchenberg (2011) included δ_{hv}-Z_{DR} and self-consistency relations in rain to estimate K_{DP} at X-band frequencies. The first relation is represented by $\delta_{hv} = e_1 {Z_{DR}}^{e_2}$ and the second by

$$K_{DP}^{SC} = c_1 10^{(c_2 Z/10)} 10^{(c_3 Z_{DR})}, \tag{4.3}$$

where Z and Z_{DR} are given in dBZ and dB units, respectively, while coefficients e_1, e_2, c_1, c_2, and c_3 establish the average fit from a set of drop size distributions (DSD's), drop shape models, and temperatures. The specific differential phase in Eq. (4.3) is indicated by K_{DP}^{SC} to distinguish between K_{DP} from the self-consistency relation and K_{DP} from the high-resolution approach. Otto and Russchenberg (2011) used a normalized Gamma distribution to model DSD's. In order to represent rain variability, 1500 DSD's were modeled by varying the parameters of the distribution (i.e., median volume diameter, concentration, and shape parameter). In addition, a hybrid drop shape model, that consists of three models, and temperatures in the range of 1-25°C were considered to express a wide range of possibilities. The coefficients for the δ_{hv}-Z_{DR} relation are e_1 = 1 and e_2 = 1.8, while for the self-consistency relation they are $c_1 = 1.37\times10^{-3}$, c_2 = 0.68, and c_3 = −0.042.

Z and Z_{DR} measurements are corrected for attenuation and differential attenuation, respectively, according to the method given by Bringi et al. (1990). For a description of this method, profiles of Z and Z_{DR} are represented as $Z = z+$ PIA and $Z_{DR} = z_{dr} +$ PIA$_{DP}$, respectively, where z[dBZ] and z_{dr}[dB] represent attenuated and differential attenuated measurements. PIA indicates the path integrated attenuation in reflectivity while PIA$_{DP}$ in differential reflectivity. PIA and PIA$_{DP}$ are proportional to $\Delta\Phi_{DP}$, which is the span of a smoothed Φ_{DP} profile. Otto and Russchenberg (2011) suggested the following relations using scattering simulations: PIA = $0.34\Delta\Phi_{DP}$ and PIA$_{DP}$ = $0.05\Delta\Phi_{DP}$. However, for simplicity, $\Delta\Psi_{DP}$ is used instead of $\Delta\Phi_{DP}$.

For a Ψ_{DP} profile represented by Eq. (4.1), the difference of Ψ_{DP} in a path $\overline{ab}$ can be approximated as $\Delta\Psi_{DP} = \Delta\Phi_{DP} + \Delta\delta_{hv}$ where $\Delta\Psi_{DP} = \Psi_{DP}(b) - \Psi_{DP}(a)$ and $b > a$. The length of $\overline{ab}$ could be as small as Δr or as large as the maximum unambiguous range. In order to identify whether $\Delta\delta_{hv}$ is negligible, the δ_{hv}-Z_{DR} relation is used in the following assumption: if $|Z_{DR}(b) - Z_{DR}(a)|$ is smaller than 0.3 dB, then $\delta_{hv}(b) - \delta_{hv}(a) \approx 0°$ or if $|\Delta Z_{DR}| < 0.3$ dB, then $\Delta\delta_{hv} \approx 0°$. In case that such condition is satisfied, $\Delta\Psi_{DP}$ is retained for further processes, otherwise, $\Delta\Psi_{DP}$ is discarded. Multiple $\Delta\Psi_{DP}$ samples ($\Delta\Psi_{DP}$'s) associated with negligible $\Delta\delta_{hv}$ are obtained by considering more paths. These samples are weighted by Z and Z_{DR} using the self-consistency relation to obtain $\Delta\Psi_{DP}$'s at Δr scale. For instance, the weight (w) at gate i within path $\overline{ab}$ is

$$w(i) = \frac{K_{DP}^{SC}(i)}{\sum_a^b K_{DP}^{SC}(g)}; \quad \text{with} \quad g = a, ..., b. \tag{4.4}$$

Weighted $\Delta\Psi_{DP}$'s are used according to Eq. (4.2) to obtain multiple K_{DP} samples. Finally, $K_{DP}(i)$ is estimated by the arithmetic mean of these samples.

Otto and Russchenberg (2011) demonstrated their method using one rainfall event, showing a visual consistency between K_{DP} and Z as well as δ_{hv} and Z_{DR}. Nevertheless,

less consistent results were observed for K_{DP} values smaller than $4\,^{\circ}\,\mathrm{km}^{-1}$. In addition, estimates of K_{DP} were associated with values of σ_K as high as $3\,^{\circ}\,\mathrm{km}^{-1}$. Moreover, the sensitivity of the self-consistency relation to DSD, drop shape, and temperature variability and its impact on estimated weights were not discussed. In addition, the effect of uncertain measurements of Z and Z_{DR} caused for example by attenuation, partial beam blockage, and miscalibration on the performance of this approach remains an open question. Besides its limited validation, another matter is the computational time required to weigh a significant amount of $\Delta\Psi_{DP}$'s at each range gate, which might be inefficient for operational purposes.

4.3. ADAPTIVE HIGH-RESOLUTION APPROACH

The presented approach is an improved version of the high-resolution method in order to address limitations associated with the conventional and high-resolution methods, mainly low accuracy of K_{DP} in light rain, contamination due to unfiltered δ_{hv}, sensitivity to Z and Z_{DR} measurements, and computational time. The inputs are measurements of Ψ_{DP}, Z, and Z_{DR} profiles in rain. In addition, a predetermined length interval $[L_{\min}; L_{\max}]$ is required to control the selection of path lengths. This interval is assumed to be defined by a user, however, possible values are discussed in section 4.3.5. The adaptive approach consists of three processes: pre-processing, path length selection, and K_{DP} estimation. A flowchart to estimate K_{DP}, among other variables, for a given radial profile, is presented in Fig. 4.1. In addition, the variables and symbols used in the adaptive high-resolution approach are summarized and described in Table 4.1

4.3.1. PRE-PROCESSING

In order to correct Z and Z_{DR} profiles for attenuation and differential attenuation, respectively, Otto and Russchenberg (2011) used noisy $\Delta\Psi_{DP}$ instead of the smoothed $\Delta\Phi_{DP}$ which may decrease the accuracy of the method given by Bringi et al. (1990). In contrast, in the adaptive high-resolution approach, a linear regression fit over a 3 km window is applied to a Ψ_{DP} profile resulting in a Φ_{DP} profile (Φ^t_{DP}). Thus, attenuation corrected reflectivity (Z^t) and differential reflectivity (Z^t_{DR}) are given as $Z^t = z + 0.34\Delta\Phi^t_{DP}$ and $Z^t_{DR} = z_{dr} + 0.05\Delta\Phi^t_{DP}$. This attenuation correction method might be sensitive to measurements errors, constant coefficients, and δ_{hv} contamination. However, Gorgucci and Chandrasekar (2005) studied the method of Bringi et al. (1990) at X-band frequencies and showed that this method performs fairly well with only a slight degradation of the average error for attenuation correction.

In this approach, an estimate of the standard deviation of a Z^t_{DR} profile, hereafter σ_{ZDR} [dB], is required by the path length selection process. A moving-window of 5-gates is applied to Z^t_{DR} profile so that local σ_{ZDR} samples are obtained. Then, σ_{ZDR} is estimated by averaging these individual samples. The estimation of K_{DP} is achieved gate-by-gate, starting from ranges near the radar and continuing downrange. Assuming that the first gate with measurements of rain is located at r_i, the estimation of K_{DP} begins at gate i. To describe the estimation of K_{DP} at gate i, a schematic diagram is given by Figs. 4.2 and 4.3, which is associated with the path length selection and K_{DP} estimation processes.

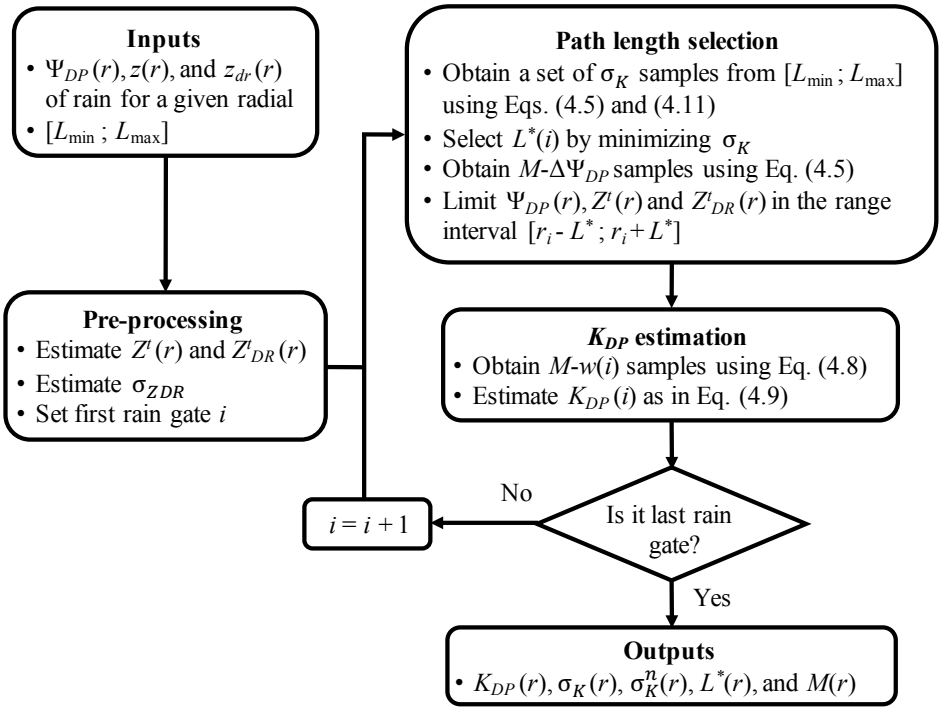

Figure 4.1: Flowchart for the adaptive high-resolution K_{DP} approach.

4.3.2. PATH LENGTH SELECTION

In the high-resolution technique, $\Delta\Psi_{DP}$ samples were obtained from Ψ_{DP} using paths of any possible length. However, K_{DP} results were associated with high values of σ_K and significant computational time. To reduce such issues, a path length L [km] for gate i is selected from $[L_{\min}; L_{\max}]$ such that a theoretical σ_K is minimized. The formulation of a theoretical σ_K is shown in section 4.3.5 but for now let theoretical σ_K be a function of two parameters L and M, where M represents the number of $\Delta\Psi_{DP}$ samples with negligible $\Delta\delta_{hv}$. In order to identify negligible $\Delta\delta_{hv}$, the high-resolution technique used a fixed threshold to constrain $|\Delta Z_{DR}|$. However, a fixed threshold might not capture possible variability of Z_{DR} within the storm. In this work, the condition to identify negligible $\Delta\delta_{hv}$ is given by

$$|\Delta Z^t_{DR}| < \sigma_{ZDR}, \tag{4.5}$$

where $\Delta Z^t_{DR} = Z^t_{DR}(b) - Z^t_{DR}(a)$ for a path $\overline{ab}$. Eq. (4.5) can be considered to be independent of any parameterized δ_{hv}-Z_{DR} relation because this relation is not used quantitatively. Instead, Eq. (4.5) relies on the existing correlation between δ_{hv} and Z_{DR}. Furthermore, sudden variability in microphysics is taken into consideration by using σ_{ZDR} rather than an arbitrary threshold. Issues such as Z_{DR} miscalibration are mitigated by the estimation of ΔZ^t_{DR}. Eq. (4.5) is referred to as the $\Delta\Psi_{DP}$ filter condition.

We suggest the reader to refer to Fig. 4.2a) for a illustrative description of the follow-

Table 4.1: List of variables and symbols used in the adaptive high-resolution approach.

Variables	Description	Unit
$\overline{ab}^{(j)}$	j^{th} path between range gates r_a and r_b	
c_2,c_3	coefficients of the self-consistency relation	
$\hat{K}_{DP}(i)$	estimated K_{DP} at gate i	$^\circ$ km^{-1}
$K_{DP}^{SC}(i)$ and K_{DP}^{SC}	K_{DP} at Δr and L scales using the self-consistency relation	$^\circ$ km^{-1}
L and $L^*(i)$	a given path length and the selected L at gate i	km
$[L_{\min}; L_{\max}]$	predefined length interval	km
M	the number of samples of $\Delta\Psi_{DP}$ with negligible $\Delta\delta_{hv}$	
M-$\hat{s}(i)$	M samples of the self-consistency ratio at gate i	
M-$\hat{w}(i)$	M samples of the weight w at gate i	
n	number of times a path is shifted within a range interval centered at r_i	
r_i	range at gate i	km
$[r_i - L^*; r_i + L^*]$	range interval centered at r_i to limit Ψ_{DP}, Z^t, and Z_{DR}^t profiles	km
z	attenuated reflectivity	dBZ
z_{dr}	attenuated differential reflectivity	dB
$\overline{Z}^{(j)}$	average of Z^t in path $\overline{ab}^{(j)}$	dBZ
$\overline{Z}_{DR}^{(j)}$	average of Z_{DR}^t in path $\overline{ab}^{(j)}$	dB
Z^t and Z	attenuation-corrected reflectivity before and after $\hat{K}_{DP}(i)$	dBZ
Z_{DR}^t and Z_{DR}	attenuation-corrected differential reflectivity before and after $\hat{K}_{DP}(i)$	dB
δ_{hv}	backscatter differential phase	$^\circ$
Δr	range resolution	km
$\Delta\delta_{hv}$	difference of δ_{hv} in a given range path (no estimated)	$^\circ$
ΔZ_{DR}^t	difference of Z_{DR}^t in a given range path	dB
$\Delta\Phi_{DP}^t$	difference of Φ_{DP}^t in a given range path	$^\circ$
$\Delta\Psi_{DP}$	difference of Ψ_{DP} in a given range path	$^\circ$
ϵ_δ	error due to neglecting $\Delta\delta_{hv}$	$^\circ$
μ_s and $\mu_s(i)$	theoretical and actual average of $\hat{s}(i)$	
σ_K and $\sigma_K(i)$	theoretical and actual standard deviation of $\hat{K}_{DP}(i)$	$^\circ$ km^{-1}
$\sigma_K^n(i)$	normalized standard deviation of $\hat{K}_{DP}(i)$	$^\circ$ km^{-1}
$\sigma_s(i)$ and $\sigma_s^n(i)$	standard deviation and normalized standard deviation of $\hat{s}(i)$	
σ_ϵ	theoretical standard deviation of ϵ_δ	$^\circ$
σ_P	theoretical standard deviation of Ψ_{DP}	$^\circ$
σ_{ZDR}	standard deviation of a Z_{DR}^t profile	dB
Φ_{DP}^t and Φ_{DP}	smoothed differential phase before and after $\hat{K}_{DP}(i)$	$^\circ$
Ψ_{DP}	measured differential phase	$^\circ$

ing steps. The path length selection starts with $L = L_{\min}$. For simplicity, a path length is of the form $L = n\Delta r$ where n is an integer larger than 1. Then, a range interval centered

at gate i is defined as $[r_i - L; r_i + L]$. This range interval is used to limit the extent of Z^t_{DR} and to obtain multiple ΔZ^t_{DR} samples. These samples are achieved by shifting a path of length L, within the interval starting at $r_i - L$, n-times with steps of Δr. In this manner, $(n+1)$-ΔZ^t_{DR} samples are obtained. Next, M is calculated by counting the number of samples that satisfy Eq. (4.5). Note that $M \leq (n+1)$. From L and M, a σ_K value is determined. In order to have a set of σ_K values the same procedure is repeated for next value of L until $L = L_{\max}$. Finally, the path length that leads to the minimum σ_K is selected and is represented by L^*.

Repeating a similar procedure but with L^* (i.e., shifting a path of length L^* and using Eq. (4.5)), M-$\Delta\Psi_{DP}$ samples with negligible $\Delta\delta_{hv}$ are retrieved from Ψ_{DP} to estimate $K_{DP}(i)$; the reader can refer to Fig. 4.2b) for a schematic illustration. Remaining $\Delta\Psi_{DP}$ samples are discarded to avoid bias on $K_{DP}(i)$. For the next steps, only Ψ_{DP}, Z^t, and Z^t_{DR} profiles in the interval $[r_i - L^*; r_i + L^*]$ are used.

4.3.3. K_{DP} ESTIMATION

In order to estimate $K_{DP}(i)$, M-$\Delta\Psi_{DP}$ samples should be downscaled from L^* to Δr scales. A downscaling weight $w(i)$ was suggested by the high-resolution method according to Eq. (4.4). In contrast, in the adaptive high-resolution approach, a different formulation of $w(i)$ is proposed in order to reduce its sensitivity to possible sources of uncertainty that were discussed in section 4.2.2, mainly the sensitivity of the self-consistency relation to rain variability, radar miscalibration, and partial beam blockage effects. Moreover, this formulation allows us to study statistics of $w(i)$ and $K_{DP}(i)$ for quality control purposes.

Consider a theoretical $\Delta\Psi_{DP} \geq 0°$ from a path $\overline{ab}$ of length L. For gate i in the interval $[a+1; b]$ the downscaling weight $w(i)$ is expressed as a factor that weighs $\Delta\Psi_{DP}$ such that $\Delta\Psi_{DP}(i) = w(i)\Delta\Psi_{DP}$ where $\Delta\Psi_{DP}(i)$ represents the difference $\Psi_{DP}(i) - \Psi_{DP}(i-1)$ (i.e., at Δr scale). For derivation purposes, let $w(i)$ be bounded by the interval $[0; 1]$ and $\sum_{a+1}^{b} w(i) = 1$. Using Eqs. (4.1) and (4.2), $\Delta\Psi_{DP}(i)$ and $\Delta\Psi_{DP}$ are expressed in terms of K_{DP} and $w(i)$ as

$$w(i) = \frac{2\Delta r K_{DP}(i) + \delta_{hv}(i) - \delta_{hv}(i-1)}{2LK_{DP} + \delta_{hv}(b) - \delta_{hv}(a)}. \tag{4.6}$$

Both $K_{DP}(i)$ and K_{DP} are estimated using the self-consistency relation according to Eq. (4.3) at scales of Δr and L, respectively. In the numerator of Eq. (4.6), adjacent δ_{hv} values are assumed to be similar so $\delta_{hv}(i) - \delta_{hv}(i-1)$ is approximately $0°$. In the denominator, assuming that $\Delta\Psi_{DP}$ satisfies Eq. (4.5), the difference $\delta_{hv}(b) - \delta_{hv}(a)$ is negligible. In this manner, $w(i)$ is formulated as

$$w(i) = \frac{\Delta r}{L} \frac{K^{SC}_{DP}(i)}{K^{SC}_{DP}}, \tag{4.7}$$

where the self-consistency relation is used two times in contrast to the high-resolution method where it is used $(n+2)$-times (see Eq. (4.4) and replace b by $a+n$). In this way, added errors associated with the self-consistency relation are reduced.

In order to downscale M-$\Delta\Psi_{DP}$ samples (i.e., $\Delta\Psi^{(j)}_{DP}$ with $j = 1, 2, \ldots M$) associated

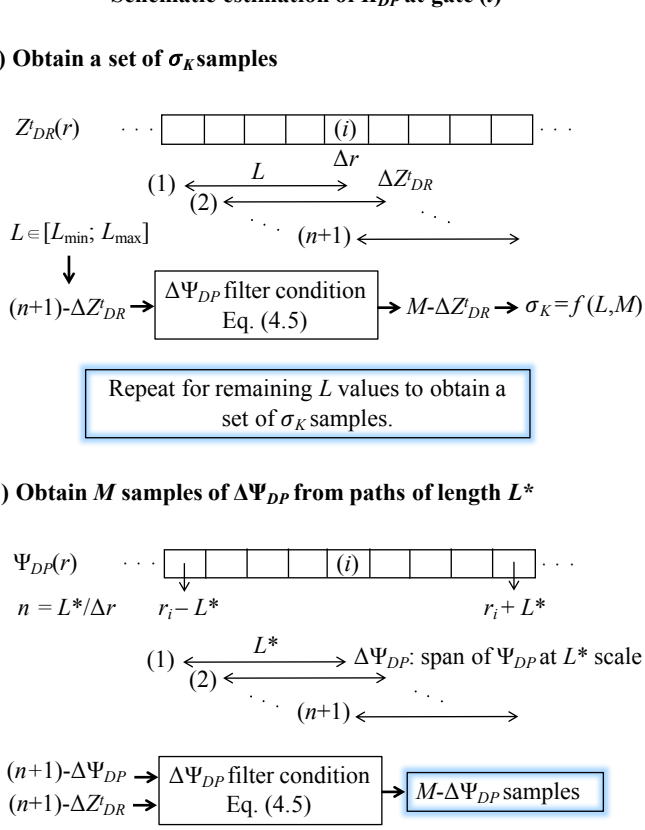

Figure 4.2: A schematic diagram for the estimation of $K_{DP}(i)$. a) Shows the process to obtain a value for σ_K, Eq. (4.11), from a given path length $L \in [L_{\min}; L_{\max}]$ and $(n+1)$ samples of ΔZ^t_{DR}. Note that the variable M is estimated using Eq. (4.5) and $M \leq (n+1)$. b) Indicates the procedure to get M samples of $\Delta\Psi_{DP}$ from $(n+1)$ samples of $\Delta\Psi_{DP}$, which are obtained from a moving path of length L^* in the range $[r_i - L^*; r_i + L^*]$ of a $\Psi_{DP}(r)$ profile.

with M-$\overline{ab}$ paths of length L^*, Eq. (4.7) is used and the j^{th} weight is given as

$$\hat{w}^{(j)}(i) = \frac{\Delta r}{L^*} 10^{c_2(Z^t(i) - \overline{Z}^{(j)})/10} 10^{c_3(Z^t_{DR}(i) - \overline{Z}^{(j)}_{DR})}, \tag{4.8}$$

where $\overline{Z}^{(j)}$ and $\overline{Z}^{(j)}_{DR}$ represent the arithmetic mean of $Z^t(i)$ and $Z^t_{DR}(i)$ values in path $\overline{ab}^{(j)}$, respectively. The reader can refer to Fig. 4.3c) for a graphical explanation of Eq. (4.8). Repeating Eq. (4.8) over remaining paths, M-$\hat{w}(i)$ samples are obtained and $K_{DP}(i)$ is estimated as

$$\hat{K}_{DP}(i) = \frac{1}{M} \sum_{j=1}^{M} \frac{\Delta\Psi^{(j)}_{DP}\, \hat{w}^{(j)}(i)}{2\Delta r}; \quad \text{with } j = 1, 2, \ldots M. \tag{4.9}$$

Fig. 4.3d) provides a schematic description of Eq. (4.9). Once $K_{DP}(i)$ is estimated, the

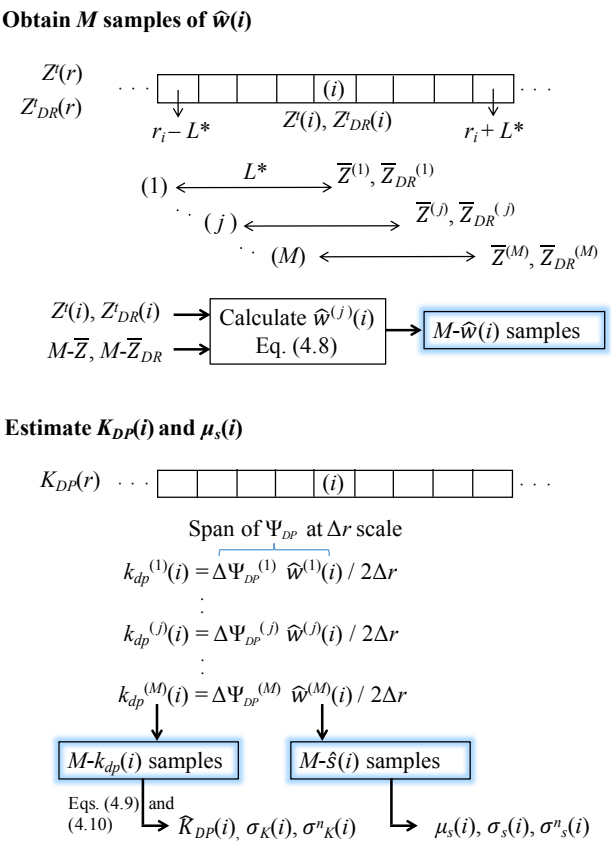

Figure 4.3: Continuation of Fig. 4.2. c) Shows the process to obtain M samples of $\hat{w}(i)$ from the pair $Z^t(i)$ and $Z^t_{DR}(i)$ and from M samples of $\overline{Z}$ and $\overline{Z}_{DR}$ using Eq. (4.8). d) Indicates the steps to get, among other variables, $\hat{K}_{DP}(i)$ and $\mu_s(i)$ from M samples of $k_{dp}(i)$ and $\hat{s}(i)$, respectively. Note that ${k_{dp}}^{(j)}(i)$ is the j^{th} specific differential phase sample at gate i and estimated at range resolution scale.

path length selection and K_{DP} estimation processes are applied to gate $i = i+1$ until the last gate measured in rain. Hence a K_{DP} profile is obtained as well as associated L^* and M profiles.

4.3.4. K_{DP} UNCERTAINTY

The K_{DP} estimator is a function of two variables ${\Delta\Psi_{DP}}^{(j)}$ and $\hat{w}^{(j)}$ which result from the $\Delta\Psi_{DP}$ filter condition and $\Delta\Psi_{DP}$ downscaling, respectively. Therefore it is important to discuss errors associated to both variables. For this purpose, ${\Delta\Psi_{DP}}^{(j)}$ is expressed as $\Delta\Psi_{DP} = \Delta\Phi_{DP} + \epsilon_\delta$, where ϵ_δ indicates possible errors due to neglecting $\Delta\delta_{hv}$. Using the scattering simulation introduced in section 4.2.2 and setting σ_{ZDR} equal to 0.2 dB, the estimated mean and standard deviation of ϵ_δ are 0.04° and 0.6°, respectively. The uncertainty of $\hat{w}^{(j)}$ depends on the self-consistency relation in rain. Trabal et al. (2014)

demonstrated that the coefficients of the self-consistency relation (c_1, c_2, and c_3) shown by Eq. (4.3) are sensitive to temperature variability while DSD and drop shape variabilities are well represented by a normalized Gamma distribution and a hybrid drop shape model. Similar findings were reported by Gourley et al. (2009) and Adachi et al. (2015). Although $\hat{w}^{(j)}$ is independent of c_1, see Eq. 4.8, any possible sensitivity to c_2 and c_3 is modulated by the difference $Z^t(i) - \overline{Z}^{(j)}$ and $Z^t_{DR}(i) - \overline{Z}^{(j)}_{DR}$, respectively (i.e., it depends on the spatial variability of Z^t and Z^t_{DR} within path $\overline{ab}^{(j)}$ instead of their absolute values). For example, in a uniform path, $\hat{w}^{(j)}$ might be constant and equal to $\Delta r/L^*$. Moreover, $\hat{w}^{(j)}$ is independent of constant biases on Z^t and Z^t_{DR}, for instance within $\overline{ab}^{(j)}$ in a given radial, as well as radar miscalibration. This independence could reduce the impact of biases on Z^t and Z^t_{DR} areas caused by partial beam blockage. For simplicity the estimated weight is rewritten as $\hat{w}^{(j)} = \hat{s}^{(j)}\Delta r/L$ where $\hat{s}^{(j)}$ is referred to as the self-consistency ratio (see Eqs. (4.7) and (4.8)). The meaning of $\hat{s}^{(j)}$ can be understood as an index of similarity between a given measurement and its surroundings. For example, in Eq.4.8, if $Z^t(i)$ and $Z^t_{DR}(i)$ are similar to $\overline{Z}^{(j)}$ and $\overline{Z}^{(j)}_{DR}$, respectively, then $\hat{s}^{(j)}$ will be approximately equal to 1. In case that $Z^t(i)$ and $Z^t_{DR}(i)$ are larger or smaller than their corresponding averaged values, then $\hat{s}^{(j)}$ will be larger or smaller than 1, respectively. In this manner, $\hat{s}^{(j)}$ takes into account the spatial variability of reflectivity and differential reflectivity within a given path.

The uncertainty of $\hat{s}^{(j)}$ can be quantified by its normalized standard error NSE. Scarchilli et al. (1996) derived an expression for NSE of K^{SC}_{DP}, hereafter NSE(K), which is a function of c_2, c_3, and variances of Z^t and Z^t_{DR}. Using this expression and basic properties of the variance, the NSE of $\hat{s}^{(j)}$ is given by $\text{NSE}(\hat{s}^{(j)}) = \sqrt{1+1/n}\,\text{NSE}(K)$. For example, setting n equal to 10 (i.e., L is 10 times Δr) and using values of c_2 and c_3 given in section 4.2.2 and conventional accuracies of 1 dB and 0.2 dB for Z^t and Z^t_{DR}, respectively, $\text{NSE}(\hat{s}^{(j)})$ results in 15.7%. This analysis can be used as a guidance to identify which elements associated to the $\Delta\Psi_{DP}$ filter condition and $\Delta\Psi_{DP}$ downscaling can lead to incorrect estimation of K_{DP}.

The uncertainty of $\hat{K}_{DP}(i)$ is measured by its standard deviation as

$$\sigma_K(i) = \sqrt{\frac{1}{M}\sum_{j=1}^{M}\left(\frac{\Delta\Psi^{(j)}_{DP}\,\hat{w}^{(j)}(i)}{2\Delta r} - \hat{K}_{DP}(i)\right)^2}\;; \quad \text{with} \;\; j = 1,2,\ldots M. \tag{4.10}$$

Eq. (4.10) is referred to as the actual σ_K. In addition, the NSE of $\hat{K}_{DP}(i)$, hereafter $\sigma^n_K(i)$, is given by $(\sigma_K(i)/|\hat{K}_{DP}(i)|)100\%$. Both, actual σ_K and σ^n_K profiles are added to the output of Fig. 4.1 which can be used for quality control purposes. In a similar manner but for the M-$\hat{s}(i)$ samples, profiles of their actual mean (μ_s), standard deviation (σ_s), and NSE (σ^n_s) are also obtained. Given the definition of $\hat{s}^{(j)}$, a μ_s profile will also indicate a degree of similarity, i.e., with values near 1 for a uniform distribution of reflectivity and differential reflectivity profiles or with values different than 1 for a more variable distribution. The reader is referred to Fig. 4.7 for an example of actual μ_s profiles.

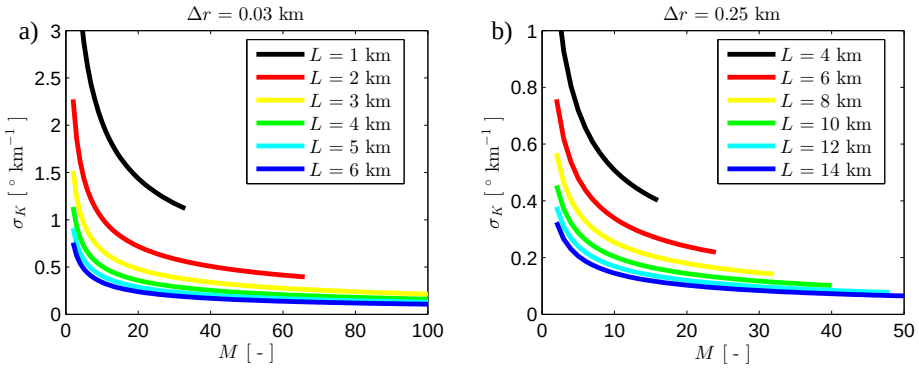

Figure 4.4: Theoretical standard deviation of the adaptive high-resolution K_{DP} estimator as a function of the number of paths M. a) Theoretical σ_K curves for $\mu_s = 3$ and $\Delta r = 0.03$ km. b) As in a) but for $\Delta r = 0.25$ km.

4

4.3.5. σ_K MODELING

The uncertainty of $\hat{K}_{DP}$ can be controlled by modeling its actual σ_K. Therefore, a theoretical σ_K is derived from Eq. (4.9) where $\hat{w}^{(j)}$ is expressed in terms of the self-consistency ratio as $\hat{s}^{(j)}\Delta r/L$. Values of Δr, L, and M are assumed to be given while $\Delta\Psi_{DP}^{(j)}$ and $\hat{s}^{(j)}$ are defined as random variables. Using properties of the variance that involve the sum and product of random variables, a theoretical σ_K is approximated as (for a detailed derivation refer to Appendix A):

$$\sigma_K = \frac{\mu_s}{L}\sqrt{\frac{2\sigma_P^2 + \sigma_\epsilon^2}{4M}}, \tag{4.11}$$

where σ_P^2 and σ_ϵ^2 are the variance of Ψ_{DP} and ϵ_δ, respectively. As discussed previously, μ_s depends on the spatial variability of the Z^t and Z_{DR}^t fields (i.e., the storm type). For example, a representative μ_s in stratiform rain (i.e., uniform rain field) may be near 1 but it can be between 2 and 5 in convective rain (i.e., variable rain field as seen in Fig. 4.7). The value of σ_P also depends on rain type while σ_ϵ is assumed equal to 0.6° as given in section 4.3.4. In order to illustrate theoretical σ_K, let us assume that μ_s and σ_P are equal to 3 and 3°, respectively. A similar value for σ_P was given by Lim et al. (2013).

Theoretical σ_K curves as a function of M and for different combinations of L are presented in Fig. 4.4. Although σ_K in Eq. (4.11) is independent of Δr, the maximum value of M for a fixed path length L is given by $(n+1)$, which is equivalent to $L/\Delta r + 1$. For Δr equal to 0.03 km, Fig. 4.4a shows that if L is near 1 km, it is expected to obtain σ_K values larger than $1\,^\circ\,\mathrm{km}^{-1}$. However, σ_K values smaller than $0.5\,^\circ\,\mathrm{km}^{-1}$ are expected if L is equal to 2 km and M is larger than 40. In terms of probability, M larger than 40 indicates that at least 60% of the total number of paths $(n+1)$ satisfies Eq. (4.5). For L larger than 3 km, σ_K curves continue for values of M beyond 100, not shown here. Note that the gap between consecutive σ_K curves decreases as L increases (e.g., σ_K curves corresponding to 5 and 6 km are almost identical). Therefore, it is recommended to avoid large values of L (i.e., lengthy paths) associated with small reduction of σ_K.

Recall that for a given value of L, M is determined only after evaluating Eq. (4.5). In order to search for the combination of L and M that leads to the smallest theoretical

σ_K, a path length interval $[L_{\min}; L_{\max}]$ is considered instead of a single path length. For example, a length interval equal to [3;5] km could be defined from Fig. 4.4a as an input to the adaptive high-resolution approach. In that case, σ_K is expected to be small with a sufficient number of paths M. Similar σ_K curves can be produced for coarser spatial resolution. For instance, if $\Delta r = 0.25$ km, a set of L values ranging from 4 to 14 km would be used to generate σ_K curves as shown in Fig. 4.4b and an interval equal to [6;10] km would be defined. Note that for larger Δr a smaller number of paths M might lead to reasonable σ_K values (compare Figs. 4.4a and 4.4b).

In this σ_K modeling, it is assumed that a user predefines a theoretical value for μ_s and σ_P according to the storm type, and sets $[L_{\min}; L_{\max}]$. For example, in a uniform Z field (i.e., low μ_s and σ_P) or more variable Z field (i.e., high μ_s and σ_P), $[L_{\min}; L_{\max}]$ can be decreased or increased according to theoretical σ_K curves. In summary, setting $[L_{\min}; L_{\max}]$ allows us to avoid high values of actual σ_K as well as unnecessary lengthy paths associated with an increased dependence on the self-consistency ratio and a large computational time.

4.4. ANALYSIS OF THE ADAPTIVE HIGH-RESOLUTION APPROACH

4.4.1. DATA SETTINGS

The polarimetric X-band weather radar IDRA [1] is a frequency modulated continuous wave system whose operational range is 15.3 km with a resolution of 0.03 km (Figueras i Ventura, 2009). IDRA is located at the Cabauw experimental site for atmospheric research (CESAR) observatory in the Netherlands at a height of 213 m from ground level (Leijnse et al., 2010). It scans at a fixed elevation of 0.50° and rotates the antenna over 360° in 1 min with a beamwidth of 1.8°. Clutter echoes are removed by a filter based on spectral polarimetric processing (Unal, 2009). Moreover, the measured linear depolarization ratio (L_{DR}) is used to filter areas that include particles other than rain and have low SNR, such that range gates with L_{DR} larger than −18 dB are removed (Bringi and Chandrasekar, 2001). This simple filtering procedure should be extended in the case of an automatic algorithm. The unwrapping of differential phase profiles is performed by detecting a differential phase jump between two adjacent gates, equal to 80% of the maximum differential phase 180°.

A convective storm event was observed by IDRA on 10 September 2011. The plan position indicators (PPIs) of z, z_{dr}, and Ψ_{DP} are shown in Fig. 4.5. Attenuation affected areas can be identified behind strong reflectivity echoes. Besides attenuation, z and z_{dr} may also be affected by radar miscalibration and azimuthal-dependence bias (see section 3.4). Here, we use the opportunity to study the impact of z and z_{dr} uncertainties (i.e., attenuation and bias) on the adaptive high-resolution approach.

4.4.2. METHODOLOGY

The proposed K_{DP} approach is analyzed using the storm event observed by IDRA. Besides the z, z_{dr}, and Ψ_{DP} fields, a path length interval is required. For this requirement, Fig. 4.4a can be used for guidance because the theoretical σ_K curves were built for the

[1] IDRA stands for IRCTR Drizzle RAdar where IRCTR stood for International Research Center for Telecommunications and Radar

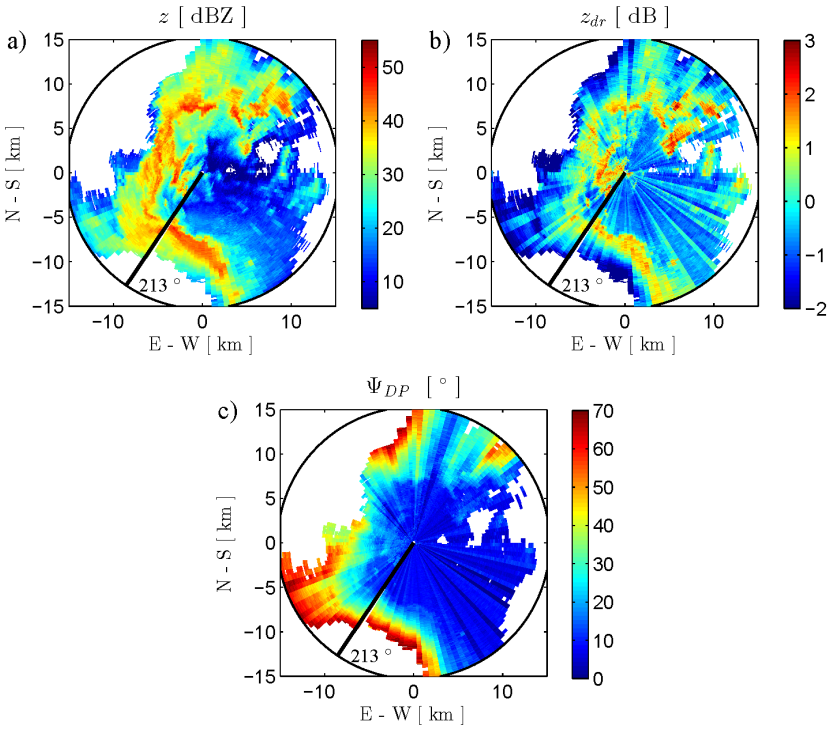

Figure 4.5: Observations by the IDRA radar at elevation angle of 0.5° in the NL on 19:50 UTC 10 September 2011. Fields of a) attenuated reflectivity, b) attenuated differential reflectivity, and c) differential phase. The black circles denote the 15.3 km range coverage of IDRA. The range resolution is 0.03 km.

same range resolution of IDRA and with theoretical μ_s and σ_P equal to 3 and 3°, respectively, which express the spatial variability of the observed z and Ψ_{DP} fields. Thus, from Fig. 4.4a, a length interval of [3;5] km, that is associated with $\sigma_K < 0.5°\,\text{km}^{-1}$ for $M > 20$, is selected. This interval is used by the path length selection process for all radials. For simplicity, $L^*(i)$ is indicated by $L(i)$ and is determined by minimizing $1/(L\sqrt{4M})$ instead of σ_K, as shown by Eq. (4.11), because theoretical μ_s, σ_P, and σ_ϵ remain constant in all radials. The coefficients c_2 and c_3 given in section 4.2.2 are used by the K_{DP} estimation process.

In order to study the performance of the K_{DP} approach in terms of spatial resolution and δ_{hv} filtering, three variations on applying the $\Delta\Psi_{DP}$ filter condition and $\Delta\Psi_{DP}$ downscaling, given by Eqs. (4.5) and (4.9) respectively, are defined and indicated in Table 4.2. In case I, K_{DP} is estimated using the $\Delta\Psi_{DP}$ filter condition without downscaling $\Delta\Psi_{DP}^{(j)}$ (i.e., $\hat{w}^{(j)} = \Delta r / L$ and the self-consistency ratio is equal to 1). This case is denoted by $\Delta\delta_{hv} \approx 0°$ and $s \approx 1$. In case II, the $\Delta\Psi_{DP}$ filter condition is not used but $\Delta\Psi_{DP}^{(j)}$ is downscaled. This case is expressed by $\Delta\delta_{hv} \neq 0°$ and $s \neq 1$. In case III, the $\Delta\Psi_{DP}$ filter condition is applied and $\Delta\Psi_{DP}^{(j)}$ is downscaled, and this case is represented by $\Delta\delta_{hv} \approx 0°$ and $s \neq 1$. Note that case III follows the proposed K_{DP} approach and cases I and II are

Table 4.2: Three cases for K_{DP} estimation using the adaptive high-resolution approach.

Cases	I	II	III
$\Delta\delta_{hv}$	$\Delta\delta_{hv} \approx 0°$	$\Delta\delta_{hv} \neq 0°$	$\Delta\delta_{hv} \approx 0°$
s	$s \approx 1$	$s \neq 1$	$s \neq 1$

defined only for analysis purposes.

After a K_{DP} profile is obtained, a Φ_{DP} profile is reconstructed by integrating Eq. (4.2) and δ_{hv} is determined as $\delta_{hv} = \Psi_{DP} - \Phi_{DP}$. Moreover, Z and Z_{DR} are obtained by correcting z and z_{dr} in a similar manner as in section 4.3.1 but replacing $\Delta\Phi^t_{DP}$ by $\Delta\Phi_{DP}$. This correction method could be improved by using more sophisticated techniques given for example by Park et al. (2005a) and Snyder et al. (2010). However, attenuation correction for z and z_{dr} is beyond the scope of this work as our goal is to assess the performance of the K_{DP} approach.

4.4.3. K_{DP} AND σ_K RESULTS FOR A PPI RADIAL

The K_{DP} approach specified by cases I, II, and III is applied to the azimuthal radial of 213° and its results are shown in Fig. 4.6. The downscaling aspect of K_{DP} is examined by comparing Ψ_{DP}, Φ_{DP} (case I), and Φ_{DP} (case III) profiles as shown in panel a). Observe that the total $\Delta\Phi_{DP}$ for cases I and III is equal to 45°. However, Φ_{DP} from case III captures the spatial variability and rapid increments of Ψ_{DP} better than Φ_{DP} from case I. This can be seen by their corresponding K_{DP} profiles, also shown in panel a) but shifted by $-10\,°\,\mathrm{km}^{-1}$, where two K_{DP} peaks (both of $10\,°\,\mathrm{km}^{-1}$ approximately) from case III correspond to fast increments of Ψ_{DP} located downrange in convective areas. Observe that the Ψ_{DP} profile includes a δ_{hv} "bump" in the range 2-4 km. In order to analyze the δ_{hv} contamination aspect of K_{DP}, Φ_{DP} from cases II and III are shown in panel b) as well as their corresponding δ_{hv} profiles shifted by $-10°$. This δ_{hv} "bump" of 2 km length does not show an impact on Φ_{DP} (case II) because its length is smaller than $L_{\min} = 3$ km. Also, Ψ_{DP} values outside the "bump" are similar and therefore most $\Delta\Psi_{DP}$'s have values near 0°. Summarizing K_{DP} estimation is not affected by this δ_{hv} "bump" in both cases, II and III. Note that in the range 7-11 km, Ψ_{DP} increases rapidly which probably means that raindrops of moderate to large size are present and thus significant δ_{hv} values are expected. However, both Φ_{DP} profiles are similar. This similarity may be due to δ_{hv} values hardly vary in this range and thus $\Delta\delta_{hv}$'s do not impact $\Delta\Psi_{DP}$'s. Such feature can be seen in δ_{hv} (case III) where it shows a slight spatial variability. Further, the estimation of δ_{hv} depends on Φ_{DP} estimation which can include accumulated K_{DP} errors (e.g., towards the end of the range). A rigorous estimation and analysis of δ_{hv} are beyond the scope of this work, the focus is given on K_{DP} estimation.

Panel c) shows attenuated z, corrected Z^t, and corrected Z profiles, the last being associated with case III. The correction of z is evident towards the convective range 7-11 km, where PIA reaches 15 dB at 11 km. Note that the Z^t profile shows values slightly larger than those of the Z profile because of unfiltered δ_{hv}. In a similar manner, the

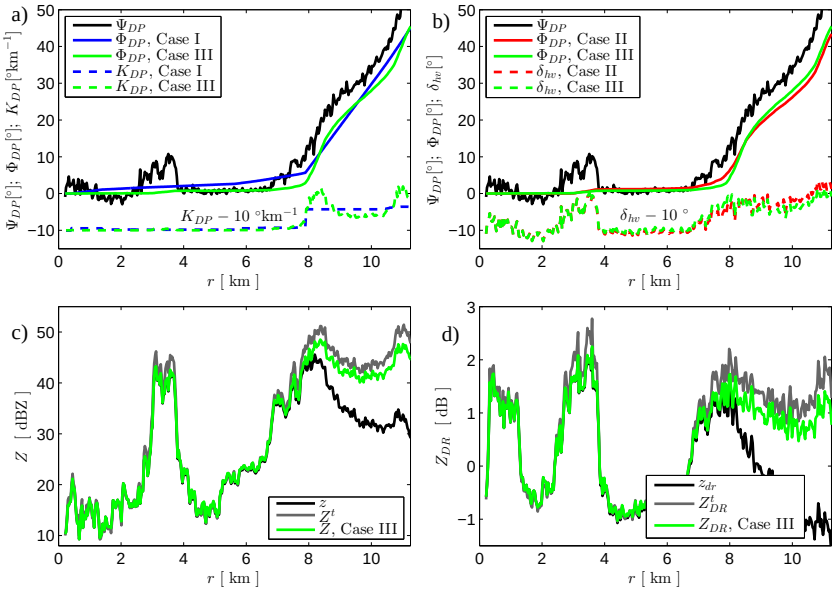

Figure 4.6: Profiles resulted from estimating K_{DP} using cases I, II, and III at azimuthal radial of 213°. a) The Ψ_{DP} profile is indicated by the black line while the reconstructed Φ_{DP} using cases I and III, are denoted by the blue and green lines, respectively. Corresponding K_{DP} profiles, with an offset of $-10\,^{\circ}\,\mathrm{km}^{-1}$, are shown in a similar manner. b) As in a) but using cases II and III and showing δ_{hv} instead of K_{DP}. c) The z profile is indicated by the black line, while Z^t and Z profiles are denoted by the gray and green lines, respectively. d) As in c) but for Z_{DR}.

correction of the z_{dr} profile is shown in panel d) where PIA_{DP} equals 2.3 dB at 11 km. Note that δ_{hv} and Z_{DR} profiles show a correlated behavior as expected from the δ_{hv}-Z_{DR} relation.

FOR A COMPLETE PPI

The results from applying the K_{DP} approach, specified by case III, to all radials of Fig. 4.5 are shown in Fig. 4.7. The field of Z is plotted in panel a) and the field of L, selected from the interval [3;5] km, in panel b). The spatial variability of L exhibits an adaptive performance with the purpose of minimizing σ_K. The K_{DP} and Φ_{DP} fields are shown in panels c) and d), respectively. It can be seen that the K_{DP} field maintains the structure and resolution of the storm illustrated by the Z field whereas the Φ_{DP} field displays the propagation phase component of the Ψ_{DP} field depicted in Fig. 4.5c. Note that the K_{DP} field presents some gaps in areas of measured Z (e.g., at approximately 8 km south from IDRA). In these areas, M is equal to 0 which means that for any bounded value of L none of the $(n+1)$-$\Delta\Psi_{DP}$ samples satisfies Eq. (4.5). Such issue could be avoided if, for instance, K_{DP} is estimated using case II instead of III or using interpolation algorithms. Panel e) shows the actual σ_K whose arithmetic mean is equal to $0.1\,^{\circ}\,\mathrm{km}^{-1}$. However, values as high as $1\,^{\circ}\,\mathrm{km}^{-1}$ are visible near convective edges. This increase in σ_K is partly due to a reduced number of $\Delta\Psi_{DP}$'s that satisfy Eq. (4.5). The actual μ_s is represented in panel f) whose values are mostly between 0 and 5. Thus, setting theoretical μ_s equal

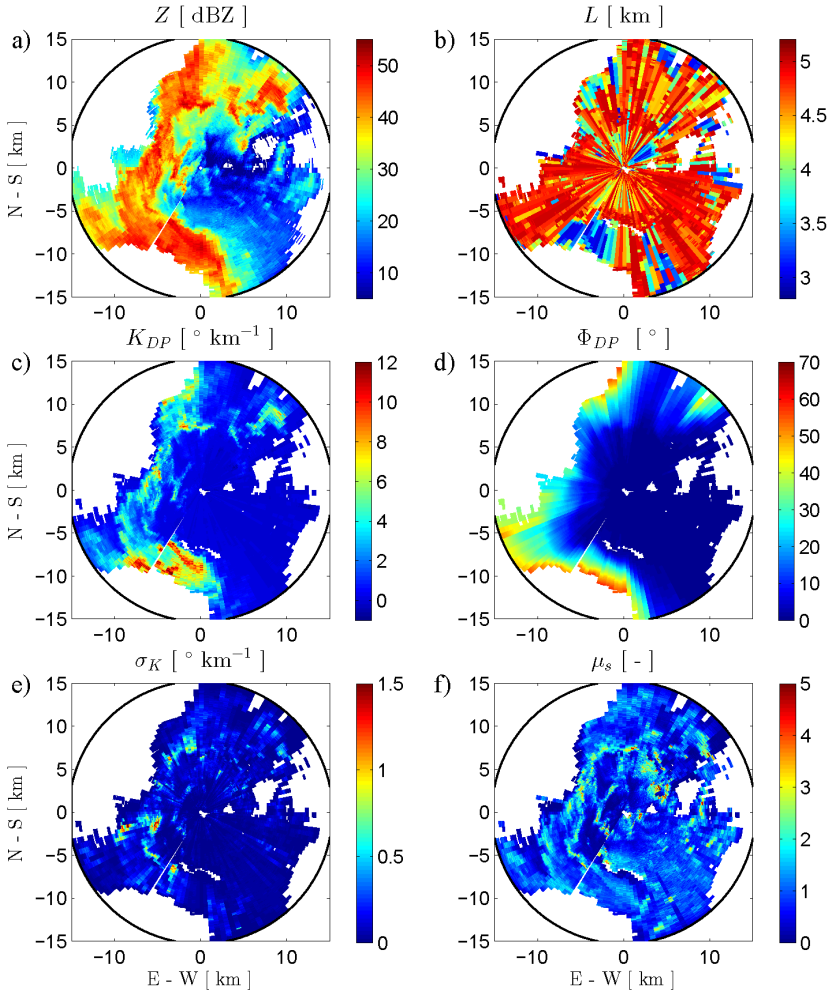

Figure 4.7: PPI fields resulting from estimating K_{DP} using case III: a) attenuation corrected Z, b) selected L, c) estimated K_{DP}, d) reconstructed Φ_{DP}, e) actual σ_K, and f) actual μ_s.

to 3 in this convective storm is a reasonable predefinition. The field of μ_s also shows an adaptive characteristic of the K_{DP} approach as it handles the spatial variability of Ψ_{DP}. In a similar manner, K_{DP} is estimated using cases I and II. PPIs resulting from the conventional K_{DP} and adaptive high-resolution techniques will be shown later in Chapter 5 using more storm events.

In order to study the impact of unfiltered δ_{hv} on the standard deviation of K_{DP}, actual σ_K resulting from cases II and III over all radials is displayed in Fig. 4.8 as a function of their corresponding number of paths M, with $M > 1$. Because of the large number of σ_K and M samples, they are plotted as 2-D histograms for a better visualization. Note that the σ_K-M histogram from case II shows a very small dependence on M as op-

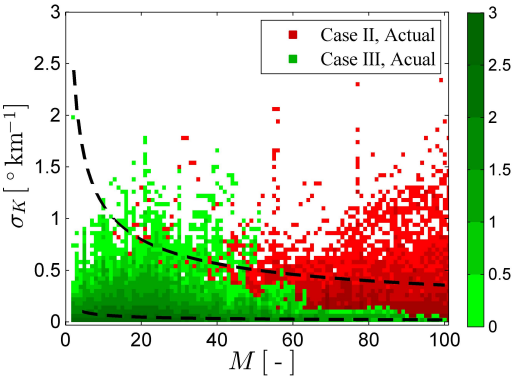

Figure 4.8: The 2-D histograms of the actual σ_K and number of paths M resulting from cases II and III are represented by the red and green scale colors, respectively. Theoretical σ_K curves, at Δr = 0.03 km, are indicated by dashed black lines where the upper curve corresponds to L = 3 km and μ_s = 5 and the lower curve to L = 5 km and μ_s = 0.5. The frequency of occurrence is given in logarithm scale and applies to all subsequent histograms.

4

posed to Eq. (4.11). This holds for values of M up to 167 (i.e., the near integer less than $L_{\max}/\Delta r + 1$). Such behavior occurs because the $\Delta\Psi_{DP}$ filter condition is not applied in case II and thereafter adjacent paths are employed to obtain $\Delta\Psi_{DP}$ samples which leads to an increased correlation coefficient between these samples. In a hypothetical situation with a correlation coefficient equal to 1, theoretical σ_K is no longer a function of M (see Eq. (A.2) in Appendix A). In addition to these adjacent samples, unfiltered $\Delta\delta_{hv}$, and thereby δ_{hv}, compromises the estimation of K_{DP} and increases the variability of actual σ_K. In contrast, the 2-D histogram from case III shows a dependence on M because σ_K decreases when M increases as expressed by the theoretical σ_K in Eq. (4.11). Two theoretical σ_K curves, for the same range resolution of IDRA, are also plotted in Fig. 4.8 to compare theoretical σ_K with actual σ_K from case III. The upper curve is set with L = 3 km (i.e., $L_{\min}$) and μ_s = 5 and the lower curve with L = 5 km (i.e., $L_{\max}$) and μ_s = 0.5, assuming the same theoretical values for σ_P and σ_ϵ as given in section 4.3.5. For a fair comparison between actual σ_K near 0 ° km^{-1} and the lower σ_K curve, only actual σ_K values slightly larger than 0 ° km^{-1}, for example ≥ 0.05 ° km^{-1}, are considered. In this comparison, 91% of the σ_K-M scatters are in between both curves while only 2% are located above the upper curve.

Z-K_{DP} RELATION

Another manner to study the downscaling and δ_{hv} contamination aspects of the K_{DP} approach is by examining the consistency between Z and K_{DP} (Park et al., 2005b). For this purpose, Fig. 4.9a compares the Z-K_{DP} histograms from cases I, II, and III. In case I, K_{DP} is estimated at coarse resolution and its values are smaller than 8 ° km^{-1}, while in cases II and III, K_{DP} is estimated at Δr scales and K_{DP} values can be as high as 12 ° km^{-1}. However, in case II, the 2-D histogram shows multiple negative outliers due to unfiltered δ_{hv}, resulting in underestimated and overestimated K_{DP} values. Among these three cases, case III provides the best consistency because of the application of the $\Delta\Psi_{DP}$ filter condition and $\Delta\Psi_{DP}$ downscaling specified by the proposed K_{DP} approach.

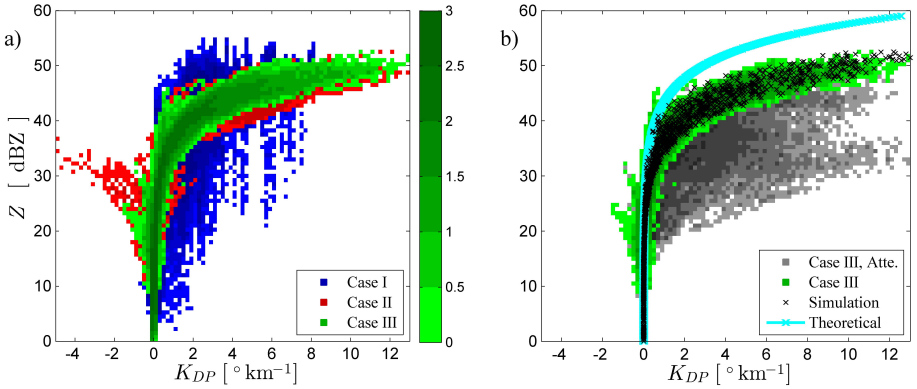

Figure 4.9: a) The Z-K_{DP} histograms resulting from cases I, II, and III are compared and denoted by blue, red, and green scale colors, respectively. b) As in a) but only for case III where the Z-axis before and after attenuation correction are represented by the gray and green scale colors, respectively. In addition, a simulated Z-K_{DP} scatterplot and its theoretical fit are indicated by 1 500 cross symbols and the cyan line, respectively. Simulated Z values are shifted by −8 dB.

For evaluation purposes, Fig. 4.9b shows the Z-K_{DP} histogram from case III, the Z-K_{DP} scatterplot using scattering simulation from section 4.2.2, and its theoretical fit Z-K_{DP} relation given by $K_{DP} = 8.7 \times 10^{(0.69Z/10)-4}$. Note that simulated Z values were shifted by −8 dB in order to match those from case III, which could be due to incorrect attenuation correction and/or bias associated with partial beam blockage and miscalibration. In contrast, the K_{DP}-axis shows a noticeable agreement between simulation and estimation. As a first step to analyze the discrepancy in the Z-axis, a similar histogram is shown but with attenuated z instead of corrected Z, keeping estimated K_{DP}. From both plots, it is clear that attenuation is not the major reason for this inconsistency but rather partial beam blockage and miscalibration.

4.4.4. K_{DP} IN SOLID OR MIXED PRECIPITATION

As part of the presented analysis, K_{DP} estimation at X-band frequencies over areas of solid and melting hydrometeors such as graupel, hail, and snow are shortly discussed. Because the shape and orientation response of particles are strongly related to their dielectric response, polarimetric signatures of solid hydrometeors is reduced because their dielectric constant factor is 20% or less than the one of raindrops. For example, Dolan and Rutledge (2009) and Snyder et al. (2010) simulated K_{DP} values at X-band for solid and melting particles showing a limited range of −1 to 1 ° km^{-1} except for melting graupel, which can be between −2 and 7 ° km^{-1} and in dendritic growth zones in which K_{DP} values can be higher than 1 ° km^{-1} Bechini et al. (2013). In addition, values of δ_{hv} from solid hydrometeors are small except for large non-spherical hail or melting hail, in which δ_{hv} can be in the order of 4 to 7° (Trömel et al., 2013). Moreover, Schneebeli et al. (2014) calculated K_{DP} in snow using a Kalman filter-based approach and found similar results when K_{DP} is estimated by the conventional technique. In this context, the spatial variability of K_{DP} in non-rain regions may be less significant than in rain regions. Thus, the

Table 4.3: Description of four storm events observed by IDRA with coverage of 15.3 km and Δr = 0.03 km.

Events	Date	Period (UTC)	Storm Type
E1	10 May 2011	21:00 - 23:00	Single cells [2], light and moderate rain.
E2	28 Jun 2011	22:00 - 00:00	A cluster of multicells (moderate rain) followed by a widespread area of light rain.
E3	10 Sep 2011	19:40 - 21:40	A cell larger than 100 km^2 followed by single cells, moderate and heavy rain.
E4	07 Oct 2011	04:20 - 06:20	Cells of irregular shapes, light and moderate rain.

[2] The area of a cell is found in the range 10 - 100 km^2 with Z larger than 30 dBZ. Similar cell characteristics are defined by Johnston et al. (1998).

conventional approach or an autoregression-based model can be considered to complement K_{DP} estimates in non-rain regions as demonstrated by Lim et al. (2013). Alternately, the adaptive high-resolution approach can be also used by setting $\hat{w}^{(j)}$ equal to $\Delta r L^{-1}$ and M equal to $n+1$, which is similar to case I but without the $\Delta\Psi_{DP}$ filter condition, at expenses of low-resolution and possibly δ_{hv} infiltration. In this scenario, the theoretical σ_K is simplified to $1.5\sqrt{2\Delta r}\,L^{-1.5}$ assuming $\sigma_P = 3°$, $\mu_s = 1$, and $M = n$. For instance, for Δr values of 0.03, 0.25, and 1 km, L can be set to 3, 6, and 9 km, respectively, in order to obtain theoretical σ_K equal to $0.07\,°\,\text{km}^{-1}$. However, further research is required to test the suggested alternative.

4.5. ASSESSMENT OF THE ADAPTIVE HIGH-RESOLUTION APPROACH

In this section, the performance of the proposed K_{DP} approach specified by case III is compared with the conventional and high-resolution techniques. For this purpose, four storm events observed by IDRA are described in Table (4.3). Although only observations of E3 at 19:50 UTC were shown in section 4.4, the other events also display similar uncertainties on z and z_{dr} fields. Hereafter, the term high-resolution is referred to as HR. In the conventional technique, the filter is designed using a 36^{th} order filter with r_c = 1 km and $\tau = 1.5\sigma_P$. More details on the filter design are included in Appendix B.

4.5.1. DURING 1-MIN

The corresponding times for E1, E2, E3, and E4 are 21:51, 22:25, 19:50, and 05:50 UTC, respectively. The reader can refer to Appendix D for the corresponding attenuation corrected Z fields. The Z-K_{DP} histograms resulting from the three K_{DP} approaches applied to each event of 1 min (i.e., one PPI) are shown in Fig. 4.10. The Z-K_{DP} scatters from the conventional technique are significantly spread because K_{DP} is estimated at coarse resolution and δ_{hv} is not properly filtered, which leads to negative and positive K_{DP} bias. In contrast, results from the HR method show more condensed relations. However, for Z values smaller than 40 dBZ, approximately, multiple outliers are noticeable. Those outliers are substantially eliminated by the adaptive HR approach, which exhibits an enhanced consistency for weak and strong Z. In order to quantify the consistency

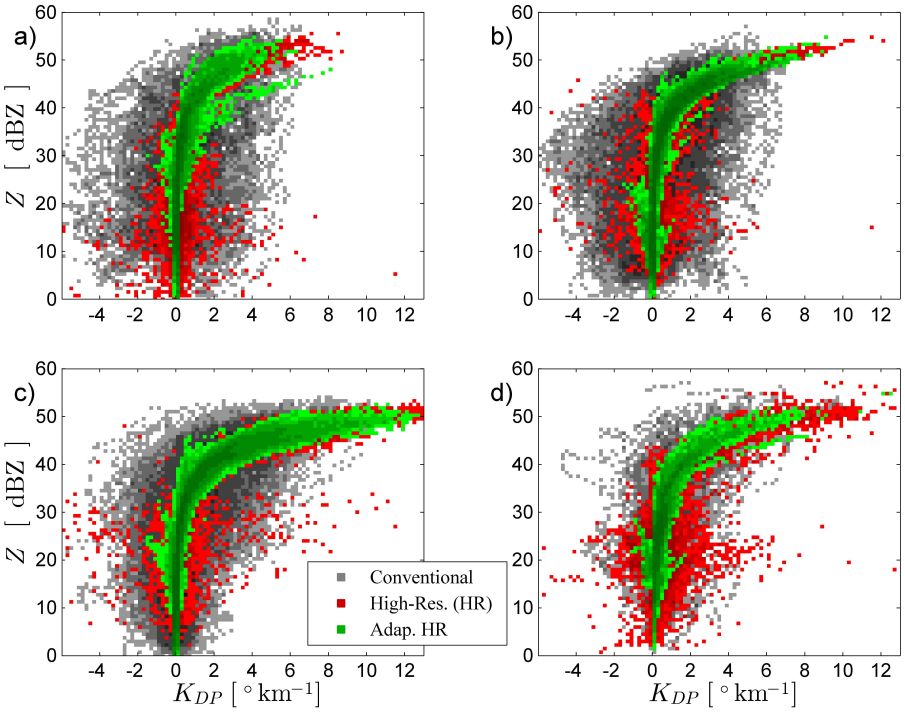

Figure 4.10: a) Z-K_{DP} histograms of storm event E1. The gray, red, and green scale colors are related to the conventional, high-resolution (HR), and adaptive HR approaches, respectively. Panels b), c), and d) as in a) but for E2, E3, and E4, respectively.

of the results, the correlation coefficient between Z and K_{DP}, hereafter $\rho_{Z,K}$, obtained from each approach is given by the 2^{nd}, 3^{rd}, and 4^{th} columns of Table (4.4). From this quantification, the adaptive HR approach outperforms the other two techniques. For reference purposes, the correlation coefficient $\rho_{Z,K}$ from the simulated Z-K_{DP} shown in Fig. 4.9b was also estimated and is equal to 0.75, which is similar to those resulted from the adaptive HR technique. Note that $\rho_{Z,K}$ values resulted from simulation or observations can change according to the range of Z and K_{DP} values because the theoretical Z-K_{DP} relation is non-linear and thereby it is suggested to use $\rho_{Z,K}$ as a relative quantity.

The results of Z and K_{DP} from the conventional and adaptive HR methods, presented in Fig. 4.10, show a similar discrepancy in the Z-axis (i.e., between Z values from theoretical fit and from estimation) as indicated in Fig. 4.9b. Although the degree of discrepancy is not the same in all events, the Z values reached by the conventional technique are in the same order as those from the adaptive HR approach. This indicates that Z is most likely biased and that the estimation of K_{DP} by the adaptive HR approach may not be affected by attenuation and biases associated with partial beam blockage and/or miscalibration.

A second manner to quantify the performance of the adaptive HR approach is by comparing its actual σ_K and σ_K^n, which were introduced as quality measures in sec-

Table 4.4: Comparison of the three K_{DP} approaches for the four storm events quantified by $\rho_{Z,K}$, $\overline{\sigma_K}$, $\overline{\sigma_K^n}$, and $\overline{\sigma_s^n}$.

	$\rho_{Z,K}$ [-]			$\overline{\sigma_K}$ [° km^{-1}]		$\overline{\sigma_K^n}$ [%]		$\overline{\sigma_s^n}$ [%]
Event	Conv.	HR	Adap. HR	HR	Adap. HR	HR	Adap. HR	Adap. HR
E1	0.38	0.61	0.72	1.12	0.09	85	16	11
E2	0.48	0.70	0.74	0.93	0.09	50	9	13
E3	0.66	0.73	0.75	0.83	0.10	42	7	16
E4	0.53	0.67	0.75	1.22	0.06	83	6	10

tion 4.3.4, with the HR method for each event. The mean values of the σ_K field ($\overline{\sigma_K}$) and σ_K^n field ($\overline{\sigma_K^n}$) resulting from these techniques are given in Table (4.4). For the calculation of $\overline{\sigma_K^n}$, only gates with $|K_{DP}| \geq 1\,^\circ\,\mathrm{km}^{-1}$ are considered. Note that $\overline{\sigma_K}$ from the adaptive HR approach is, in average, 1/10 of the HR method. In addition, $\overline{\sigma_K^n}$ results from the adaptive HR approach are smaller than a reasonable error of 20% while those from the HR method are much larger than 20%. Another quality measure, also given in section 4.3.4, is σ_s^n which measures the percentage error of the actual μ_s estimated by the adaptive HR approach. The mean of the σ_s^n field ($\overline{\sigma_s^n}$) for each event is found reasonably small as indicated in Table (4.4). Finally, in terms of computational time required by both techniques, the adaptive HR approach needs, in average, 1/3 of the time required by the HR method, which is in the order of few minutes for 1 min of data while for the conventional technique it is in the order of seconds.

4.5.2. DURING 2-H

Next, the three K_{DP} techniques are compared and evaluated using the same quality measures $\rho_{Z,K}$, $\overline{\sigma_K}$, $\overline{\sigma_K^n}$, and $\overline{\sigma_s^n}$ and storm events E1, E2, E3, and E4 but during periods of 2-h as illustrated in Figs. 4.11, 4.12, 4.13, and 4.14, respectively. In general, it can be observed that the adaptive HR approach outperforms the other two methods, although the performance of each technique varies according to the storm scenario. For example, the conventional technique can lead to reasonable results when a storm consists of a large area of heavy rain because Ψ_{DP} profiles carry sufficient data samples with high SNR levels, reducing the impact from Ψ_{DP} outliers. In the HR method, acceptable results can be obtained in a scenario given by a large cell or a cluster of multiple cells with moderate to heavy rain because it allows consideration of multiple $\Delta\Psi_{DP}$ samples over extended paths which reduces the impact of small and sometimes negative $\Delta\Psi_{DP}$ values. In addition, this scenario may reduce the sensitivity of the downscaling weight $w(i)$ to noisy measurements of Z and Z_{DR}. In contrast, the adaptive HR approach yields reliable results even when storm cells cover relatively small areas with light rain because $\Delta\Psi_{DP}$ samples are adaptively selected over paths with lengths determined from a predefined interval so that a theoretical value of σ_K is minimized. Moreover, uncertainties associated to the self-consistency relation are reduced due to the improved formulation of $w(i)$ in this method. In case a storm cell becomes significantly small such that the extents of

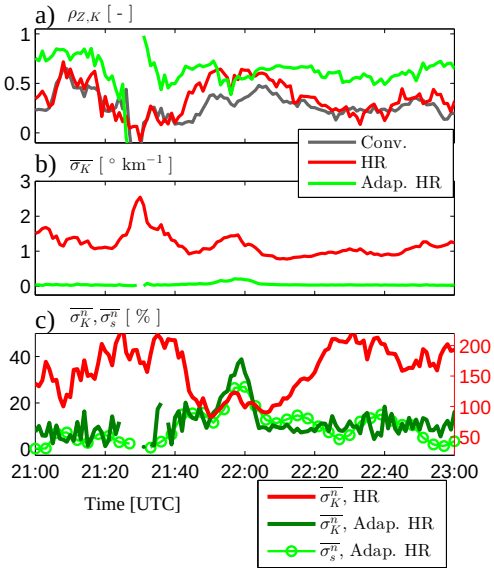

Figure 4.11: Time series of quality measures from the three K_{DP} approaches for event E1. a) The correlation coefficients from the conventional, HR, and adaptive HR techniques are denoted by the gray, red, and green lines, respectively. b) Mean values $\overline{\sigma_K}$ from the HR and adaptive HR approaches are indicated by the red and green lines, respectively. c) $\overline{\sigma_K^n}$ from the HR and adaptive HR approaches are illustrated by the red line (right y-axis) and green line (left y-axis), respectively. Also $\overline{\sigma_s^n}$ from the adaptive HR approach is indicated by the green line with circles (left y-axis).

Ψ_{DP} profiles are in the order of $L_{\min}$, estimates of K_{DP} by the adaptive HR approach are not possible; this feature could be beneficial because accurate estimation of K_{DP} from limited data samples is rarely achieved.

The resulting time series of $\rho_{Z,K}$ for event E3 indicate that during the first hour the three K_{DP} approaches performed in a similar manner because K_{DP} estimates were obtained from a large cell with heavy rain in which the conventional and HR methods perform at their best. During the second hour, small cells with moderate rain were observed, leading to decreased performance of the conventional and HR methods. In event E2, during 22:20-23:00 UTC, the HR and adaptive HR approaches provided similar results and performed better than the conventional technique because this time period was associated with a cluster of cells with moderate rain. After this period, the adaptive HR approach maintained a satisfactory performance while the performance of the conventional and HR methods decreased because values of K_{DP} were estimated from light rain. For events E1 and E4, $\rho_{Z,K}$ time series obtained from the conventional and HR techniques are similar but smaller than those from the adaptive HR approach because in these events single cells with irregular shapes and light rain were observed. Although $\rho_{Z,K}$ time series from the three K_{DP} techniques can show similar results for a given storm scenario, Z-K_{DP} relations might include multiple scatters as illustrated in Fig. 4.10, especially for weak Z values. As a result, the adaptive HR approach provides the best Z-K_{DP} consistency for storm scenarios with different cell sizes and rain amounts.

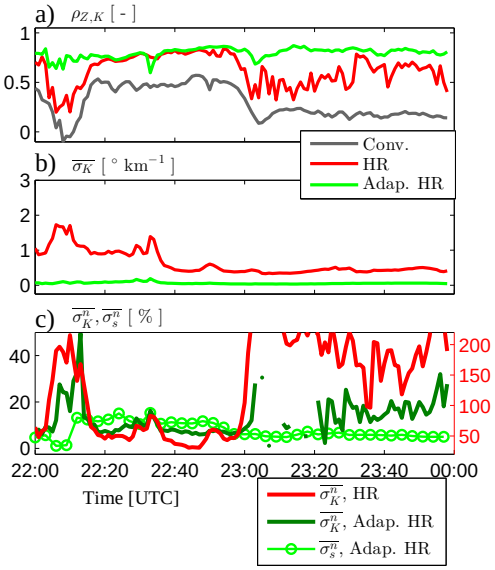

Figure 4.12: As in Fig. 4.11 but for event E2.

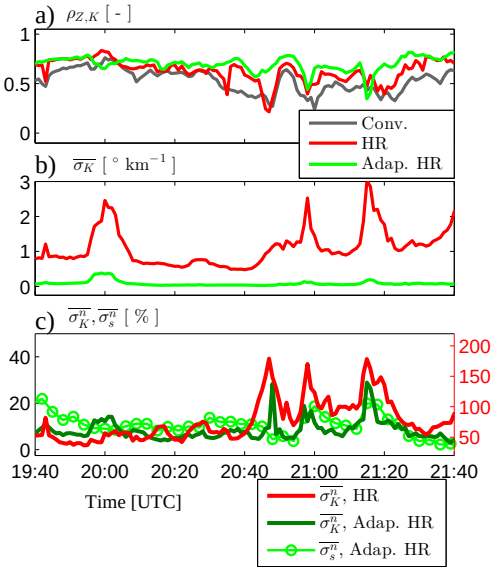

Figure 4.13: As in Fig. 4.11 but for event E3.

Time series of $\overline{\sigma_K}$ from the HR and adaptive HR techniques for the four events exhibited values between 1 and 3 ° km^{-1} and near 0 ° km^{-1}, respectively. However, the results from the HR technique for event E2 showed values smaller than 1 ° km^{-1} because of a widespread area of rain with low variability on Z, Z_{DR}, and Ψ_{DP} fields. Nonetheless, its

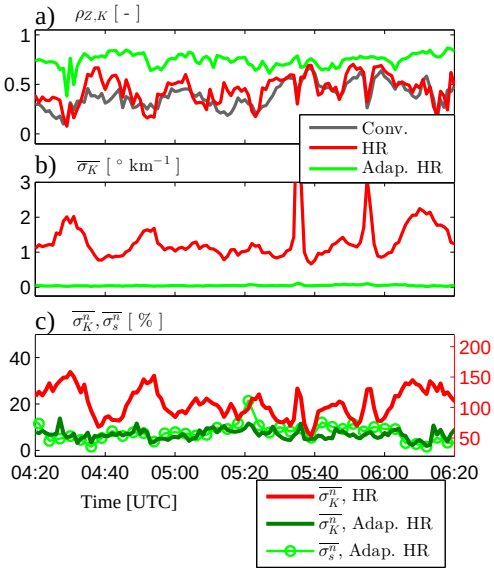

Figure 4.14: As in Fig. 4.11 but for event E4.

performance measured by $\rho_{Z,K}$ remains below the adaptive HR approach. This shows a persistent accuracy in estimating K_{DP} by the adaptive HR approach. Furthermore, time series of $\overline{\sigma_K^n}$ and $\overline{\sigma_s^n}$ resulting from the adaptive HR approach depicted, in all events, consistent percentage errors smaller than 20%. However, for events E1 (around 22:00 UTC) and E3 (during some periods after 20:40 UTC), the percentage errors increased because of inaccurate measurements of Z and Z_{DR} resulting from storm cells with heavy rain located adjacent or on top of the radar, leading to power saturation in the receiver. This is an example of how $\sigma_K^n(i)$ or $\overline{\sigma_K^n}$ and $\sigma_s^n(i)$ or $\overline{\sigma_s^n}$ can be used to identify areas where K_{DP} estimates could be compromised. Another example of large $\overline{\sigma_K^n}$ can be seen in E2 around 22:10 UTC where $\overline{\sigma_K^n}$ values are as high as 40% because of small areas of light rain with a reduced number of $\Delta\Psi_{DP}$ samples, affecting the accuracy of K_{DP} estimates. The discontinuity seen between 23:00 and 23:20 UTC is due to the constraint $|K_{DP}| \geq 1\,^\circ\,\text{km}^{-1}$. A similar discontinuity is observed in event E1 around 21:30 UTC. In the same event, a decreasing and discontinued behavior of $\rho_{Z,K}$ is observed in the period 21:20-21:40 UTC. Such behavior is associated with a progressive reduction of storm cells in intensity and size which led to light rain echoes with areas smaller than 5 km^2 where the extents of Ψ_{DP} profiles are not sufficient for the estimation of K_{DP}. For the case of the HR method, time series of $\overline{\sigma_K^n}$ indicated a limited performance as $\overline{\sigma_K^n}$ values are mostly larger than 50%.

4.6. CONCLUSIONS

Polarimetric studies have continuously focused on the estimation of K_{DP} because of its capability to overcome power attenuation and radar miscalibration. However, accurate

estimation of K_{DP} at scales of the range resolution is challenging because K_{DP} requires significant spatial smoothing due to noisy Ψ_{DP} profiles, for example, in light rain. This problem is intensified at short wavelengths when Ψ_{DP} profiles include δ_{hv} components, for example in moderate and heavy rain. In this work, an adaptive HR approach has been presented to address these problems. The standard deviation of the proposed K_{DP} estimator has been derived and formulated in order to provide a path length interval that could lead to K_{DP} estimates with reduced error. This formulation takes into account the spatial variability of the storm and the radar range resolution.

A storm event observed by a polarimetric X-band weather radar during 1-min was used to analyze and test the performance of the K_{DP} estimator. Results showed that the estimated K_{DP} field kept the structure of the attenuation corrected Z field without significant spatial distortion and that its estimation was associated with reduced errors indicated by the actual standard deviation (i.e., the σ_K field). The consistency between Z and K_{DP} showed that negative values of K_{DP}, associated with weak Z, can be reduced and high K_{DP} values, associated with strong Z, can be obtained. In order to assess the performance of the adaptive HR approach to obtain accurate K_{DP} at range resolution scales, four storm events observed by the same radar but during periods of 2-h, were considered and the K_{DP} results were compared with the conventional and HR techniques. In general, the proposed approach was able to provide a correlation coefficient between Z and K_{DP} higher than the other two methods. In terms of standard deviations, the adaptive HR approach showed significant improvements compared to the HR technique. The actual mean μ_s field, introduced by the adaptive HR approach, was associated with reduced uncertainty as indicated by $\overline{\sigma_s^n}$ results. Although the adaptive HR approach considers measurements of Z and Z_{DR} and constant coefficients related to the self-consistency relation and attenuation correction, results of this method did not highlight issues related to radar miscalibration, radial patterns in Z_{DR}, power attenuation, and variability on DSD and drop shape. Consequently, the adaptive HR approach, which uses the correlation between δ_{hv} and Z_{DR} and the self-consistency relation, is able to filter δ_{hv} and maintain the spatial variability of Ψ_{DP}. Therefore accurate K_{DP} profiles at high spatial resolution in light and heavy rain are achieved.

In order to achieve the ambitions of implementing the proposed K_{DP} algorithm for real-time operation, further studies are required. This effort includes estimating and updating the coefficients, which are used in the attenuation correction method and in the self consistency principle, to operational C and S-band frequencies and, if possible, taking into account temperature variability. Note that at S-band frequencies, the $\Delta\Psi_{DP}$ filter condition can be excluded from the K_{DP} algorithm because δ_{hv} is usually negligible. Moreover, an automatic algorithm might be needed to classify areas of rain, non-rain, and non-hydrometeors. For solid or mixed rain areas, either, the self consistency ratio should be set to 1, so that, K_{DP} is given at expenses of coarse spatial resolution or another K_{DP} algorithm should be employed. Furthermore, $[L_{\min}; L_{\max}]$ should be selected according to values of Δr and to predefined values of μ_s and σ_P, which the latter two can be set as a function of the rain scenario (e.g., 4 and 3° for convective and 1 and 2° for stratiform rain). Alternatively, theoretical values of μ_s can be adjusted according to previous actual values of μ_s.

A reliable K_{DP} is one of the most powerful observables from polarimetric weather

radars. The adaptive HR approach may prove to be key in addressing the dilemma between the spatial resolution and accuracy of K_{DP}. Moreover, the formulation of the theoretical σ_K and the capability of calculating the uncertainty of K_{DP} estimates gate-by-gate allow to reduce and control errors in the estimation of K_{DP}. Though this approach still needs to be tested at longer ranges, where attenuation and non-uniform beam filling affect Z and Z_{DR} measurements, and in scenarios where partial beam blockage is associated with complex terrain features, urban-hydrology and weather-forecast communities may benefit from the proposed approach in terms of spatial resolution, accuracy, and quality control of K_{DP} estimates leading to significant improvements on K_{DP}-based products.

5

Differential Phase Processing at X-Band Frequencies for an Improved Estimation of A and δ_{hv} in Convective Storm Cells

Abstract: In weather radar polarimetry, attenuation correction methods are based on the propagation differential phase Φ_{DP} and the optimization of the parameter α that connects the specific attenuation A and specific differential phase K_{DP}. However, accurate estimation of A can become challenging in the presence of, among others, unfiltered backscatter differential phase δ_{hv} and noise on Φ_{DP}, especially over short paths. In this work, established methods to estimate Φ_{DP} and A in rain are implemented in order to examine the impact of Φ_{DP} estimation on the optimization of α and on the estimation of A. In addition, a new approach to compute δ_{hv} is proposed to depict the spatial distribution of raindrop sizes in convective storms. These methods were examined using diverse storm events observed with a maximum range of 15 km and spatial resolution of 0.03 km by a polarimetric X-band radar in the Netherlands. A detailed analysis showed how Φ_{DP} profiles, obtained by the conventional range-filtering technique, led to erroneous α values and incorrect A estimates. In contrast, an adaptive approach that estimates Φ_{DP} at range resolution scales provided α values consistent with expected variability of raindrop size distribution. δ_{hv} estimates were cross-checked with K_{DP} estimates and showed strong agreement to predefined empirical relations. By following the presented analyses, the reader can identify benefits and limitations of the considered methods, emphasizing the challenge of estimating α and δ_{hv} at X-band frequencies.

5.1. INTRODUCTION

Operational weather radars at S and C-band frequencies have been used for several decades to monitor the evolution of precipitation. In recent years the technology of those conventional radars has been upgraded to polarimetric technology in order to further improve weather radar measurements (Doviak et al., 2000). However, severe weather can produce rapid and localized surface damage associated with heavy rainfall, hail, and strong winds. In this context, a network of small polarimetric X-band weather radars may be suitable to obtain observations of fast-developing storms at close range and at resolutions higher than those from conventional radars (McLaughlin et al., 2009). Moreover, Wang and Chandrasekar (2010) and Mishra et al. (2016) showed the potential of polarimetric X-band radars to improve rainfall rate estimation.

One of the advantages of polarimetric radars is given by the measurements of differential phase between the horizontally and vertically polarized signals caused by the delay of one with respect to the other, in the forward direction, as both signals propagate throughout hydrometeors. In this way this differential phase, Ψ_{DP} [°], is independent of attenuation, miscalibration, and partial beam blockage effects (Doviak and Zrnić, 1993). However, Ψ_{DP} measurements can include phase shifts in the backward direction due to Mie-scattering, the so-called backscatter differential phase δ_{hv} [°], and random fluctuations ϵ [°] in the order of few degrees. In general, a Ψ_{DP} range profile is modeled as

$$\Psi_{DP}(r) = \Phi_{DP}(r) + \delta_{hv}(r) + \epsilon, \tag{5.1}$$

where $\Phi_{DP}(r)$ [°] represents the differential phase in the forward direction and r [km] indicates the distance from the radar. Two useful variables derived from Φ_{DP} are the specific differential phase K_{DP} [° km^{-1}] and the specific attenuation A [dB km^{-1}] which are commonly used for the estimation of rainfall rate and attenuation correction (Bringi and Chandrasekar, 2001).

The traditional method to estimate K_{DP} from noisy Ψ_{DP}, when δ_{hv} is significant, is given by Hubbert and Bringi (1995) and several attempts have been proposed to improve K_{DP} estimates at S-band (Matrosov et al., 2006), C-band (Vulpiani et al., 2012), and X-band frequencies (Wang and Chandrasekar, 2009; Otto and Russchenberg, 2011; Giangrande et al., 2013; Schneebeli et al., 2014; Reinoso-Rondinel et al., 2018). K_{DP} can be used to correct measurements of reflectivity Z [dBZ] and differential reflectivity Z_{DR} [dB] for signal attenuation (Bringi et al., 1990) and for biases due to miscalibration and partial beam blockage (Giangrande and Ryzhkov, 2005). In addition, K_{DP} has led to improved estimation of rainfall rate compared to those from Z and Z_{DR} because of its quasi-linear relation to liquid water content (Ruzanski and Chandrasekar, 2012; Lim et al., 2013). Although radar measurements seem to benefit from using K_{DP}, comprehensive research on K_{DP} is still needed because it is still a challenge to provide accurate K_{DP} values operationally.

Existing methods to estimate A in rain assume that $A = \alpha K_{DP}$ where α is a constant for a given frequency (Bringi et al., 1990). Testud et al. (2000) also used the relation between A and K_{DP}, in their rain profiling technique, to express A in terms of the difference of Φ_{DP} and measurements of Z, avoiding K_{DP} calculation. However, it is known that α is sensitive to temperature, drop size distribution (DSD), and drop size variabilities and therefore Bringi et al. (2001) extended the approach given by Testud et al. (2000) to avoid

a priori value for α. At C-band frequencies, an extensive literature has been presented to further improve attenuation correction procedures (Vulpiani et al., 2008; Tabary et al., 2011; Gu et al., 2011). Because attenuation is also inevitable at X-band frequencies, several methods have been proposed to address attenuation problems (Matrosov et al., 2002, 2005; Gorgucci and Chandrasekar, 2005; Gorgucci et al., 2006; Park et al., 2005a; Snyder et al., 2010; Lim and Chandrasekar, 2016). More recently, Ryzhkov et al. (2014), Wang et al. (2014), and Diederich et al. (2015) modified the method of Testud et al. (2000) to improve rainfall rate estimation and to demonstrate that A can be used to reduce issues related to miscalibration and partial beam blockage. Despite of these promising benefits, the potential of using A might be limited depending on the approach to obtain Φ_{DP} and α while reducing δ_{hv} components (Bringi et al., 2001; Ryzhkov and Zrnić, 2005; Snyder et al., 2010). As an alternative to reduce such limitation, different schemes included attenuation measurements obtained from microwave links (Trömel et al., 2014) and from collocated S and X-band radars (Matrosov et al., 2014).

Because several approaches have focused on filtering δ_{hv}, limited research has been conducted to estimate δ_{hv} and study its possible benefits given its relation to Z_{DR}. For example, Hubbert and Bringi (1995) and Otto and Russchenberg (2011) derived δ_{hv} from Eq. (5.1) after estimating Φ_{DP} using a low-pass filter and polarimetric self-consistency, respectively. Schneebeli and Berne (2012) estimated K_{DP} and δ_{hv} simultaneously using a Kalman filter approach. Moreover, Trömel et al. (2013) modified the method of Bringi et al. (2001) to calculate Φ_{DP} and thereby δ_{hv} using Eq. (5.1). Nonetheless, these procedures can lead to inaccurate estimates of δ_{hv} due to fluctuations and noise that could remain on Φ_{DP}.

The purpose of this work is to 1) explore the role and impact of estimated Φ_{DP} profiles on the performance of the attenuation correction method given by Bringi et al. (2001) in order to improve estimates of α and A and 2) propose an advanced technique to compute δ_{hv} in rain at X-band frequencies. For such purpose, two K_{DP} methods to obtain Φ_{DP} profiles, Hubbert and Bringi (1995), which uses only Ψ_{DP} measurements, and Reinoso-Rondinel et al. (2018), which uses Ψ_{DP} and non-calibrated measurements of Z and Z_{DR}, are described in section 5.2. In addition, attenuation correction methods from Bringi et al. (1990); Testud et al. (2000) and Bringi et al. (2001) are also reviewed. In section 5.3, a storm event observed at close range by a polarimetric X-band weather radar in the Netherlands is used to analyze and compare the relation between A and K_{DP} resulted from both K_{DP} methods and from Testud et al. (2000). This comparison is extended in section 5.4 to examine the effectiveness of Bringi et al. (2001) for the selection of α profile-by-profile. In section 5.5, the algorithm to calculate δ_{hv} is presented and its performance is evaluated. The algorithm integrates the results given by Hubbert and Bringi (1995), Bringi et al. (2001), and Reinoso-Rondinel et al. (2018) together with an interpolation method in order to reduce possible errors on δ_{hv} derived from Eq. (5.1). In section 5.6, two more storm events, one associated with a mini-supercell and the other with a tornadic storm, are used to conduct further assessments of the investigated methods. Finally, section 5.7 draws conclusions of this article.

5.2. ESTIMATION TECHNIQUES FOR Ψ_{DP}-BASED VARIABLES

The horizontal polarization reflectivity $Z(r)$ [dBZ] and differential reflectivity $Z_{DR}(r)$ [dB] profiles can be expressed as

$$Z(r) = z(r) + 2\int_0^r A(s)\,ds, \tag{5.2}$$

$$Z_{DR}(r) = z_{dr}(r) + 2\int_0^r A_{DP}(s)\,ds, \tag{5.3}$$

where $z(r)$ [dBZ] represents the attenuated reflectivity and $A(s)$ [dB km^{-1}] the one-way specific attenuation whereas $z_{dr}(r)$ [dB] represents the attenuated differential reflectivity and $A_{DP}(s)$ [dB km^{-1}] the one-way specific differential attenuation. The two-ways path integrated attenuation and differential attenuation terms in Eqs. (5.2) and (5.3) are commonly referred to as PIA(r) and PIA$_{DP}(r)$, respectively.

5

5.2.1. ESTIMATION OF K_{DP}

In the conventional technique given by Hubbert and Bringi (1995), a low-pass filter is designed such that gate-to-gate fluctuations on $\Psi_{DP}(r)$ are filtered (i.e., at range resolution scale Δr [km]). Fluctuations at spatial scales larger than Δr (i.e., δ_{hv} "bumps") are removed by applying the same filter multiple times to new generated Ψ_{DP} profiles until insignificant changes between two consecutive Ψ_{DP} profiles are observed, and therefore, a Φ_{DP} profile is obtained. A new Ψ_{DP} profile is generated gate-by-gate selecting data from either the original Ψ_{DP} profile or the previous filtered Ψ_{DP} profile according to a predetermined threshold τ [°]. This threshold is found to be in the order of 1 to 2 times the standard deviation of Ψ_{DP} profile, hereafter σ_P[°]. A K_{DP} profile is obtained by deriving Φ_{DP}. One of the limitations of this technique is that accurate estimates of $\Phi_{DP}(r)$ and $K_{DP}(r)$ at Δr scales are hardly achieved.

A more recent approach that estimates $K_{DP}(r)$ at Δr scales while controlling its standard deviation σ_K [° km^{-1}] is given by Reinoso-Rondinel et al. (2018). This approach was demonstrated at X-band frequencies. The inputs are $z(r)$, $z_{dr}(r)$, $\Psi_{DP}(r)$ profiles and also a predefined path length interval $[L_{\min}; L_{\max}]$ [km]. This interval is obtained in a qualitative manner from a mathematically derived relation that expresses a theoretical σ_K in function of Δr, σ_P, the length of a path L [km], and the spatial variability of a storm type (i.e., stratiform or convective) μ_s [-]. Values for σ_P and μ_s are found in the order of 2 to 4° and 1 to 5, respectively. Thus, depending on the storm type, a user can define σ_P and μ_s and set few values for L to choose a path length interval that is associated with small σ_K values. Once $[L_{\min}; L_{\max}]$ is predefined, K_{DP} in gate i, located at r_i, is estimated as

$$K_{DP}(i) = \frac{1}{M}\sum_{j=1}^{M}\frac{\Delta\Psi_{DP}^{(j)}\, w^{(j)}(i)}{2\Delta r};\ \text{with}\ \ j = 1,2,...M, \tag{5.4}$$

where $\Delta\Psi_{DP}^{(j)}$ represents the difference of $\Psi_{DP}(r)$ at the edges of the j^{th}-path of length $L(i)$ within the interval $[r_i - L(i);\ r_i + L(i)]$. The length $L(i)$ is selected from $[L_{\min}; L_{\max}]$

in an adaptive manner by minimizing the theoretical σ_K. The variable M indicates the number of paths that satisfy $|\Delta Z_{DR}^{(j)}| < \sigma_{Z_{DR}}$, where $\Delta Z_{DR}^{(j)}$ is the difference of a given $Z_{DR}(r)$ profile at the edges of the j^{th}-path while $\sigma_{Z_{DR}}$ [dB] is the standard deviation of the $Z_{DR}(r)$ profile. $Z_{DR}(r)$ is obtained after correcting $z_{dr}(r)$ for differential attenuation. The given constraint on $\Delta Z_{DR}^{(j)}$ is used to filter $|\Delta\delta_{hv}| > 0°$ from $\Delta\Psi_{DP}^{(j)}$ because similar values of Z_{DR} are related to similar values of δ_{hv}. Therefore, the contribution of δ_{hv} is mitigated using the appropriate differential phase differences. Such filtering process will be referred to as the $\Delta\Psi_{DP}$ filter condition. The weighting term $w^{(j)}(i)$ in Eq. (5.4) downscales $\Delta\Psi_{DP}^{(j)}$ from $L(i)$ to Δr scale in order to capture the spatial variability of a storm and is given by

$$w^{(j)}(i) = \frac{\Delta r}{L(i)} 10^{c_2(Z(i)-\overline{Z}^{(j)})/10} 10^{c_3(Z_{DR}(i)-\overline{Z}_{DR}^{(j)})}, \tag{5.5}$$

where $\overline{Z}^{(j)}$ and $\overline{Z}_{DR}^{(j)}$ represent the arithmetic mean of $Z(i)$ and $Z_{DR}(i)$ in the j^{th}-path, respectively. $Z(r)$ is obtained after correcting $z(r)$ for attenuation whereas the constant coefficients c_1, c_2, and c_3, although c_1 is not used in Eq. (5.5), are the parameters that establish the relation between K_{DP}, Z, and Z_{DR} based on the self-consistency principle. For attenuation correction purposes, it was suggested to follow the method introduced by Bringi et al. (1990) such that $\text{PIA}(r) = \alpha\Phi_{DP}^{'}(r)$ and $\text{PIA}_{DP}(r) = \beta\Phi_{DP}^{'}(r)$ where α and β are constant coefficients in dB $(°)^{-1}$ units while $\Phi_{DP}^{'}(r)$ is estimated from $\Psi_{DP}(r)$ using a linear regression fit. The mean of $w^{(j)}(i)$ samples is related to actual values of μ_s. Once a K_{DP} profile is obtained, a Φ_{DP} profile is calculated by simply integrating K_{DP} in range.

At X-band frequencies all coefficients listed above are sensitive to DSD, drop shape, and temperature variabilities. In order to capture such variabilities, the coefficients are estimated as the mean fit of empirical polarimetric relations obtained from 1 500 DSDs modeled by a Gamma distribution and combining multiple drop shape models and temperatures (Otto and Russchenberg, 2011). Resulted coefficients are given by $c_1 = 1.37 \times 10^{-3}$; $c_2 = 0.68$; $c_3 = -0.042$; $\alpha = 0.34$ dB $(°)^{-1}$; and $\beta = 0.055$ dB $(°)^{-1}$. Although these coefficients may not always represent their true values, a significant impact on K_{DP} estimates was not observed. It was also showed that this approach does not require i) calibrated measurements of Z and Z_{DR}, ii) bias corrections due to partial beam blockage effects given that biases are constants along a profile, iii) any parameterized relation between δ_{hv} and Z_{DR}, and iv) corrections for system phase-offset on $\Psi_{DP}(r)$. However, i) any undetected contamination on Z and Z_{DR} from hydrometeors other than rain and ii) effects from non-uniform beam filling can severely impact K_{DP} estimates. Fortunately, it is possible to identify localized areas where K_{DP} estimates are associated with high uncertainty using its normalized standard error (NSE [%]). The method from Reinoso-Rondinel et al. (2018) will be referred to as the adaptive high-resolution (AHR) approach.

5.2.2. ESTIMATION OF A AND A_{DP}

In the attenuation correction method introduced by Bringi et al. (1990), the relations $A(r) = \alpha K_{DP}(r)$ and $A_{DP}(r) = \beta K_{DP}(r)$ are used to estimate $A(r)$ and $A_{DP}(r)$ and thereby $\text{PIA}(r)$ and $\text{PIA}_{DP}(r)$, respectively, (i.e., it requires K_{DP} estimation). Although both linear relations are valid at most weather radar frequencies (Jameson, 1992), inaccurate esti-

mates of $K_{DP}(r)$, due to $\delta_{hv}(r)$, could impact estimates of $A(r)$ and $A_{DP}(r)$ (Gorgucci and Chandrasekar, 2005). In addition, assuming constant values for α and β may lead to limited approximations of PIA(r) and PIA$_{DP}(r)$ in storm events with a strong variability of DSD, drop shape, and temperature. However, such limitation depends on the radar frequency. According to Jameson (1992), the sensitivity of α to temperature variability and the sensitivity of β to temperature and DSD variabilities at X-band frequencies is less than at C- and S-band frequencies. This method of estimating $A(r)$ and $A_{DP}(r)$ or PIA(r) and PIA$_{DP}(r)$ is commonly referred to as the differential phase (DP) method.

Another technique for attenuation correction is the so-called ZPHI method introduced by Testud et al. (2000) that estimates $A(r)$ and $A_{DP}(r)$ at Δr scale. The estimation of $A(r)$ in a path interval $[r_p; r_q]$, where $r_q > r_p$, consists of two steps. In the first step, $A(r)$ is expressed in terms of $z(r)$, $z(r_q)$, and unknown $A(r_q)$ as

$$A(r) = A(r_q)\frac{10^{bz(r)/10}}{10^{bz(r_q)/10} + A(r_q)I(r, r_q)}, \text{ where} \tag{5.6}$$

$$I(r, r_q) = 0.46b\int_r^{r_q} 10^{bz(s)/10} ds. \tag{5.7}$$

The coefficient b parametrizes the power law relation $A = a10^{bZ/10}$ where a, not used in Eqs. (5.6) and (5.7), and b can be considered constants for a given frequency. For example, Testud et al. (2000) and Park et al. (2005a) suggested mean values for b at X-band frequencies equal to 0.764 and 0.780, respectively. In the second step, the empirical relation $\Delta\text{PIA} = \alpha\Delta\Phi_{DP}$, where $\Delta\text{PIA} = \text{PIA}(r_q) - \text{PIA}(r_p)$ and $\Delta\Phi_{DP} = \Phi_{DP}(r_q) - \Phi_{DP}(r_p)$, is used to estimate $A(r_q)$ as

$$A(r_q) = \frac{10^{bz(r_q)/10}}{I(r_p, r_q)}[10^{0.1b\alpha\Delta\Phi_{DP}} - 1]. \tag{5.8}$$

Although $[r_p; r_q]$ in the ZPHI method can be freely selected, $\Delta\Phi_{DP}$ could be noisy at short intervals and/or be contaminated by $\delta_{hv}(r)$ at ranges r_p and r_q. In addition, if $z(r)$ includes localized observations of hail or mixed rain in $[r_p; r_q]$, $A(r)$ might be biased over the entire path interval.

In the ZPHI method, $A_{DP}(r)$ is estimated in the same path interval using $A(r)$ and the intercept parameter of a modified Gamma distribution $N_0^*(r)$ [m^{-4}]; however, the estimation of $N_0^*(r)$ requires a well calibrated radar. If such requirement is not fulfilled, $N_0^*(r)$ is assumed to be constant in $[r_p; r_q]$. For example, at X-band frequencies, $A_{DP}(r)$ is estimated as $A_{DP}(r) = 0.124\ A^{1.22}(r)$.

In order to take into account the sensitivity of α and β to DSD, drop shape, and temperature variabilities, Bringi et al. (2001) extended the ZPHI method to search for optimal α and β values. This extended method was demonstrated at C-band frequencies and will be referred to as the CZPHI method. An initial value for α is selected from a predefined interval $[\alpha_{\min}; \alpha_{\max}]$ and $A(r)$ is estimated using Eq.(5.6). Resulted $A(r)$ is integrated over $[r_p; r_q]$ to built a differential phase profile denoted as $\Phi_{DP}(r, \alpha)$. Repeating this procedure for remaining values of α, the optimal α is the one that minimizes the error E [°]

given as

$$E = \sum_{i=p}^{q} |\Phi_{DP}(r_i, \alpha) - \Phi_{DP}(r_i)|; \text{ with } i = p, ...q, \tag{5.9}$$

where $\Phi_{DP}(r)$ is obtained after filtering $\Psi_{DP}(r)$. This means that the optimization process requires a proper way to filter spatial fluctuations such as noise and δ_{hv} from $\Psi_{DP}(r)$ while maintaining its spatial resolution. However, meeting such requirements is not straightforward and it depends on the approach employed to process $\Psi_{DP}(r)$, and therefore, the reliability of an "optimal" α to estimate $A(r)$ and PIA(r) depends on the performance of the chosen approach to estimate accurate $\Phi_{DP}(r)$.

For the estimation of β, Bringi et al. (2001) used the attenuation corrected $Z(r_q)$ to obtain the intrinsic Z_{DR} at range r_q, represented as $Z'_{DR}(r_q)$, based on an empirical relation between Z and Z_{DR}. Thus, β is estimated as

$$\beta = \frac{|z_{dr}(r_q) - Z'_{DR}(r_q)|}{\Delta\Phi_{DP}}, \tag{5.10}$$

if $z_{dr}(r_q) - Z'_{DR}(r_q)$ is less than 0 dB. When $Z_{DR}(r_q, \beta)$ (i.e., Z_{DR} after differential attenuation correction) differs from $Z'_{DR}(r_q)$ more than an allowed error, a predetermined set of β values is used to search for an optimal β that leads to the smallest difference $|Z_{DR}(r_q, \beta) - Z'_{DR}(r_q)|$. However, such technique of estimating β requires that measurements of Z and Z_{DR} are corrected for miscalibration, partial beam blockage effects, and other sources of uncertainties.

In the following sections, $A(r)$ will be estimated by the DP, ZPHI, and CZPHI methods for comparison purposes while $A_{DP}(r)$ will be given by the DP method as $A_{DP}(r) = \gamma A(r)$, where $\gamma = \beta/\alpha$, because γ is less sensitive to DSD variability (i.e., rain type) at X-band frequencies than at C- and S-band frequencies (Ryzhkov et al., 2014). Using the constant values for β and α given in section 5.2.1, γ is estimated and is equal to 0.1618. Similar values at X-band frequencies were found in literature review; for example, Snyder et al. (2010) suggested a value for γ equal to 0.1543 while Ryzhkov et al. (2014) estimated γ equal to 0.14 for tropical rain (i.e., low Z_{DR} and high K_{DP}) and 0.19 for continental rain (i.e., high Z_{DR} and low K_{DP}).

5.3. EVALUATION OF K_{DP} PROCESSING BY THE ZPHI METHOD

5.3.1. RADAR DESCRIPTION AND PREPROCESSING

The polarimetric X-band weather radar IDRA[1] is a frequency modulated continuous wave system whose operational range and range resolution Δr are equal to 15.3 km and 0.03 km, respectively, (Figueras i Ventura, 2009). IDRA is located at the Cabauw Experimental Site for Atmospheric Research (CESAR) observatory in the Netherlands (NL) at a height of 213 m from ground level (Leijnse et al., 2010). It scans at a fixed elevation of 0.50° and rotates the antenna over 360° in 1 min. Clutter echoes are removed from collected data by a filter based on spectral polarimetric processing (Unal, 2009). In addition, areas that include particles other than rain and/or areas with low signal-to-noise

[1] IDRA stands for IRCTR Drizzle RAdar and IRCTR stood for International Research Center for Telecommunications and Radar

ratio (SNR) are removed off-line based on L_{DR} measurements such that range gates with L_{DR} larger than -18 dB are discarded from Ψ_{DP}, z, and z_{dr} fields.

Further off-line preprocessing includes suppressing isolated segments of a Ψ_{DP} profile smaller than 0.25 km and rejecting a Ψ_{DP} profile if the percentage of gates with measurements is less than 5%. Because a Ψ_{DP} profile could be noisy at ranges far from the radar and/or behind strong reflectivity echoes associated with low SNR and fully attenuated signals, its range extent needs to be determined. The ending range of a Ψ_{DP} profile is determined based on $\overline{\sigma}_P$ which represents the average of multiple σ_P samples by running a 5-gates window along the Ψ_{DP} profile. If $\overline{\sigma}_P$ is less than 1.5°, the ending range is given by the last measured gate in the downrange direction. Otherwise, the ending range is set by the middle gate of the second consecutive window whose σ_P values are less than $\overline{\sigma}_P$, starting at the last measured gate and moving towards the radar. The ending range is used to limit the corresponding extent of z and z_{dr} profiles. After this, $\overline{\sigma}_P$ is calculated again to estimate K_{DP} by the conventional technique.

5.3.2. COMPARISON BETWEEN K_{DP} AND A

Estimates of K_{DP} by the conventional and AHR techniques, hereafter denoted as K_{DP}(C) and K_{DP}(AHR), are compared using the empirical relation $A(r) = \alpha K_{DP}(r)$ where α is 0.34 dB $(°)^{-1}$ and $A(r)$ is estimated by the ZPHI method, hereafter represented as A(ZPHI). In this scheme, A(ZPHI) is used as a reference to evaluate both techniques.

In the conventional method, a low-pass filter is designed using a finite impulse response (FIR) filter such that the order of the filer is 36 along with a Hann window and r_c is 1 km while the required threshold τ is $1.5\overline{\sigma}_P$. Such filter design is found suitable for Δr of 0.03 km. On the other hand, the AHR approach requires an interval $[L_{\min}; L_{\max}]$ that is associated with low values of theoretical σ_K. Reinoso-Rondinel et al. (2018) suggested that for $\Delta r = 0.03$ km, values of L in the order of 3 km are associated with theoretical values of $\sigma_K < 0.5\,° \text{km}^{-1}$, assuming theoretical μ_s and σ_P values equal to 3 and 3°, respectively. Therefore, the length interval [2;5] km is selected, which is the same for all radial profiles. The AHR approach also requires an estimate of $\sigma_{Z_{DR}}$, profile by profile, to establish the $\Delta\Psi_{DP}$ filter condition. $\sigma_{Z_{DR}}$ is estimated by running a 5-gates window along a Z_{DR} profile. Z and Z_{DR} profiles are corrected for attenuation and differential attenuation according to section 5.2.1, where a linear regression fit of 1 km is applied to Ψ_{DP} profiles.

For the calculation of A(ZPHI), Φ_{DP} is estimated by filtering Ψ_{DP} using the conventional approach instead of the AHR approach in order to evaluate K_{DP}(AHR) in an independent manner. The path interval $[r_p; r_q]$ is defined by the first and last data, in the downrange direction, of the estimated Φ_{DP} profile in order to avoid range segmentation as suggested by Ryzhkov et al. (2014). The constant b is set to 0.780 as advised by Park et al. (2005a). In case that $\Delta\Phi_{DP} < 0°$ as a result of a reduced SNR profile, the estimation of A(ZPHI) is avoided.

In order to analysis the methods described in section 5.2, three more storm events observed by IDRA will be used. These events are described in Table 5.1. Results from the storm event on 18 June 2011 (event E5) at 12:16 UTC is shown in Fig. 5.1. The Ψ_{DP} field shows a rapid increment in range on the north-side of the storm whereas Ψ_{DP} rarely increases on the south-side. The attenuated z field represents a relatively small cell

Table 5.1: Description of three more storm events observed by IDRA with coverage of 15.3 km and Δr = 0.03 km.

Event	Date	Period (UTC)	Storm Type
E5	18 Jun 2011	12:00 - 12:30	Single cell, 40 km^2 area and range extent up to 5 km moderate rain.
E6	25 Aug 2011	14:45 - 14:55	Mini-supercell with an echo-appendage and Z_{DR}-arc, 80 km^2 area and range extent up to 10 km, moderate rain.
E7	10 Sep 2011	19:30 - 20:15	Tornadic cell with a leading bow apex, 500 km^2 area and range extent up to 30 km, heavy rain.

of a non-uniform structure in close proximity to the radar. The 30 dBZ contour is obtained from the attenuation corrected Z using the ZPHI method (i.e., after calculating A(ZPHI) as previously explained). The conventional method shows a smoothed K_{DP}(C) field whereas the AHR approach shows a K_{DP}(AHR) field that maintains the spatial variability of the storm down to range resolution scale. Note that K_{DP}(AHR) eliminates areas of K_{DP} smaller than $-1\,^\circ\,\mathrm{km}^{-1}$ which are present in K_{DP}(C). However, the coverage of the K_{DP}(C) field is larger than that of K_{DP}(AHR). This is because in the AHR approach, it is not always possible to obtain $M > 0$ (i.e., multiple paths that satisfy the $\Delta\Psi_{DP}$ filter condition) to proceed with the estimation of K_{DP}(AHR). Note that isolated K_{DP} segments smaller than 2 km were removed from K_{DP}(C) and K_{DP}(AHR) fields in order to avoid estimates of K_{DP} that could be associated with noisy areas and/or low accuracy.

A(ZPHI) estimates for the same event E5 are used to compare the relations K_{DP}(C)-A(ZPHI) and K_{DP}(AHR)-A(ZPHI) as shown in Fig. 5.2. In panel a), it can be seen that the K_{DP}(AHR)-A(ZPHI) scatterplot (14 783 data points) is more consistent than that of K_{DP}(C)-A(ZPHI) (15 490 data points) with respect to the empirical relation $A(r) = 0.34K_{DP}(r)$. In a quantified comparison, the correlation coefficients ρ_{KA} between K_{DP}(C) and A(ZPHI) is equal to 0.65 whereas for K_{DP}(AHR) and A(ZPHI) is of 0.96. Their corresponding standard deviations σ_{KA} with respect to the empirical relation are 1.20 and $0.41\,^\circ\,\mathrm{km}^{-1}$, respectively. In order to compare the impact of both K_{DP} techniques on attenuation correction, Z measurements are corrected for attenuation using the DP and ZPHI correction methods. The attenuation corrected Z from the DP method using K_{DP}(C) and K_{DP}(AHR) is denoted as Z(DP,C) and Z(DP,AHR), respectively, whereas resulted Z from the ZPHI method is indicated by Z(ZPHI). The scatterplots Z(DP,C)-Z(ZPHI) and Z(DP,AHR)-Z(ZPHI) are shown in panel b) such that Z(ZPHI) estimates are used as a reference for comparison purposes. It is observed that for relatively high values of Z(ZPHI), estimated Z(DP,C) values are slightly over-corrected, which agrees with Gorgucci and Chandrasekar (2005) and Snyder et al. (2010). In contrast, estimated Z(DP,AHR) values are found significantly consistent with Z(ZPHI) results. In term of bias, the mean biases resulting from the relations Z(DP,C)-Z(ZPHI) and Z(DP,AHR)-Z(ZPHI) are equal to 0.95 and -0.21 dB, respectively, for Z(ZPHI) $\geq$ 35 dBZ. The errors quantified by ρ_{KA}, σ_{KA}, and bias Z, are summarized in Table (5.2).

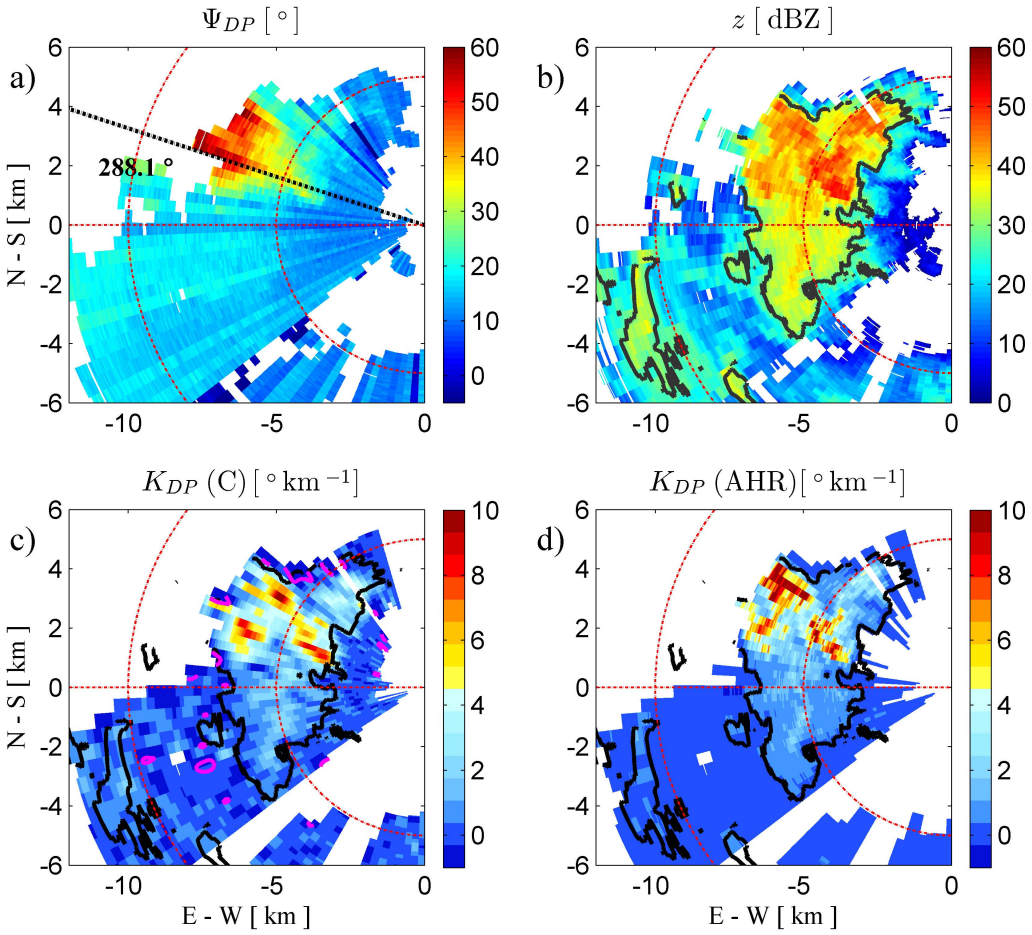

Figure 5.1: Observations by IDRA radar at elevation angle of 0.5° in the NL on 12:16 UTC 18 June 2011, event E5. Fields of a) differential phase Ψ_{DP}, b) attenuated reflectivity z, c) K_{DP}(C) from the conventional approach, and d) K_{DP}(AHR) from the AHR approach. Note that the Ψ_{DP} field is not adjusted for phase-offset. In panels b)-d), attenuation-corrected 30 dBZ levels are indicated by black contour lines and in panels c)-d), $-1\,^{\circ}\,\mathrm{km}^{-1}$ levels are indicated by magenta contour lines. The red rings are at 5 km increments.

From the analysis of Fig. 5.2, the following can be highlighted. The K_{DP}(AHR)-A(ZPHI) scatterplot agreed with the empirical relation $A(r) = \alpha K_{DP}(r)$. In addition, the DP and ZPHI correction methods provided equivalent Z(DP,AHR) and Z(ZPHI) values after attenuation correction. This is because the AHR approach is able to estimate K_{DP} at Δr scale while avoiding significant contamination from δ_{hv}. In the contrary, the conventional K_{DP} approach showed a low agreement between $K_{DP}(r)$ and $A(r)$ and although it barely included substantial errors on attenuation corrected Z(DP,C) it can significantly impact estimates of $A(r)$ performed by the DP method (Gorgucci and Chandrasekar, 2005).

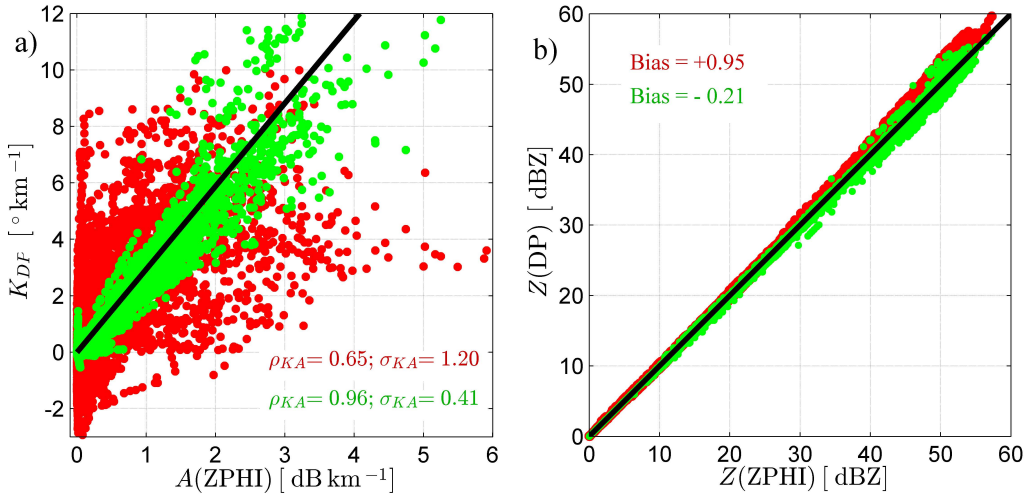

Figure 5.2: a) The K_{DP}(C)-A(ZPHI) scatterplot resulted from event E5 at 12:16 UTC is indicated by red dots and K_{DP}(AHR)-A(ZPHI) scatterplot indicated by green dots. In addition, the empirical relation $K_{DP} = (1/\alpha)A$ is indicated by the black line where $\alpha = 0.34$ dB $(°)^{-1}$. b) As in a) but for Z(DP,C)-Z(ZPHI) and Z(DP,AHR)-Z(ZPHI) scatterplots. Also, the relation Z(DP) = Z(ZPHI) is indicated by the black line. The biases are computed for Z(ZPHI) ≥ 35 dBZ.

5.4. IMPACT OF K_{DP} PROCESSING ON THE CZPHI METHOD

In this section, the ability to estimate Φ_{DP} from Ψ_{DP} profiles by both K_{DP} approaches is studied and their impact on the performance of finding an optimal value for $\alpha \in [\alpha_{\min}; \alpha_{\max}]$ by the attenuation correction CZPHI method is quantified. In order to estimate A(CZPHI,C) and A(CZPHI,AHR), Eq. (5.9) requires Φ_{DP}(C) and Φ_{DP}(AHR) profiles which are obtained by integrating K_{DP}(C) and K_{DP}(AHR), respectively, in their corresponding path intervals $[r_p; r_q]$. In order to represent the variability of α at X-band frequencies, the required α interval is predefined as [0.1; 0.6] dB $(°)^{-1}$ with steps of 0.02 dB $(°)^{-1}$ (Park et al., 2005b; Ryzhkov et al., 2014).

For a correct optimization process, it is recommended that $r_q - r_p$ should be at least 3 km and $\Delta\Phi_{DP}$ larger than 10°. In addition, if the Φ_{DP}(C) profile is used, the percentage of gates with $K_{DP} > 0\,°\,\text{km}^{-1}$ should be at least 50%; whereas in case Φ_{DP}(AHR) is used, the percentage of gates with $K_{DP} > 0.5\,°\,\text{km}^{-1}$ and normalized standard error NSE < 20% should be larger than 80%. The percentage threshold for Φ_{DP}(C) is less than for Φ_{DP}(AHR) because the conventional method rarely avoids negative K_{DP} values. A NSE profile, which is related to K_{DP}(AHR), is obtained gate-by-gate as the ratio between σ_K and K_{DP}, both estimated from the M-K_{DP} samples given in Eq. (5.4). Once these conditions are met, α is selected by minimizing E in Eq. (5.9) but considering only range gates that satisfy the stated conditions. In this way, an optimal value for α is selected, otherwise the constant value for α equal to 0.34 dB $(°)^{-1}$ is selected.

Results involved in the optimization process along azimuth 288.1° for storm event E5 at 12:16 UTC are shown in Fig. 5.3 panels a)-c). In panel a), it is seen that the minimum error E when Φ_{DP}(C) is used is much larger than when Φ_{DP}(AHR) is used while

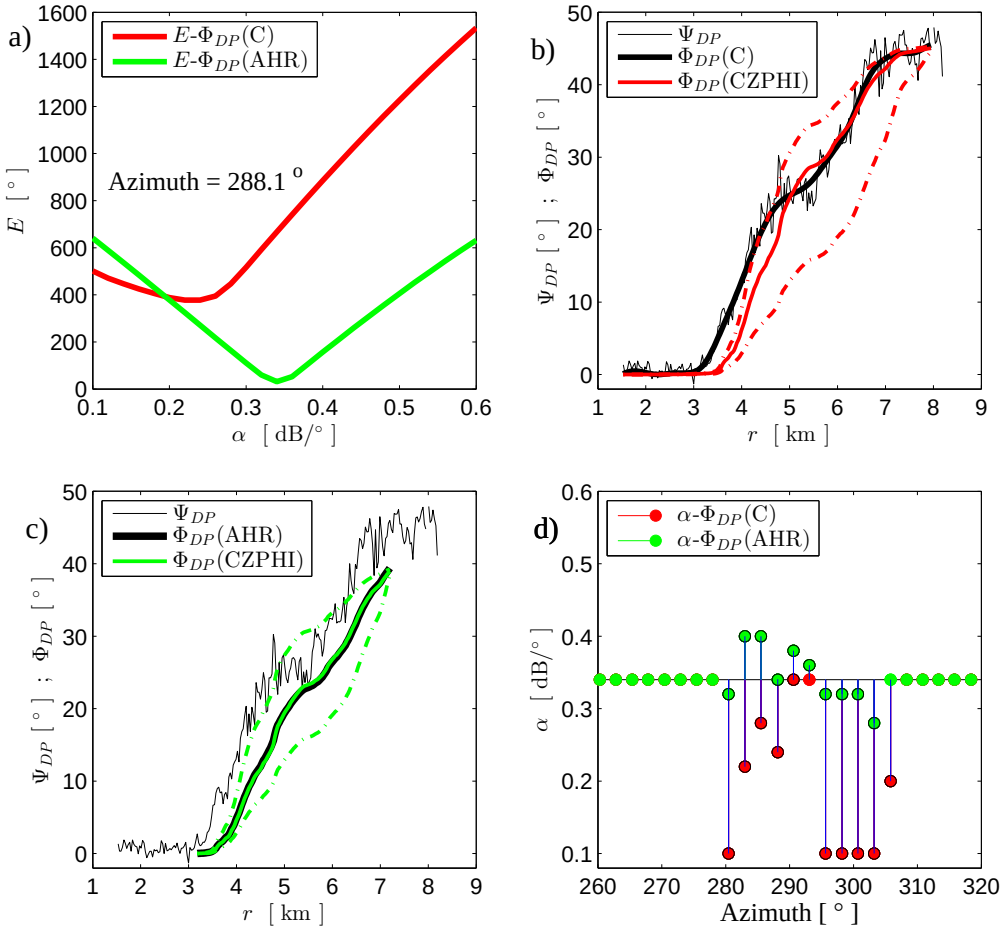

Figure 5.3: a) Errors obtained from Eq. (5.9) using Φ_{DP}(C) and Φ_{DP}(AHR) in the azimuth 288.1°, are indicated by the red and green lines, respectively, as a function of $\alpha \in [\alpha_{\min};\alpha_{\max}]$. b) Profiles of Ψ_{DP}, Φ_{DP}(C), and Φ_{DP}(CZPHI) are shown as a function of range. In addition, upper and lower Φ_{DP}(CZPHI) bounds corresponding to $\alpha_{\min}$ and $\alpha_{\max}$, respectively, are shown by dashed lines. c) As in b) but using Φ_{DP}(AHR) rather than Φ_{DP}(C). d) Selected αs using Φ_{DP}(C) and Φ_{DP}(AHR) are shown by the stemplots in red and green, respectively, as a function of azimuth.

their corresponding optimal values for α are equal to 0.24 and 0.34 dB $(°)^{-1}$. The reason why the two α values are different can be explained by observing the measured Ψ_{DP} and the smoothed Φ_{DP}(C) and Φ_{DP}(AHR) profiles shown in panels b) and c), respectively. First, note that Ψ_{DP} might include i) a δ_{hv} "bump" in the range [3.5;5.5] km and ii) small bumps or oscillations in the range [6.5;8.5] km. Second, the Φ_{DP}(C) profile shows a smoothed version of Ψ_{DP} but the δ_{hv} bump is still present. In consequence, Φ_{DP}(CZPHI), which is estimated by integrating A(CZPHI,C) in range, is not able to match the entire Φ_{DP}(C) profile. In the contrary, in panel c), Φ_{DP}(AHR) seems to mitigate the

δ_{hv} bump on Ψ_{DP} and therefore a good match between the Φ_{DP}(AHR) profile and the corresponding Φ_{DP}(CZPHI) is obtained. Note that the extent of the Φ_{DP}(AHR) profile is less than that of Φ_{DP}(C) because in the AHR approach values of M equal to 0 are possible at the beginning and ending ranges of a Ψ_{DP} profile. Similar discussion was given in section 5.3.2 when the fields of K_{DP}(C) and K_{DP}(AHR) were compared. However, this limited extent of Φ_{DP}(AHR) avoids the oscillations seen at the ending range of Ψ_{DP}.

The selected values for α related to Φ_{DP}(C) and Φ_{DP}(AHR) as a function of azimuth of the same storm are depicted in panel d). Selected values for α that are related to a minimum E (i.e., optimal α values) are encircled by black edges, while those that are non-related to a minimum E are represented without edges. Note that optimal α values associated with Φ_{DP}(AHR) are close to 0.34 dB $(°)^{-1}$ whereas those related to Φ_{DP}(C) are mostly smaller than 0.34 dB $(°)^{-1}$ and sometime equal to $\alpha_{\min}$. An optimal α that equals $\alpha_{\min}$ or $\alpha_{\max}$ could be associated with an inadequate matching between $\Phi_{DP}(r)$ and $\Phi_{DP}(r,\alpha)$ in Eq. 5.9, which can lead to incorrect values of α. The azimuthal sector of [280;310]° covers approximately the north-side of the storm showed in Fig. 5.1. Outside this sector, the constant α was selected, associated either with Φ_{DP}(C) or Φ_{DP}(AHR), because the stated conditions were not met.

For further analyses, the minimum E obtained from Eq. (5.9) is expressed as $E = \sum e_i$; with $i = p,...,q$, such that e_i represents the minimum error at range r_i. As such, the arithmetic mean values $\bar{e}_{\min}$ of those minimum errors for the same azimuthal sector associated with Φ_{DP}(C) and Φ_{DP}(AHR) profiles, are equal to 2.16 and 0.20° and their standard deviations $\sigma_{e_{\min}}$ are 0.75 and 0.08°, respectively. Then, the arithmetic mean of e_i can be used as an indicator that quantifies the impact of both K_{DP} approaches on the performance of the CZPHI method.

In order to analyze the impact of the optimal selection of α on the estimation of A(CZPHI) for event E5, K_{DP}(AHR) is used as a reference due to 1) the consistency between K_{DP}(AHR) and A(ZPHI) demonstrated in section 5.3.2 and 2) the fact that data were collected from one radar. Hence, the following assessment is based only on internal polarimetry consistency. The scattersplots A(CZPHI,C)-K_{DP}(AHR) and A(CZPHI,AHR)-K_{DP}(AHR) are represented in Fig. 5.4 panel a). Observe that multiple A(CZPHI,C) estimates are smaller than those from A(CZPHI,AHR) as a consequence of selecting "small optimal" values for α. The correlation coefficient ρ_{AK} from A(CZPHI,C)-K_{DP}(AHR) (14 783 data points) is equal to 0.78 while from A(CZPHI,AHR)-K_{DP}(AHR) (13 614 data points) is 0.98. Their corresponding standard deviations σ_{AK} with respect to $A = \alpha K_{DP}$(AHR) are 0.28 and 0.05 dB km^{-1}, respectively, where α values are associated with Φ_{DP}(AHR). In panel b), attenuation corrected Z(CZPHI,C) and Z(CZPHI,AHR) are compared against Z(DP,AHR), where Z(DP,AHR) values were estimated using values for α associated with Φ_{DP}(AHR). Their root-mean-square errors RMSE are equal to 1.67 and 0.10 dB, respectively, for Z(DP,AHR) ≥ 35 dBZ. This means that the attenuation correction CZPHI method can lead to lower performance than the ZPHI method, comparing Fig. 5.4b with Fig. 5.2b. In this analysis, the RMSE was used instead of the mean bias to take into account the standard deviation of Z(CZPHI) estimates associated with the variability of α. The quantified errors used to evaluate the CZPHI method are summarized in Table (5.3).

For an objective analysis, a similar evaluation of the CZPHI method is presented but setting K_{DP}(C) as a reference instead of K_{DP}(AHR). For such purpose, the scatterplots

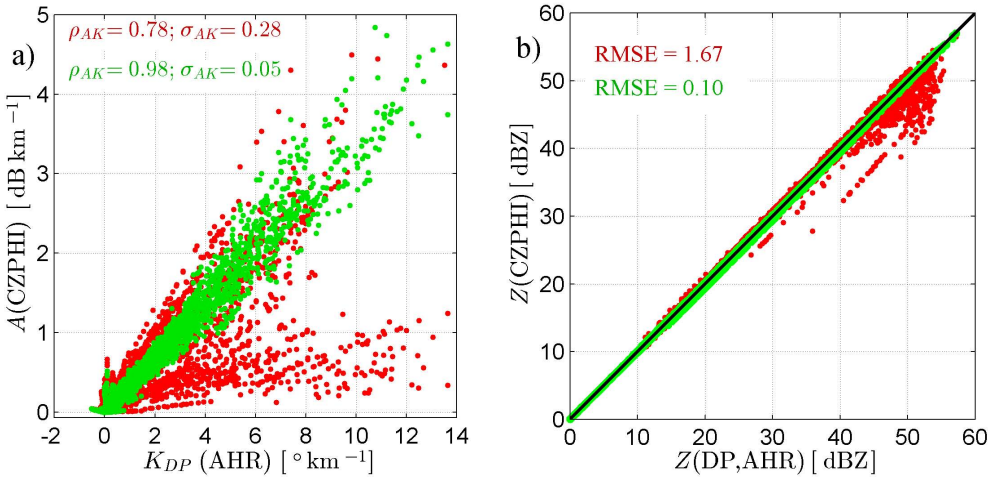

Figure 5.4: a) The A(CZPHI,C)-K_{DP}(AHR) and A(CZPHI,AHR)-K_{DP}(AHR) scatterplots resulted from event E5 at 12:16 UTC are represented by the red and green dots, respectively. b) As in a) but for Z(CZPHI,C)-Z(DP,AHR) and Z(CZPHI,AHR)-Z(DP,AHR) scatterplots. In addition, the relation Z(CZPHI) = Z(DP) is indicated by the black line.

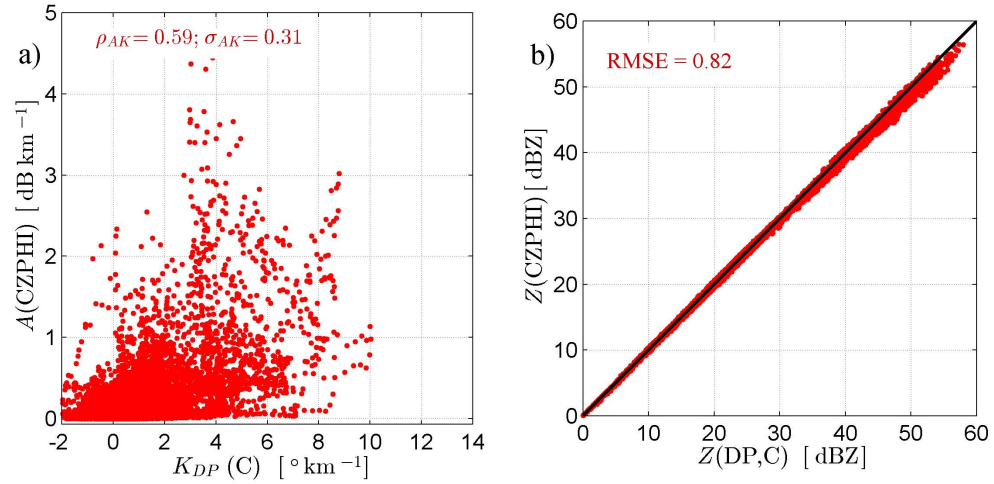

Figure 5.5: As in Fig. 5.4 but only for results associated with K_{DP}(C).

A(CZPHI,C)-K_{DP}(C) and Z(CZPHI,C)-Z(DP,C) are shown in Fig. 5.5. Note that the correlation coefficient between A(CZPHI,C) and K_{DP}(C) in panel a) is equal to 0.59, which is smaller than the one seen in Fig.5.4a). This is because of the limited accuracy associated with K_{DP}(C). In addition, the A(CZPHI,C)-K_{DP}(C) scatterplot is similar to the K_{DP}(C)-A(ZPHI) scatterplot, shown in Fig. 5.2a), but with a smaller correlation coefficient. This is due to the fact that A(CZPHI,C) is associated with a variable α. In Fig. 5.5b), the scatterplot Z(CZPHI,C)-Z(DP,C) has a RMSE equal to 0.82, which is smaller than that of

Z(CZPHI,C)-Z(DP,AHR), as indicated in Fig.5.4b). This is because of the DP and CZPHI methods use the same selected values for α, associated with K_{DP}(C), leading to consistent attenuation correction results. Nonetheless, the RMSE of Z(CZPHI,C) is still larger than the of Z(CZPHI,AHR) even if Z(DP,C) is set as a reference.

Attenuated z and z_{dr} measurements and attenuation corrected Z(CZPHI,AHR) and Z_{DR} fields from event E5 are displayed in Fig. 5.6. It is seen that the Z(CZPHI,AHR) field restored attenuated z areas mostly in the north-side of the storm cell, which is associated with high values of K_{DP}(AHR) (see Fig. 5.1). PIA was estimated by integrating A(CZPHI,AHR), reaching values up to 14 dB. For the estimation of $Z_{DR}(r)$, PIA$_{DP}(r)$ was given by 0.1618PIA(r), according to section 5.2.2. By comparing z_{dr} and Z_{DR}, areas of big drops are most likely placed in the north-side of the storm cell. From the Z_{DR} field, it seems that its lower bound is between -2 and -1 dB which could be due to radar miscalibration rather than prolate-shaped particles. In addition, the Z_{DR} field might be associated with an azimuthal dependence bias. The reader is referred to section 3.4 for a discussion about error sources that can affect IDRA measurements.

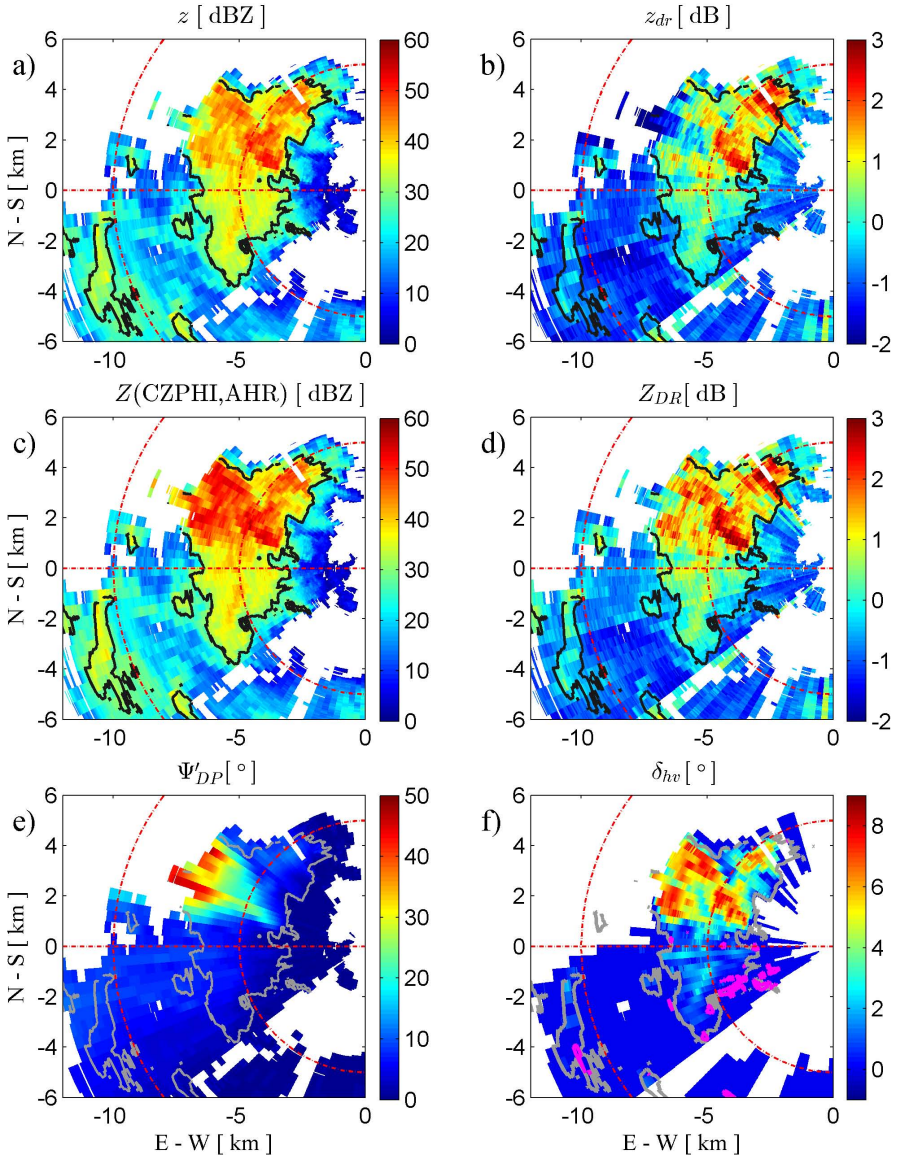

Figure 5.6: Fields of z and z_{dr} from event E5 at 12:16 UTC are given in panels a) and b), respectively. The contour lines represent 30 dBZ levels. Fields of Z(CZPHI,AHR) and Z_{DR} are shown by panels c) and d), respectively, while smoothed Ψ'_{DP} and δ_{hv} fields are indicated in panels e) and f), respectively. In panel f), magenta contour lines represent 0° levels of δ_{hv}.

5.5. ESTIMATION TECHNIQUE FOR δ_{hv}

Rather than estimating δ_{hv} in rain as $\delta_{hv} = \Psi_{DP} - \Phi_{DP}$ (Hubbert and Bringi, 1995; Otto and Russchenberg, 2011; Trömel et al., 2013), a new approach is presented. The flowchart

of the proposed method is shown in Fig. 5.7. Three inputs are required for this approach: the preprocessed Ψ_{DP} field (section 5.3.1) and corresponding K_{DP}(AHR) and A(CZPHI,AHR) fields. Given these inputs, the corresponding δ_{hv} field is based on 6 steps:

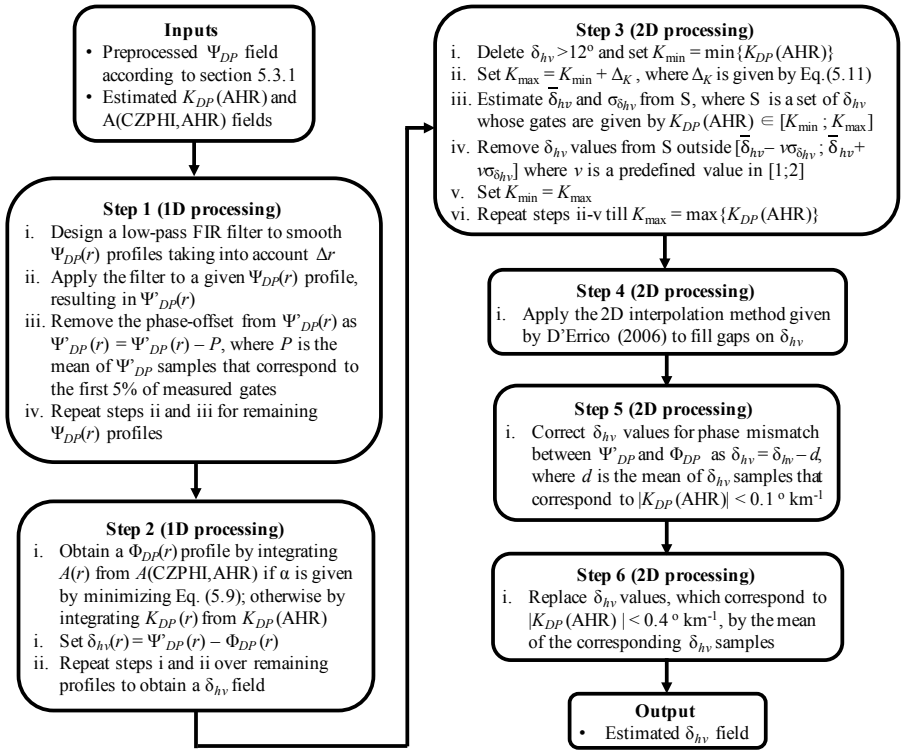

Figure 5.7: A flowchart for the estimation of δ_{hv}. The flowchart consists of 6 main steps. Steps 1-2 are processed in 1D (i.e., along a PPI radial) while steps 3-6 are processed in 2D (i.e., a complete PPI).

1. Design a filter to smooth strong outliers from a $\Psi_{DP}(r)$ profile, taking Δr into account. In this work, a low-pass FIR filter is designed with a filter order equal to 32 and r_c equal to 1 km. The smoothed Ψ_{DP} field is denoted hereafter as Ψ'_{DP}. If needed, correct each $\Psi'_{DP}(r)$ profile for system phase-offset by subtracting the mean of $\Psi'_{DP}(r)$ over the first 5% of measured gates.

2. Obtain the Φ_{DP} field by integrating A(CZPHI,AHR) profiles in range associated with a minimum error E; otherwise, by integrating K_{DP}(AHR) profiles. Next, subtract the reconstructed Φ_{DP} field from Ψ'_{DP} as a first attempt to estimate the corresponding δ_{hv} field. The next steps are related to a 2D processing.

3. Remove unusual δ_{hv} values larger than 12° from the δ_{hv} field. According to Testud et al. (2000); Trömel et al. (2013) and Schneebeli et al. (2014) simulated δ_{hv}

values at X-band frequencies rarely reach 12°. To further reduce δ_{hv} outliers, reject δ_{hv} estimates outside the interval $[\overline{\delta}_{hv} - v\sigma_{\delta_{hv}}; \overline{\delta}_{hv} + v\sigma_{\delta_{hv}}]$ [°] where $\overline{\delta}_{hv}$ and $\sigma_{\delta_{hv}}$ indicate the arithmetic mean and standard deviation of selected δ_{hv} gates, respectively, and v is a predefined threshold in the interval [1;2]. A value of 1.5 for v is chosen while the values for $\overline{\delta}_{hv}$ and $\sigma_{\delta_{hv}}$ are obtained by selecting multiple gates that correspond to similar values of K_{DP}(AHR), assuming that similar values of K_{DP} are collocated with similar values of δ_{hv}. Thus, a narrow K_{DP} interval $[K_{\min}; K_{\max}]$ [° km^{-1}] is required, where $K_{\max} - K_{\min} = \Delta_K$ and $K_{\min}$ is initiated as the minimum of K_{DP}(AHR). This process is iterated by shifting $[K_{\min}; K_{\max}]$ towards high values in small steps such that $K_{\min} = K_{\max}$ and $K_{\max} = K_{\min} + \Delta_K$ until $K_{\max}$ is equal to the maximum of K_{DP}(AHR). The values for Δ_K are given as follows

$$\Delta_K = \begin{cases} 0.2 & K_{\min} \leq 2.5\,^\circ\,\mathrm{km}^{-1}, \\ 0.5 & 2.5 < K_{\min} < 8\,^\circ\,\mathrm{km}^{-1}, \\ 1.0 & K_{\min} \geq 8\,^\circ\,\mathrm{km}^{-1}; \end{cases} \tag{5.11}$$

in order to obtain sufficient samples of δ_{hv} since high estimates of K_{DP} are less frequent than small estimates (e.g. see the K_{DP} fields in Fig. 5.1 and those in Figs. 5.9 and 5.12, which will be presented in the next section). Although the values for Δ_K can be optimized according to the distribution of K_{DP}(AHR), for demonstration purposes they are considered constants.

4. Apply a 2D interpolation method in order to fill empty gaps on δ_{hv} field caused by step 3. For this task, the inpainting (or image fill-in) algorithm (Bertalmio et al., 2003; Criminisi et al., 2004; Elad et al., 2005) is selected because it is one of the image processing algorithms commonly used to smoothly interpolate 2D and 3D images. The essential idea is to formulate a partial differential equation (PDE) for the "hole" (interior unknowns) and use the perimeter of the hole to obtain boundary values. The solution for the interior unknowns involves the discretization of PDEs on the unknowns points into a system of linear equations. D'Errico (2006) implemented an inpainting code for 2D arrays which is freely available and used for this step.

5. Correct the δ_{hv} field for possible mismatch between Ψ'_{DP} and Φ_{DP} at beginning ranges due to noise and/or oscillations, by subtracting the mean of δ_{hv} estimates that are associated with $|K_{DP}(\mathrm{AHR})| < 0.1\,^\circ\,\mathrm{km}^{-1}$ from the δ_{hv} field.

6. (Optional) To better distinguish storm cells from their background (i.e., for radar displaying purposes), it is recommended to replace δ_{hv} estimates that are collocated with $|K_{DP}(\mathrm{AHR})| < 0.4\,^\circ\,\mathrm{km}^{-1}$ by the mean of these δ_{hv} estimates. The value of $0.4\,^\circ\,\mathrm{km}^{-1}$ is found to match the 30 dBZ level used in this work for storm cell identification.

The corrected Ψ'_{DP} field for phase-offset and the estimated δ_{hv} field resulting from storm event E5 at 12:16 UTC are shown in Fig. 5.6. As expected, the δ_{hv} field depicts a structure that is correlated, by definition, with the Z_{DR} field. Areas of $\delta_{hv} < 0°$ can be associated with oscillations on Ψ'_{DP} profiles or a decreasing behavior of Ψ'_{DP} with range.

The total number of gates with interpolated δ_{hv} is equivalent to 15.67% (step 4). The mean of δ_{hv} values in which $|K_{DP}(\text{AHR})| < 0.1\,^\circ\,\text{km}^{-1}$ is equal to 0.66° (step 5). Moreover, δ_{hv} estimates collocated with $|K_{DP}(\text{AHR})| < 0.4\,^\circ\,\text{km}^{-1}$ were replaced by 0.07° (step 6).

An empirical relation in rain between δ_{hv} and K_{DP} at 9.41 GHz was demonstrated by Schneebeli et al. (2014) and is used for validation purposes. In their work, range profiles of stochastically simulated DSDs were obtained such that their DSD properties, in terms of spatial and temporal structures (i.e., small-scale variability), match the properties of DSDs measured by a network of ground-based disdrometers. Profiles of δ_{hv} and K_{DP} were generated, gate-by-gate, according to these simulated DSDs and scattering amplitudes given by T-matrix calculations. Three different but commonly used models for drop shape were considered while equivolumetric spherical drop diameters were limited to [0.1;7.0] mm. In addition, three temperatures of 27, 17 and 7 °C were included. From their simulated δ_{hv}-K_{DP} scatterplot (not shown here), two empirical linear fits were given as

$$\mathfrak{L}_1: \quad \delta_{hv} = 2.37 K_{DP} + 0.054 \qquad 0 \le K_{DP} \le 2.5\,^\circ\,\text{km}^{-1}, \tag{5.12}$$

$$\mathfrak{L}_2: \quad \delta_{hv} = 0.14 K_{DP} + 5.5 \qquad 2.5 < K_{DP} \le 15\,^\circ\,\text{km}^{-1}. \tag{5.13}$$

For storm event E5, the δ_{hv}-K_{DP}(AHR) scatterplot, excluding step 6, is represented in Fig. 5.8 where 14 783 range resolution volumes were included. In addition, the $\overline{\delta}_{hv}$

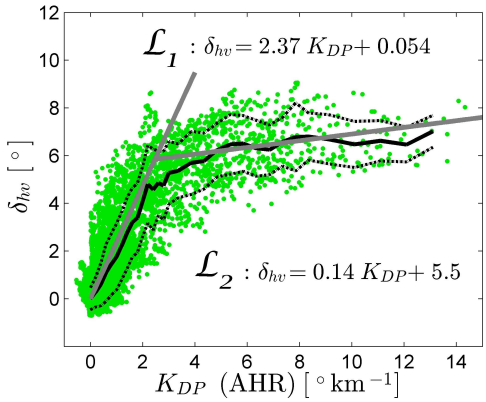

Figure 5.8: δ_{hv}-K_{DP}(AHR) scatterplot from event E5 at 12:16 UTC. The continuous black line represents $\overline{\delta}_{hv}$ (i.e, mean values of δ_{hv} estimates) as a function K_{DP}(AHR) while the dashed lines represent $\overline{\delta}_{hv} \pm \sigma_{\delta_{hv}}$. The gray lines indicate two linear relations $\mathfrak{L}_1$ and $\mathfrak{L}_2$ derived from scattering simulations. Step 6 is excluded for scatterplot analysis.

and $\overline{\delta}_{hv} \pm \sigma_{\delta_{hv}}$ curves as a function of K_{DP}(AHR) are also shown. Both statistical curves were obtained from δ_{hv} estimates similar to step 3. The strong agreement between the $\overline{\delta}_{hv}$ curve and linear fits $\mathfrak{L}_1$ and $\mathfrak{L}_2$ shows an indirect validation of the presented method to estimate 2D δ_{hv} in rain. In addition, the spread of estimated δ_{hv}-K_{DP}(AHR) is found comparable to the spread of simulated δ_{hv}-K_{DP} scatterplot. The mean of $\sigma_{\delta_{hv}}$ values is equal to 1.20°. Because the Z_{DR} field may suffer from miscalibration and partial beam blockage effects (see Fig. 5.6 panels b) and d)), Z_{DR} values would not be suitable to cross-check δ_{hv} estimates. Otto and Russchenberg (2011) and Trömel et al. (2013) suggested

that δ_{hv} estimates can be used to identify dominant drop sizes and correct Z_{DR} measurements affected by issues related to miscalibration and partial beam blockage such as those presented in event E5. Although such applications from δ_{hv} are encouraging, it is outside the scope of this paper.

Table 5.2: Comparison results between K_{DP}(C) estimates from the conventional approach and K_{DP}(AHR) from the AHR technique using as a reference values of A(ZPHI) resulted from the ZPHI method for three storm events.

	ρ_{KA} [-]		σ_{KA} [° km^{-1}]		Bias Z [dB]	
Events	Conv	AHR	Conv	AHR	Conv	AHR
E5	0.65	0.96	1.20	0.41	0.95	−0.21
E6	0.48	0.95	1.75	0.52	1.05	−0.56
E7	0.76	0.97	1.74	0.54	0.90	−0.57

Table 5.3: Comparison results between A(CZPHI,C) and A(CZPHI,AHR) using K_{DP}(AHR) as a reference for three storm events.

	$\bar{e}_{\min}$[°]		$\sigma_{e_{\min}}$ [°]		ρ_{AK} [-]		σ_{AK} [dB km^{-1}]		RMSE Z [dB]	
Events	Conv	AHR	Conv	AHR	Conv	AHR	Conv	AHR	Conv	AHR
E5	2.16	0.20	0.75	0.08	0.78	0.98	0.28	0.05	1.67	0.10
E6	2.28	0.27	0.79	0.25	0.91	0.97	0.29	0.11	1.87	0.32
E7	1.72	0.45	0.50	0.17	0.94	0.98	0.28	0.12	1.60	0.34

5.6. RESULTS ON TWO MORE STORM EVENTS

5.6.1. MINI-SUPERCELL STORM

A non-tornadic mini-supercell storm was observed by the IDRA radar on 25 August 2011 during 14:45 - 14:55 UTC (storm event E6). At 14:45 UTC, in-situ measurements at the CESAR observatory registered an environmental temperature and relative humidity equal to 22 °C and 70%, respectively. A photograph of this mini-supercell was taken at 14:54 UTC in Oudewater, a town in the province of Utrecht and 4 km northwest of IDRA, showing a low-topped storm with a tilted updraft structure (see picture link [2])

The resulted A(CZPHI,AHR) from event E6 was used to correct z and z_{dr} measurements for attenuation and differential attenuation, respectively, in the same manner as for event E5 (section 5.4). At 14:50 UTC, calculated PIA and PIA$_{DP}$ reached values of 10 and 1.6 dB, respectively, and the resulted Z(CZPHI,AHR) and Z_{DR} fields are shown in Fig. 5.9. In the Z(CZPHI,AHR) field a significant gradient can be seen along the inflow edge of the storm (arrow #1) and a narrow echo-appendage (arrow #2). An echo-appendage typically curves in the presence of a mesocyclone process; however, this feature was not shown during the observed period. The Z_{DR} field shows an area of significantly enhanced values along the inflow edge (arrow #3). This feature, commonly seen in supercell storms, is referred to as the Z_{DR}-arc signature as a result of possible size sorting processes (Kumjian and Ryzhkov, 2008). It can be observed that the Z_{DR} field also depicts a radial pattern, similar to event E5. The fields of K_{DP}(C) and K_{DP}(AHR) are also illustrated in Fig. 5.9. It is seen that the K_{DP}(AHR) field retains the spatial variability of the storm better than the K_{DP}(C) field while reducing negative K_{DP} estimates. Note that both K_{DP} fields show enhanced values along the inflow edge of the storm with values as high as 12 ° km^{-1} collocated with the Z_{DR}-arc. Such values were maintained during 5 min as a result of a large concentration of raindrops possibly due to a warm inflow air with high relative humidity. Note that K_{DP} estimates over the echo-appendage, in both K_{DP} fields, are not possible because of its narrow width of less than 1 km. The results related to Ψ'_{DP} and δ_{hv} will be discussed later in this section.

The selected values for α (CZPHI) using Φ_{DP}(C) and Φ_{DP}(AHR) in Eq. (5.9) are given in Fig. 5.10 panel a) as a function of azimuth. Observe that the optimization of α using Φ_{DP}(C) was only possible in three azimuthal profiles of the mini-supercell. This is because, in multiple azimuthal profiles, the percentage of gates with K_{DP}(C) > 0 ° km^{-1} in a given profile is less than 50% which led to the selection of the constant value for α. On the other hand, when Φ_{DP}(AHR) was used in Eq. (5.9), the optimization of α occurred in multiple azimuthal profiles and optimal values for α, mostly larger than 0.34 dB (°)$^{-1}$, were selected. Such values may be associated with areas of large raindrops along Φ_{DP} profiles because α is sensitive to DSD and raindrop shape variability (Ryzhkov and Zrnić, 1995; Carey et al., 2000; Bringi and Chandrasekar, 2001). For example, Bringi and Chandrasekar (2001) argued that α and β increase for increased values of the median volume diameter larger than 2.5 mm at weather radar frequencies. The $\bar{e}_{\min}$ and $\sigma_{e_{\min}}$ from using Φ_{DP}(C) and Φ_{DP}(AHR) in Eq. (5.9) are given in Table (5.3). The selected values for α and statistics of e_i suggest that the optimization process in the CZPHI method can lead to incorrect α estimates if Φ_{DP} profiles are not well estimated.

[2] https://www.weerwoord.be/uploads/16820112527543.jpg

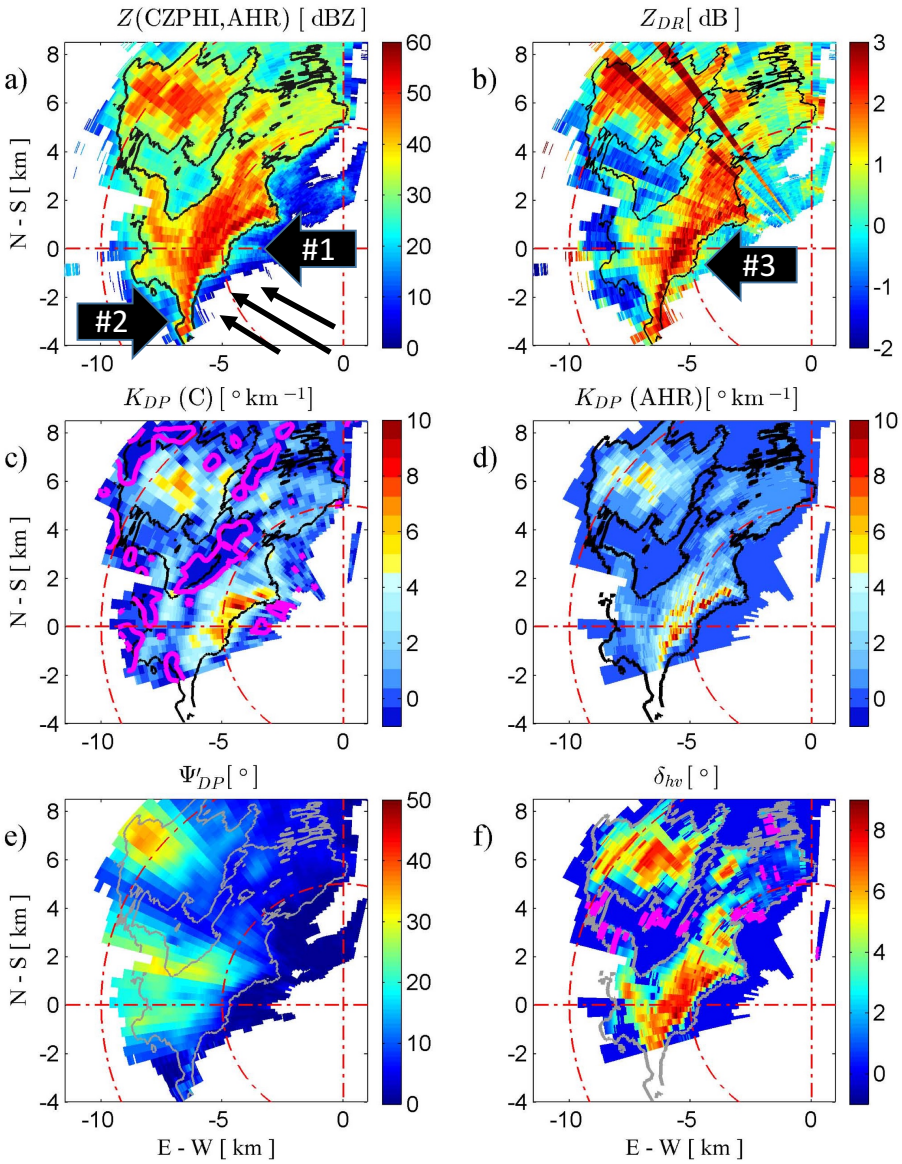

Figure 5.9: Results from event E6 at 14:50 UTC. Fields of Z(CZPHI,AHR), Z_{DR}, K_{DP}(C), K_{DP}(AHR), Ψ'_{DP}, and δ_{hv} are indicated in panels a), b) ... f), respectively. The 30 dBZ levels are given by black and gray contour lines. In addition, the Z gradient along the inflow edge, the Z narrow appendage, and the Z_{DR}-arc signatures are indicated by the arrows #1, #2, and #3, respectively. In panel a), the three arrows represent the low-level inflow. The magenta contour lines, in panels c) and d), show $-1°$ km^{-1} levels while in panel f) they indicate 0° levels.

K_{DP}(C) and K_{DP}(AHR) estimates resulting from event E6 were compared against A(ZPHI) in a similar way as in section 5.3.2 and the results are summarized in Table (5.2).

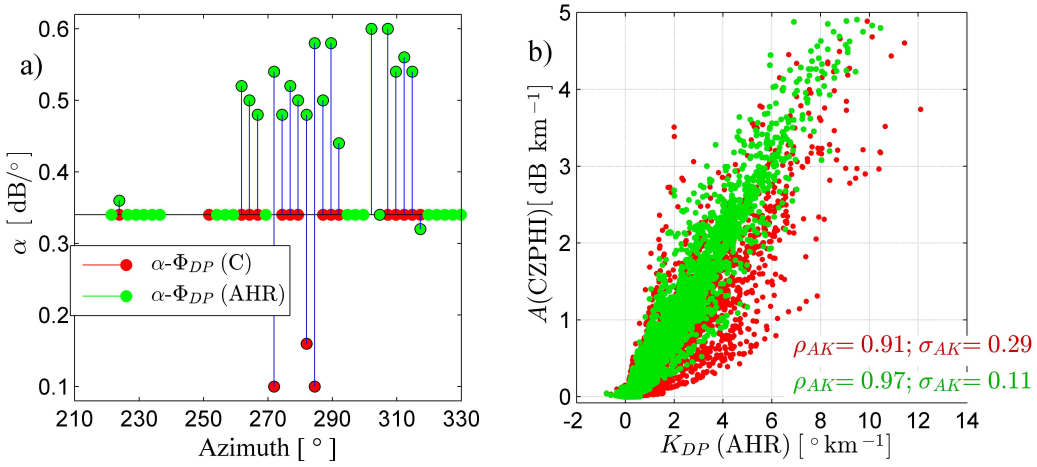

Figure 5.10: a) Selected values for α using Φ_{DP}(C) and Φ_{DP}(AHR) are given by the stemplots in red and green, respectively, as a function of azimuth from event E6 at 14:50 UTC. b) Resulted A(CZPHI,C)-K_{DP}(AHR) and A(CZPHI,AHR)-K_{DP}(AHR) relations are represented by red and green scatterplots, respectively.

5

Clearly, K_{DP}(AHR) outperformed K_{DP}(C) estimates in terms of ρ_{KA}, σ_{KA}, and bias on Z, showing a strong agreement with A(ZPHI). Therefore, K_{DP} estimates given by K_{DP}(AHR) are employed to test the impact of selected values for α on the CZPHI method as explained in section 5.4. As a result, the A(CZPHI,C)-K_{DP}(AHR) and A(CZPHI,AHR)-K_{DP}(AHR) scatterplots are given in Fig. 5.10 panel b). Observe that both scatterplots partly overlap even though A(CZPHI,C) estimates are associated with α values smaller than those from A(CZPHI,AHR). This is due to an improper δ_{hv} filtering by the conventional approach at edges of the mini-supercell storm that leads to overestimated $\Delta\Phi_{DP}$ inputs. The reasonable correlation seen in A(CZPHI,C)-K_{DP}(AHR) is because A(CZPHI,C) estimates were mostly given by the ZPHI method, avoiding suboptimal α values. For a more quantitative analysis, the performance of A(CZPHI,C) and A(CZPHI,AHR) were quantified with respect to K_{DP}(AHR) by ρ_{AK} and σ_{AK} and the results are indicated in Table (5.3). This quantification measures the degradation of the CZPHI method due to incorrect α values obtained when the conventional K_{DP} approach was used to estimate Φ_{DP} profiles. The impact of A(CZPHI,C) and A(CZPHI,AHR) on attenuation corrected Z was quantified by the RMSE such that Z(CZPHI,C) and Z(CZPHI,AHR) are compared against Z(DP,AHR) estimates as indicated in section 5.4. From Table (5.3), RMSE results indicate a low performance of the attenuation correction CZPHI method when Φ_{DP} profiles are obtained by the conventional K_{DP} technique. In this analysis, 13 680 data points were considered in A(CZPHI,C)-K_{DP}(AHR) and 13 339 in A(CZPHI,AHR)-K_{DP}(AHR).

The Ψ'_{DP} field corrected for system phase-offset and the estimated δ_{hv} field resulting from event E6 were illustrated in Fig. 5.9. It is seen that areas of enhanced δ_{hv} are collocated with areas of increased Z, Z_{DR}, and K_{DP} values, showing a consistent storm structure of the δ_{hv} field. Such δ_{hv} areas, mostly depicted by the 30 dBZ contouring level, could indicate the presence of DSDs associated with big raindrops because those areas were related to α values larger than 0.34 dB $(°)^{-1}$ as indicated in Fig. 5.10. Areas of

negative δ_{hv} are also present which may be due to Ψ_{DP} oscillations. The remaining area of δ_{hv} field is associated with light rain (i.e., with $|K_{DP}(\text{AHR})| < 0.4\,^{\circ}\,\text{km}^{-1}$) and has a δ_{hv} value equal to 0.02° as a result of step 6 of the δ_{hv} algorithm given in section 5.5. In addition, the phase mismatch was calculated and is equal to 1.32° (step 5) and the number of interpolated δ_{hv} values represents a 27% of the total δ_{hv} field (step 4).

In order to further evaluate δ_{hv} results, the δ_{hv}-K_{DP}(AHR) scatterplot (14 347 data points) is shown in Fig. 5.11 along with the $\overline{\delta}_{hv}$ and $\overline{\delta}_{hv} \pm \sigma_{\delta_{hv}}$ curves. Also the empirical linear fits given by Eqs. (5.12) and (5.13) are plotted. The $\overline{\delta}_{hv}$ curve seems to agree the linear fits $\mathfrak{L}_1$ and $\mathfrak{L}_2$, except for K_{DP} values larger than $8\,^{\circ}\,\text{km}^{-1}$ due to lack of data. Furthermore, the mean of $\sigma_{\delta_{hv}}$ values is equal to 1.65° which represents a reasonable spread given the natural variability between δ_{hv} and K_{DP}. Such variability may be also due to unfiltered fluctuations on Ψ'_{DP}.

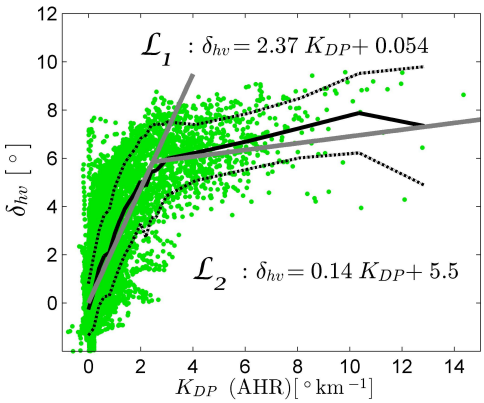

Figure 5.11: As in Fig. 5.8 but for event E6 at 14:50 UTC.

5.6.2. TORNADIC STORM

Another storm event was observed by IDRA on 10 September 2011 from 19:30 to 20:15 UTC, hereafter storm event E7. Radar-based signatures and surface damage reports suggest that E7 was a tornadic storm. The exact tornado time period is not known; however examination in the radial velocity field showed a persistent area of convergence and gate-to-gate wind shear during 19:51 - 19:56 UTC. Storm event E7 resulted from an early supercell storm observed in the city of Gent, Belgium, 130 km southwest from IDRA location. The shape of this supercell changed continuously because of dynamic processes such as cell splitting and merging, resulting in a non-supercell shaped storm.

Reflectivity fields z and Z(CZPHI,AHR) at 19:55 UTC are shown in Fig. 5.12. Values of PIA (PIA$_{DP}$) in the order of 18 dB (3 dB) led to fully attenuated areas in the south-side of the storm, behind strong rain echoes. The K_{DP}(C) and K_{DP}(AHR) fields are also illustrated in Fig. 5.12. It can be observed that the K_{DP}(AHR) field mitigates two issues i) a segmented K_{DP} texture and ii) negative K_{DP} values, which are present in the K_{DP}(C) field. Therefore, K_{DP}(AHR) preserves the storm structure better than K_{DP}(C). Note that the fully attenuated regions are located behind areas of significant K_{DP} values in the

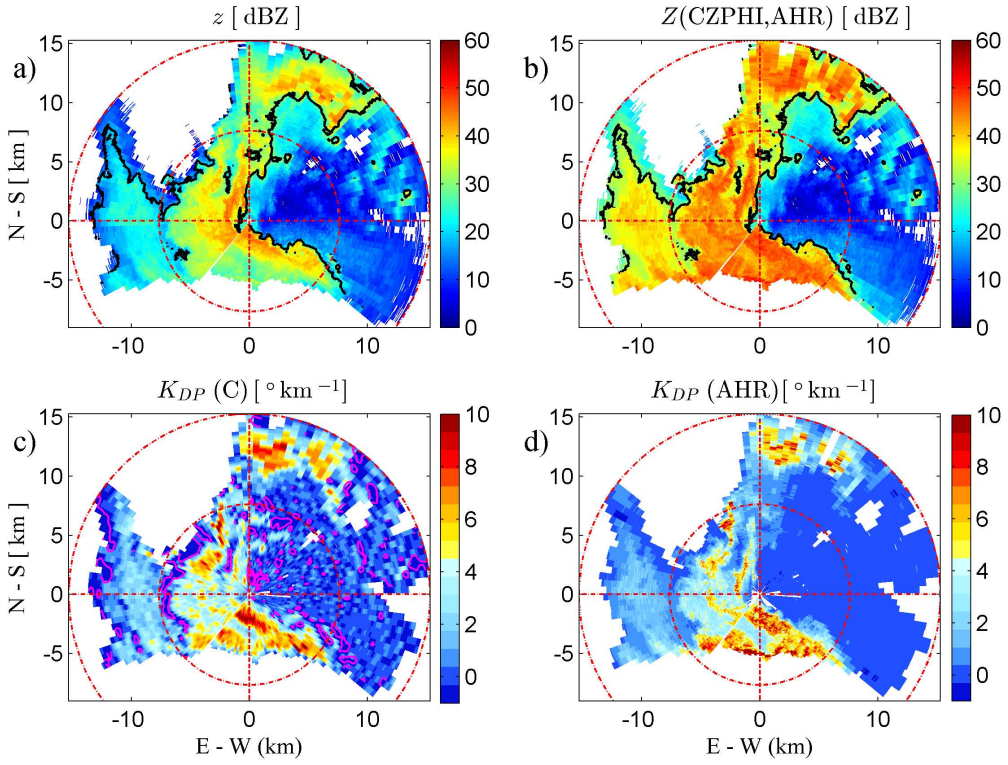

Figure 5.12: Results from event E7 at 19:55 UTC. Fields of z, Z(CZPHI,AHR), K_{DP}(C), and K_{DP}(AHR) are indicated in panels a)...d), respectively. Contour lines represent same levels as those given in Fig. 5.9 whereas the red rings are at 7.5 km increments.

order of 10 ° km^{-1}. The performance of K_{DP}(C) and K_{DP}(AHR) were also quantified using A(ZPHI) and the results are summarized in Table (5.2). Those results indicate that K_{DP}(AHR) and A(ZPHI) estimates agree significantly with the empirical relation $K_{DP} = (1/\alpha)A$, whereas the performance of K_{DP}(C) degrades as for events E5 and E6. Z_{DR} corrected for differential attenuation will be shown in Fig. 5.14.

The values for α resulting from including Φ_{DP}(C) and Φ_{DP}(AHR) profiles in the CZPHI method are presented in Fig. 5.13 panel a) as a function of the complete azimuth. It can be seen that for most azimuthal profiles, selected α values are associated with an existing minimum error E (encircled by black edges). However, in the azimuthal sector of 40 - 120°, the optimization process was not possible and therefore estimates of A were determined by the ZPHI method. This sector was related to light and uniform rain profiles, see Fig. 5.12, where $\Delta\Phi_{DP}$ values are smaller than 10 °. Values of α associated with Φ_{DP}(AHR) are predominantly equal to or larger than 0.34 dB (°)$^{-1}$ where for many azimuthal profiles the optimization process led to α values equal to 0.34 dB (°)$^{-1}$. It is clear to see the absence of $\alpha > 0.5$ dB (°)$^{-1}$, which in contrast to event E6, may indicate the lack of big drops present at this time. On the contrary, selected values for α related to Φ_{DP}(C), are frequently smaller than or equal to 0.34 dB (°)$^{-1}$. In addition, it is seen that

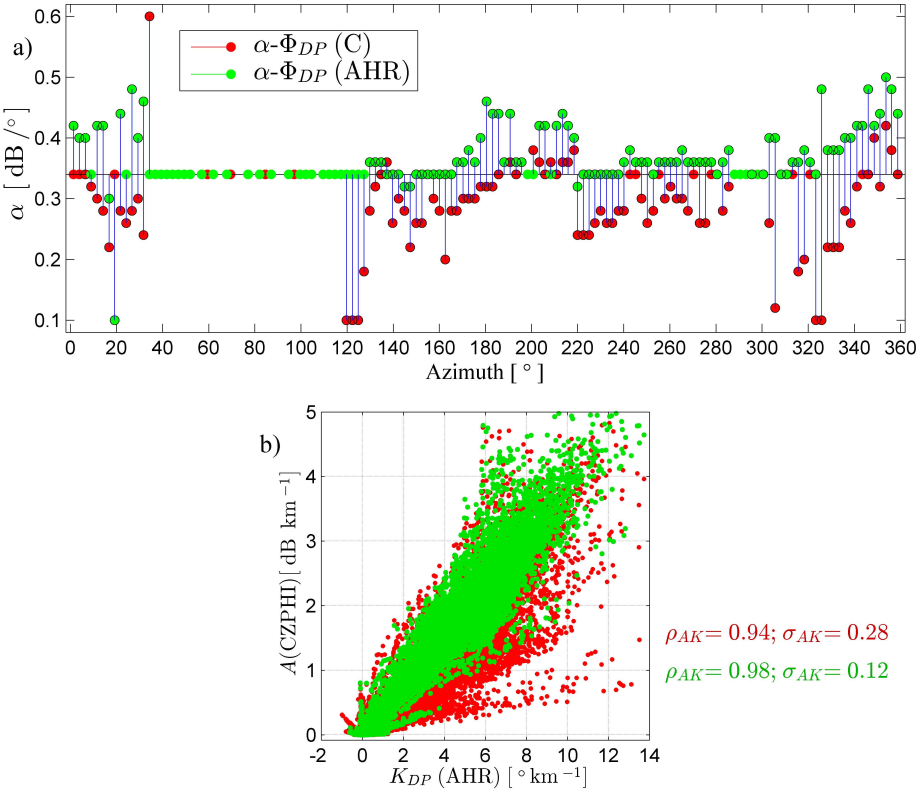

Figure 5.13: As in Fig. 5.10 but for event E7 at 19:55 UTC.

in few profiles, α equal to 0.1 and 0.6 dB $(°)^{-1}$ were selected, most likely as a result of an inadequate optimization process. The resulted $\bar{e}_{\min}$ and $\sigma_{e_{\min}}$ of e_i from using Φ_{DP}(C) and Φ_{DP}(AHR) in Eq. (5.9) are given in Table (5.3), showing that Φ_{DP}(AHR) profiles can lead to more reliable values for α.

Similar to events E5 and E6, K_{DP}(AHR) estimates are considered in order to evaluate A(CZPHI) results and therefore the A(CZPHI,C)-K_{DP}(AHR) and A(CZPHI,AHR)-K_{DP}(AHR) scatterplots are given in Fig. 5.13 panel b). A strong correlation can be observed in A(CZPHI,AHR)-K_{DP}(AHR) because of adequate estimates of K_{DP} and therefore proper α selection mainly found between 0.34 and 0.50 dB $(°)^{-1}$. On the other hand, underestimated A(CZPHI,C) values are noticeable as a result of α values smaller than 0.34 dB $(°)^{-1}$. A(CZPHI,C) and A(CZPHI,AHR) estimates were compared quantitatively as for events E5 and E6 and the results in terms of ρ_{AK} and σ_{AK} are presented in Table (5.3). Results are consistent with those found in events E5 and E6, that is, the CZPHI method shows an improved performance when Φ_{DP} profiles are given by the AHR approach rather than the conventional approach. In this comparison, the A(CZPHI,C)-K_{DP}(AHR) and A(CZPHI,AHR)-K_{DP}(AHR) scatterplots consisted of 43 389 and 40 157 data points, respectively.

During the observed period, this tornadic event was not associated with an echo-appendage but with a bow apex feature along the leading edge of the storm. For a better visualization of the bow apex signature, Fig. 5.14 illustrates closer observations (south-east side) of the Z(CZPHI,AHR) and K_{DP}(AHR) fields as well as corrected Z_{DR} and estimated δ_{hv} fields. The Z(CZPHI,AHR) field shows a strong gradient along the leading

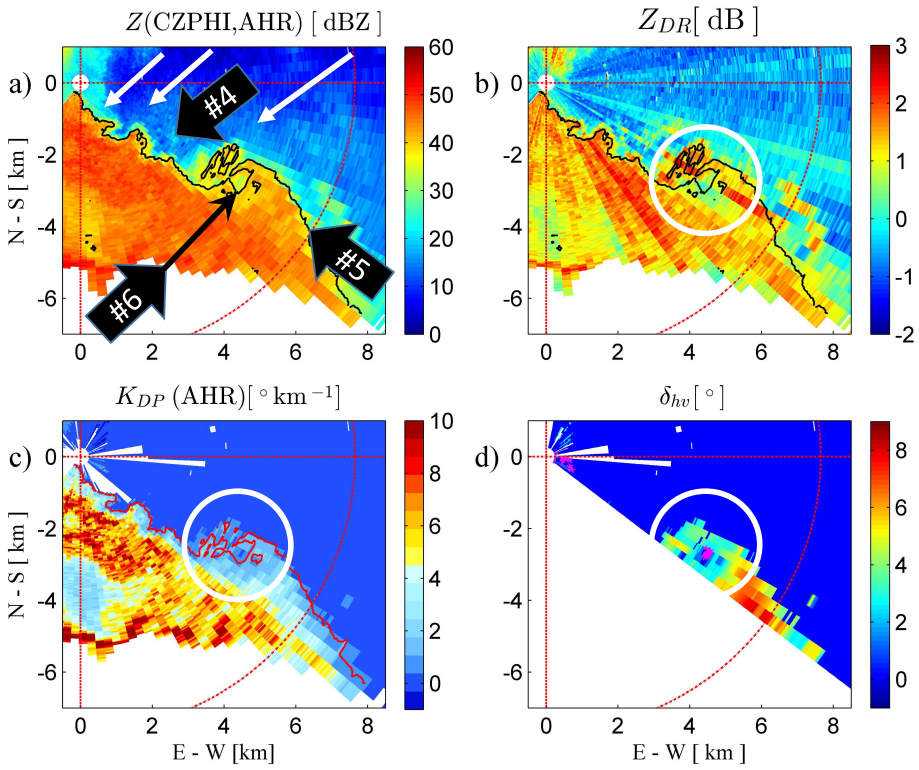

Figure 5.14: Zoom-in results from E7 at 19:55 UTC. Fields of Z(CZPHI,AHR), Z_{DR}, K_{DP}(AHR), and δ_{hv} are indicated in panels a)...d), respectively. The black contour lines, in panels a)-b), represent 40 dBZ levels. The Z gradient along the inflow edge, the bow apex, and the echo-weak hole are indicated by arrows #4, #5, and #6, respectively. In addition, the white arrows illustrate the low-level inflow. In panel c), the red contour lines indicate $1\,^{\circ}\,\mathrm{km}^{-1}$ levels while the magenta contour lines, in panel d), 0° levels. The white circles show the rotation pattern associated with the echo-weak hole.

edge (arrow #4) indicating a region of strong convergence and low-level inflow (white arrows). A bow apex attribute resulting possibly from a descending rear inflow jet (Weisman and Trapp, 2003) is also noticeable (arrow #5). This feature seems to be associated with a rotation pattern in form of a hook or echo-weak hole (Bluestein et al., 2007) depicted by the 40 dBZ contouring level (extended arrow #6). It is also observed that the core of the hole is related to bounded weak values of Z_{DR}, K_{DP}(AHR), and δ_{hv}, located in the center of the white circles. According to Funk et al. (1999), cyclonic circulations can occur along or near the leading bow apex, which can produce tornadoes of F0-F3 intensity. The core of the echo-weak hole, whose inner diameter is approximately 0.75 km,

was located 4.71 km south-east from the radar in Ameide town, where wind and possibly tornado damages were reported to local news and few photographs were taken (see news link [3] and pictures link [4]).

Because of the close proximity of the storm to IDRA, estimates of δ_{hv} were only achieved for an azimuthal sector as shown in Fig. 5.14 panel d), where it was possible to correct Ψ'_{DP} profiles for system phase-offset at beginning ranges (step 1 of the δ_{hv} algorithm). The percentage of interpolated δ_{hv} data is only 22% (step 4) and the correction for phase mismatch is equal to 1.21° (step 5). Furthermore, the uniform δ_{hv} area, which corresponds to $|K_{DP}(\text{AHR})| < 0.4\,^{\circ}\,\text{km}^{-1}$, has a δ_{hv} value equal to 0.19° (step 6). The δ_{hv}-K_{DP}(AHR) scatterplot resulted from event E7 is shown in Fig. 5.15 for evaluation purposes. As for the previous events, the $\overline{\delta}_{hv}$ curve indicates a reasonable agreement

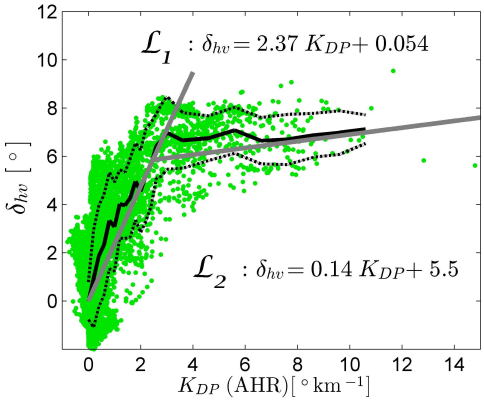

Figure 5.15: As in Fig. 5.8 but for event E7 at 19:55 UTC.

with empirical fits $\mathfrak{L}_1$ and $\mathfrak{L}_2$ for $K_{DP} < 10\,^{\circ}\,\text{km}^{-1}$. Moreover, estimated $\sigma_{\delta_{hv}}$ values have a mean value equal to 1.47° which is in the same order as for events E5 and E6. For this analysis, only 21 010 data points were considered due to the limited sector of the δ_{hv} field.

[3] https://www.rtlnieuws.nl/nieuws/binnenland/gewonde-door-windhoos-bij-noodweer
[4] https://www.hartvannederland.nl/top-nieuws/2011/overlast-en-schade-door-noodweer

5.7. CONCLUSIONS

The use of Ψ_{DP}-based variables such as the specific differential phase K_{DP} and the specific attenuation A has improved radar measurements affected by, for example, attenuation, miscalibration, and partial beam blockage. More recently, the backscattering differential phase δ_{hv} has been studied at short wavelengths because of its empirical relation to Z_{DR}. However, the accuracy of K_{DP}, A, and δ_{hv} strongly depends on the ability to separate Φ_{DP} and δ_{hv} from Ψ_{DP} and the mitigation of random oscillations on Ψ_{DP}. For the estimation of A, established methods such as the DP and the ZPHI methods use the relation $A = \alpha K_{DP}$, assuming a constant α. This assumption, however, might lead to limited results because α is sensitive, among other factors, to DSD variability. As an alternative solution, the CZPHI method, which is an extension of the ZPHI solution, requires the estimation of Φ_{DP} to select an optimal α. Therefore, this work has explored the impact of Φ_{DP} profiles on the estimation of α and A, and correction of Z in rain by the CZPHI method, and has proposed an advanced technique to compute δ_{hv} in rain at X-band frequencies, with emphasis on convective storm cells observed at close range.

The conventional range-filtering method and the adaptive high-resolution AHR approach were implemented to estimate K_{DP} in rain, denoted as K_{DP}(C) and K_{DP}(AHR), while the ZPHI method (with a constant α) and the CZPHI technique (with a variable α) were adapted to estimate A at X-band frequencies. Three summertime storm events observed within a range coverage of 15 km and spatial resolution of 0.03 km were used to examine the performance of these methods in detail. In the analysis associated with a constant α, the estimation of A obtained from the ZPHI method was used as a reference to compare the two K_{DP} approaches. It was shown that estimates of K_{DP}(AHR) were more consistent than K_{DP}(C) with respect to A(ZPHI) results. However, the analyses with respect to Z(ZPHI) demonstrated that the resulted bias related to Z(DP,AHR) estimates was just slightly smaller than that of Z(DP,C). The effects associated with the optimization of α on estimating A and correcting Z were analyzed using K_{DP}(AHR) as reference because of the strong relation seen between K_{DP}(AHR) and A(ZPHI) and the fact that data were obtained from one radar (i.e., without independent measurements at the same time of the storm events). Quantitative analyses indicated that in the optimization of α, Φ_{DP}(AHR) profiles led to minimum-errors smaller than those related to Φ_{DP}(C) profiles, and therefore, the α values associated with Φ_{DP}(AHR) appear to better represent the variability of DSD in the observed storms. More quantified results, with respect to K_{DP}(AHR), showed that estimates of A given by A(CZPHI,AHR) were more consistent than those given by A(CZPHI,C) in terms of ρ_{AK} and σ_{AK} and that Z(CZPHI,AHR) estimates were associated with RMSEs lower than those from Z(CZPHI,C). These findings confirm the conclusions of similar studies that when K_{DP} (or Φ_{DP}) is not properly estimated, the performance of DP and ZPHI methods (constant α) for attenuation correction purposes are similar, with a lower performance of the DP method in estimating A (Gorgucci and Chandrasekar, 2005); whereas, the performance of the CZPHI technique (optimal α) for attenuation correction purposes can decrease compared to the ZPHI approach (Snyder et al., 2010).

Values of δ_{hv} were obtained from computing Ψ_{DP}, K_{DP}(AHR), and A(CZPHI,AHR) fields, including an interpolation technique. Significant agreement between estimated δ_{hv}-K_{DP}(AHR) scatterplots and experimental linear fits in rain were demonstrated, with

a standard deviation in the order of 1.5°. In these results, the percentage of δ_{hv} estimates resulting from interpolation was, in average, equal to 21%. Estimates of δ_{hv} were cross-checked using K_{DP}(AHR) results because these are characterized by normalized standard error values smaller than 20% and σ_K magnitudes in the order of 0.1° km^{-1}(Reinoso-Rondinel et al., 2018). It is also worth mentioning that the AHR method provided K_{DP} fields that significantly matched the structure of the storms, whereas the range-filtering method led to smoothed fields of K_{DP}, including areas of negative K_{DP} as a result of unfiltered fluctuations on Ψ_{DP}. As a parallel relation, δ_{hv} fields exhibited a spatial distribution similar to the one of Z_{DR}, after differential attenuation correction. Despite the fact that δ_{hv} cannot be estimated when the slope of Ψ_{DP} is of significance at beginning ranges (i.e., when a storm is on top of or adjacent to a radar), the proposed δ_{hv} algorithm is able to depict areas of moderate to large raindrops while maintaining the structure of the storm.

A careful Ψ_{DP} processing is vital to unleash the full potential of polarimetric weather radars, especially at X-band frequencies. Such detail analysis shows an alternative to process Ψ_{DP} profiles in rain and thereby allowing an improved selection of α in difficult scenarios characterized by small $\Delta\Phi_{DP}$ magnitudes (~10 - 50°) and short path intervals (~5 - 10 km). This alternative could be beneficial when a path needs to be segmented due to detected areas of hail along a beam. Although the results of α, Z, and δ_{hv} may need further validation using external data from, for example, a network of disdrometers, microwave links, or collocated S and X-band radars to consolidate the findings of this work, it is foreseen that in the context of Ψ_{DP} processing, such as the one presented in this work, users can benefit from better observations of Ψ_{DP}-based variables in convective storm cells.

6

CONCLUSIONS AND OUTLOOK

6.1. CONCLUSIONS

During the last decade, researchers have encouraged the operation of X-band weather radars with polarimetric capabilities to improve the quality of radar data for weather meteorology and hydrology applications. The advantages of using X-band radar systems come from their relatively small size, low price, high mobility, as well as their configuration to obtain measurements at spatial and temporal resolutions higher than those of conventional S-band and C-band radars. The polarimetric ability to measure differential phase shifts (Ψ_{DP}) has been used to mitigate signal attenuation, which is one of the main limitations of X-band radars. In addition, meaningful information can be derived from Ψ_{DP} because it is independent of radar miscalibration, signal attenuation, and it is less sensitive to the presence of hail in rain. Two radar variables are typically derived from Ψ_{DP}; the specific differential phase (K_{DP}) and the specific attenuation (A), in which researchers have found several applications such as attenuation correction, radar calibration, and rainfall rate estimation. However, a correct usage of Ψ_{DP} is not straightforward, especially at X-band frequencies, because of the nature of noise behavior, random fluctuations, and resonance components (δ_{hv}) in measurements of Ψ_{DP}. In the presented work, the basics of weather radars at X-band frequencies have been reviewed. Moreover, the performance of a polarimetric X-band radar located in the Netherlands (NL) has been analyzed. Finally, new techniques have been proposed to accurately estimate K_{DP}, A, and δ_{hv} at X-band frequencies in rain.

6.1.1. WEATHER RADAR OBSERVATIONS IN THE NETHERLANDS: A SQUALL LINE EVENT

In Chapter 3, the benefits and limitations of the KNMI C-band radar, located in De Bilt, and the polarimetric X-band radar IDRA, located in Cabauw, were examined using a squall line storm that occurred in the wintertime of 2012. In addition, a framework to study convective events in the NL was provided. On the one hand, Z observations at C-band frequencies showed that the squall line progressively broke into multiple bowed-

shape segments as a result of possible rear inflow forces, where the S-broken signature (i.e., two adjacent segments) was identified at range resolution of 1 km every 5 min. On the other hand, attenuation corrected Z fields obtained from IDRA at resolutions of 0.03 km and 1 min allowed a more detailed visualization of vortex signatures, such as the reflectivity hook echo and WER related to the observed S-broken signature during a period of 6 min. Attenuation issues, at X-band frequencies, were addressed using a simple method based on Ψ_{DP} measurements. However, IDRA measurements behind heavy precipitation, at a distance of 5 km, suffered from full attenuation which was identified by the anomalous behavior of the linear depolarization ratio (L_{DR}) and Ψ_{DP}. Thus, the capabilities of measuring convective storms such as squall lines by a single X-band radar, even with polarimetric capabilities, can be limited. Therefore, it is desirable to implement a network of polarimetric X-band radars in the NL to extend the observation range while keeping the spatial and temporal resolution of the measurements for a detailed visualization and improved interpretation of Z fields.

6.1.2. ADAPTIVE AND HIGH-RESOLUTION ESTIMATION OF K_{DP}

A new algorithm to accurately estimate K_{DP} at X-band frequencies in rain and at high-spatial resolution was presented in Chapter 4. One of the novelties of this approach is the mathematical formulation of the standard deviation σ_K of the K_{DP} estimator, which allows predefining a path length interval for a given range resolution Δr. From this interval and at each range gate, a path length L is adaptively selected in order to minimize σ_K. The presence of δ_{hv} components in Ψ_{DP} measurements was reduced by controlling the paths in which the range derivatives of Ψ_{DP} are obtained. The effect is reduced by filtering paths where the corresponding absolute difference of Z_{DR} is larger than the standard deviation of a given Z_{DR} profile. Another novelty is that the high-resolution aspect of the algorithm is based on the formulation of a weight that downscales the range derivatives of Ψ_{DP} from L to Δr scales by measuring the spatial variability of the storm. This formulation is a variation of the SC principle and thereby it depends on Z and Z_{DR}. It was demonstrated that the algorithm is independent of constant biases in profiles of Z and Z_{DR}, which could be caused by miscalibration and partial beam blockage. In addition, errors associated with a simple attenuation correction, based on Ψ_{DP}, (i.e., the DP method) do not seem to affect the performance of the algorithm. The performance of the K_{DP} algorithm was characterized by a strong consistency between Z and K_{DP} in light and heavy rain, reduced negative K_{DP} values, and detected K_{DP} peaks compared to a conventional method to estimate K_{DP}. Although this algorithm needs to be tested at long ranges, where attenuation and non-uniform beam filling affect Z and Z_{DR} measurements, and in scenarios where partial beam blockage is associated with complex terrain features, the proposed approach is able to obtain accurate K_{DP} profiles at high spatial resolution in light and heavy rain while filtering δ_{hv} and maintaining the spatial variability of Ψ_{DP}.

6.1.3. IMPROVED ESTIMATION OF A AND δ_{hv} IN CONVECTIVE STORM CELLS

In Chapter 5, two applications of the new K_{DP} approach were given: 1) enhanced estimation of the specific attenuation A and 2) a new technique to estimate δ_{hv} at X-band frequencies in rain, with an emphasis on convective storm cells observed at close range.

Three storm events observed by IDRA (i.e., within a range coverage of 15 km and Δr equal to 0.03 km) were used to perform the analysis. The first application studied the impact of estimated Φ_{DP} profiles on the performance of the attenuation correction method given by Bringi et al. (2001) in order to improve estimates of α and A. For this application, Φ_{DP} was estimated using the conventional method (C method) given by Hubbert and Bringi (1995) and a more recent approach (AHR method) introduced by Reinoso-Rondinel et al. (2018) while A was obtained using three methods given by Bringi et al. (1990) (DP method), Testud et al. (2000) (ZPHI method), and Bringi et al. (2001) (CZPHI method). It was demonstrated that K_{DP} estimates resulting from the AHR method were more consistent than K_{DP} obtained from the C method when they are compared against A(ZPHI) results. It was also shown that Φ_{DP} profiles resulting from the C method can lead to erroneous values of "optimal" α, affecting the results of A and Z from the CZPHI method. Quantitative analyses indicate that in the optimization of α, Φ_{DP}(AHR) profiles lead to minimum-errors smaller than those related to Φ_{DP}(C) profiles, and therefore, "optimal" α values associated with Φ_{DP}(AHR) appear to better represent the spatial variability of DSD in the observed storms.

In the second application, the technique to estimate δ_{hv} integrates the results obtained from the C method (i.e., to smooth strong outliers from Ψ_{DP} profiles) and from the AHR and CZPHI approaches (i.e., to estimate corresponding Φ_{DP} profiles), so that a δ_{hv} profile is given by $\Psi_{DP}-\Phi_{DP}$. In order to reduce remaining δ_{hv} outliers, this method applies a 2-D adaptive filter based on K_{DP} values and a 2-D image fill-in interpolation algorithm. The resulted scatterplot δ_{hv}-K_{DP}(AHR) showed significant agreement with respect to experimental linear fits in rain. In these results, the percentage of δ_{hv} estimates resulting from interpolation is, in average, equal to 21% while the standard deviation of δ_{hv} is in the order of 1.5°. Furthermore, δ_{hv} fields displayed a spatial distribution similar to that of Z_{DR}. It is also worth mentioning that K_{DP}(AHR) fields were able to preserve storm features at Δr scales such as Z_{DR}-arc and vortex signatures. In spite of the fact that the presented δ_{hv} algorithm is only valid in rain and when heavy precipitation is not located on top or adjacent to the radar, the algorithm is able to depict areas of moderate to large raindrops while maintaining the structure and spatial variability of the observed storm cells.

Summarizing the previous 3 subsections, a framework for the processing of polarimetric weather radar data at X-band frequencies was developed, mainly focused on the processing of Ψ_{DP} in rain to obtain accurate K_{DP}, A, and δ_{hv} at range resolution scales. The challenges and results of performing weather observations at X-band frequencies were demonstrated through a combination of (1) the comparison of Z fields obtained from C-band and X-band radars at different temporal and spatial resolutions, (2) the adaptive AHR approach that estimates K_{DP} at range resolution scales using measurements of Z and Z_{DR} at X-band frequencies, and (3) the analysis of attenuation correction methods to improve estimates of A and (4) the technique to estimate δ_{hv} in convective storm cells. Researchers interested to develop algorithms based on polarimetric radar technology with the goal of increasing the reliability of weather radar measurements will be able to use the proposed framework, which provides desirable aspects such as spatial resolution, accuracy, quality control, and a better interpretation of convective storm events. It is foreseen that urban-hydrology and weather research communities will ben-

efit from better radar data inputs, which can be derived from this framework, leading to significant improvements in both weather monitoring and warning.

6.2. OUTLOOK

Small X-band weather radars are designed such that it is possible to obtain weather measurements at high spatial and temporal resolutions, however, the disadvantage of such systems is the possibility of experiencing a high level of rain attenuation, especially when a heavy rainstorm is adjacent or on top of the radar. Even though it was shown that the polarimetric X-band radar IDRA can depict small features of observed storms at close range, more can be done to mitigate fully attenuated areas, to increase its scanning capabilities, and to perform radar calibration. For example, it is recommended to increase its operation range from 15 to 60 km and to add the capability of scanning in elevation. In addition, because attenuation is inevitable, a network of polarimetric X-band radars should be strategically implemented to ensure the range coverage and quality of radar data. Moreover, operationally polarimetric C-band radars can be used to provide data over fully attenuated areas as well as to check calibration bias. A related recommendation is to collect additional convective storms, that occur in the region of the NL, in order to archive several storm events and find a consistency among signatures that are associated with the microphysical and dynamical processes of storms.

The adaptive and high-resolution K_{DP} approach needs information on the path length interval to adaptively select a path length at each range gate. However, the path length interval depends on the spatial variability of the storm and therefore it is suggested to update the interval in time such that it corresponds to the actual storm scenario. An example of updating the interval in time is by using a representative value of the actual mean of the SC ratio that is obtained once the K_{DP} field is estimated. Another recommendation is related to the path length selection process which can be time-consuming if the number of gates is in the order of several thousand and the radar update time in the order of 1 min or less. In such case, the selection of path lengths can be completely or partially avoided in successive scans, for example, in areas of uniform storm structure or during a time-period in which it is expected that the structure of the storm will not change dramatically.

In this work, the identification of rain areas was accomplished with a rudimentary filter approach. For general applications, it is suggested to include an automatic algorithm that classifies hydrometeors and removes non-hydrometeor echoes. In case of solid or mixed precipitation, the proposed K_{DP} approach should be modified in order to avoid the use of polarimetric relations in rain. Fortunately, given that the formulation of the weight of the K_{DP} approach can be set as a constant and that the spatial variability of these precipitation types is often less than that of rain, K_{DP} can be still estimated but at expenses of low resolution and possible contamination of δ_{hv}. Therefore, further research on the suggested or on other suitable K_{DP} approaches is recommended to improve Ψ_{DP} processing for areas other than rain. It is also recommended to investigate techniques for an improved estimation of δ_{hv} in non-rain areas.

Even though it was shown that the presented framework can provide accurate estimates of K_{DP}, A, and δ_{hv} in rain using radar data at X-band frequencies, further development of the proposed algorithms is required to achieve the ambitions of implementing

the presented framework for real-time operations, not only at X-band, but also at C-band and S-band frequencies. This effort may require an automatic algorithm to discriminate between hydrometeors, quality control to assess the impact of complex terrains associated with beam blockage on measurements of Z and Z_{DR}, tuning of the frequency-dependent coefficients in the relations between polarimetric variables, as well as a study on the effects of non-uniform beam filling on polarimetric measurements, and a sensitivity analysis to temperature conditions. Related activities can involve the inclusion of external data from, for instance, a network of collocated disdrometers, rain gauges, microwave links, and radars to further establish the effectiveness of the achieved analysis and improve the quality of polarimetric radar data.

Given the importance of providing high-quality high-resolution radar data to the meteorological and hydrological research and operational communities and the limitations of conventional radars and established retrieval techniques, it is essential to experiment and evaluate the feasibility of alternative radar systems and more advantageous methods for weather signal processing. Even though additional improvements for accurate estimation of polarimetric variables are possible by following these recommendations, this research establishes a framework for improved processing of weather radar data with polarimetric technology.

A

STANDARD DEVIATION OF THE K_{DP} ESTIMATOR

For the purpose of deriving σ_K, the weight in Eq. (4.8) is expressed as $\hat{w}^{(j)} = \hat{s}^{(j)}\Delta r/L$ and therefore the K_{DP} estimator given by Eq. (4.9) is rewritten as

$$K_{DP} = \frac{1}{2L}\left[\frac{1}{M}\sum_{j=1}^{M}\Delta\Psi_{DP}^{(j)}\, s^{(j)}\right]; \quad \text{with} \quad j = 1,2,\ldots M. \tag{A.1}$$

Note that this expression includes the path length L and omits the index (i) for simplicity. Both $\Delta\Psi_{DP}^{(j)}$ and $s^{(j)}$ are considered to be independent random variables (r.v.'s) and hence their product is also a r.v. and denoted by $\kappa^{(j)}$ with $j = 1, 2, \ldots M$. Assume that $\kappa^{(1)}, \kappa^{(2)}, \ldots$ $\kappa^{(M)}$ have the same variance σ_κ^2 and that the pair $(\kappa^{(j)}, \kappa^{(m)})$, with $j \neq m$, has a constant covariance γ_κ. Using the variance property of the sum of correlated r.v.'s and the relation $\gamma_\kappa = \sigma_\kappa^2\rho_\kappa$, where ρ_κ is the correlation coefficient, the variance of the K_{DP} estimator σ_K^2 is expressed as

$$\sigma_K^2 = \frac{1}{(2ML)^2} M\sigma_\kappa^2[1 + (M-1)\rho_\kappa]. \tag{A.2}$$

If the term σ_κ^2 is rewritten using $\Delta\Psi_{DP}^{(j)}$ and $s^{(j)}$, we obtain

$$\sigma_K^2 = \frac{1}{(2L\sqrt{M})^2}\left[\mu_s^2\sigma_\Delta^2 + \sigma_s^2\left(\mu_\Delta^2 + \sigma_\Delta^2\right)\right]\left[1 + (M-1)\rho_\kappa\right], \tag{A.3}$$

where μ_s and μ_Δ represent the mean of $s^{(j)}$ and $\Delta\Psi_{DP}^{(j)}$, respectively. Similarly, σ_s^2 and σ_Δ^2 indicate their variance. Eq. (A.3) can be reduced if ρ_κ and σ_s^2 are assumed to be significantly small. In consequence, Eq. (A.3) is simplified to

$$\sigma_K^2 = \frac{\mu_s^2\,\sigma_\Delta^2}{\left(2L\sqrt{M}\right)^2}. \tag{A.4}$$

A

In order to include residuals from the $\Delta\Psi_{DP}$ filter condition (i.e., neglecting $\Delta\delta_{hv}$), the difference in differential phase is represented by the sum of two uncorrelated r.v.'s, $\Delta\Psi_{DP}^{(j)} + \epsilon_{\delta}^{(j)}$ where $\epsilon_{\delta}^{(j)}$ has a mean and variance equal to 0° and σ_{ϵ}^2, respectively. Thus, Eq. (A.4) is rewritten as

$$\sigma_K^2 = \frac{\mu_s^2 \left(\sigma_{\Delta}^2 + \sigma_{\epsilon}^2\right)}{\left(2L\sqrt{M}\right)^2}. \tag{A.5}$$

For a given path $\overline{ab}$, $\Delta\Psi_{DP}^{(j)}$ is expressed as $\Psi_{DP}(b) - \Psi_{DP}(a)$, which is the difference between two r.v.'s. If both r.v.'s have the same variance σ_P^2, the variance of $\Delta\Psi_{DP}^{(j)}$ is given by $\sigma_{\Delta}^2 = 2\sigma_P^2$. As a result, a theoretical σ_K for the K_{DP} estimator is defined as

$$\sigma_K = \frac{\mu_s}{L}\sqrt{\frac{2\sigma_P^2 + \sigma_{\epsilon}^2}{4M}}. \tag{A.6}$$

B

FILTER DESIGN TO ESTIMATE K_{DP} BY THE CONVENTIONAL TECHNIQUE

A finite impulse response (FIR) filter type is selected for designing the “light" filter (first step). The filter order is set to 36 while the required r_c is set to 1 km. In addition, a Hann window function is included to obtain a magnitude response (H [dB]) with small sidelobes. H is shown in Fig. B1a, as a function of the normalized range scale $f_n = \Delta r / r_s$ where r_s[km] $\geq \Delta r$. Note that H reaches approximately -40 dB at $f_n = 0.1$. This means

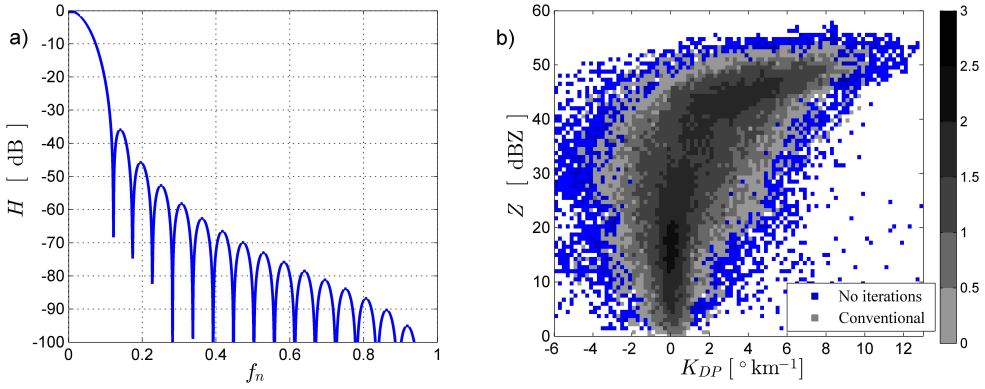

Figure B.1: a) Magnitude response of a FIR low-pass filter specified by r_c = 1 km, Δr = 0.03 km, filter order of 36, and Hann window. b) Z-K_{DP} histograms from the first step (blue scale) and both steps (gray scale) of the conventional approach.

that the “light” filter is designed such that spatial variations at range scales smaller than 0.3 km are suppressed. Next, this filter is iterated several times (second step) by setting

τ equal to $1.5\sigma_P$. The storm event E3 at 19:50 UTC is used for demonstration purposes. Z-K_{DP} histograms from the first and second step are shown in Fig. B1b. Observe that the iterative step eliminates several outliers without excessively smoothing K_{DP}.

C

SUPPLEMENT DISCUSSION

This supplement provides additional discussions related to the proposed K_{DP} technique which was not given in Chapter 4. The following discussions summarize the peer-review process of the work given by Reinoso-Rondinel et al. (2018). In this manner, researchers that want to use the K_{DP} technique can refer to this material.

- *The effectiveness of such methodology seems to be limited because it considers measurements of Z and Z_{DR} through the self-consistency principle and the correlation between Z_{DR} and δ_{hv}, especially at X-band.*

  Although Z and Z_{DR} may present significant uncertainties, several articles revealed remarkable advantages. For example, Gorgucci et al. (2006) and Adachi et al. (2015) used the self-consistency relation to improve the estimation of specific attenuation profiles ($A(r)$) while Lang et al. (2009) used it to correct $Z(r)$ and $Z_{DR}(r)$ measurements for partial beam blockage (PBB) effects. Schneebeli and Berne (2012) also recurred to $Z(r)$ and $Z_{DR}(r)$ to decouple $K_{DP}(r)$ and $\delta_{hv}(r)$ from Ψ_{DP} through polarimetric relations between Z and K_{DP} as well as Z_{DR} and δ_{hv}. Giangrande et al. (2013) incorporated the consistency between Z and K_{DP} to obtain $K_{DP}(r)$ without negative values and suggested to explore the incorporation of more polarimetric relations and evaluate their impact on polarimetric retrieved variables. Last, the well known ZPHI method introduced by Testud et al. (2000) included a relation between $Z(r)$ and $A(r)$ along with a Z_{DR} and δ_{hv} relation to improve estimations of $A(r)$ and rainfall rate. In this context, Z and Z_{DR} measurements can be used during the processing of noisy Ψ_{DP} measurements.

- *The impact of attenuation issues on estimated weights*

  The effective impact of attenuation corrected Z and differential attenuation corrected Z_{DR} depends of their difference with respect to their local mean instead of their absolute values. Moreover, the impact of possible uncertainties of Z and Z_{DR} on the estimation of weights are bounded within a given path of length L instead

of an entire radial profile. At ranges longer than 15 km, attenuation and differential attenuation corrections may still be possible given measurements of $\Psi_{DP}(r)$. The impact of attenuation correction on estimated weights (or samples of self-consistency ratio) may be controlled to some extend given short path lengths L and the NSE of the self-consistency ratio, which is estimated at each gate.

- *What would be the sensitivity of the self-consistency coefficients with respect to DSD variability?*

  Several authors analyzed the sensitivity of the self-consistency relation to DSD, drop shape, and temperature variabilities. For example, Gourley et al. (2009) studied the impact of drop shape model for radar calibration carried out by the self-consistency relation. Gourley et al (2009) recommended to use combined models in order to represent a wide variety of drop shapes such as the BZV model (Brandes et al 2012) which combines Pruppacher and Pitter 1971, Chandrasekar et al 1998, Beard and Kubesh 1991, and Andsager 1999. Moreover, it was found that the nature variability of DSD in rain was well represented by a normalized Gamma distribution. However, it seems the temperature may have a more significant impact on the self-consistency relation. For example, Trabal et al. (2014) used scattering simulation to analyze the sensitivity of the self-consistency relation to temperature variability in the range 0°- 30°. For such simulation, the DSD and drop shape were modeled by a normalized Gamma distribution and the BZV model, respectively. For a temperature of 20°, it was shown that the NSE is in the range of 10% - 25% while the normalized bias (NB) near 0%. Thus, selecting those coefficients according to the temperature may lead to improved NSE at X-band.

- *What would be the reliability of the weights in presence of orographic obstacles?*

  Biases due to PBB can be identified and corrected by estimating the beam blockage fraction (BBF) or by a consistency between K_{DP} and Z (Lang et al. 2009). This BBF depends on the complexity of the terrain (i.e., blockage pattern) such that BBF could be constant or not within a given radial profile (i.e., one or more "blocks" along a profile). If the BBF varies at range resolution scales, Z and Z_{DR} values in path $\overline{ab}$ of length L^* will be affected differently and will compromise the accuracy of weights. However, if the BBF is approximately constant within $\overline{ab}$, associated biases on Z and Z_{DR} are not relevant as in the case of miscalibration. In addition, the actual NSE of the self-consistency ratio and standard deviation of K_{DP}, estimated gate-by-gate, can be used to identify and study how PBB effects can lower the accuracy of the self-consistency ratio and K_{DP} estimates.

- *How the algorithm will perform in the presence of snow, hail or rain/hail mixture?*

  Incorrect weights are expected in non-rain areas if the self-consistency relation is not adapted to hydrometeors types different than rain. However, it is well known that non-rain areas can be identified using polarimetric thresholds. Moreover, note that any non-rain contamination on Z and Z_{DR} will only affect the accuracy of weights within path $\overline{ab}$ rather than the entire radial profile. In addition, the impact of inaccurate weights on K_{DP} may be reduced if the values of $\Delta\Psi_{DP}$ samples are near 0°.

- *The self-consistency principle is sensitive to non-uniform beam filling affecting Z and Z_{DR}. What would happen to the estimated weights?*

  The accuracy of estimated weights may decrease in presence of non-uniform beam filling (NBF). It is also known that Ψ_{DP} may have an oscillation pattern due to NBF. In such case, any approach to estimate K_{DP} will not perform as desired. However it is subject of future work to analyze the sensitivity of weights to NBF related issues.

- *It seems that the originality of this technique is only given by the optimization of the path lengths. Is it enough?*

  This work is an improved version of the technique given by Otto and Russcheberg (2011) and the novel contribution of this work is the optimal selection of path lengths from a predetermined path length interval, the adaptive selection of $\Delta\Psi_{DP}$ samples based on σ_{ZDR} threshold, another downscaling weight based on the self-consistency principle, the analysis and reduction of σ_K, and the assessment of this type of methodology.

  The optimization of a path length (L), gate-by-gate in an adaptive manner, is an intermediate step towards the estimation of K_{DP} with reduced error. In fact, this optimization is only possible given three elements: a length interval $[L_{\min}; L_{\max}]$, a mathematical formulation of the standard deviation of the K_{DP} estimator, and finally the number of paths M. In order to get these elements, the required weight was derived in order to establish its relation to a path length as well as to Z and Z_{DR} for quality control purposes. In this way, K_{DP} and therefore its standard deviation could be linked to L, Δr, M, and to an introduced variable μ_s that takes into account the storm type. Although we have kept the two polarimetric relations used for δ_{hv} filtering and Ψ_{DP} weighting according to Otto and Russcheberg (2011), they have been incorporated in the proposed approach in a different manner. Furthermore, the method given by Hubbert and Bringi (1995) was implemented and analyzed in this work at X-band frequencies and 0.03 km range resolution, which results have not been shown before to our knowledge.

- *Why the presented technique is not compared against more recent algorithms?*

  The proposed approach have been compared with those from Hubbert and Bringi (1995) and Otto and Russchenberg (2011) because of two reasons. First, the approach of Hubbert and Bringi (1995), hereafter the conventional approach, is widely accepted for K_{DP} estimation at C and X-band, where δ_{hv} is significant. Therefore, recent publications that provide new ways to estimate K_{DP} still refer to the conventional approach for comparison purposes. For example, Wang and Chandrasekar 2009 and Schneebeli et al. 2014 compared their K_{DP} estimates with those from the conventional approach. Recent publications that require K_{DP} also used the conventional approach. For example, Wang et al. 2013 calculated K_{DP} at different elevation tilts to estimate rainfall rate in mountainous areas. More recently, Trabal et al. 2014 estimated K_{DP} in order to calibrate the CASA radar network. Second, the proposed approach is based on Otto and Russchenberg (2011), and therefore, its performance are used for comparison purposes to show the improvements achieved by the presented work.

- *Some estimated K_{DP} values are around 10-12° km^{-1} . At X-band frequencies, it corresponds to rain rates of 110-120 mm h^{-1}. Was the rain that heavy on the date of those measurements?*

  The convective storm event E3 was associated with a supercell located near the border between Belgium and Netherlands. Pictures of this supercell can be found in http://www.weerfotos.be/Stormchase/10-09-11.html. Also, archived images provided by the operational radar of the Netherlands showing heavy precipitation can be found here: https://www.buienradar.nl/nederland/neerslag/buienradar-terugkijken/archief/201109102150. Moreover, storm damage including broken trees were found near the location of IDRA radar in the Netherlands, which corresponds to event E3 but at 19:56 UTC. For photos of this storm damage, please refer to pictures web-link [1].

  Given the circumstances of this storm, high values of K_{DP} at X-band are reasonable. Similar high K_{DP} values (i.e., larger than 10° km^{-1}) at X-band were estimated by Wang and Chandrasekar, 2010 and by Schneebeli et al. 2014.

- *The identified signals at ranges 8-11 km (see Fig. 4.4) are hardly associated with δ_{hv}*

  In the azimuthal radial 213°, the range interval 8-11 km is associated with heavy rain which is indicated by a rapid increment of Ψ_{DP} in an interval of only 3 km. In consequence, areas beyond 11 km are extinct. It is widely known that at X-band, δ_{hv} is significant in heavy rain and therefore it is expected to obtain δ_{hv} values larger than 0°as shown in Fig. 4.4. Definitely, errors in its estimation are expected because Φ_{DP} may present accumulated errors in K_{DP}, particularly towards the end of the radial. However, similar identified δ_{hv} profiles at X-band associated with a rapid increase of Ψ_{DP} were estimated by Schneebeli and Berne (2012). In their work, two rain events were analyzed using a Kalman filter approach to estimate K_{DP} and δ_{hv} profiles which results were shown by Figs. 12 and 13.

- *In which conditions σ_P is equal to 3° ? it depends probably on the range gate spacing and the number of gates involved in the least-squares fit*

  According to Bringi and Chandrasekar (2001), the standard deviation of measured Ψ_{DP} (i.e., σ_P) depends on the number of pulses, normalized Doppler spectrum width (σ_{vn}), and ρ_{hv}. In their book, Figs. 6.27 and 6.30 show values of σ_P in the range 2-5°for $|\rho_{hv}| > 0.95$ and for different values of σ_{vn} and number of pulses. In other words, σ_P depends on the radar waveform and weather environment. This is why a value for σ_P equal to 3° was selected for demonstration purposes.

- *How will the 3 km window in the linear regression affect the high resolution estimation at 0.03 km?*

  The linear regression fit is applied to Ψ_{DP} and denoted as Φ^t_{DP} in order to obtain attenuation corrected Z^t and Z^t_{DR} range profiles. The $\Delta\Psi_{DP}$ samples required to obtain K_{DP} are obtained from measured Ψ_{DP} as indicated by Eq. (4.9) and without using linear regression. For illustration purposes, Fig. 4.4 showed the spatial

[1] http://www.hartvannederland.nl/top-nieuws/2011/overlast-en-schade-door-noodweer/831957

variability of z, Z^t, and Z (case III) as well as Ψ_{DP} and Φ_{DP} (case III). In addition, the PPI plots of z, Z, and K_{DP} given in Figs. 4.3 and 4.5 can be used to observe and compare small spatial features of the storm where the K_{DP} field is successfully maintained. Moreover, the high-resolution aspect of the proposed approach is also seen in Fig. 4.7a by comparing Z-K_{DP} from case I (i.e., self-consistency ratio equal to 1) and case III (i.e., self-consistency ratio different than 1). Last, Fig. 4.7b of the revised manuscript also demonstrates that the adaptive high-resolution method is able to estimate K_{DP} values as high as those resulted from simulation.

- *The conventional method given by Hubbert and Bringi (1995) is commonly applied to pulsed radar systems with range resolution larger than 0.03 km. Thus, is this method really appropriate for a radar system similar to IDRA?*

  The conventional method may provide their best results over areas of heavy rain and depending on the capability of filtering δ_{hv} "bumps" of different extents; however its performance should be independent of the range extent of Ψ_{DP} profiles, unless they are of course in the order of Δr. Thus, the usage of the conventional method is not limited to radars of large range spacing. In fact, for the demonstration of the conventional approach, Hubbert and Bringi (1995) used Ψ_{DP} measurements that were collected at range resolution (Δr) of 0.15 km while Wang and Chandrasekar (2009) applied it to simulated X-band data at Δr of 0.10 km and to observed CASA X-band data at 0.048 km. In addition, Park et al. (2005b) used the conventional technique to estimate Φ_{DP} and K_{DP} from Ψ_{DP} measured at 0.10 km range resolution for attenuation correction, rainfall rate estimation, and DSD retrieval purposes. Trabal et al. (2014) demonstrated their calibration technique based on the self-consistency principle in which the conventional method was applied to the CASA radars. Similar work but at C-band frequencies was given by Carey et al. (2000) who processed Ψ_{DP} measurements at 0.30 km for attenuation correction purposes. More recently, Mishra et al. (2016) also applied the conventional technique at Δr of 0.075 km or less for high-resolution observations of precipitation events as part of a field campaign. Therefore, the method of Hubbert and Bringi (1995) was implemented in our work using appropriate filter parameters because it is a widely accepted technique to remove δ_{hv}, which is an issue at C- and X-band frequencies, from Ψ_{DP} data without excessive smoothing.

- *Combining the selection of L and M, the conventional approach could possibly perform much better for general applications, especially when the path lengths are long. Would the proposed method work well for general applications?*

  For general applications, the proposed method might not work well when Z and Z_{DR} measurements are obtained from non-rain particles or when they are affected for instance by NBF or PBB issues. Another limitation is that our approach requires that the extent of a given Ψ_{DP} profile should be larger than $L_{\min}$ in order to obtain enough $\Delta\Psi_{DP}$ samples. For example, K_{DP} estimates over a Ψ_{DP} profile of 2 km length will not be possible if $L_{\min}$ is set equal 3 km. For observations at long ranges with Δr for instance of 1 km, a path length interval of [8;12] km can be suitable to obtain σ_K in the order of $0.3\,^{\circ}\,\mathrm{km}^{-1}$ according to Eq. (4.11). In the case of the conventional approach, which can be understood as a weighted moving average

filter, the spatial resolution of estimated K_{DP} would be of 6 km (i.e., 6 range gates moving filter) instead of 1 km in order to achieve a σ_K value of 0.35 $^\circ$ km^{-1} (Carey et al. 2000). In both examples, the proposed approach will not provide K_{DP} values for Ψ_{DP} segments less than $L_{\min}$ unless the user sets lower $L_{\min}$ and $L_{\max}$ at expenses of higher σ_K while the conventional technique will not provide K_{DP} estimates at spatial resolution of 1 km.

- *Besides the radial pattern issue on Z_{DR}, the Z and K_{DP} fields show discontinuities (e.g., see Fig. 4.5). Is there a signal processing issue?*

  The radar variables obtained by the IDRA radar show two kind of azimuthal discontinuity signatures. The first one is due to the time IDRA takes to rotate the antenna 360°, which is approximately 1 min. During this time the storm did not stop moving so we can expect an azimuthal discontinuity such as those observed in the Z and K_{DP} fields and indicated by the small circles. The second discontinuity in azimuth is because IDRA does not revisit the same azimuthal radial at exactly 1 min rate due to mechanical factors. In other words, the radar acquires measurements continuously and those measurements are segmented into blocks every 1 min and therefore a small gap (or an extra beam) is possible between the first and last revisited radial of each block as seen in the PPIs of Figs. 4.3 and 4.5. Similar discontinuities of the second type were also seen in Wang and Chandrasekar (2009), Fig. 6, and Marzano et al. (2010), Figs. 3 - 6 and 10. However, such discontinuities should not affect the processing of Ψ_{DP} nor the estimation of K_{DP} because both are treated in a radial-by-radial basis.

- *How high is the correlation coefficient between simulated K_{DP} and Z?*

  A theoretical value of the correlation coefficient $\rho_{Z,K}$ was estimated and equals to 0.75. This value might seem low but it is due to the non-linear relation between Z and K_{DP}. If K_{DP} is expressed in a logarithm scale then the relation Z-K_{DP} becomes linear leading to a $\rho_{Z,K}$ equal to 0.98. However, the computation of $\rho_{Z,K}$ in a linear Z-K_{DP} relation is limited to $Z > 0$ dBZ and $K_{DP} > 0\,^\circ$ km^{-1}; otherwise the logarithm of K_{DP} is not defined. Thus, the value of 0.75 is used as a theoretical reference in order to evaluate all possible values of estimated K_{DP}.

- *One of the criterion of "goodness" of the approach is the correlation between Z and K_{DP}. Is it a robust manner to assess the quality of K_{DP}. Z and K_{DP} are proportional to very different DSD moments, so their correlation is dependent on DSD details.*

  The Z-K_{DP} correlation depends on DSD details. However, the purpose of using $\rho_{Z,K}$ is to compare/measure the performance among different K_{DP} approaches using a given storm event (i.e., a given set of DSD's). The criterion to test K_{DP} results may not be ideal. However, it is always difficult to assess K_{DP} estimates resulting from radar measurements rather than simulations because the true K_{DP} is unknown, and therefore, several authors have recurred to similar evaluation procedures (e.g., Wang and Chandrasekar 2009, Giangrande et al. 2013, and Schneebeli et al. 2014).

- *Is it a dilemma to convince researchers that Z_{DR} and Z can be used to enhance the quality of K_{DP}?. Is the main advantage of K_{DP} not to use attenuated parameters?*

  Despite the fact that main advantages of estimating K_{DP} from noisy Ψ_{DP} in rain are immunity to attenuation and miscalibration issues, the main disadvantage of K_{DP} is its poor spatial resolution, and this disadvantage is one of the primary motivation of this work. Several articles revealed remarkable advantages of recurring to Z and Z_{DR}. For example, Gorgucci et al. (2006) and Adachi et al. (2015) used the self-consistency relation to improve the estimation of specific attenuation profiles $A(r)$ while Lang et al. (2009) used it to correct $Z(r)$ and $Z_{DR}(r)$ measurements for partial beam blockage (PBB) effects. Schneebeli and Berne (2012) also recurred to $Z(r)$ and $Z_{DR}(r)$ to decouple $K_{DP}(r)$ and $\delta_{hv}(r)$ from Ψ_{DP} through polarimetric relations between Z and K_{DP} as well as Z_{DR} and δ_{hv}. Giangrande et al. (2013) incorporated the consistency between Z and K_{DP} to obtain $K_{DP}(r)$ without negative values and suggested to explore the incorporation of more polarimetric relations and evaluate their impact on polarimetric retrieved variables. Last, the well known ZPHI method introduced by Testud et al. (2000) and modified recently by Ryzhkov et al. (2014) included a relation between $Z(r)$ and $A(r)$ to obtain improved estimates of A and rainfall rate while avoiding effects related to miscalibration, wet radomes, and PBB. In this context, I believe that Z and Z_{DR} measurements can be included during the processing of noisy Ψ_{DP} measurements in rain at X-band frequencies to obtain high-resolution K_{DP}.

- *Is necessary to use rainfall rate measurements to verify a new K_{DP} approach?*

  No it is not, multiple K_{DP} methods were demonstrated and published without the use of rainfall rate analyses. For example, Giangrande et al. (2013) proposed and evaluated a linear programming method by comparing scatterplots of Z-K_{DP} against those obtained from least square fitting at C-band and X-band frequencies. Trömel et al. (2013) modified the ZPHI method to estimate δ_{hv} and K_{DP} at X-band frequencies where the reliability of the technique consisted on showing the spatial and temporal continuity of δ_{hv} estimates and comparing K_{DP} estimates resulted from their proposed technique with those resulting from a least square fitting method. Wang and Chandrasekar (2009) introduced a regularization method to control the balance between estimation bias and variance in the estimation of K_{DP} at S-band and X-band frequencies. Their K_{DP} approach was evaluated by comparing K_{DP} values from the introduced method against those resulting from a least square fitting (at S-band) and from the conventional approach (i.e., Hubbert and Bringi (1995) at X-band). The comparisons were based on showing K_{DP} fields and Z-K_{DP} scatterplots. Last, Schneebeli et al. (2014) evaluated a new K_{DP} approach, which is based on the compilation of ensembles of Kalman filter estimates, by comparing Z-K_{DP} scatterplots between the proposed and the conventional approach using simulated and observed data at X-band without the usage of raingauge measurements.

- *Is 15 km radar range enough to test a new K_{DP} approach at X-band frequencies?*

  Yes it is, there are similar publications where X-band data were collected or simu-

C

lated at close range. For example, Testud et al. 2000 evaluated the ZPHI algorithm using a simulation scheme to mimic dual-polarimetric variables at X-, C-, and S-band frequencies limited to a range extend of 20 km. Gorgucci et al. (2006) presented and tested a new algorithm for attenuation correction purposes using the self-consistency principle at X-band frequencies using approximately 5000 simulated range profiles limited to 15 km. Wang and Chandrasekar (2009) also validated their K_{DP} approach using simulated data limited to 15 km and real data limited to 20 km at X-band frequencies. Schneebeli and Berne (2012) evaluated their K_{DP} Kalman-based method using measured data at X-band limited to a range of 10 km. Moreover, a wide research has focused on the observation of convective storm events at close range (~10 to 15 km) using dual-polarimetric signatures at X-band frequencies (e.g., Bluestein et al. (2007), Snyder et al. (2010), and Kurdzo et al. (2015).

D

REFLECTIVITY FIELDS

In section 4.5, four storm events E1-E4 were described in order to test the adaptive high-resolution approach. The four PPIs of Z at 21:51, 22:25, 19:50, and 05:50 UTC corresponding to E1-E4, respectively, are shown in Fig. D.1. The Z fields were corrected from attenuation such that $Z = z + 0.34\Delta\Phi_{DP}$, where Φ_{DP} is calculated by integrating K_{DP} resulting from the adaptive high-resolution method.

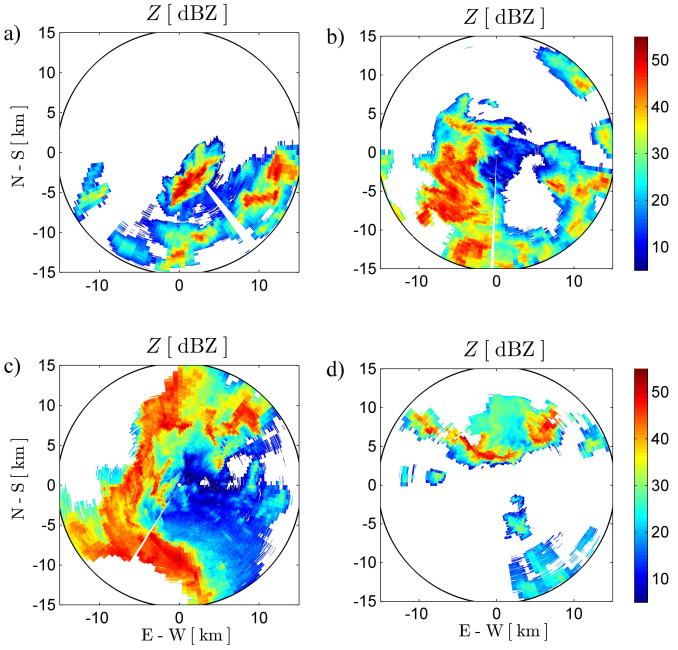

Figure D.1: Attenuation corrected reflectivity fields a)-d) associated to storm events E1-E4 resulting from the adaptive high-resolution technique.

REFERENCES

Adachi, A., T. Kobayashi, and H. Yamauchi, 2015: Estimaiton of raindrops size distribution and rainfall rate from polarimetric radar measurements at attenuating frequency based on the self-consistency principle. *Journal of the Meteorological Society of Japan*, **93 (3)**, 359–388.

Andsager, K., K. V. Beard, and N. F. Laird, 1999: Laboratory measurements of axis ratios for large raindrops. *Journal of the Atmospheric Sciences*, **56**, 2673–2683.

Aydin, K., S. Park, and T. Walsh, 1998: Bistatic dual-polarization scattering from rain and hail at S- and C- band frequencies. *J. Atmos. Oceanic Technol.*, **15**, 1110–1121.

Beard, K., and R. Kubesh, 1991: Laboratory measurements of small raindrop distortion. Part ii: Oscillation frequencies and modes. *Journal of Atmospheric Sciences*, **48**, 2245–2264.

Beard, K. V., and C. Chuang, 1987: A new model for the equilibrium shape of raindrops. *Journal of the Atmospheric Sciences*, **44**, 1509–1524.

Bechini, R., L. Baldini, and V. Chandrasekar, 2013: Polarimetric radar observations in the ice region of precipitation clouds at C-band and X-band frequencies. *J. Appl. Meteor. and Climatology*, **52**, 1147 – 1169.

Beekhuis, H., and I. Holleman, 2008: From pulse to product: Highlights of the digital-IF upgrade of the Dutch national radar network. *5^{th} European Conference of Radar Meteorology and Hydrology*, Helsinki, Finland.

Benard, P., J. Vivoda, J. Masek, P. Smolikova, K. Yessad, C. Smith, R. Brozkova, and J. F. Geleyn, 2010: Dynamical kernel of the Aladin-NH spectral limited-area model: revised formulation and sensitivity experiments. *Quart. J. R. Met. Soc.*, **136**, 155 – 169.

Berne, A., and W. Krajewski, 2013: Radar for hydrology: Unfulfilled promise or unrecognized potential? *Advances in Water Resources*, **51**, 357–366.

Bertalmio, M., L. Vese, G. Spario, and S. Osher, 2003: Simultaneous structure and texture image inpainting. *IEEE Trans. on Image Process.*, **12**, 882 – 889.

Bluestein, H., M. French, R. Tanamachi, S. Frasier, K. Hardwick, F. Junyent, and A. Pazmany, 2007: Close-range observations of tornadoes in supercells made with a dual-polarization, X-band, mobile Doppler radar. *Mon. Wea. Rev.*, **135**, 1522–1543.

Bluestein, H. B., M. M. French, I. PopStefanija, R. T. Bluth, and J. B. Knorr, 2010: A mobile, phased-array Doppler radar for the study of severe convective storms. *Bull. Amer. Meteor. Soc.*, **91**, 579–600.

Bluestein, H. B., W. P. Unruh, and H. Stein, 1997: Doppler radar analysis of the Northfield, Texas, tornado of 25 May 1994. *Mon. Wea. Rev.*, **125**, 212–230.

Brandes, E., G. Zhang, and J. Vivekanandan, 2002: Experiments in rainfall estimation with a polarimetric radar in a subtropical environment. *Journal of Applied Meteorology*, **41**, 674–685.

Bringi, V., T. Kennan, and V. Chandrasekar, 2001: Correcting C-band reflectivity and differential reflectivity data for rain attenuation: a self-consistent method with constraints. *IEEE Trans. Geosci. Remote Sens.*, **39**, 1906 – 1915.

Bringi, V. N., and V. Chandrasekar, 2001: *Polarimetric Doppler Weather Radar Principles and Applications*. Cambridge University Press, Cambridge, UK, 636 pp.

Bringi, V. N., V. Chandrasekar, N. Balakrishman, and D. Zrnić, 1990: An examination of propagation effects in rainfall on radar measurements at microwave frequencies. *J. Atmos. Oceanic Technol.*, **7**, 829 – 840.

Brotzge, J. A., K. Brewster, B. Johnson, B. Philip, M. Preston, D. Westbrook, and M. Zink, 2005: CASA's first test bed: Integrative project #1. 32^{nd} *Conference on Radar Meteorology*, Albuquerque, NM, Amer. Meteor. Soc., 14R.2, URL http://ams.confex.com/ams/pdfpapers/97188.pdf.

Bruni, G., R. Reinoso-Rondinel, N. van de Giesen, F. Clemens, and J. ten Veldhuis, 2015: On the sensitivity of urban hydrodynamic modelling to rainfall spatial and temporal resolution. *Hydrology and Earth System Sciences*, **19**, 691 – 709.

Carey, L., S. Rutledge, D. Ahijevych, and T. Keenan, 2000: Correcting propagation effects in C-band polarimetric radar observations of tropical convecton using differential propagation phase. *J. Appl. Meteor.*, **39**, 1405–1433.

Clark, M., 2011: Doppler radar observations of mesovortices within a cool-season tornadic squall line over the UK. *Atmos. Res.*, **100**, 749–764.

Criminisi, A., P. Perez, and K. Toyama, 2004: Region filling and object removal by exemplar-based image inpainting. *IEEE Trans. on Image Process.*, **13**, 1200 – 1212.

Davis, J., and M. Parker, 2014: Radar climatology of tornadic and nontornadic vortices in high-shear, low-CAPE environments in the mid-atlantic and southeastern United States. *Wea. Forecasting*, **29**, 828–853.

D'Errico, J., 2006: Data interpolation by image inpaiting. MATLAB Central File Exchange, URL http://www.mathworks.com/matlabcentral/fileexchange/4551.

Diederich, M., A. Ryzhkov, C. Simmer, P. Zhang, and S. Trömel, 2015: Use of specific attenuation for rainfall measurement at X-band radar wavelengths. part I: Radar calibration and partial beam blockage estimation. *J. Hydrometeorology*, **16**, 487 – 502.

Dolan, B., and S. A. Rutledge, 2009: A theory-based hydrometeor identification algorithm for X-band polarimetric radars. *J. Atmos. Oceanic Technol.*, **26**, 2071 – 2088.

Doviak, R. J., V. Bringi, A. Ryshkov, A. Zahrai, and D. Zrnic, 2000: Considerations for polarimetric upgrades to operational WSR-88D radars. *J. Atmos. Oceanic Technol.*, **17**, 257–278.

Doviak, R. J., and D. S. Zrnić, 1993: *Doppler Radar and Weather Observations*. Academic, San Diego, Calif., 562 pp.

Elad, M., J. Starck, P. Querre, and D. Donoho, 2005: Simultaneous cartoon and texture image inpainting using morphological component analysis. *Appl. Comput. Harmon. Analy.*, **19**, 340 – 358.

Figueras i Ventura, J., 2009: Design of a high resolution X-band Doppler polarimetric radar. Ph.D. thesis, Delft University of Technology.

Funk, T. W., K. E. Darmofal, J. D. Kirkpatrick, V. L. Dewald, R. W. Przybylinski, G. K. Schmocker, and Y.-J. Lin, 1999: Storm reflecitivity and mesocyclone evoltuion associated with the 15 April 1994 squall line over Kentucky and southern Indiana. *Wea. Forecasting*, **14**, 976 – 993.

Giangrande, S., R. McGraw, and L. Lei, 2013: An application of linear programming to polarimetric radar differential phase processing. *J. Atmos. Oceanic Technol.*, **30**, 1716–1729.

Giangrande, S. E., and A. V. Ryzhkov, 2005: Calibration of dual-polarization radar in the presence of partial beam blockage. *J. Atmos. Oceanic Technol.*, **22**, 1156 – 1166.

Goddard, J., S. M. Cherry, and V. N. Bringi, 1982: Comparison of dual-polarization radar measurements of rain with ground-based disdrometer measurements. *J. Appl. Meteor.*, **21**, 252 – 256.

Goddard, J., J. Tan, and M. Thurai, 1994: Technique for calibration of meteorological radars using differential phase. *Elec. Letters*, **30**, 166–167.

Gorgucci, E., and V. Chandrasekar, 2005: Evaluation of attenuation correction methodology for dual-polarizaiton radars: Application to X-band systems. *J. Atmos. Oceanic Technol.*, **22**, 1195 – 1206.

Gorgucci, E., V. Chandrasekar, and L. Baldini, 2006: Correction of X-band radar observations for propagation effects based on the self-consistency principle. *J. Atmos. Oceanic Technol.*, **23**, 1668 – 1681.

Gorgucci, E., G. Scarchilli, and V. Chandrasekar, 1992: Calibration of radars using polarimetric techniques. *IEEE Trans. Geosci. Remote Sens.*, **30**, 853–858.

Gorgucci, E., G. Scarchilli, and V. Chandrasekar, 1999: Specific differential phase estimation in the presence of nonuniform rainfall medium along the path. *J. Atmos. Oceanic Technol.*, **16**, 1690–1697.

Gorgucci, E., G. Scarchilli, V. Chandrasekar, and V. N. Bringi, 2001: Rainfall estimation from polarimetric radar measurements: Composite algorithms immune to variability in raindrop shape-size relation. *J. Atmos. Oceanic Technol.*, **18**, 1773–1786.

Gourley, J. J., A. J. Illingworth, and P. Tabary, 2009: Absolute calibration of radar reflectivity using redundancy of the polarization observations and implied constraints on drop shapes. *J. Atmos. Oceanic Technol.*, **26**, 689 – 703.

Gourley, J. J., P. Tabary, and J. P. D. Chatelet, 2006: Data Quality of the Meteo-France C-Band Polarimetric Radar. *J. Atmos. Oceanic Technol.*, **23**, 1340 – 1356.

Grazioli, J., M. Schneebeli, and A. Berne, 2014: Accuracy of phase-based algorithm for the estimation of the specific differential phase shift using simulated polarimetric weather radar data. *IEEE Geosci. Remote Sens. Lett.*, **11 (4)**, 763–767.

Groenemeijer, P., 2005: Three events of strong deep moist convection in the Netherlands. Tech. rep., KNMI.

Grumm, R. H., and M. Glazewski, 2004: Thunderstorm types associated with the "broken-S" radar signature. 22^{nd} *Conf. on Severe Local Storms*, Hyannis, MA, Amer. Meteor. Soc.

Gu, J.-Y., A. Ryshkov, P. Zhang, P. Neilley, M. Knight, B. Wolf, and D.-I. Lee, 2011: Polaimetric attenuation correction in heavy rain at C-band. *J. Appl. Meteor. Climatol.*, **50**, 39 – 58.

Haddad, Z. S., S. L. Durden, and E. Im, 1996: Parameterizing the raindrop size distribution. *J. Appl. Meteor.*, **35**, 3 – 13.

Hagen, M., 1992: On the appearance of a cold front with a narrow rainband in the vicinity of the Alps. *Meteorol. Atmos. Phys.*, **48**, 231 – 248.

Hazenberg, P., H. Leijnse, and R. Uijlenhoet, 2014: The impact of reflectivity correction and conversion methods to improve precipitation estimation by weather radar for an extreme low-land mesoscale convective system. *Int. Symp. - Wea. Radar and Hydro.*, ASCE-EWRI.

Heijnen, S., L. Ligthart, and H. Russchenberg, 2000: First measurement with TARA: An S-band transportable atmopsheric radar. *Phys. Chem. Earth*, **25**, 995–998.

Heinselman, P. L., and S. Torres, 2011: High-Temporal-Resolution Capabilities of the National Weather Radar Testbed Phased-Array Radar. *J. Appl. Meteor. and Climatology*, **50**, 579–593.

Holleman, I., A. Huuskonen, M. Kurri, and H. Beekhuis, 2010: Operational monitoring of weather radar receiving chain using the sun. *J. Atmos. Oceanic Technol.*, **27**, 159 – 166.

Holt, A., and J. Shepherd, 1979: Electromagnetic scattering by dielectric spheroids in the forward and backward directions. *J. Phys. A: Math. Gen.*, **12**, 159–166.

Huang, H., K. Zhao, and G. Zhang, 2015: The improvement to the specific differential phase estimation with the modified linear programming method. 37^{th} *Conf. on Radar Meteor.*, Norman, OK, Amer. Meteor. Soc., 13B.5.

Hubbert, J., and V. N. Bringi, 1995: An iterative filtering technique for the analysis of copolar differential phase and dual-frequency radar measurements. *J. Atmos. Oceanic Technol.*, **12**, 643–648.

Hufford, G., 1991: A model for the complex permittivity of ice at frequencies below 1 THz. *Internatinal Journal of Infrared and Millimeter Waves*, **7**, 677–682.

Huuskonen, A., L. Delobe, and B. Urban, 2012: EUMETNET OPERA: Achievements of OPERA-3 and challenges ahead. 7^{th} *European Conf. on Radar in Meteo. and Hydrol.*

i Ventura, J. F., and H. W. Russchenberg, 2009: Towards a better understanding of the impact of anthropogenic aerosols in the hydrological cycle: Idra, {IRCTR} drizzle radar. *Physics and Chemistry of the Earth, Parts A/B/C*, **34 (1–2)**, 88 – 92, doi:http://dx.doi.org/10.1016/j.pce.2008.02.038, URL http://www.sciencedirect.com/science/article/pii/S1474706508000594, <ce:title>Sustainable Water Solutions</ce:title>.

Illingworth, A., and T. Blackman, 2002: The need to represent raindrop size spectra as normalized gamma distributions for the interpretation of polarization radar observations. *J. Appl. Meteor.*, **41**, 286 – 297.

Illingworth, A., T. Blackman, and J. Goddard, 2000: Improved rainfall estimates in convective storms using polarisation diversity radar. *Hydrology and Earth System Sciences*, **4**, 555–563.

Jameson, A. R., 1992: The effect of temperature on attenuation correction schemes in rain using polarization propagation differential phase shift. *J. Appl. Meteor.*, **31**, 1106 – 1118.

Johnston, J. T., P. L. MacKeen, A. Witt, E. D. Mitchell, G. J. Stumpf, M. . D. Eilts, and K. W. Thomas, 1998: The storm cell identification and tracking algorithm: An enhanced WSR-88D algorithm. *Wea. Forecasting*, **13**, 263–276.

Keenan, T., L. Carey, D. Zrnić, and P. May, 2001: Sensitivity of 5-cm wavelength polarimetric radar variables to raindrop axial ratio and drop size distribution. *Journal of Applied Meteorlogy*, **40**, 526–545.

Krikken, F., 2012: Sensitivity analysis for a model physics in HARMONIE. Trainee report, KNMI. URL http://www.knmi.nl/knmi-library/traineereport.html.

Kumjian, M. R., 2013: Principles and applications of dual-polarization weather radar. part II: Warm- and cold-season applications. *J. Operational Meteor.*, **1**, 243 – 264.

Kumjian, M. R., and A. V. Ryzhkov, 2008: Polarimetric signatures in supercell thunderstorms. *J. Appl. Meteor. and Climatology*, **47**, 1940 – 1961.

Lakshmanan, V., C. Karstens, J. Krause, and L. Tang, 2013: Quality control of weather radar data using polarimetirc variables. *J. Atmos. Oceanic Technol.*, **31**, 1234 – 1249.

Lamb, D., and J. Verlinde, 2011: *Physics and Chemistry of Clouds*. Cambridge University Press, New York, USA, 584 pp.

Lane, J. D., and P. D. Moore, 2006: Observations of a non-supercell tornadic thunderstorm from a terminal Doppler weather radar. 23^{rd} *Conf. on Severe Local Storms*, St. Louis, AB, Amer. Meteor. Soc.

Leijnse, H., and Coauthors, 2010: Precipitation measurement at CESAR, The Netherlands. *Journal of Hydrometeorology*, **11**, 1322–1329.

Lemon, L. R., and C. A. Doswell, 1979: Severe thunderstorm evolution and mesocyclone structure as related to tornadogenesis. *Mon. Wea. Rev.*, **107**, 1184–1197.

Lengfeld, K., M. Clemens, C. Merker, H. Münster, and F. Ament, 2016: A simple method for attenuation correction in local X-band radar mesurements using C-band radar data. *J. Atmos. Oceanic Technol.*, **33**, 2315 – 2329.

Liebe, H., G. A. Hufford, and T. Manabe, 1991: A model for the complex permittivity of water at frequencies below 1 THz. *International Journal of Infrared and Millimeter Waves*, **12**, 659–675.

Lim, S., and V. Chandrasekar, 2016: A robust attenuation correction system for reflectivity and differential reflectivity in weather radars. *IEEE Trans. Geosci. Remote Sens.*, **54**, 1727 – 1737.

Lim, S., R. Cifelli, V. Chandrasekar, and S. Y. Matrosov, 2013: Precipitation classification and quantification using X-band dual-polarization weather radar: application in the hydrometeorology testbed. *J. Atmos. Oceanic Technol.*, **30**, 2108 – 2120.

Maki, M., and Coauthors, 2010: X-band polarimetric radar networks in urban areas. 6^{th} *European Conference on Radar in Meteorology and Hydrology*.

Marshall, J. S., W. Hitschfeld, and K. L. S. Gunn, 1955: Advances in radar weather. *Advances in Geophysics*, **2**, 1 – 56.

Marshall, J. S., and W. Palmer, 1948: The distribution of raindrops with size. *J. of Meteorol.*, **5**, 165 – 166.

Matrosov, S., K. Clark, B. Martner, and A. Tokay, 2002: X-band polarimetric radar measurements of rainfall. *J. Appl. Meteor.*, **41**, 941 – 952.

Matrosov, S. Y., R. Cifelli, P. C. Kennedy, S. W. Nesbitt, S. A. Rutledge, V. N. Bringi, and B. E. Martner, 2006: A comparative study of rainfall retrievals based on specific differential phase shifts at X- and S- band radar frequencies. *J. Atmos. Oceanic Technol.*, **23**, 952 – 963.

Matrosov, S. Y., P. C. Kennedy, and R. Cifelli, 2014: Experimentally based estimates of relations between X-band radar signal attenuation characteristics and differential phase in rain. *J. Atmos. Oceanic Technol.*, **31**, 2442 – 2450.

Matrosov, S. Y., D. E. Kingsmill, B. E. Martner, and F. M. Ralph, 2005: The utility of X-band polarimetric radar for quantitative estimates of rainfall parameters. *J. Hydrometeorology*, **6**, 248–262.

McAvoy, B. P., W. A. Jones, and P. D. Moore, 2000: Investigation of an unusual storm structure associated with weak to occasionally strong tornadoes over the Eastern United States. 20^{th} *Conf. on Severe Local Storms*, Orlando, FL„ Amer. Meteor. Soc.

McLaughlin, D., and Coauthors, 2009: Short-wavelength technology and the potential for distributed networks of small radar systems. *Bull. Amer. Meteor. Soc.*, **90 (12)**, 1797 – 1817.

Mishra, K. V., and Coauthors, 2016: Deployment and performance analyses of high-resoltuion Iowa XPOL radar system during the NASA IFloodS campaign. *J. of Hydrometeorology*, **17**, 455 – 479.

Nolen, R. H., 1959: A radar pattern associated with tornadoes. *Bull. Amer. Meteor. Soc.*, **40**, 277–279.

Ochoa-Rodriguez, S., and Coauthors, 2015: Impact of spatial and temporal resolution of rainfall inputs on urban hydrodynamic modelling outputs: A multi-catchment investigation. *Journal of Hydrology*, **531**, 389 – 407.

Oguchi, T., 1983: Electromagnetic wave propagation and scattering in rain and other hydrometeors. *Proceedings of the IEEE*, **71**, 1029 – 1078.

Otto, T., and H. W. J. Russchenberg, 2010: Estimation of the raindrop-size distribtuion at X-band using specific differential phase and differential backscatter phase. *The* 6^{th} *Euro. Conf. on Radar in Meteor. and Hydrol.*, Sibiu, Romania.

Otto, T., and H. W. J. Russchenberg, 2011: Estimation of specific differential phase and differential backscatter phase from polarimetric weather radar measurements of rain. *IEEE Geosci. Remote Sens. Lett.*, **8**, 988–992.

Park, S.-G., V. N. Bringi, V. Chandrasekar, M. Maki, and K. Iwanami, 2005a: Correction of radar reflectivity and differential reflectivity for rain attenuation at X band. Part I: Theoretical and empirical basis. *J. Atmos. Oceanic Technol.*, **22**, 1621–1632.

Park, S.-G., M. Maki, K. Iwanami, V. N. Bringi, and V. Chandrasekar, 2005b: Correction of radar reflectivity and differential reflectivity for rain attenuation at X band. Part II: Evaluation and application. *J. Atmos. Oceanic Technol.*, **22**, 1633–1655.

Pruppacher, H. R., and K. V. Beard, 1970: A wind tunnel investigation of the internal circulation and shape of water drops falling at terminal velocity in air. *Quart. J. R. Met. Soc.*, **96**.

Przybylinski, R., 1995: The bow echo: Obeservations, numerical simulations, and severe weather detection methods. *Wea. Forecasting*, **10**, 203–218.

Ray, P. S., 1972: Broadband complex refractive indices of ice and water. *Appl. Opt.*, **11**, 1836 – 1844.

Reinoso-Rondinel, R., 2011: A framework for adaptive weather sensing using phased-array radar. M.S. thesis, School of Electrical and Computer Engineering, University of Oklahoma, USA.

Reinoso-Rondinel, R., G. Bruni, M. ten Veldhuis, and H. Russchenberg, 2013: Toward the optimal resolution of rainfall estimates to obtain reliable urban hydrological response: X-band polarimetric radar estimates applied to Rotterdam urban drainage system. *36th AMS Weather Radar Conference*, Colorado, USA.

Reinoso-Rondinel, R., H. Russchenberg, T. IJpelaar, G. . Bruni, and M. ten Veldhuis, 2014a: The use of X-band polarimetric radar to assess the impact of severe convection in urban drainage system. *International Symposium Weather Radar and Hydrology, ASCE*, Washington DC, USA.

Reinoso-Rondinel, R., C. Unal, and H. Russchenberg, 2018: Adaptive and high-resolution estimation of specific differential phase for polarimetric X-band weather radars. *J. Atmos. Oceanic Technol.*, **35**, 555–573.

Reinoso-Rondinel, R., C. Unal, H. Russchenberg, T. IJpelaar, and Y. Dufournet, 2014b: Polaimetric weather signatures and Doppler spectral analysis of a convective squall line. *8th European Conference on Radar in Meteorology and Hydrology*, G-P, Germany.

Reinoso-Rondinel, R., T.-Y. Yu, and S. Torres, 2010: Multifunction Phased-Array Radar: Time Balance Scheduler for Adaptive Weather Sensing. *J. Atmos. Oceanic Technol.*, **27**, 1854–1867.

Rinehart, R. E., 2004: *Radar for Meteorologists*. Rinehart Publishing, Columbia, MO, 464 pp.

Russchenberg, H., 1992: Ground-based remote sensing of precipitation using a multi-polarized FM-CW Doppler radar. Ph.D. thesis, Delft University of Technology, delft University Press.

Ruzanski, E., and V. Chandrasekar, 2012: Nowcasting rainfall fields derived from specific differential phase. *J. Appl. Meteor. and Climatology*, **51**, 1950 – 1959.

Ryde, J. W., 1946: *The attenuation and radar echoes produced at centimeter wavelengths by various meteorological phenomena*. Physical Society, Physical Society, pp.

Ryzhkov, and D. S. Zrnić, 1995: Precipitation and attenuation measurements at 10 cm wavelength. *J. Appl. Meteor.*, **34**, 2121–2134.

Ryzhkov, A., M. Diederich, P. Zhang, and C. Simmer, 2014: Potential utilization of specific attenuation for rainfall estimation, mitigation of partial beam blockage, and radar networking. *J. Atmos. Oceanic Technol.*, **31**, 599–619.

Ryzhkov, A., and D. Zrnić, 1996: Assessment of rainfall measurement that uses specific differential phase. *J. Appl. Meteor. Climatol.*, **35**, 2080 – 2090.

Ryzhkov, A., and D. Zrnić, 2005: Radar polarimetry at S, C, and X bands: comparative analysis and operational implications. *32nd Conf. on Radar Meteor.*, Albuquerque, NM, Amer. Meteor. Soc., 9R.3.

Ryzhkov, A. V., S. E. Giangrande, and T. J. Schuur, 2005a: Rainfall estimation with a polarimetric prototype of WSR-88D. *J. Appl. Meteor.*, **44**, 502 – 515.

Ryzhkov, A. V., T. J. Schuur, D. W. Burgess, S. Giangrande, and D. S. Zrnic, 2005b: The joint polarization experiment: polarimetric rainfall measurements and hydrometeor classification. *Bull. Amer. Meteor. Soc.*, **86**, 809–824.

Scarchilli, G., E. Gorgucci, V. Chandrasekar, and A. Dobaie, 1996: Self-consistency of polarization diversity measurement of rainfall. *IEEE Trans. Geosci. Remote Sens.*, **34 (1)**, 22 – 26.

Scarchilli, G., E. Gorgucci, V. Chandrasekar, and T. A. Seliga, 1993: Rainfall estimation using polarimetric techniques at C-band frequencies. *J. Appl. Meteor. Climatol.*, **32**, 1150–1160.

Schellart, A., W. Shepherd, and A. Saul, 2012: Influence of rainfall estimation error and spatial variability on sewer flow prediction at a small urban scale. *Adv. in Water Resour.*, **45**, 65–75.

Schneebeli, M., and A. Berne, 2012: An extended Kalman filter framework for polarimetric X-band weather radar data processing. *J. Atmos. Oceanic Technol.*, **29**, 711–730.

Schneebeli, M., J. Grazioli, and A. Berne, 2014: Improved estimation of the specific differential phase shift using a compilation of Kalman filter ensembles. *IEEE Trans. Geosci. Remote Sens.*, **52 (8)**, 5137–5149.

Schuurmans, J., M. Bierkens, E. Pebesma, and R. Uijlenhoet, 2007: Autmatic predicition of high-resoltuion daily rainfall fields for multiple extends: the potential of operational radar. *Journal of Hydrometeorology*, **8**, 1204–1224.

Schwarz, C., and D. Burgess, 2011: Supercell polarimetric signatures at X-band: Data from VORTEX2. *35^{th} Conf. on Radar Meteor., AMS*.

Seity, Y., P. Brousseu, S. Malardel, G. Hello, P. Bernard, F. Bouttier, C. Lac, and V. Masson, 2011: The AROME-France convectivescale operational model. *Mon. Wea. Rev.*, **139**, 976 – 991.

Snyder, J., H. Bluestein, V. Venkatesh, and S. Frasier, 2013: Observations of polaimetric signatures in supercells by an X-band mobile Doppler radar. *Mon. Wea. Rev.*, **141**, 3 – 29.

Snyder, J., H. Bluestein, and G. Zhang, 2010: Attenuation correction and hydrometeor classification of high-resolution, X-band, dual-polarized mobile radar measurements in severe convective storms. *J. Atmos. Oceanic Technol.*, **27**, 1979–2001.

Steadham, R. M., R. A. Brown, and V. T. Wood, 2002: Prospects for faster and denser WSR-88D scanning strategies. *18^{th} Int. Conf. on Interactive Information and Processing Systems (IIPS) for Meteorology, Oceanography, and Hydrology*, Orlando, FL, Amer. Meteor. Soc., J3.16.

Steinert, J., and M. Chandra, 2008: Cloud physical properties and empirical polarimetric measurements of rain signatures at C-band. *Advances in Radio Science*, **6**, 315–318.

Storm, B., M. Parker, and D. Jorgensen, 2007: A convective line with leading stratiform precipitation from BAMEX. *Monthly Weather Review*, **135**, 1769–1785.

Tabary, P., A.-A. Boumahmoud, H. Andrieu, R. J. Thompson, A. J. Illingworth, E. L. Bouar, and J. Testud, 2011: Evaluation of two "integrated" polarimetric Quantitative Precipitation Estimation (QPE) algorithm at C-band. *J. of Hydrology*, **405**, 248 – 260.

Testud, J., E. L. Bouar, E. Obligis, and M. Ali-Mehenni, 2000: The rain profiling algorithm applied to polarimetric weather radar. *J. Atmos. Oceanic Technol.*, **17**, 332–356.

Thurai, M., G. Huang, V. Bringi, W. Randeu, and M. Sch´onhuber, 2007: Drop shapes, model comparisons, and calculations of polarimetric radar parameters in rain. *Journal of Atmospheric and Oceanic Technology*, **24**, 1019–1032.

Trabal, J. M., E. Gorgucci, V. Chandrasekar, and D. J. McLaughlin, 2014: Evaluation of the self-consistency principle for calibration of the CASA radar network using properties of the observed precipitation medium. *IEEE Trans. Geosci. Remote Sens.*, **52**, 149 – 162.

Trömel, S., M. R. Kumjian, A. V. Ryzhkov, C. Simmer, and M. Diederich, 2013: Backscatter differential phase - Estimation and variability. *J. Appl. Meteor. Climatol.*, **52**, 2529–2548.

Trömel, S., M. Ziegert, A. V. Ryzhkov, C. Chwala, and C. Simmer, 2014: Microwave backhaul links to optimize the performance of algorithms for rainfall estimation and attenuation correction. *J. Atmos. Oceanic Technol.*, **31**, 1748 – 1760.

Ulbrich, C. W., 1983: Natural variations in the analytical form of the raindrop size distribution. *J. Climate Appl. Meteor.*, **22**, 1764–1775.

Unal, C., 2009: Spectral polarimetric radar clutter suppression to enhance atmospheric echoes. *J. Atmos. Oceanic Technol.*, **26**, 1781–1797.

Unden, P., 2002: Hirlam-5 scientific documentation. Tech. rep., HIRLAM-5 Project Rep. SMHI, 143 pp. URL http://www.hirlam.org/.

van de Beek, C. Z., H. Leijnse, P. Hazenberg, and R. Uijlenhoet, 2016: Close-range radar rainfall estimation and error analysis. *Atmos. Meas. Tech.*, **9**, 3837 – 3850.

Vulpiani, G., M. Montopoli, L. D. Passeri, A. G. Gioia, P. Giordano, and F. S. Marzano, 2012: On the use of dual-polarized C-band radar for operational rainfall retrieval in mountainous areas. *J. Appl. Meteor. Climatol.*, **51**, 405–425.

Vulpiani, G., P. Tabary, J. P. D. Chatelet, and F. S. Marzano, 2008: Comparison of advanced radar polarimetric techniques for operational attenuation correction at C band. *J. Atmos. Oceanic Technol.*, **25**, 1118 – 1135.

Wang, Y., and V. Chandrasekar, 2009: Algorithm for estimation of the specific differential phase. *J. Atmos. Oceanic Technol.*, **26**, 2565–2578.

Wang, Y., and V. Chandrasekar, 2010: Quantitative precipitation estimation in the CASA X-band dual-polarization radar network. *J. Atmos. Oceanic Technol.*, **27**, 1665 – 1676.

Wang, Y., J. Zhang, A. V. Ryzhkov, and L. Tang, 2013: C-band polarimetric radar QPE based on specific differential propagation phase for extreme typhoon rainfall. *J. Atmos. Oceanic Technol.*, **30**, 1354–1370.

Wang, Y., P. Zhang, A. V. Ryzhkov, J. Zhang, and P.-L. Chang, 2014: Utilization of specific attenuation for tropical rainfall estimation in complex terrain. *J. of Hydrometeorology*, **15**, 2250 – 2266.

Wauben, W., 2006: KNMI contribution to the WMO laboratory intercomparison of rainfall intensity gauges. Tech. rep., KNMI. [Availabe online at http://www.knmi.nl/bibliotheek/knmipubTR/TR287.pdf].

Weisman, M., and R. Rotunno, 2004: "a theory for strong long-lived squall lines" revisited. *Journal of the Atmospheric Sciences*, **61 (4)**, 361–382.

Weisman, M., and R. Trapp, 2003: Low-level mesovortices within squall lines and bow echoes. part i: Overview and dependence on environment shear. *Mon. Wea. Rev.*, **131**, 2779–2803.

Willis, P. T., 1984: Functional fits to some observed drop size distributions and parameterization of rain. *J. Atmos. Sci.*, **41**, 1648 – 1661.

Zhang, G., J. Vivekanandan, and E. Brandes, 2001: A method for estimating rain rate and drop size distribtuion from polarimetric radar measurements. *IEEE Trans. Geosci. Remote Sens.*, **39**, 830–841.

Zhiqun, H., L. Liping, W. Linlin, and W. Qing, 2015: A comparison of de-noising methods for differential phase shift and associated rainfall estimation. *J. Meteor. Res.*, **29 (2)**, 315–327.

Zrnić, D. S., 1996: Weather radar polarimetry- trends toward operational applications. *Bull. Amer. Meteor. Soc.*, **77 (7)**, 1529–1534.

Zrnić, D. S., and A. Ryzhkov, 1999: Polarimetry for weather surveillance radars. *Bull. Amer. Meteor. Soc.*, **80**, 389–406.

CURRICULUM VITÆ

Ricardo REINOSO-RONDINEL

Ricardo was born on July 23, 1981, in Latin America, more specifically in Lima, Peru. Coming from a school of limited educational resources (http://www.feyalegria.org.pe/) he was admitted to and graduate from a prestigious Peruvian university, obtaining a bachelor degree in Engineering. At the age of 25, he left Peru to seek for higher education programs and to experience and learn from different cultures.

EDUCATION

1999 – 2006	BSc in Electrical Engineering,	
	Pontifical Catholic University of Peru (PUCP)	
	Thesis:	Design and Implementation of a Vehicle Robot to Perform Agriculture Activities
	Supervisor:	Prof. Andres Flores
		Prof. Javier Chang-Fu
2008 – 2011	MSc Electrical & Computer Engineering,	
	The University of Oklahoma (OU)	
	Thesis:	A Framework for Adaptive Weather Sensing using Phased-Array Radar
	Supervisors:	Dr. Tian-You Yu
		Dr. Sebastian Torres
		Dr. Robert Palmer
2012 – 2018	PhD Civil Engineering and Geosciences,	
	Delft University of Technology (TU Delft)	
	Thesis:	New Techniques to Process Differential Phase Measurements in Rain for Polarimetric X-band Weather Radars
	Promotor:	Prof. Dr. Herman Russchenberg

AWARDS

2005	Scholarship award for one academic year Exchange Program Peru-USA, Faculty of Electrical & Computer Engineering (ECE) at the University of Oklahoma (OU), USA
2008	Scholarship award for a Master of Science Program at ECE, OU, USA
2009	Outstanding poster presentation on the Graduate Student Program of OU, USA
2010	Student conference paper award, Advanced Radar Research Center, OU, USA
2015	3^{rd} Best poster presentation on the 37^{th} American Meteorology Society Radar Conference, USA
2015	1^{st} Best poster presentation on the 10^{th} International Workshop on Precipitation on Urban Areas, Switzerland

JOURNAL PUBLICATIONS

1. Yu T.-Y., **R. Reinoso-Rondinel**, R. D. Palmer, 2009: Investigation of Non-Gaussian Doppler Spectra Observed by Weather Radar in a Tornadic Supercell. *J. Atmos. Oceanic Technol.*, 26, 444-461

2. **Reinoso-Rondinel R.**, T.-Y. Yu, S. Torres, 2010: Multifunction Phased-Array Radar: Time Balance Scheduler for Adaptive Weather Sensing. *J. Atmos. Oceanic Technol.*, 27, 1854-1867

3. Bruni G., **Reinoso-Rondinel R.**, N. van de Giesen, F. Clemens, and J. ten Veldhuis, 2015: On the Sensitivity of Urban Hydrodynamic Modelling to Rainfall Spatial and Temporal Resolution. *Hydrol. Earth Syst. Sci.*, 19, 691-709

4. Ochoa-Rodriguez S., L.-P. Wang, A. Gires, **R. Reinoso-Rondinel**, and Co-Authors, 2015: Impact of Spatial and Temporal Resolution of Rainfall Inputs on Urban Hydrodynamic Modelling Outputs: A Multi-Catchment Investigation. *Journal of Hydrology*, 531, 389-407

5. **Reinoso-Rondinel R.**, C. Unal, H. Russchenberg, 2018: Adaptive and High-Resolution Estimation of Specific Differential Phase for Polarimetric X-Band Weather Radars. *J. Atmos. Oceanic Technol.*, 35, 555-573

6. **Reinoso-Rondinel R.**, C. Unal, H. Russchenberg, 2018: Improved Estimation of the Specific Attenuation and Backscatter Differential Phase over Short Rain Paths. *J. Atmos. Oceanic Technol.*, minor revision

CONFERENCE PUBLICATIONS

1. **Reinoso-Rondinel R.**, T.-Y. Yu, R. D. Palmer, 2007: Investigation of Doppler Spectra from a Tornadic Supercell Thunderstorm: Are They Gaussian? Preprints, *33rd Int. Conf. on Radar Meteorology*, Queensland, Australia, Amer. Meteor. Soc. (AMS), Paper P8B.6

2. Yu T.-Y., **R. Reinoso-Rondinel**, R. D. Palmer, 2008: A New Way to Investigate Dynamics in a Storm using Doppler Spectra from Weather Radar. Preprints, *24th Int. Conf. on Interactive Information and Processing Systems (IIPS) for Meteorology, Oceanography, and Hydrology*, New Orleans, LA, AMS, Paper 6B.9

3. **Reinoso-Rondinel R.**, T.-Y. Yu, S. Torres, 2009: Multifunction Phased-Array Radar: Time Balance Scheduler for Adaptive Weather Sensing. Preprints, *34th Int. Conf. on Radar Meteorology*, Williamsburg, VA, AMS, Paper P10.13

4. **Reinoso-Rondinel R.**, S. Torres, T.-Y. Yu, 2010: Task Prioritization on Phased-Array Radar Scheduler for Adaptive Weather Sensing. Preprints, *26th Int. Conf. on IIPS for Meteorology, Oceanography, and Hydrology*, Atlanta, GA, AMS, Paper 14B.6

5. Yu T.-Y., S. Torres, **Reinoso-Rondinel R.**, D. Vigouroux, 2011: Maximizing the Benefits of Adaptive Scanning for Weather Radars: The Development of an Adaptive Weather Sensing Framework to Investigate the Effectiveness of Task-Specific Update Time Assignments. Preprints, *35th Int. Conf. on Radar Meteorology*, Pittsburgh, PA, AMS, Paper 174

6. **Reinoso-Rondinel R.**, G. Bruni, M.-C. ten Veldhuis, H. Russchenberg, 2013: Toward the Optimal Resolution of Rainfall Estimates to Obtain Reliable Urban Hydrological Response: X-band Polarimetric Radar Estimates Applied to Rotterdam Urban Drainage System. Preprints, *36th Int. Conf. on Radar Meteorology*, Breckenridge, CO, AMS, Paper 119

7. **Reinoso-Rondinel R.**, H. Russchenberg, T. IJpelaar, G. Bruni, M.-C. ten Veldhuis, 2014: The Use of X-Band Polarimetric Radar to Assess the Impact of Severe Convection in Urban Drainage System. Preprints, *9th Weather Radar and Hydrology (WRaH) International Symposium*, Washington DC, Envir. & Water Resour. Inst. (EWRI) of the Amer. Soc. of Civil Engineers (ASCE), Paper 75

8. ten Veldhuis M.-C., S. Ochoa-Rodriguez, G,. Bruni, A. Gires, J. van Assel, L. Wang, **R. Reinoso-Rondinel**, S. Kroll, D. Schertzer, C. Onof, P. Willems, 2014: Weather Radar for Urban Hydrological Applications: Lessons Learnt and Research Needs Identified from 4 Pilot Catchments in North-West Europe. Preprints, *9th WRaH International Symposium*, Washington DC, Envir. & Water Resour. Inst. (EWRI) of the Amer. Soc. of Civil Engineers (ASCE), Paper 60

9. **Reinoso-Rondinel R.**, C. Unal, H. Russchenberg, T. IJpelaar, Y. Dufournet, 2014: Polarimetric Weather Signatures and Doppler Spectral Analysis of a Convective Squall Line. Preprints, *8th European Conference on Radar in Meteorology and Hydrology (ERAD)*, Garmisch-Partenkirchen, Germany, Paper 216